

Advanced nonlinear stability analysis of boiling water nuclear reactors

Technische Universität Dresden, Fakultät Maschinenwesen

DISSERTATION

zur Erlangung des akademischen Grades

Doktor-Ingenieur (Dr.-Ing.)

vorgelegt von

Dipl.-Phys. Carsten Lange

geboren am 01.01.1979 in Dohna

Abstract

This thesis is concerned with nonlinear analyses of BWR stability behaviour, contributing to a deeper understanding in this field. Despite negative feedback-coefficients of a BWR, there are operational points (OP) at which oscillatory instabilities occur. So far, a comprehensive and an in-depth understanding of the nonlinear BWR stability behaviour are missing, even though the impact of the significant physical parameters is well known. In particular, this concerns parameter regions in which linear stability indicators, like the asymptotic decay ratio, lose their meaning.

Nonlinear stability analyses are usually carried out using integral (system) codes, describing the dynamical system by a system of nonlinear partial differential equations (PDE). One aspect of nonlinear BWR stability analyses is to get an overview about different types of nonlinear stability behaviour and to examine the conditions of their occurrence. For these studies the application of system codes alone is inappropriate. Hence, in the context of this thesis, a novel approach to nonlinear BWR stability analyses, called RAM-ROM method, is developed. In the framework of this approach, system codes and reduced order models (**ROM**) are used as complementary tools to examine the stability characteristics of fixed points and periodic solutions of the system of nonlinear differential equations, describing the stability behaviour of a BWR loop. The main advantage of a ROM, which is a system of ordinary differential equations (ODE), is the possible coupling with specific methods of the nonlinear dynamics. This method reveals nonlinear phenomena in certain regions of system parameters without the need for solving the system of ROM equations. The stability properties of limit cycles generated in Hopf bifurcation points and the conditions of their occurrence are of particular interest. Finally, the nonlinear phenomena predicted by the ROM will be analysed in more details by the system code. Hence, the thesis is not focused on rendering more precisely linear stability indicators like DR.

The objective of the ROM development is to develop a model as simple as possible from the mathematical and numerical point of view, while preserving the physics of the BWR stability behaviour. The ODEs of the ROM are deduced from the PDEs describing the dynamics of a BWR. The system of ODEs includes all spatial effects in an approximated (spatial averaged) manner, e.g. the space-time dependent neutron flux is expanded in terms of a complete set of orthogonal spatial neutron flux modes. In order to simulate the stability characteristics of the in-phase and out-of-phase oscillation mode, it is only necessary to take into account the fundamental mode and the first azimuthal mode.

The ROM, originally developed at PSI in collaboration with the University of Illinois (PSI-Illinois-ROM), was upgraded in significant points:

- Development and implementation of a new calculation methodology for the mode feedback reactivity coefficients (void and fuel temperature reactivity)

- Development and implementation of a recirculation loop model; analysis and discussion of its impact on the in-phase and out-of-phase oscillation mode
- Development of a novel physically justified approach for the calculation of the ROM input data
- Discussion of the necessity of consideration of the effect of subcooled boiling in an approximate manner

With the upgraded ROM, nonlinear BWR stability analyses are performed for three OPs (one for NPP Leibstadt (cycle7), one for NPP Ringhals (cycle14) and one for NPP Brunsbüttel (cycle16) for which measuring data of stability tests are available. In this thesis, the novel approach to nonlinear BWR stability analyses is extensively presented for NPP Leibstadt. In particular, the nonlinear analysis is carried out for an operational point (OP), in which an out-of-phase power oscillation has been observed in the scope of a stability test at the beginning of cycle 7 (KKLc7_rec4). The ROM predicts a saddle-node bifurcation of cycles, occurring in the linear stable region, close to the KKLc7_rec4-OP. This result allows a new interpretation of the stability behaviour around the KKLc7_rec4-OP.

The results of this thesis confirm that the RAM-ROM methodology is qualified for nonlinear BWR stability analyses.

Content

1	Introduction	1
1.1	Focus of the thesis	3
1.2	State of the art and previous work	7
1.3	Thesis outline	14
1.4	Codes and programs used in this thesis	15
2	Methodology	17
2.1	An overview	17
2.2	Nonlinear stability analysis	19
2.3	Semi-analytical bifurcation analysis using BIFDD	23
2.4	Numerical integration	25
2.5	ROM analysis with both, BIFDD code and numerical integration code	26
2.6	Novel approach for calculation of the ROM input	27
2.7	Stability map	29
3	ROM extensions	31
3.1	Summary of the ROM	31
3.1.1	Neutron kinetic model	32
3.1.2	Fuel heat conduction model	36
3.1.3	Thermal hydraulic model	37
3.2	Mode feedback reactivity calculation	41
3.2.1	Calculation of the mode feedback reactivity in the ROM	41
3.2.2	Calculation of C_{mm}	46
3.3	Recirculation loop	49
3.3.1	The recirculation loop model	49
3.3.2	The effect of the recirculation loop model on the stability behaviour of a simple thermal-hydraulic one heated channel model	52
3.3.2.1	Bifurcation analysis using BIFDD	52
3.3.2.2	Numerical integration	55
3.3.2.3	Summary	58

3.3.3	The effect of the recirculation loop model on the stability behaviour of the ROM (coupled model).....	59
3.3.3.1	Bifurcation analysis using BIFDD	61
3.3.3.2	Numerical integration	66
3.3.3.3	RAMONA5 analysis.....	68
3.3.3.4	Physical interpretation	71
3.3.3.5	Conclusions.....	72
3.4	Subcooled boiling	73
3.4.1	The modified profile fit model	73
3.4.2	Analysis with the TH-model.....	78
3.4.3	Analysis with the ROM for KKLc7rec4.....	84
4	BWR Stability Analyses for NPP Leibstadt	87
4.1	RAMONA5 analysis at the reference OP.....	91
4.1.1	Steady state analysis	91
4.1.2	Transient analysis	93
4.2	Calculation of the ROM input parameters.....	97
4.2.1	Adjustment of the axial void profile.....	97
4.2.2	Estimation of the drift-flux parameters V_{gj} and C_0	101
4.2.3	Calculation of the ROM pressure drops	102
4.2.4	Summary of the ROM input calculation for NPP Leibstadt	105
4.3	Local nonlinear stability analysis	107
4.3.1	Numerical integration at the reference OP	107
4.3.2	Bifurcation analysis	109
4.3.2.1	Semi-analytical bifurcation analysis	109
4.3.2.2	Numerical integration	111
4.3.2.3	Summary.....	112
4.4	Comparative study with RAMONA5 and ROM: Local consideration.....	113
4.4.1	Variation of the core inlet subcooling.....	113
4.4.1.1	RAMONA results	113
4.4.1.2	ROM results	118
4.4.2	Variation of the steady state external pressure drop	119
4.4.2.1	RAMONA results	119

4.4.2.2	ROM results.....	124
4.4.3	Conclusion	126
4.5	Global nonlinear stability analysis	127
4.6	Stability boundary in the N_{sub} - DP_{ext} -parameter space and its relation to the N_{sub} - N_{pch} -parameter space.....	138
4.6.1	Part1:	138
4.6.2	Part 2:	141
4.6.3	Part 3:	144
4.6.4	Conclusions	147
5	Summary and conclusions.....	149
5.1	Modifications of the ROM.....	150
5.1.1	Recirculation loop	150
5.1.2	Subcooled boiling.....	151
5.1.3	Calculation methodology for C_{mn} -coefficients	152
5.2	Novel approach for calculation of the ROM input.....	152
5.3	Nonlinear stability analysis for NPP Leibstadt (KKLc7_rec4).....	153
5.3.1	Local consideration	154
5.3.2	Global consideration	155
5.4	Conclusions	156
5.5	Recommendations to future work	156
6	Literatur.....	159
	Appendix A: Nonlinear stability analysis	165
	Appendix B: ROM description.....	181
	Appendix C: RAMONA5 description.....	199
	Appendix D: Nomenclature	207
	Appendix E: Dimensionless variables.....	215
	Appendix F: ROM input parameters	217
	Appendix G: Summary of the KKB-Analysis	223
	Appendix H: Summary of the KKR-Analysis.....	237

Appendix I: Comparative study TOBI-ROM 249

Acknowledgment 257

1 Introduction

Boiling water reactor (BWR) stability analysis is of paramount interest since it affects the operation of a large number of commercial nuclear reactors. Due to power increase which is the current trend, stability becomes a limiting design concern. The introduction of high efficiency fuels, triggered by improved design of fuel assemblies, enables operation at higher power densities resulting in higher void feedback reactivity and decreased heat transfer time constants which destabilize the BWR system. Another trend of future design of BWRs is to increase the core size which causes a weaker spatial coupling within the neutron field leading to a stronger susceptibility to regional power oscillations. In fact, these trends affect unfavourably the BWR stability behaviour. Hence, in order to guarantee safe and stable BWR operation, an in-depth understanding of the BWR stability behaviour is necessary [1,2].

From theoretical and experimental studies, it is well known that for dynamical systems where two phase flow occurs like BWRs there are **operational points (OP)** in which unstable behaviour is observed. Instabilities of such systems can be subdivided into two main classes. These are

- 1) static instabilities (thermal-hydraulic nature such as excursive Ledingegg instability [3,4]) and
- 2) dynamic instabilities [3,4].

A common feature of the class of static instabilities is that the system suddenly departs from the initial operational point to reach a new operational point. In contrast to static instabilities, dynamic instabilities are characterized by either self-sustained periodic or diverging oscillations of the state variables. Examples of dynamic instabilities are density wave oscillations, pressure-drop oscillations, acoustic instabilities, condensation-induced instabilities (appearing in TH-systems) and power oscillations (neutron kinetic – thermal hydraulic coupled oscillations).

In the context of the nonlinear BWR stability analysis, dynamic instabilities, in particular power oscillations of coupled TH-neutron kinetic systems are of paramount interest. The physical mechanism behind stable and unstable oscillatory behaviour is based on the nonlinear character of the hydraulic equations and on the nonlinear coupling between the neutron kinetics and the thermal hydraulics via void and Doppler feedback reactivity [5-14].

In BWRs, stable or unstable power oscillations usually occur in the low-flow high-power region of the power flow map. Concerning operational safety, this region should be excluded from the nominal operating domain. If the amplitudes of the power oscillations become large enough, technical safety limit values, such as the critical power ratio, could be exceeded and fuel element failure could be expected, if monitoring systems fail. To this end, in GE-BWRs, the so-called exclusion region enclosing the low-flow high-power region is conservatively defined for the specific cycle. Thereby, the definition of the exclusion region is based on validated system code

analyses in combination with stability experiments. In addition to that, the definition of specific counteractive measures allows leaving operational points in which power oscillations are detected by the installed measuring equipment. Figure 1.1 shows the exclusion region for NPP Leibstadt (KKL) cycle 7 [5].

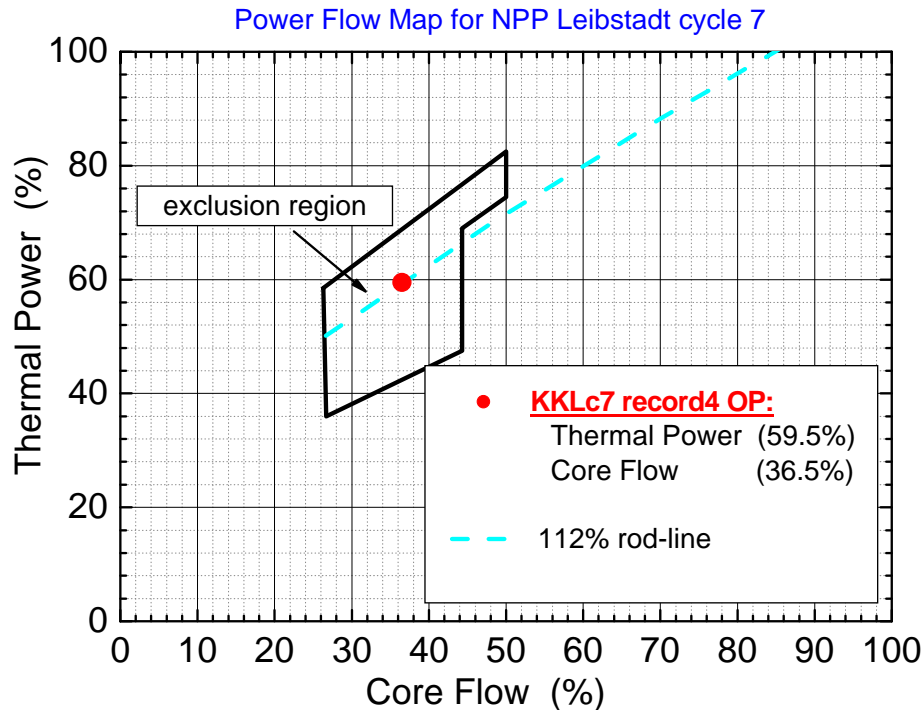


Figure 1.1: Power flow map for NPP Leibstadt cycle 7. An out-of-phase power oscillation was observed in the KKLc7_rec4-OP (KKL cycle 7 record #4) during the stability test at the beginning of cycle 7 [6].

Global or in-phase oscillations and regional or out-of-phase oscillations are two kinds of observed power oscillations. Detailed investigations revealed [1] that in the in-phase mode, the fundamental mode oscillates, while in the out-of-phase mode the first (and/or second) azimuthal mode(s) oscillates: when the power or flow rises in one half of the core, it decreases in the other half whereas the total mass flow and the core power remain constant. The detection of regional power oscillation requires more effort than for the detection of global power oscillation because the phase shifts between signals of all LPRMs have to be evaluated separately to determine the regional power oscillation state [12].

NPP owners are generally interested in minimizing the exclusion region because it restricts significantly the nominal operation domain. For shrinking of the exclusion region sufficient knowledge about the cycle specific BWR stability behaviour is necessary. In particular, conditions of the excitation of power oscillation and its stability behaviour should be taken into account.

1.1 Focus of the thesis

In general, the dynamics of a BWR can be described by a system of coupled nonlinear partial differential equations. From nonlinear dynamics, it is well known that such systems show, under specific conditions, a very complex temporal behaviour which is reflected in the solution manifold of the corresponding system of equations. Consequently, to understand the nonlinear stability behaviour of a BWR, the solution manifold of the system of differential equations must be examined. In particular, with regard to the existence of operational points in which stable and unstable power oscillations are observed, stable or unstable fixed points and stable or unstable periodic solutions are of specific interest [16] in the frame of this thesis. Note that stable or unstable periodical solutions correspond to stable or unstable limit cycles. Saddle-node bifurcation of cycles (turning points or fold bifurcations) [17], period doubling and other nonlinear phenomena [17-22] could also be important from the reactor safety point of view.

It is stressed here that unstable limit cycles (repellers) require special attention regarding safe BWR operation. If the unstable limit cycle is “born” in a subcritical Hopf bifurcation point, stable fixed points and unstable limit cycles will coexist in the linear stable region [16,17]. The corresponding phase space portrait (see Appendix A) is depicted in Figure 1.2. If a sufficiently small perturbation is imposed on the system, the state variables will return to the steady state solution. The terminology “sufficiently small perturbation” means that the trajectory starts within the basin of attraction of the fixed point (see Appendix A). Roughly speaking, the perturbation amplitude of the phase state variables is less than the repeller amplitude (see Appendix A). But if a sufficiently large perturbation is imposed on the system, the state variables will diverge in an oscillatory manner. The terminology “sufficiently large perturbation” means that the perturbation amplitude is larger than the repeller amplitude. In this case the trajectory will start out the basin of attraction of the fixed point.

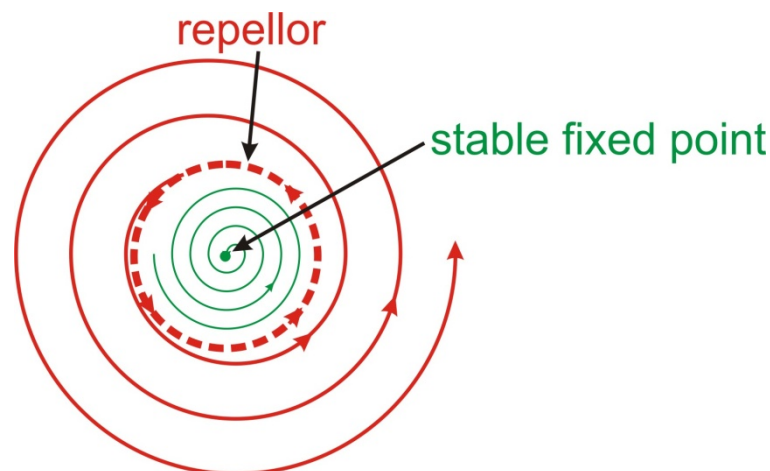


Figure 1.2: Phase space portrait of an unstable limit cycle (unstable periodical solution) close to subcritical Hopf bifurcation (see Appendix A).

It should be noticed here that a linear stability analysis does not allow to examine the existence of unstable limit cycles, e.g. the asymptotic decay ratio is less than one ($DR < 1$). This example shows that conceivably unstable conditions (from the nonlinear point of view) are not recognized and the operational safety limits could be violated. Hence, in order to reveal this kind of phenomena, nonlinear BWR stability analysis is necessary.

This thesis is concerned with nonlinear analyses of BWR stability behaviour, contributing to a deeper understanding in this field. Despite negative feedback-coefficients of a BWR, there are operational points (OP) at which oscillatory instabilities occur. So far, a comprehensive and an in-depth understanding of the nonlinear BWR stability behaviour are missing, even though the impact of the significant physical parameters is well known. In particular, this concerns parameter regions in which linear stability indicators, like the asymptotic decay ratio, lose their meaning.

Nonlinear stability analysis is usually carried out using integral (system) codes, describing the dynamical system by a system of nonlinear partial differential equations (PDE). One aspect of nonlinear BWR stability analyses is to get an overview about different types of nonlinear stability behaviour and to examine the conditions for which they occur. This means:

- 1) to find the critical values of selected parameters at which the dynamical system experiences a bifurcation and
- 2) to analyse the bifurcation type revealing the type of oscillatory instabilities generated at the bifurcation point.

For these studies, the application of system codes alone is inefficient and cumbersome. System codes are not able to exactly determine, for instance, the critical values of parameters at which subcritical Hopf bifurcations, generating unstable limit cycles, occur. These critical values of parameters can be calculated by system codes in an approximated manner under large computational effort only. In addition to that, the behaviour of the algorithms, employed by system codes, in the close neighbourhood of bifurcation points is not well known. They should, however, correctly simulate the temporal behaviour sufficient far away from bifurcation points.

In the context of this thesis, a novel approach to nonlinear BWR stability analyses, called **RAM-ROM** method, is developed. Here, "RAM" is a synonym for system codes. In the framework of this approach, integrated BWR (system) codes (**RAMONA5**, Studsvik/Scandpower) and simplified BWR models (**reduced order model, ROM**) are used as complementary tools to examine the stability characteristics of fixed points and periodic solutions of the nonlinear differential equation system describing the stability behaviour of a BWR loop [23-26]. The intention is, firstly, to identify the stability properties of certain operational points by performing ROM analysis and, secondly, to apply the system code RAMONA5 for a detailed nonlinear stability investigation in the neighbourhood of these operational points. The advantage of ROMs is the possible straightforward coupling with specific methods of the nonlinear dynamics. From this methodology, new stability indicators for nonlinear

phenomena like limit cycles can be calculated [16-22]. In the scope of this work, the ROM is coupled with methods of the semi-analytical bifurcation analysis (bifurcation code BIFDD [16]). This method allows the calculation of a stability indicator (Floquet parameter) for limit cycles which are generated particularly by Hopf bifurcations [16,19].

In other words, in the context of the ROM analysis, an overview about different types of nonlinear behaviour of the BWR for selected parameter spaces will be obtained. In particular, the stability properties of limit cycles generated in Hopf bifurcation points and the conditions under which they occur will be analysed. The nonlinear analysis using system codes is applied to verify the ROM results and to perform a more detailed analysis. Hence, the use of RAM and ROM as complementary tools leads to a more reliable nonlinear BWR stability analysis.

The objective of the ROM development is to develop a model as simple as possible from the mathematical and numerical point of view while preserving the physics of the BWR stability behaviour. The ODEs of the ROM are deduced from the PDEs describing the dynamics of a BWR. The system of ODEs includes all spatial effects in an approximated (spatial averaged) manner, e.g. the space-time dependent neutron flux is expanded in terms of a complete set of orthogonal spatial neutron flux modes. In order to simulate the stability characteristics of the in-phase and out-of-phase oscillation mode, for instance, it is only necessary to take into account the fundamental mode and the first azimuthal mode¹. The neglecting of all the other higher modes reduces the number of ODEs significantly because each neutron flux mode requires an ODE for its mathematical description.

Note that, in some cases, the application of linear stability analyses is sufficient for BWR stability analysis (see Appendix A). Here, the decay ratio (DR) is often used as linear stability indicator that loses its physical meaning in nonlinear operational regime. The thesis, however, is not focused on rendering more precisely linear stability indicators like DR.

This work is a continuation of the previous work at the Paul Scherrer Institute (PSI, Switzerland) and the University of Illinois (USA) on this field [7-15]. The current ROM developed originally at PSI in collaboration with the University of Illinois (PSI-Illinois-ROM) was upgraded in two significant points:

- Development and implementation of a new calculation methodology for the mode feedback reactivity coefficients (void and fuel temperature reactivity)
- Development and implementation of a recirculation loop model, analysis and discussion of its impact on the in-phase and out-of-phase oscillation mode
- Development of a novel physically justified approach for the calculation of the ROM input data

¹ In the neutron kinetic model of the ROM, only the fundamental mode and the first/second azimuthal mode are taken into account, because the higher modes have never been observed.

- Discussion of the necessity of consideration of the effect of subcooled boiling in an approximate manner

With the upgraded ROM, nonlinear BWR stability analyses are performed for three OPs (one for NPP Leibstadt (cycle7), one for NPP Ringhals (cycle14) and one for NPP Brunsbüttel (cycle16) for which measuring data of stability tests are available. In this thesis, the novel approach to nonlinear BWR stability analyses is extensively presented for NPP Leibstadt. The nonlinear stability analysis for NPP Leibstadt and NPP Ringhals will be carried out for operational points (KKLc7_rec4-OP [6], see Figure 1.1 and KKRc14_rec9-OP [28]) in which linear unstable out-of-phase power oscillations were observed during stability tests. In contrast to KKL and KKR, the investigation for NPP Brunsbüttel was conducted for an operational point in which an increasing in-phase power oscillation was observed during the stability test at the beginning of cycle 16 [29].

1.2 State of the art and previous work

Complex system codes such as RAMONA [30-32] are common practice for BWR stability analyses. System codes include relative, detailed physical models of all nuclear power plant components significant for specific transient analyses. For BWR stability analyses, the 3D core models used by system codes are of particular importance to simulate spatial effects such as regional power oscillations [8].

In preparation of the RAMONA input, as a first step, it is necessary to calculate the microscopic and macroscopic cross sections for a defined uniform cell using lattice codes such as CASMO or HELIOS [7,8,12,30-32]. The resulting macroscopic cross sections (XS) are stored in multidimensional XS-tables. Here the XS are functionalized with respect to the actual parameters (like void, fuel temperature...) and history parameters (like burn-up, void history...). The steady state core simulators (PRESTO2, POLCA7, SIMULATE, ...) calculate the 3D distributions of all significant reactor parameters such as power, burn-up, 3D xenon distribution and 3D void distribution. These 3D distributions are code inputs for system codes that calculate the BWR transient behaviour in selected operational points.

In the framework of BWR stability analysis, application of so-called linearized versions of system codes is common practice to calculate the linear stability boundary. In these system codes, the system of differential equations, describing the BWR stability behaviour, are linearized. Hence, these code versions are only able to calculate the local stability characteristics of fixed points as long as the Hartmann-Großmann-theorem [16-22] is fulfilled. As stated before, a linear stability analysis is not capable to reveal nonlinear phenomena such as limit cycles.

In order to analyse the stability characteristics of limit cycles and the conditions under which they occur in the exclusion region and its close neighbourhood, nonlinear stability analysis is necessary. It should be pointed out that user of system codes must pay attention to the stability behaviour of their algorithms employed. In particular, physical and numerical effects [33,34] regarding power oscillations and the behaviour of numerical damping of the algorithms should be known in detail. Numerical diffusion, for example, can corrupt the results of system codes significantly, which is explained in more detail in the following. Consider the one-dimensional advection equation

$$\frac{\partial \Phi}{\partial t} + v \frac{\partial \Phi}{\partial z} = S \quad . \quad (1.1)$$

This type of differential equation is frequently used in thermal-hydraulics. The solution is $\Phi(z,t) = F(z - vt)$ where v is the propagation velocity. If $\Phi(z,t=0) = F(z)$ is an initial condition, and S ($S=0$) is the source term (is not considered continuously), the solution describes a translation of the initial distribution of the transported quantity Φ with the propagation velocity v .

In order to integrate the partial differential equation (1.1), a spatial discretization method using an explicit time-integration algorithm is applied. It follows

$$\Phi_i^{k+1} = N_c \Phi_{i-1}^k + (1 - N_c) \Phi_i^k \quad (1.2)$$

$$TE = \Delta z (v \Phi_{zz} / 2 - \Delta z \Phi_{zzz} / 6 + \dots) + \Delta t (\Phi_{tt} / 2 + \Delta t \Phi_{ttt} / 6 + \dots) \quad , \quad (1.3)$$

where TE is the truncation error of the spatial and time discretization. The truncation error specifies the spatial and temporal approximations introduced by the discretization (represented in this case by a Taylor expansion of the third order). In other words, the discretization changes the original partial differential equation significantly. For small Δt and Δz , the resulting equation in this approximation contains a dispersion term as well as a diffusion term

$$\frac{\partial \Phi}{\partial t} + v \frac{\partial \Phi}{\partial z} = S \quad \leftrightarrow \quad \frac{\partial \Phi}{\partial t} + v \frac{\partial \Phi}{\partial z} - S = \mu \frac{\partial^2 \Phi}{\partial z^2} + \varepsilon \frac{\partial^3 \Phi}{\partial z^3} \quad , \quad (1.4)$$

where $\mu = v / 2(\Delta z - v \Delta t) = v \Delta z / 2(1 - N_c)$ is the numerical diffusivity, $N_c = v \Delta t / \Delta z$ is the Courant number, $\varepsilon = v(\Delta z)^2 / 6 \cdot (1 - N_c)(N_c - 1)$ is the numerical dispersion coefficient, Δt is the time step and Δz is the lattice spacing. The corresponding solution can be written as

$$\Phi(z, t) = \Phi_0 e^{\left(-\mu \left(\frac{2\pi}{l} \right)^2 t + i \left(\frac{2\pi}{l} \right) (z - c \Delta t) \right)} \quad . \quad (1.5)$$

Here, $\Phi_0 = \Phi(z, t = 0)$ is the initial condition. Roughly speaking, the solution (1.5) is a damped wave with dispersion. This means, the solution will be dampened and broadened during the time evolution.

As can be seen in the above example, the errors introduced by the numerical algorithms including discretization method, change both the amplitude of the initial distribution (numerical dissipation) and the translational velocity (numerical dispersion). This means, during the time evolution an initial Φ -distribution is deformed and the summary effect, called numerical diffusion, corrupts the correct solution significantly. As a consequence, after a sufficient number of time steps the numerical algorithms deliver a wrong solution.

Numerical diffusion can be reduced by a suitable choice of algorithm related constants like e.g. the Courant number (see equations (1.3) and (1.4)) and time integration algorithms (e.g. explicit time integration has often less numerical diffusion than implicit) [33,34]. Note that, some minimal numerical diffusion is necessary to prevent the growth of numerical induced oscillations. In some modern thermal-hydraulics codes like RETRAN-3D numerical diffusion is eliminated by the method of characteristics (MOC). By using system codes with a free nodalization like TRAC(-B) or some RELAP versions, strong damping effects by numerical diffusion should be expected. Hence, this type of codes is not suitable for stability analysis without modifications (as introduction of higher order difference schemes). It is stressed that the integration of the momentum equation along a closed recirculation loop as defined in RAMONA

reduces significantly the numerical diffusion effect caused by the momentum equation (see Appendix C).

In reduced order models, where the partial differential equation (PDE) system is transformed into an ordinary differential equation (ODE) system, numerical diffusion does not exist. A question then arises: Is it in principle possible to describe the nonlinear BWR stability behaviour with a system of ODEs instead of a system of PDEs? The goal of application of ROMs is to reveal the solution manifold of the BWR system.

One of the first simplified BWR models was published by March-Leuba, Cacuci and Perez [35-37]. The intention was to demonstrate the solution manifold of a relatively simple system of nonlinear differential equations (phenomenological, reduced order, five-equation model), where the nonlinear analyses were carried out entirely numerically. This model is represented by a nonlinear dynamic feedback system including a point kinetic model with one effective group of delayed neutrons, a model for fuel heat transport with a fuel heat transfer constant, and a second-order void reactivity model describing the void reactivity behaviour. In order to yield the transfer function measured from real BWRs, the parameters of the model were adjusted appropriately. They showed that bifurcating solutions exist (see also Rizwan-uddin [38]) when selected parameters are varied. In particular, they demonstrated that higher bifurcations (bifurcating periodical solutions) and aperiodic states in certain parameter regions also exist.

It should be pointed out that this simple reduced order model does not include the momentum transport [8]. The second-order equation of the void reactivity is developed only from the mass and energy balance equations. Hence, the March-Leuba model is not able to describe the density wave phenomenon because of the absence of the pressure drop balance. However limit cycle power oscillations have been found with this model. This shows that density wave mechanism does not play a significant role in power oscillations. This means that the BWR system can be unstable even if it is stable in a purely hydraulic sense [8]. Later, an extended version (including momentum balance and recirculation loop) of this model was used to investigate the fuel behaviour under large amplitude oscillations.

Munoz-Cobo and Verdù (1991) performed an analytical local bifurcation analysis of the March-Leuba five-equation system using Hopf bifurcation theory [39]. This is the first BWR stability analysis (known from literature research) for which purely analytical bifurcation analysis was performed. To this end, they selected one of the system parameters to be the bifurcation parameter. In order to find the critical value of the bifurcation parameter, this parameter was varied systematically as long as the Hopf-conditions are fulfilled while keeping all the other parameters in this model fixed. Passing the critical parameter value, the fixed points bifurcate to periodic solutions (limit cycles). To determine the stability characteristics of the periodic solution, they applied the centre manifold reduction technique for the critical parameter value to reduce the five-equation system to a two-dimensional equation system [19]. Afterwards, they transformed the resulting two-dimensional equation system into the

Poincarè normal form [19,20] which yields the information of the stability properties of the periodic solution at the critical point. This analysis confirmed the results obtained by March-Leuba et al. (1986) [35-37].

Later, Munoz-Cobo et al. [40-43] developed a ROM in order to study the stability characteristics of in-phase and out-of-phase power oscillations by performing numerical integration. The neutron kinetic model of this ROM is based on the mode expansion approach where the space and time dependent neutron flux is expanded in terms of the LAMBDA modes [44-46]. The thermal-hydraulic behaviour is described by two hydraulic heated channels which are divided into two axial regions, namely the single phase region and the two phase region, respectively. The two phase region is represented by a homogeneous equilibrium model (HEM). They demonstrated that limit cycle out-of-phase power oscillations only appear when the reactivity feedback of the first azimuthal mode is increased artificially. This ROM was later extended by a mechanistic subcooled boiling model [43]. This means, they introduced a third axial channel region between the single and two phase region. In effect, they pointed out qualitatively that the feedback gain necessary to achieve out-of-phase power oscillations when subcooled boiling is not included in the ROM is more than twice the gain that is necessary when subcooled boiling is included.

Karve et al. [47] developed an advanced ROM consisting of three sub-models: the neutron kinetic model (fundamental and first azimuthal mode), the fuel heat conduction model (three radial regions) and the thermal-hydraulic model (two heated flow channels, HEM). In the neutron kinetics the mode expansion approach is also applied (see Munoz-Cobo et al [40-43]) but the space and time dependent neutron flux is expanded in terms of the so-called OMEGA modes [48] (In particular, Karve used analytical expression for the OMEGA modes instead of the real 3D power distributions as used by Munoz-Cobo et al. [40-43] and Dokhane et al. [12]). The fuel heat conduction model is based on the one-dimensional (radial), time dependent heat conduction equation (PDE) for the fuel rod where three distinct radial regions, the fuel pellet, the gap and the clad are modelled (see Appendix B). In order to reduce the PDE to ODEs, they assumed a two-piecewise quadratic spatial approximation for the fuel rod temperature and applied the variation principle approach. To test the validity of the model (four ODEs) using the variation principle method, they also developed a model (sixty-four ODEs) which is based on the eigenfunction expansion method. They chose the variation principle method as a reasonable compromise between the accuracy of the solution and the simplicity of the model. In order to convert the PDEs of the thermal-hydraulics into ODEs, they applied the weighted residual approach introduced by Clauss and Lahey [49]. Thereby, instead of simple linear approximations for the space dependence of the single phase enthalpy and the two phase quality, they introduced simple quadratic approximations for these quantities (see Appendix B). These approximations lead to a five equation system (ODE) describing the thermal-hydraulics of a heated (or boiling) flow channel. The author's showed, that these approximations yield stability results of a boiling flow channel that compare well with the rather complicated functional differential equation (FDE) analysis performed

in [50]. The BWR stability analysis with this ROM was carried out entirely by numerical integration.

Most of the previous studies mentioned above applied either pure analytical mathematical manipulations, or pure numerical integration. The application of pure analytical bifurcation analysis, for instance as applied in [51], is limited to few dimensional equation systems (few order models like 3 or 4 dimensions) with a fixed parameter configuration because the algebraic complexity increases rapidly with the number of system equations. This method is not suited for parameter variation studies because the specific mathematical manipulation must be repeated for each changed parameter value. Numerical integration, on the other hand, can only be carried out for a limited number of parameter values. Hence, both methods are limited to a small region of the rather large parameter space. Hence, computer programs which are capable to evaluate appropriately the differential equation system could be helpful to avoid cumbersome algebra. Tsuji et al. (1993) [81] used a computer program called BIFOR2 [16] to perform bifurcation analysis of a simplified BWR model.

Van Bragt et al. [52-54], Dokhane et al. [9-15], Zhou et al. [55-57] and Rizwan-uddin [38] used a new version of BIFOR, called BIFDD, to perform semi-analytical bifurcation analysis of their own simplified BWR models. Firstly, they carried out semi-analytical bifurcation analysis using BIFDD to examine the stability properties of fixed points and periodical solutions in selected parameter spaces and secondly they applied numerical integration method for selected parameters. Note that, the results of the bifurcation analysis using BIFDD are restricted to Hopf bifurcation points (local bifurcation analysis). Hence, numerical integration methods are necessary, on one hand, to independently confirm the results of the bifurcation analysis using BIFDD and, on the other hand, to study the solution manifold in parameter regions far away from Hopf bifurcation points.

The ROM analysis method explained in the previous paragraph was used by van Bragt et al. [52-54] for stability analyses of natural circulation BWRs. Zhou and Rizwan-uddin coupled the Karve-ROM [47] with BIFDD and carried out semi-analytical bifurcation analysis to obtain a better physical understanding of BWR instabilities. One of their studies was focused on the role of the pairs of complex conjugated eigenvalues of the Jacobian matrix (see Appendix A) with the largest and second largest real parts in determining the in-phase and out-of-phase oscillation modes (eigenstate) [55,56].

In any of the studies (except van Bragt et al. [54]) mentioned in the last two paragraphs, the existence of turning points has not been a focus. Rizwan-uddin [38] was the first who showed the existence of turning points in the March-Leuba five-equation system. For this purpose: (1) he coupled the March-Leuba model with BIFDD to perform semi-analytical bifurcation analysis where (in contrast to Munoz-Cobo and Verdù (1991)) any of the model parameters can be used as bifurcation parameter and (2) he carried out numerical integration to confirm the predictions of the bifurcation analysis and to investigate the nonlinear behaviour more distant from the Hopf bifurcation point. The study of van Bragt et al. [54] was devoted to analyse the impact

of the void distribution parameter C_0 and the axial power profile on the thermal-hydraulic stability behaviour (heated channel model [54]). He found a turning point for a symmetrically peaked axial power profile. This type of bifurcation does not exist for a uniformly heated channel.

Dokhane et al. [9-15] developed the PSI-Illinois-ROM and performed nonlinear BWR stability analysis where the RAM-ROM method was applied for the first time. The PSI-Illinois-ROM (summarized in Appendix B) consists of three coupled sub-models which are similar to the Karve-ROM. These are a neutron kinetic model, a fuel heat conduction model and a thermal-hydraulic model. The goal was to develop a BWR model as simple as possible from the mathematical and numerical point of view while preserving the physics of the BWR stability behaviour. A further demand was that the solution manifold of the ROM should be as close as possible to that one of RAMONA5. Hence the physical sub-models of the ROM should be similar to that one of RAMONA5. The neutron kinetic model of this ROM is based on the two energy group diffusion approach, where the mode expansion approach is used. Thereby the space and time dependent neutron flux is expanded in terms of the LAMBDA modes [46]. The diffusion problem is transformed into the mode-kinetic equations in which the mode-feedback reactivities describe the feedback from the thermal-hydraulics to the neutron kinetics via the void- and Doppler-effect. In the expressions for the mode-feedback reactivities, the so-called mode-feedback reactivity coefficients will be calculated from the specific RAMONA5 model.

The fuel heat conduction model of the PSI-Illinois ROM is completely adopted from the Karve-ROM [47]. The thermal-hydraulic model is described by two representative heated flow channels. As used by Karve et al. [47], the single phase enthalpy and the two phase quality have spatially quadratic profiles and the partial differential equation system is transformed into an ordinary differential equation system by applying the weighed residual procedure [12,47]. The main advantage of the thermal-hydraulic model of the PSI-Illinois-ROM is that the behaviour of the two phase flow is represented by the drift flux model developed by Rizwan-uddin [58-61].

Dokhane et al. (2004) [12] applied the PSI-Illinois-ROM to analyse the Leibstadt operational point KKLc7 record 4. Comprehensive parameter variation study was performed and its impact on the stability boundary and nature of the Hopf bifurcation was analysed. This investigation allowed the first direct assessment of the sensitivity of the developed ROM, viz. of both its applicability and its limitations. It was found that the SB and bifurcation characteristics are sensitive regarding variation of certain operating and design parameters, e.g. the drift flux parameters (V_{gi} and C_0) or the inlet and exit pressure loss coefficients (K_{inlet} and K_{exit}) [12]. From these results follows that particular attention should be paid to evaluate adequately the design and operating parameters.

The main discrepancies between RAMONA and PSI-Illinois-ROM are:

- 1) The PSI-Illinois-ROM could not predict the correct oscillation mode. While the stability test and RAMONA predict an increasing out of phase power oscillation

tion, the ROM predicts an in-phase power oscillation. This was justified only by the limitations of the feedback reactivity model [12].

- 2) The location of the reference OP with respect to the stability boundary in the $N_{sub} - DP_{ext}$ -operating plane is not correctly predicted by the PSI-Illinois-ROM (see Figure 1.3) [12]:
 - RAMONA predicts the qualitative behaviour in the neighbourhood of the reference OP as follows: (1) The higher the core inlet subcooling, the more unstable the system is. (2) The reference OP is located in the linear unstable region close to the SB whereby $N_{sub,c} < N_{sub,ref}$ ($N_{sub,c}$ is the critical core inlet subcooling for which the Hopf conditions are fulfilled and $N_{sub,ref}$ is the core inlet subcooling corresponding to the reference OP).
 - The opposite behaviour is predicted by the PSI-Illinois-ROM: (1) The higher the core inlet subcooling, the more stable the system becomes. (2) The reference OP is located in the linear unstable region close to the SB whereby $N_{sub,c} > N_{sub,ref}$.

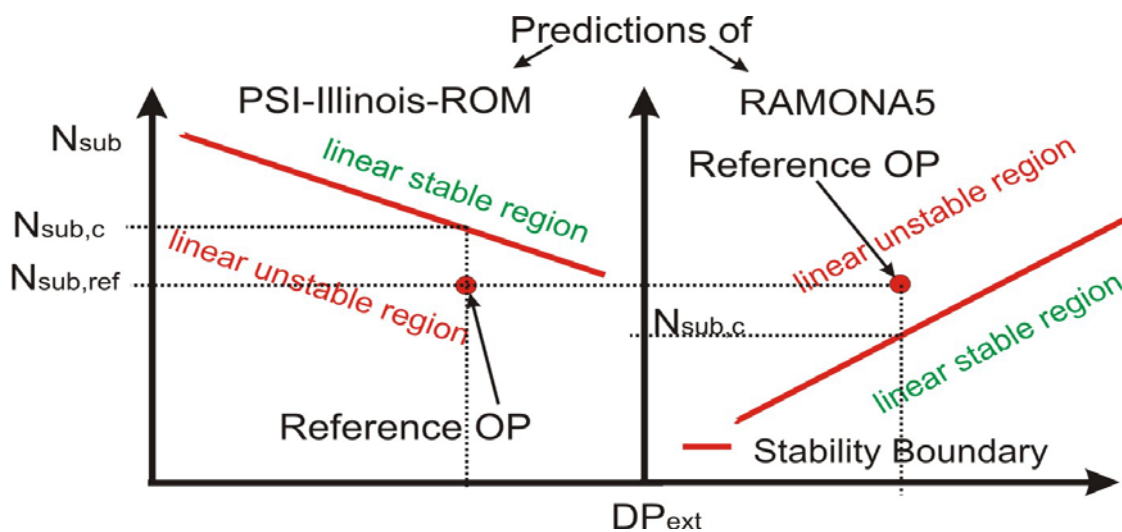


Figure 1.3: Locations of the reference OP respect to the stability boundary predicted by RAMONA5 and PSI-Illinois-ROM.

1.3 Thesis outline

The thesis has two principle aspects:

- ROM extensions (chapter 3) and
- BWR stability analysis using the RAM-ROM method (chapter 4).

In particular, the RAM-ROM method is applied to NPP Leibstadt, NPP Ringhals and NPP Brunsbüttel. A detailed demonstration of the RAM-ROM method is given for NPP Leibstadt in chapter 4. The analysis for NPP Brunsbüttel and NPP Ringhals are summarized briefly in Appendix G and Appendix H.

Chapter 2 provides an introductory description of the methodology of the present nonlinear BWR stability analysis research. This chapter includes general remarks to nonlinear stability analysis (section 2.2, more details of the mathematical description is given in Appendix A). Sections 2.3 and 2.4 present the two independent ROM-techniques: (a) the semi-analytical bifurcation analysis with the bifurcation code BIFDD and (b) numerical integration of the ROM differential equation system. A general description of the new calculation method of the ROM-input is presented in section 2.6 and a corresponding example is presented in section 4.2 of chapter 4 for NPP Leibstadt.

In section 3.1, a brief overview about the three sub-models of the PSI-Illinois ROM is shown, while a detailed description is presented in Appendix B. In section 3.2 the mode feedback reactivity calculation is discussed and the new calculation methodology of the mode feedback reactivity coefficients is presented.

The recirculation loop model and its effect on the stability behaviour are presented in section 3.3. The physical model of the recirculation loop and the final ODE for the channel inlet velocities is developed in subsection 3.3.1. As a starting point, its effect on the stability behaviour of a simple thermal-hydraulic one heated channel model (sub-model of the ROM) is analysed in subsection 3.3.2. The following investigation, carried out in subsection 3.3.3, is devoted to study the effect of the recirculation loop on the BWR stability behaviour using the ROM. Thereby the effect on the in-phase and out-of-phase oscillation modes (oscillation state) are analysed.

In section 3.4, the necessity of consideration of the effect of subcooled boiling in an approximate manner using a profile fit model will be discussed [27]. In subsection 3.4.1 is presented the profile fit model developed originally by Levy et al. (1967) [27]. The first analysis with the profile fit model carried out in subsection 3.4.2 was devoted to study the differences between the axial void profiles provided by the original two-phase flow model and the subcooled boiling model. The aim of the analysis performed in subsection 3.4.3 is to compare the effect of the use of the uniform axial power profile in the ROM with the effect of neglecting subcooled boiling on the axial void profiles.

An in-depth nonlinear BWR stability analysis employing the RAM-ROM method is demonstrated in chapter 4. To this end, at first, in section 4.1 RAMONA analysis at the reference OP is performed. In particular, the steady state analysis and the corre-

sponding transient analyses are presented in subsections 4.1.1 and 4.1.2. After the RAMONA analysis, the calculation of the ROM input parameters is carried out in section 4.2. The adjustment of the axial void profile, the estimation of the drift flux parameters (V_{gi} and C_0) and the calculation of the ROM pressure drops are presented explicitly in the subsections 4.2.1, 4.2.2 and 4.2.3. In section 4.3 the ROM analysis at the reference OP is performed and semi-analytical bifurcation analysis is carried out in appropriated parameter spaces. The comparative study with RAMONA and ROM is carried out in section 4.4, where a parameter variation study is performed for the core inlet subcooling and the steady state external pressure drop.

In section 4.5, an in-depth nonlinear stability analysis is carried out in which the discrepancy between results of the semi-analytical bifurcation analysis, achieved with BIFDD, and numerical integration of the ROM equation system is explained by the existence of saddle-node bifurcation of cycles (also called fold bifurcation or turning point).

Section 4.6 is devoted to reveal the relation of the stability boundary, calculated in the $N_{sub} - DP_{ext}$ -parameter space, to the $N_{sub} - N_{pch}$ -parameter space. This section is organized in three parts. In the first part is discussed the physical meaning of the SB calculated in the $N_{sub} - N_{pch}$ -parameter space. In Part 2 is shown the relation of the SB calculated in the $N_{sub} - DP_{ext}$ -parameter space to the SB calculated in the $N_{sub} - N_{pch}$ -parameter space. The last part of this section is an extension of part 2.

Finally, summary and conclusions based on the thesis results are given in chapter 5. Besides, recommendations to future work are also given in this chapter.

1.4 Codes and programs used in this thesis

In this section, a brief overview over the different codes employed in this thesis is given.

- **System code RAMONA5:** All system code analyses carried out for BWR stability analyses have been performed with the Studsvik-Scanpower-BWR code RAMONA5 [30-32]. This code is described shortly in Appendix C.
- **Bifurcation code BIFDD:** The local bifurcation analysis (semi-analytical bifurcation analysis) is performed with the bifurcation code BIFDD [16] written in FORTRAN language. A short description of BIFDD is given in section 2.3. The input parameter vector, the initial guess for the phase space variables, the ROM equation system and its Jacobian matrix are also represented by FORTRAN-subroutines calling the BIFDD code.
- **MATLAB:** The numerical integration is carried out with the numerical integration code written in the MATLAB environment (see section 2.4) [12].
- **LAMBDA_REAC code:** The LAMBDA_REAC code is used to calculate the mode reactivities, the spatial neutron flux modes (LAMBDA-modes, eigenvectors $\bar{\Psi}_n(\vec{r})$) and the corresponding eigenvalues (see subsection 3.2.2) [46].

2 Methodology

2.1 An overview

In the framework of the applied methodology of nonlinear BWR stability analyses, integrated BWR (system) codes and simplified BWR models are used as complementary tools to examine the stability properties of fixed points and periodical solutions (Figure 2.1). ***It will be repeated that this thesis is devoted to reveal and identify nonlinear core behaviour of a BWR. A refinement, for instance, of the DR (as linear stability indicator) estimation is not the objective of this work.*** The intention is, firstly, to identify the stability properties of certain operational points by performing ROM analysis and, secondly, to apply the system code for a detailed stability investigation in the neighbourhood of these operational points. All system code analyses reported in this thesis have been carried out with the Studsvik-Scanpower-BWR code RAMONA5.

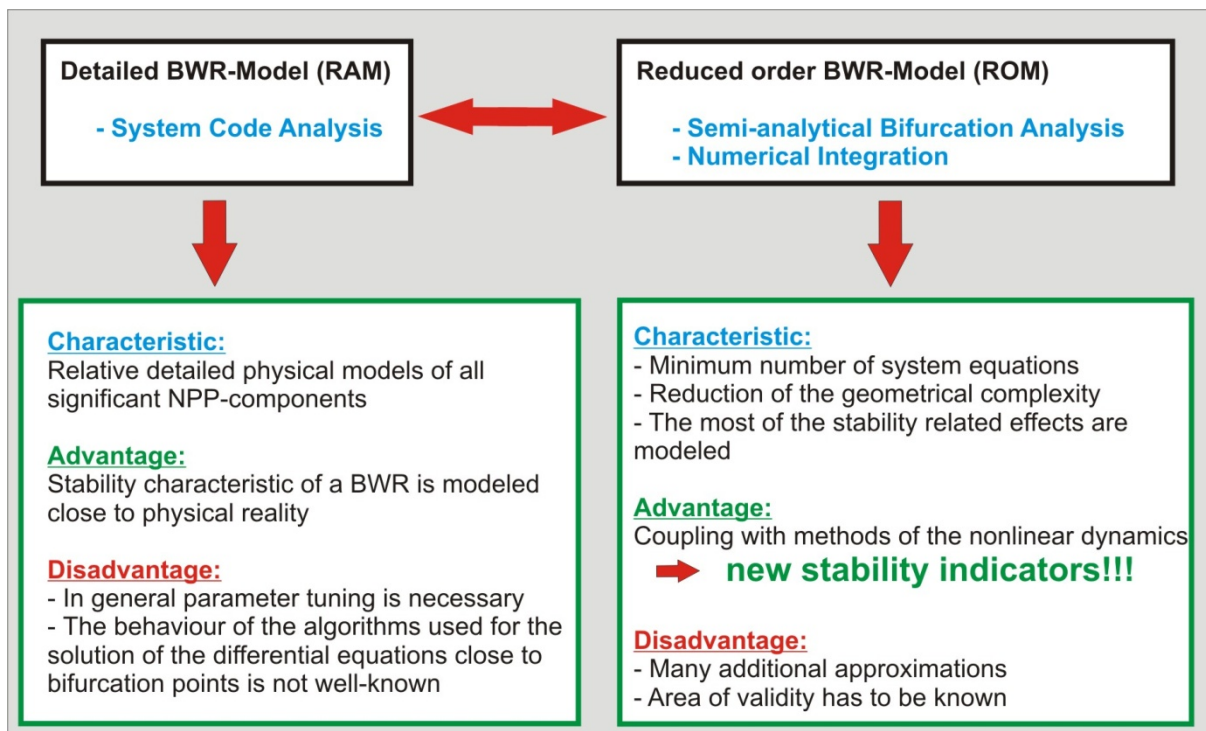


Figure 2.1: Overview over the methodology applied for the nonlinear BWR stability analyses where RAMONA5 and ROM are used as complementary tools.

System codes are computer programs which include detailed (space-dependent) physical models of all nuclear power plant components which are significant for a particular transient analysis. Therefore, such detailed BWR models should be able to represent the stability characteristics of a BWR close to the physical reality. Nonlinear BWR stability analysis using large system codes is currently common practice in many laboratories [12]. A particular requirement is the integration of a 3D neutron

kinetic model, which permits the analysis of regional or higher mode stability behaviour. A detailed investigation of the complete solution manifold of the nonlinear equations describing the BWR stability behaviour by applying system codes needs comprehensive parameter variation studies which require large computational effort. Hence system codes are inappropriate to reveal the complete nonlinear stability characteristics of a BWR. Furthermore, in section 1.2 was mentioned that user of system codes must pay attention to the stability behaviour of the algorithms employed [33,34]. In particular, physical and numerical effects regarding power oscillations and the behaviour of numerical damping of the algorithms should be known in detail. As demonstrated in section 1.2, numerical diffusion can corrupt the results of system codes significantly. Therefore, reduced order analytical models could be helpful to get a first overview over the stability landscape to be expected.

The ROM is characterized by a minimum number of system equations which is realized by the reduction of the geometrical complexity. One demand on the ROM is, because the ROM sub-models should be as close as possible to the sub-models used in RAMONA, that the solution manifold of the RAMONA model should be as close as possible to the solution manifold of the ROM. E.g., both neutron kinetic models (ROM and RAMONA) are based on the two neutron energy group diffusion equations. Both thermal-hydraulic two phase flow models are represented by models which consider the mechanical non-equilibrium (different velocities of the phases of the fluid) [9-15,30,32].

The main advantage of employing ROM's is the possible coupling with codes which include methods of nonlinear dynamics like bifurcation analysis. In the framework of application of such techniques, the scope of BWR stability analyses can be expanded significantly. For example, bifurcation analysis of a BWR system leads to an overview over types of instabilities. The existence of **stable and unstable periodical solutions** (correspond to limit cycles) can be examined reliably. Further, the stability behaviour of global and regional power oscillation states can be investigated in detail.

In the scope of the present ROM analyses two independent techniques are employed. These are the semi-analytical bifurcation analysis with the bifurcation code BIFDD and the numerical integration of the ROM differential equation system. Bifurcation analysis with BIFDD determines the stability properties of fixed points and periodical solutions. For independent confirmation of these results, the ROM system will be solved directly by numerical integration for selected parameters.

Another advantage of the present ROM application is that the ROM-input is based on the specific RAMONA5 model and its steady state solution for a selected operational point, called reference operational point (reference OP). This means, in the framework of our approach, a steady state RAMONA5 run for the reference OP is necessary before the ROM analyses can be performed. One principle demand on the procedure for calculating the ROM-input is that the steady state conditions of the reference OP, predicted by the RAMONA5 model, are simulated correctly by the ROM. Only in this case it is reasonable to perform specific system code investigations in an environment where unstable behaviour is predicted by the ROM analysis.

2.2 Nonlinear stability analysis

Generally, stability analysis is the investigation of the temporal behaviour of the state variables after an internal or external perturbation is imposed on the dynamical system, while one or more system parameters will be varied in their domain of definition. If the system is stable, all state variables converge to the equilibrium point also called singular fixed point (or in its close neighbourhood, also called “Lyapunov stability” [17-20,22]). If the system is unstable, at least one of the state variables is diverging in an oscillatory or exponential manner. The critical value of the system parameter(s) which separates stable fixed points from unstable ones is the so-called stability boundary. A detailed description is given in Appendix A.

For BWR stability analysis, application of linear stability analysis is common practice. A linear stability analysis allows analysing the local stability behaviour of fixed points only (see Figure 2.2). It can be applied as long as the Hartmann-Großmann-theorem (HG-theorem, see Appendix A) is fulfilled. The terminology “analysing the local stability behaviour of fixed points” means to reveal all solutions of the dynamical system near an equilibrium point (or singular fixed point) of the state space (or phase space). The HG-theorem is of particular importance because it justifies the application of linear stability analysis of nonlinear dynamical systems.

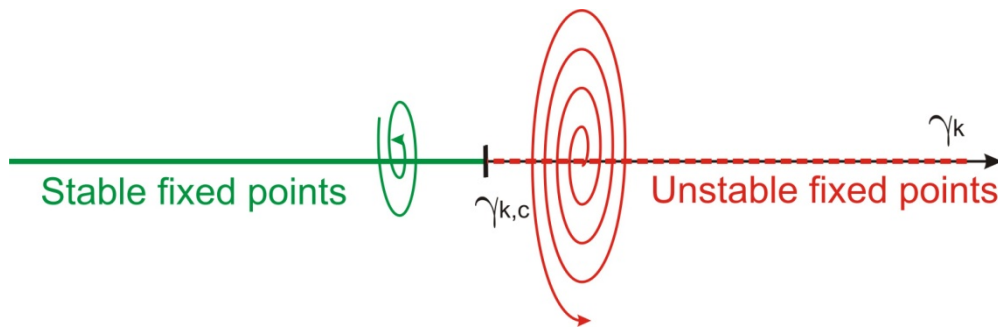


Figure 2.2: Linear stability analyses reveal only the local stability behaviour of fixed points, while the stability behaviour of limit cycles cannot be analysed. Figuratively, a linear stability analysis can reveal only the phase space portrait in a close neighbourhood of the singular fixed point.

In order to explain the limitation of a linear stability analysis more in detail, the following consideration is made. Supposing the system parameter γ_k (will be defined later) is varied in its domain of definition. For all $\gamma_k \in \mathbb{R}$ the temporal behaviour of the state variables is analysed. The local stability behaviour of the fixed point can change when reaching the critical value $\gamma_k = \gamma_{k,c}$. When passing $\gamma_{k,c}$, the fixed point will lose its local stability, viz. the phase space portrait will change significantly at $\gamma_k = \gamma_{k,c}$. At $\gamma_{k,c}$ the dynamical system will have at least one eigenvalue (pair of complex conjugated eigenvalues) with a zero real part ($\text{Re}(\lambda_i) = 0$ with $\lambda_i(\gamma_{k,c})$). As a consequence, at $\gamma_{k,c}$ the dynamical system lost its hyperbolicity [17-20,22] and thus the HG-theorem is not fulfilled. Hyperbolicity is an important property of nonlinear dynamic systems: If only hyperbolic fixed points exist (the real part of all eigenvalues of the (system) Jacobian matrix is different from zero), the application of linear stability

analysis methods is allowed (In this case, there exist either stable or unstable fixed points, either decreasing or increasing oscillations for all system parameter values). Hence in many cases linear stability analysis is sufficient (e.g. frequency domain codes use the transfer function technique). But if a so-called Hopf bifurcation occurs at $\gamma_{k,c}$ the solution of the nonlinear systems can bifurcate from a singular fixed point solution **to** a limit cycle solution (periodic solution) **and** a singular fixed point solution. The limit cycle which is born at $\gamma_{k,c}$ can either be stable (see Figure 2.3) or unstable (see Figure 2.4) depending on the nature of the bifurcation (bifurcation characteristics). It should be noted that at $\gamma_{k,c}$ the HG-theorem is not fulfilled and thus nonlinear stability analysis like bifurcation analysis is necessary to analyse the system behaviour. Independently on whether a stable or an unstable limit cycle exist, a linear stability analysis is able to analyse only the local stability behaviour of fixed points (depicted in Figure 2.2) while the bifurcation analysis carried out at $\gamma_{k,c}$ reveals the existence of limit cycles and provides their stability characteristics (depicted in Figure 2.3 and Figure 2.4).

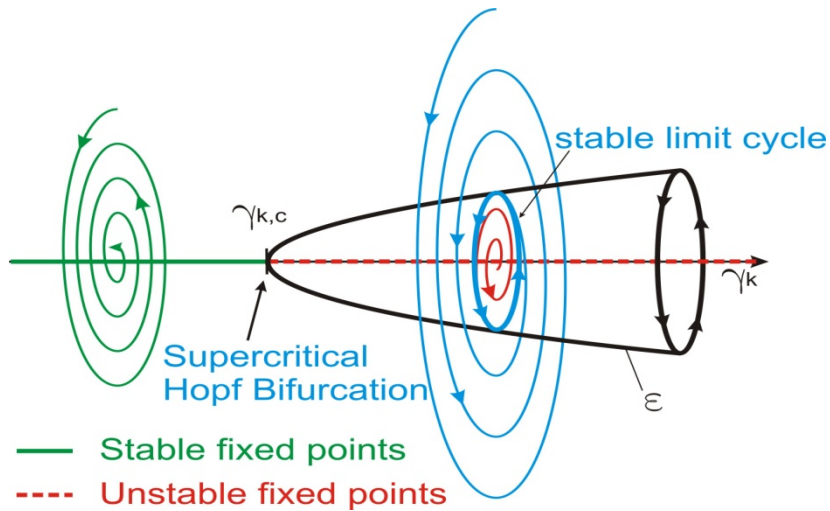


Figure 2.3: The nature of the Hopf bifurcation at $\gamma_{k,c}$ is supercritical. This means, at $\gamma_{k,c}$ a stable limit cycle is born and coexist with unstable fixed points in the linear unstable region.

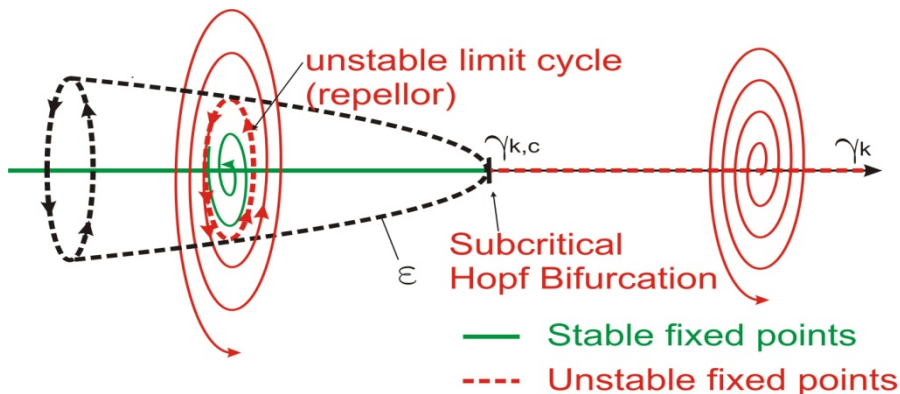


Figure 2.4: The nature of the Hopf bifurcation at $\gamma_{k,c}$ is subcritical. This means, at $\gamma_{k,c}$ an unstable limit cycle is born and coexist with stable fixed points in the linear stable region.

The existence of a Hopf bifurcation is the (mathematical) reason for the sudden appearance of periodic oscillations (limit cycles). These periodic solutions will be observed in the BWR dynamics as global (in-phase) or regional (e.g. out-of-phase or azimuthal mode) power oscillations.

In the literature, the nonlinear phenomenon **limit cycle** is defined to be an isolated closed trajectory in the state space [17]. The term **isolated** means that neighbouring trajectories are not closed which means that they spiral either toward or away from the limit cycle. The limit cycle is stable, if all neighbouring trajectories approach it (see linear unstable region in Figure 2.3). In this case, the limit cycle acts as an attractor. The limit cycle is unstable, if all neighbouring trajectories are repelled from it. In this case, the limit cycle acts as a repeller (see linear stable region in Figure 2.4).

As indicated in the previous paragraphs, in the framework of the present nonlinear BWR stability research (in particular, the semi-analytical bifurcation analysis), the so-called Hopf bifurcations play a dominant role. The occurrence of such type of dynamical bifurcations is ensured by the Hopf theorem [16-19]. This theorem, which is also called Poincarè-Andronov-Hopf bifurcation (PAH-B) theorem, guarantees the existence of stable and unstable periodic solutions of nonlinear differential equations if certain conditions are satisfied [16-19]. For a mathematical description, the autonomous dynamical system,

$$\frac{d}{dt}\vec{X}(t) = \vec{F}(\vec{X}(t), \gamma) \quad (2.1)$$

is considered. Thereby, $\vec{X} \in \mathbb{R}^n$ is the state vector, \vec{F} (with $\vec{F} : \mathbb{R}^n \times \mathbb{R} \rightarrow \mathbb{R}^n$ is C^∞) is a vector field and $\gamma \in \mathbb{R}^m$ is a parameter vector (also called control parameter vector with m components). Let \vec{X}_0 be the steady state solution $0 = \vec{F}(\vec{X}_0, \gamma)$ of Eq. (2.1) for all γ and $J(\gamma)$ be the Jacobian matrix of $\vec{F}(\vec{X}_0, \gamma)$ [16]. It is assumed that one parameter γ_k (with $k \in [1, \dots, m]$) of the vector γ is selected as bifurcation parameter. This means, γ_k is varied in a region of interest. If the following Hopf conditions are fulfilled:

- 1) For a critical parameter value $\gamma_{k,c}$ there exists a pair of complex conjugate eigenvalues $\lambda(\gamma_{k,c}) = \pm i\omega$,
- 2) all the other eigenvalues have strictly negative real parts, and
- 3) $\frac{\partial \lambda(\gamma_k = \gamma_{k,c})}{\partial \gamma_k} \neq 0$

a family of periodic solutions

$$\vec{X}(t, \gamma) = \vec{X}_0(\gamma_{k,c}) + \varepsilon \operatorname{Re} \left[e^{\frac{i2\pi t}{T(\varepsilon)}} \vec{p}_1 \right] + 0(\varepsilon^2) \quad (2.2)$$

of (2.1) with small amplitude ε exist in \vec{X}_0 for $\gamma_{k,c}$ [16], where \vec{p}_1 is the eigenvector of the linearized system associated with the pair of complex conjugated eigenvalues responsible for the bifurcation and T is the period of the oscillation.

In order to get information about the stability property of the periodic solution, the (linear) Floquet theory is applied where the so-called Floquet exponent (Floquet parameter, see Appendix A) β appears [19] which determines the stability of the periodic solution. If $\beta < 0$, the periodic solution is stable (supercritical bifurcation, see Figure 2.3) while if $\beta > 0$, the periodic solution is unstable (subcritical bifurcation, see Figure 2.4) [16,19]. Roughly spoken, the Floquet parameter can be interpreted as a stability indicator for limit cycles. It is a result of a special technique from nonlinear dynamics. A more detailed description is given in Appendix A.

If the Hopf theorem is satisfied, the nonlinear equation system can be reduced to a two-dimensional nonlinear equation system by applying the centre manifold reduction approach [16-19]. The resulting equation system, which represents the dynamical behaviour of the complete system of equations in a close neighbourhood of the fixed point where the Hopf theorem is fulfilled, will be transformed into the Poincaré normal form [16-20] (see Appendix A). From this equation system parameters (in particular the Floquet exponents) which determine the stability properties of the fixed point, can be extracted numerically.

2.3 Semi-analytical bifurcation analysis using BIFDD

As mentioned in the previous sections, the bifurcation code BIFDD is used to perform semi-analytical bifurcation analysis of the ROM differential equation system. BIFDD was developed by Hassard in 1980 to perform numerically bifurcation analysis for ordinary differential equations (ODEs) with time delays [16]. Methods applied in BIFDD allow determining the stability properties of fixed points and periodical solutions without the need for solving the corresponding equation system.

In order to calculate the critical value $\gamma_{k,c}$ of the bifurcation parameter, the frequency ω and the amplitude ε of the oscillation and the Floquet parameter β , BIFDD applies several methods, such as Lindstedt-Poincaré asymptotic expansion [21], centre manifold reduction technique and transformation technique into the Poincaré Normal Form, commonly used in nonlinear dynamics [16-20]. These methods are summarized in Appendix A. In the scope of the Lindstedt-Poincaré expansion, (for example) the Floquet exponent β is expanded in terms of small amplitudes ε as $\beta = \varepsilon\beta_1 + \varepsilon^2\beta_2$, where $\beta_1 = 0$ and thus $\beta \approx \beta_2$ [21].

Figure 2.5 summarizes the bifurcation analysis using BIFDD.

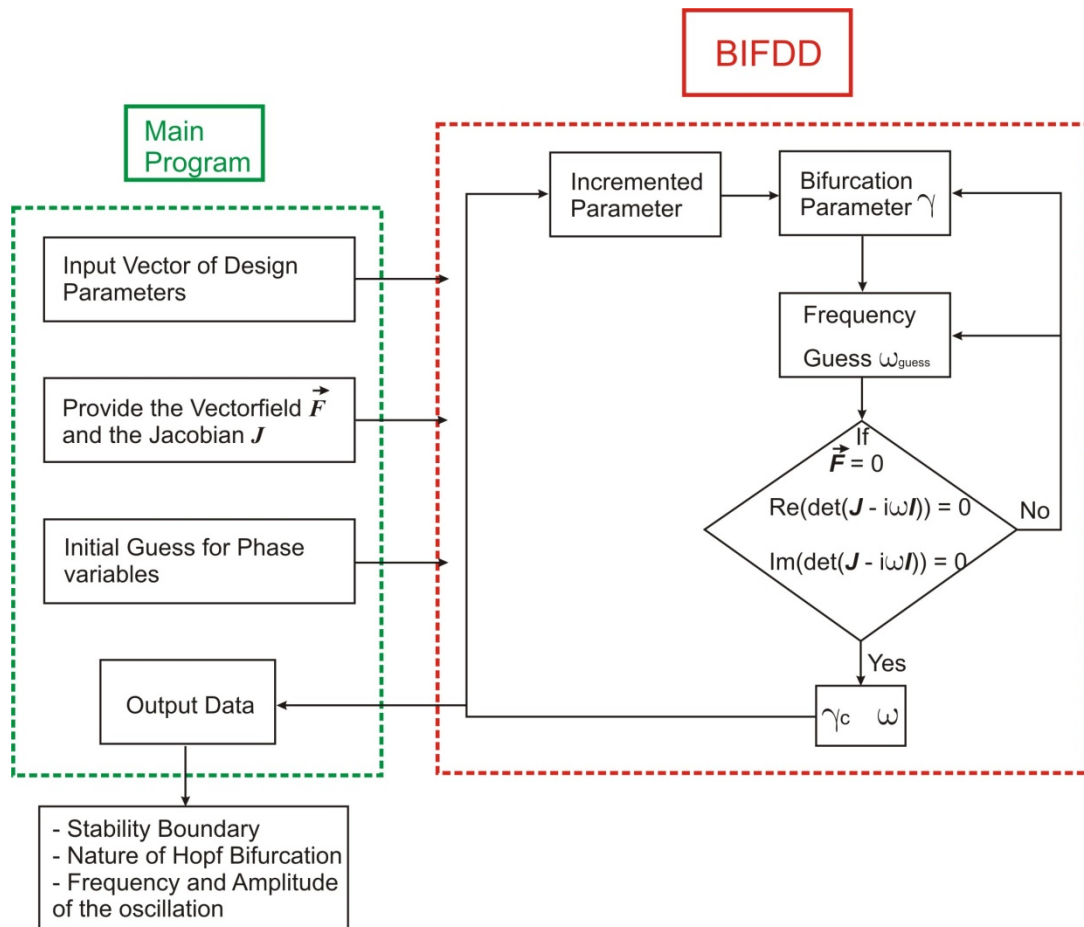


Figure 2.5: Sketch summarizing the bifurcation analysis using BIFDD [12,16].

The user has to provide the input parameter vector, a set of nonlinear ODEs, the corresponding Jacobian matrix and the initial guess for the phase space variables.

The bifurcation analysis starts with selection of the so called iteration and bifurcation parameter. Thereby the iteration parameter will be varied in the interval defined by the user. For each iteration step BIFDD computes the critical value $\gamma_{k,c}$ of the bifurcation parameter, the amplitude ε of the oscillation and the expansion parameters μ_2 , τ_2 and β_2 . The parameters ε , τ_2 , μ_2 and β_2 determine the nature of the PAH bifurcation and thus called bifurcation characteristics (see Appendix A). Thereby τ_2 is a correction factor of the oscillation frequency and μ_2 is a expansion factor for γ_k and relates the oscillation amplitude ε to the bifurcation parameter γ_k according to

$$\varepsilon = \sqrt{\frac{\gamma_k - \gamma_{k,c}}{\mu_2}} \quad (2.3)$$

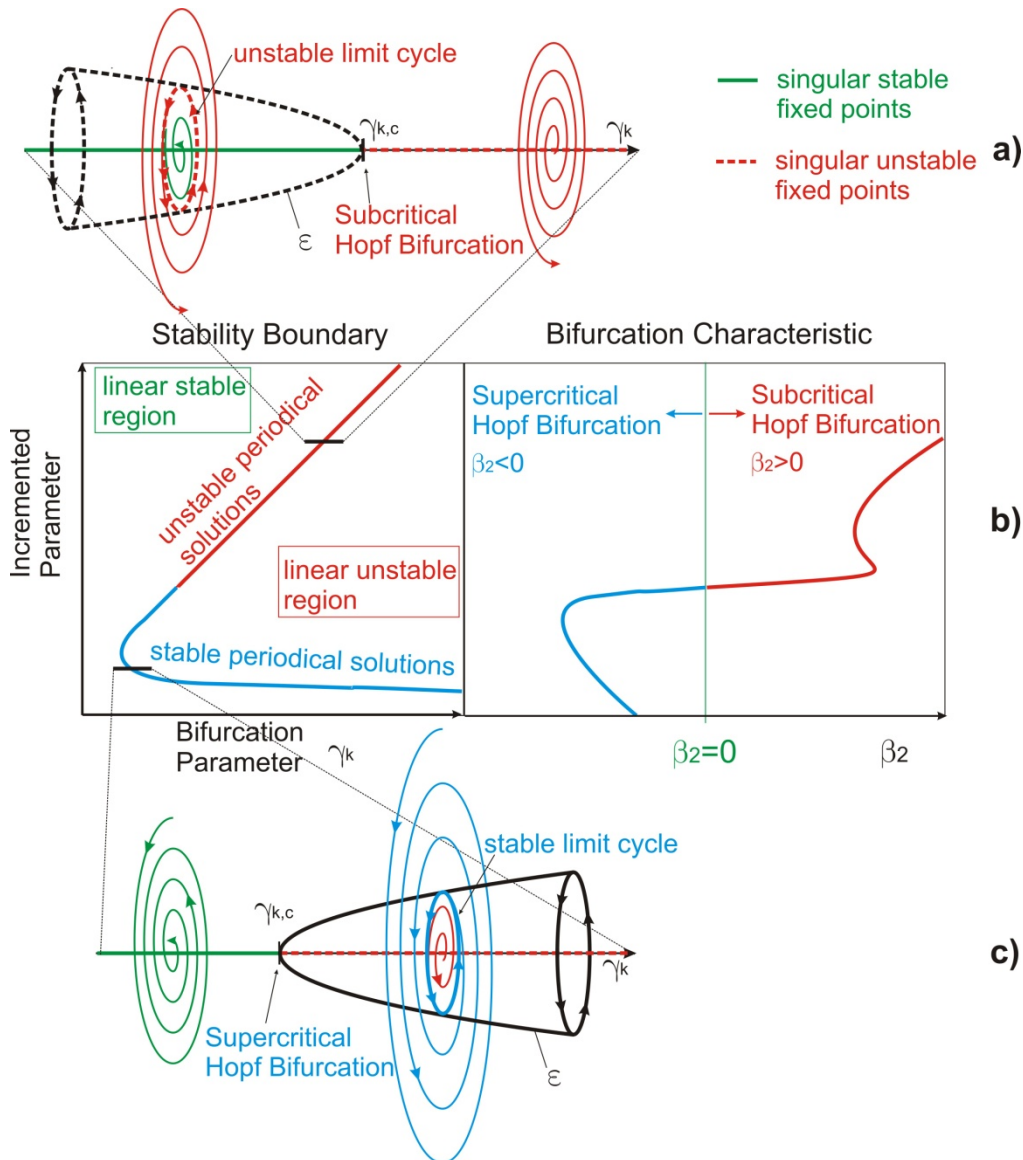


Figure 2.6: Stability boundary in the two dimensional parameter space which is spanned by the iteration and bifurcation parameter and the corresponding bifurcation characteristics.

As a result of the semi-analytical bifurcation analysis using BIFDD, a set of fixed points where the Hopf conditions are fulfilled will be obtained in the two dimensional parameter space, which is spanned by the iteration and bifurcation parameter (left diagram of Figure 2.6 b)). This set of fixed points is called linear stability boundary. In each of these fixed points a periodical solution is born whose stability property is determined by the Floquet exponent. The right diagram of Figure 2.6 b) shows the Floquet exponent $\beta \approx \beta_2$ for each iteration step.

To summarize, in all fixed points where the Hopf conditions are fulfilled limit cycles will be born and exist in the neighbourhood of $\gamma_{k,c}$. As stated previously, a stability indicator for limit cycle solutions can be derived from the Floquet theory for differential equations with periodical coefficients (see Floquet theory in Appendix A). The Floquet exponent β_2 determining the stability characteristics of the limit cycle emerges from this theory. If $\beta_2 < 0$, supercritical Hopf bifurcation occurs in $\gamma_{k,c}$ and their corresponding periodical solution is stable (blue part of SB in Figure 2.6 b)). In this case stable limit cycles exist in the linear unstable region close to the stability boundary (Figure 2.6 c)). This means, all trajectories in phase space will approach the limit cycle in this region. If $\beta_2 > 0$, subcritical Hopf bifurcation occurs in $\gamma_{k,c}$ and their corresponding periodical solution is unstable (red part of SB in Figure 2.6 b)). As depicted by Figure 2.6 a), unstable limit cycles exist in the linear stable region. If small perturbations are imposed on the system the trajectories will return to the steady state solution (stable behaviour) while, if a critical perturbation amplitude is exceeded, the trajectories will diverge in an oscillatory manner, which means the dynamical system becomes unstable [19]. Roughly speaking, an unstable limit cycle “born” in a subcritical Hopf bifurcation separates a set of trajectories (in phase space) which spiral into the steady state solution (singular fixed point) from a set of trajectories which spiral away ad infinitum of the phase space.

2.4 Numerical integration

Semi-analytical bifurcation analysis is only valid in the vicinity of the critical bifurcation parameter (SB). In order to get information of the stability behaviour beyond the local bifurcation findings numerical integration of the set of the ODEs is necessary. Besides, the predictions of the semi-analytical bifurcation analysis can be confirmed independently [9-15,23-26,38].

The numerical integration code which is written in the MATLAB environment was extended by an option which allows performing separately steady state or transient analysis. Thereby the steady state output contains the steady state solution \vec{X}_0 , the axial void and quality profiles within the thermal-hydraulic flow channels and the dimensional pressure drops Δp_i^* along the closed flow path.

The numerical integration starts with choosing the point on the two dimensional parameter space, spanned by the iteration and bifurcation parameter. Further, the user has to define the value of the transient time $t_{transient}$. If $t_{transient} = 0$, the numerical inte-

gration code will only perform steady state calculation. If $t_{transient} > 0$, transient analysis will be carried out. In this case, according to

$$\vec{X}(t) = \vec{X}_0 + \delta\vec{X} \quad , \quad (2.4)$$

the steady state \vec{X}_0 will be perturbed by the small perturbation $\delta\vec{X}$ and the code starts numerical integration. As a result, the solution $\vec{X}(t)$ will be obtained which corresponds to the time evolution of all phase space variables for $t_{transient}$ seconds. Figure 2.7 shows the flow diagram of the numerical integration code.

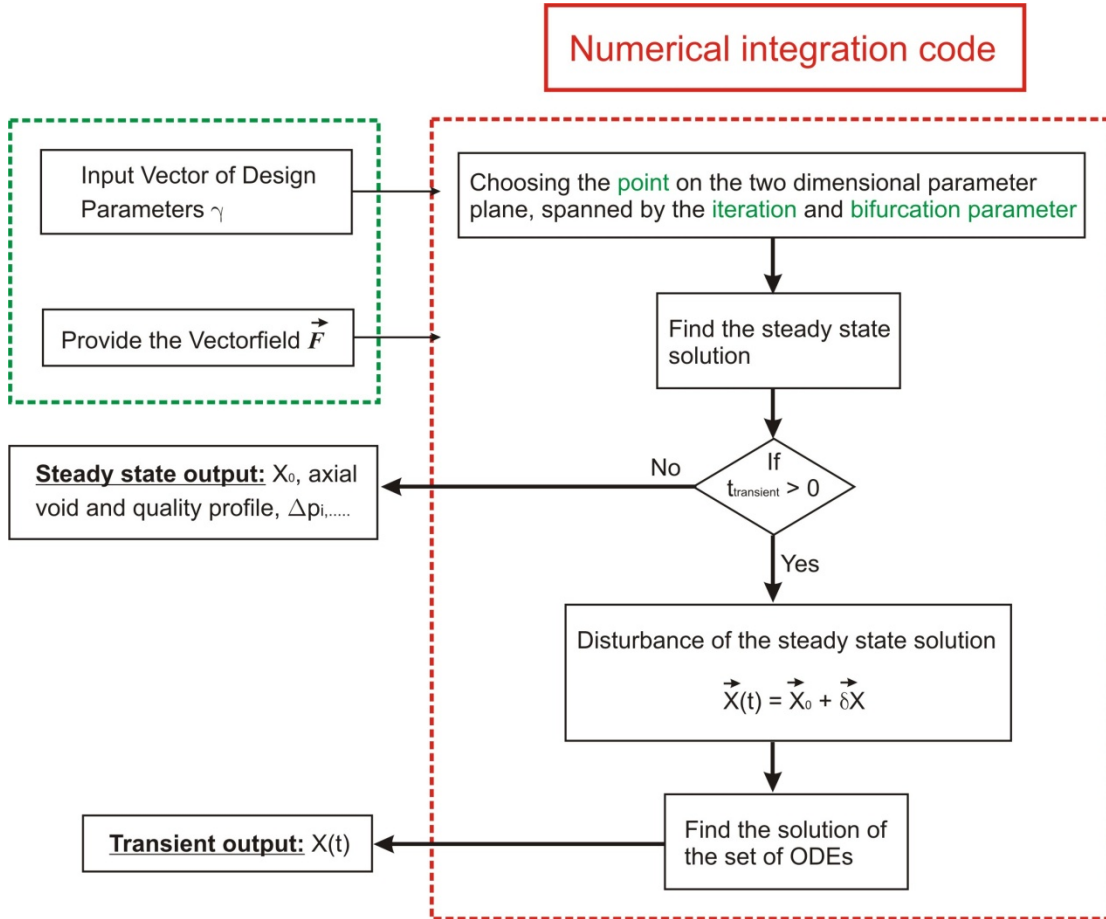


Figure 2.7: Summarizing (flow diagram) the analysis using the numerical integration code

2.5 ROM analysis with both, BIFDD code and numerical integration code

In order to check the results of BIFDD and of numerical integration for consistencies, in a first step, the steady state solution \vec{X}_0 provided by BIFDD will be compared with the solution provided by the numerical integration code. This check reveals e.g. inconsistencies in the input parameter vector. Secondly, the transient behaviour predicted by BIFDD will be verified by numerical integration for selected points. In particular, the location of the SB will be examined for some significant points. When the point of interest is located on the SB, the numerical integration should result in a self-sustained oscillation.

2.6 Novel approach for calculation of the ROM input

Dokhane et al. [12] have shown that discrepancies exist between ROM predictions and RAMONA5 results for the kklc7_rec4 OP. They can be explained by significant differences of modelling assumptions between RAMONA and ROM and the uncertainties in evaluating the design and operating parameters (input parameters of the ROM) as core averaged values. Hence, the calculation of the ROM input parameters should be reconsidered (by taking into account differences of modelling assumptions between RAMONA5 and ROM) in a critical way. To this end, the principles of the TU Dresden ROM will be summarized.

It was mentioned in section 2.1, that the main advantage of employing ROM's is the possibility of coupling them with methods of semi-analytical bifurcation analysis. Within this framework the stability properties of fixed points and periodic solutions are investigated analytically without the need for solving the system of nonlinear differential equations [9-15,23-26,38]. The ROM result is the basis for systematic system code analyses. For this purpose, the solution manifold of the ROM should be as close as possible to that of RAMONA5.

The objective of the ROM development is to construct a model as simple as possible from the mathematical and numerical point of view while preserving the physics of the BWR stability behaviour [23-26]. Hence, the partial differential equations (PDE) describing the BWR will be converted into ordinary differential equations (ODE) for example. The ODE system includes all spatial effects in an approximated (spatial averaged) manner because e.g. by application of the mode expansion methodology [44-46] spatial effects are taken into account by calculation of the amplitude functions of the higher spatial modes and realistic assumptions to the higher mode spatial distributions (calculated by a 3D code called LAMBDA [46]). Furthermore, the PDE of the single and two phase region of the thermal-hydraulic heated channels are converted into ODEs by applying the weighted residual method in which spatial approximations (spatially quadratic time dependent profiles) for the single phase enthalpy and the two-phase quality are used (is equivalent to a coarse grained axial discretization) [12,47]. Hence, the final ODE describes the dynamics of spatial averaged variables where the 3D distributions are taken into account in an approximated manner by appropriate parameters.

The multi-channel system is reduced to a few channel system. This means, the geometrical complexity is reduced considerably. The actual ROM is represented by two thermal-hydraulic flow channels. It should be noted that all spatially averaged variables of the ROM correspond to a real stationary core. This means the 3D distributions (power, void) are calculated by solution of the steady state 3D diffusion equation. As a consequence, all steady state 3D distributions corresponding to the selected operational point must be determined before a ROM analysis is conducted. Hence, in preparation of the ROM inputs, at first, a steady state RAMONA5 run is necessary. Secondly, the spatial averaging of the appropriate ROM input variables can be conducted [26].

Note, if the reactor core configuration will be changed significantly (e.g. by control rod movement) all 3D-distributions have to be recalculated. This means, a parameter variation in the ROM equation system shouldn't lead to a significant change of the 3D-distributions based on the considered operational point. In other words, present ROM analyses are valid in an appropriate environment of the selected (reference) operational point along a rod line (with fixed control rod configuration).

According to the main characteristics of the ROM, the approach depicted in Figure 2.8 is proposed for nonlinear BWR stability analyses using RAMONA5 and ROM as complementary tools (RAM-ROM methodology) [26].

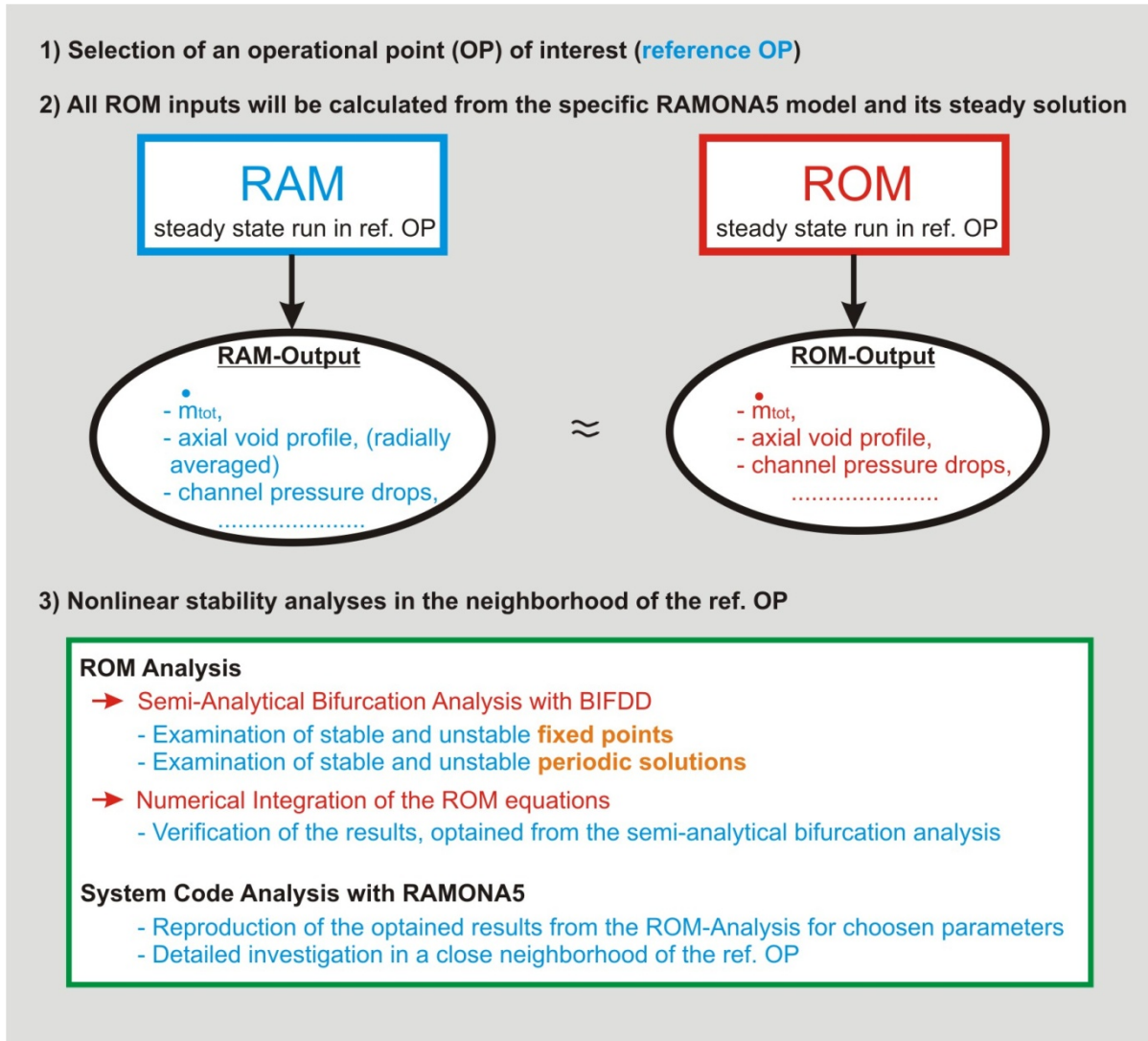


Figure 2.8: Novel approach for nonlinear BWR stability analyses using RAMONA5 and ROM as complementary tools. The demand is that the ROM should provide the correct steady state values at the reference operational point. Thereby the most essential values are the mode feedback reactivity coefficients, the core inlet mass flow, the axial void profile and the channel pressure drops over the reactor vessel components along the closed flow path [26].

The goal is to analyse the stability behaviour of the power plant with the ROM as close as possible to a real BWR (RAMONA5 model is the reference system) in a neighbourhood of a selected operational point. Hence, at first the reference OP has to be determined for which the nonlinear BWR stability analysis will be performed. Secondly, a novel approach for the ROM input calculation is applied. All ROM inputs are calculated from the specific RAMONA5 model and its steady state solution corresponding to the reference point. Thereby differences of model assumptions between RAMONA5 and ROM are taken into account as far as possible in the ROM input calculation. Because the axial power profile and the pressure drop along the closed flow path are calculated by different types of models and different calculation methodologies in both codes the subcooling number and the pressure loss coefficients cannot be calculated directly from the RAMONA5 model and its steady state output. Hence a calculation procedure for the pressure loss coefficients and the core inlet subcooling by taking into account the different axial power profiles used by RAMONA5 and ROM is developed and applied [26].

In the framework of the new calculation methodology of the ROM input parameters it is assumed that when the steady state solution of the reference OP is described by the ROM as close as possible to the real one (system code prediction), the stability behaviour of the BWR system can be represented properly by the ROM in a close neighbourhood of this reference point. In particular the specific thermal-hydraulic and neutron kinetic states should be described correctly. Thermal-hydraulic states are mainly characterized by system pressure, (axial) power profile, core mass flow, core inlet subcooling and the pressure drops along the closed flow path [26]. These quantities should provide the correct (axial) void and (axial) quality profile of the heated channel. It is assumed when the axial void profiles and the pressure drops along the flow channels of two different models or of an experimental facility and its model are sufficiently similar, the corresponding thermal hydraulic states and thus their stability behaviour should be equivalent (defined similitude-criteria) [26].

2.7 Stability map

In general, the stability boundary which separates linear stable singular fixed points from linear unstable one, is a multi dimensional structure in the m -dimensional parameter space. The task “calculation of the stability boundary” means: 1) selection of one or more parameters γ_k which will be varied within the domain of definitions and 2) calculate the critical parameters $\gamma_{k,c}$ for which the Hopf-conditions are fulfilled. As explained previously, in the framework of the semi-analytical bifurcation analysis using BIFDD, the stability characteristics are projected into the two dimensional parameter space (stability map) spanned by the iteration and bifurcation parameter.

From the mathematical point of view, arbitrary design and operating parameters of the ROM can be selected to be the iteration and bifurcation parameter in bifurcation analyses with BIFDD. But the two parameters N_{sub} (subcooling number) and DP_{ext} (steady state external pressure drop) yield the most practical information about BWR

operating conditions. The variation of DP_{ext} corresponds to a variation of the pump head which changes the coolant mass flow. When the coolant mass flow is changed, the power will also be changed while the spatial neutron flux distribution will not be changed significantly because the control rod positions are kept constant. As a consequence, the stability properties of fixed points and periodical solutions along the rod-line of the power flow map which crosses the reference OP can be examined.

In literature, the $N_{sub} - N_{pch}$ -parameter space (N_{pch} is the phase change number) is commonly used as stability map for thermal-hydraulic systems. In a BWR, a variation of the N_{pch} is effected by variation of the control rod positions which changes the spatial neutron flux distribution within the multiplying medium while DP_{ext} (and thus the pump head) is fixed. As stated previously, a significant change of the neutron flux distribution is not allowed during a parameter variation. In addition to that the $N_{sub} - N_{pch}$ -parameter space is an unfavourable stability map which will be explained in detail in section 4.6. In this section is also shown that in the $N_{sub} - DP_{ext}$ -parameter space the phase change number is a function of the subcooling number **and** the steady state external pressure drop **while** in the $N_{sub} - N_{pch}$ -parameter plane the phase change number is only a function of the subcooling number. Hence, if the bifurcation analysis is carried out in the $N_{sub} - DP_{ext}$ -parameter space, all information of the $N_{sub} - N_{pch}$ -parameter space will be included. In other words, the $N_{sub} - DP_{ext}$ -parameter space provides more information than the $N_{sub} - N_{pch}$ -parameter space (see section 4.6).

3 ROM extensions

Firstly, a brief overview about the physics models of the simplified BWR model is given (section (3.1)). Secondly, the main ROM extensions in the neutron kinetics and thermal hydraulics will be described. The original ROM developed at PSI (PSI-Illinois-ROM) is summarized in Appendix B.

3.1 Summary of the ROM

The current BWR reduced order model (TU Dresden ROM, TUD-ROM) consists of three coupled sub-models. These are a neutron kinetic model, a fuel heat conduction model and a two-channel thermal-hydraulic model (presented in detail in [12,47]). The main characteristics of the ROM are depicted in Figure 3.2. The sub-models of the ROM are presented in detail in Appendix B. To summarize, the ROM is a dynamical system consisting of 22 ODEs, four from the neutron kinetic model, eight to describe the fuel rod heat conduction (two equations for each phase, in each channel) and ten that describe the thermal hydraulic model (five for each channel) [12]. Consequently $\vec{X}(t)$ is a vector of 22 state variables presented in detail in [12].

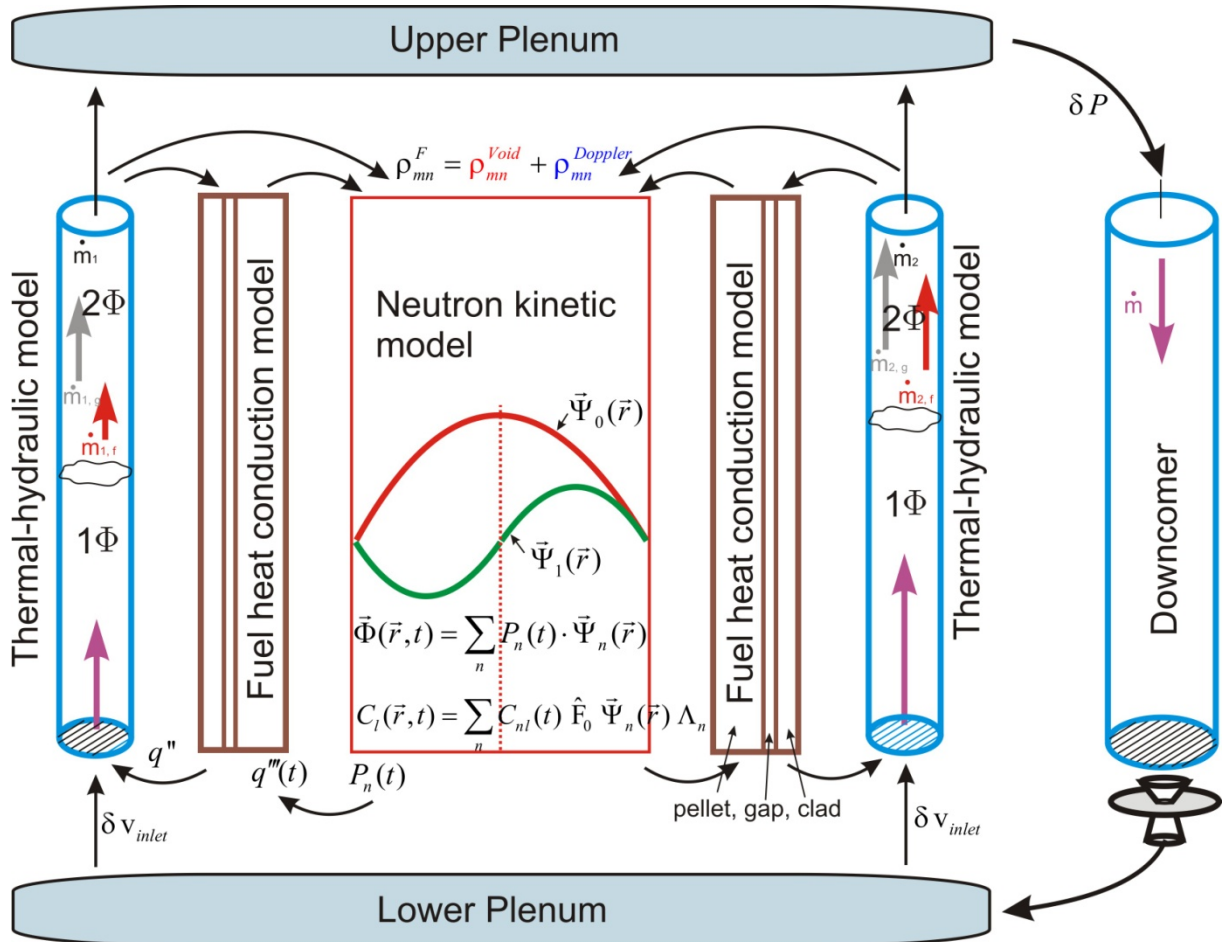


Figure 3.1: Schematic sketch of the TUD-ROM

3.1.1 Neutron kinetic model

The neutron kinetic model is based on the following assumptions:

- 1) Two effective energy groups (thermal and fast neutrons)
- 2) Spatial mode expansion approach of the neutron flux in terms of lambda modes (λ -modes) [46,62,63]
- 3) Only the first two modes (fundamental and first mode) are considered [12].
- 4) Only a single, effective group of delayed neutron precursors is considered [12].
- 5) The contribution of the delayed neutron precursors to the feedback reactivity is neglected [12].

Taking into account these assumptions, four mode kinetic equations could be developed, coupled to equations of the heat conduction and the thermal-hydraulic via the feedback reactivity terms (void and Doppler feedback reactivities). The methodology to calculate the feedback reactivity is presented in 3.2.

The time dependent two-group neutron diffusion equation can be written compactly as

$$\begin{aligned} [v^{-1}] \cdot \frac{\partial \vec{\Phi}(\vec{r}, t)}{\partial t} &= \left[(1-\beta) \cdot \hat{F}(\vec{r}, t) - \hat{L}(\vec{r}, t) \right] \cdot \vec{\Phi}(\vec{r}, t) + \sum_{l=1}^6 \lambda_l \cdot C_l(\vec{r}, t) \cdot \vec{X}_l^v \\ \frac{\partial}{\partial t} C_l(\vec{r}, t) \vec{X}_l^v &= \beta_l \hat{F} \cdot \vec{\Phi}(\vec{r}, t) - \lambda_l \cdot C_l(\vec{r}, t) \vec{X}_l^v \end{aligned} \quad (3.1)$$

where $\vec{X}_l^v = \begin{bmatrix} 1 \\ 0 \end{bmatrix}$ [12,64-67].

$\vec{\Phi}(\vec{r}, t)$ is the neutron flux vector consisting of

$$\vec{\Phi}(\vec{r}, t) = \begin{bmatrix} \Phi_1(\vec{r}, t) \\ \Phi_2(\vec{r}, t) \end{bmatrix} \quad (3.2)$$

the fast (first component) and thermal neutron fluxes (second component), \hat{L} is the net-loss operator including leakage by diffusion, scattering and absorption, and \hat{F} is the fission production operator. λ_l, C_l and β_l are the decay constants, concentrations and delayed neutron fractions, respectively, for the l -th delayed neutron precursor group. A detailed description is given in Appendix B.

In the steady state case of (3.1), the so-called λ -Eigenvalue problem can be written as

$$\begin{aligned} \frac{1}{k_n} \hat{F}_0(\vec{r}) \vec{\Psi}_n(\vec{r}) &= \hat{L}_0(\vec{r}) \vec{\Psi}_n(\vec{r}) \\ \text{with } n &= 0, \dots, \infty. \end{aligned} \quad (3.3)$$

where $\vec{\Psi}_n(\vec{r})$ are the eigenvectors, $k_n = 1/\lambda_n$ are the corresponding eigenvalues and \hat{F}_0, \hat{L}_0 are the steady state fission production and steady state net-loss operators.

The eigenvectors $\vec{\Psi}_n(\vec{r})$ are so-called Lambda-Modes (λ -modes) and satisfy the biorthogonality relation

$$\int_V dV \vec{\Psi}_m^\dagger \hat{F}_0 \vec{\Psi}_n = \left\langle \vec{\Psi}_m \left| \hat{F}_0 \right| \vec{\Psi}_n \right\rangle = \delta_{mn} F_n \quad (3.4)$$

where $\vec{\Psi}_m^\dagger$ are the adjoint eigenvectors.

The space and time dependent neutron flux $\vec{\Phi}(\vec{r}, t)$ and the space and time dependent delayed neutron precursor concentration $C_l(\vec{r}, t)$ of (3.1) can be expanded in terms of the λ -modes as

$$\vec{\Phi}(\vec{r}, t) = \sum_n \hat{P}_n(t) \cdot \vec{\Psi}_n(\vec{r}) \quad (3.5)$$

$$C_l(\vec{r}, t) \vec{X}_l^v = \sum_n C_{nl}(t) \hat{F}_0 \vec{\Psi}_n(\vec{r}) \Lambda_n \quad (3.6)$$

where

$$\hat{P}_n(t) = \begin{bmatrix} P_n^{11}(t) & P_n^{12}(t) \\ P_n^{21}(t) & P_n^{22}(t) \end{bmatrix} \equiv \begin{bmatrix} P_n^1(t) & 0 \\ 0 & P_n^2(t) \end{bmatrix}. \quad (3.7)$$

$P_n^1(t)$ are the time dependent expansion functions of the first energy group, $P_n^2(t)$ are the time dependent expansion functions of the second energy group and $C_{nl}(t)$ are the time dependent expansion functions of the delayed neutron precursor concentration. Physically, the time and space dependent neutron flux $\vec{\Phi}(\vec{r}, t)$ is proportional to the reactor power $Q(t)$. Thus, in the current neutron kinetic model it is assumed that both neutron energy groups have the same time evolution. In other words, the amplitude functions are energy independent. In this case, according to $P_n^1(t) = P_n^2(t) = P_n(t)$, the matrix (3.7) reduces to (the matrix is ‘‘collapsing’’ to a scalar)

$$\hat{P}_n(t) = \begin{bmatrix} P_n(t) & 0 \\ 0 & P_n(t) \end{bmatrix} \quad (3.8)$$

and the expansion (3.5) can be written as

$$\vec{\Phi}(\vec{r}, t) = \sum_n P_n(t) \cdot \vec{\Psi}_n(\vec{r}) \quad (3.9)$$

Substituting (3.9) into the biorthogonality relation (3.4)

$$\int_V dV \vec{\Psi}_m^\dagger(\vec{r}) \hat{F}_0 \vec{\Phi}_n(\vec{r}, t) = \sum_n P_n(t) \underbrace{\int_V dV \vec{\Psi}_m^\dagger(\vec{r}) \hat{F}_0 \vec{\Psi}_n(\vec{r})}_{\delta_{mn} F_n} = P_m(t) F_m \quad (3.10)$$

justifies the definition of the time dependent amplitude functions $P_n(t)$ according to

$$P_m(t) = \frac{1}{F_m} \int_V dV \vec{\Psi}_m^\dagger(\vec{r}) \hat{F}_0 \vec{\Phi}_n(\vec{r}, t) = \frac{1}{F_m} \left\langle \vec{\Psi}_m \left| \hat{F}_0 \right| \vec{\Phi}_n(\vec{r}, t) \right\rangle \quad (3.11)$$

In order to solve the diffusion equation (3.1) for the space and time dependent neutron flux $\vec{\Phi}(\vec{r}, t)$ the expansion (3.9) and (3.6) are substituted into (3.1)

$$\begin{aligned} \sum_n [v^{-1}] \bar{\Psi}_n(\vec{r}) \frac{\partial P_n(t)}{\partial t} &= \sum_n P_n(t) \left[(1-\beta) \cdot [\hat{F}_0 + \delta\hat{F}] \right] \cdot \bar{\Psi}_n(\vec{r}) \\ &- \sum_n P_n(t) [\hat{L}_0 + \delta\hat{L}] \bar{\Psi}_n(\vec{r}) + \sum_{l=1}^6 \lambda_l \cdot \sum_n C_{nl}(t) \hat{F}_0 \bar{\Psi}_n(\vec{r}) \Lambda_n \end{aligned} \quad (3.12)$$

and

$$\begin{aligned} \sum_n \hat{F}_0 \bar{\Psi}_n(\vec{r}) \Lambda_n \frac{\partial}{\partial t} (C_{nl}(t)) &= \sum_n \beta_l P_n(t) \hat{F}_0 \cdot \bar{\Psi}_n(\vec{r}) + \sum_n \beta_l P_n(t) \delta\hat{F} \cdot \bar{\Psi}_n(\vec{r}) \\ &- \sum_n \hat{F}_0 \bar{\Psi}_n(\vec{r}) \Lambda_n \lambda_l C_{nl}(t) \quad , \end{aligned} \quad (3.13)$$

where the operators \hat{L} and \hat{F} are expressed as

$$\hat{L} = \hat{L}_0 + \delta\hat{L} \quad (3.14)$$

$$\hat{F} = \hat{F}_0 + \delta\hat{F} \quad (3.15)$$

in terms of a steady state plus an oscillating term (small perturbation), respectively. In the next step, (3.12) and (3.13) will be multiplied by $\bar{\Psi}_m^\dagger$ from the left hand side. Afterwards the equations are weighted (divided) by (3.4) and integrated over the whole multiplying medium of the reactor core. The result is presented in Appendix B.

In the next step, the following definitions will be introduced:

$$\Lambda_{mn} = \frac{\langle \bar{\Psi}_m | [v^{-1}] | \bar{\Psi}_n \rangle}{\langle \bar{\Psi}_m | \hat{F}_0 | \bar{\Psi}_n \rangle}; \quad \rho_{mn}^F = \frac{\langle \bar{\Psi}_m | [\delta\hat{F} - \delta\hat{L}] | \bar{\Psi}_n \rangle}{\langle \bar{\Psi}_m | \hat{F}_0 | \bar{\Psi}_n \rangle}; \quad \rho_m^s = \frac{\langle \bar{\Psi}_m | [\hat{F}_0 - \hat{L}_0] | \bar{\Psi}_n \rangle}{\langle \bar{\Psi}_m | \hat{F}_0 | \bar{\Psi}_n \rangle} \quad (3.16)$$

$$\rho_{mn}^D = \beta \frac{\langle \bar{\Psi}_m | \delta\hat{F} | \bar{\Psi}_n \rangle}{\langle \bar{\Psi}_m | \hat{F}_0 | \bar{\Psi}_n \rangle}; \quad \rho_{mn}^{D_l} = \beta_l \frac{\langle \bar{\Psi}_m | \delta\hat{F} | \bar{\Psi}_n \rangle}{\langle \bar{\Psi}_m | \hat{F}_0 | \bar{\Psi}_n \rangle} \quad (3.17)$$

Taking into account that $\Lambda_{mm} \gg \Lambda_{mn}$ with $n \neq m$ [12] and using the definitions in (3.16) and (3.17), the final neutron kinetic (spatial) mode equations can be written as

$$\begin{aligned} \frac{d}{dt} P_m(t) &= \frac{1}{\Lambda_{mm}} [(\rho_m^s - \beta) P_m(t)] + \frac{1}{\Lambda_{mm}} \left[\sum_n \rho_{mn}^F P_n(t) - \sum_n \rho_{mn}^D P_n(t) \right] + \sum_l \lambda_l C_{ml}(t) \\ \frac{d}{dt} C_{ml}(t) &= \frac{1}{\Lambda_m} \left[\beta_l P_m(t) + \sum_n \rho_{mn}^{D_l} P_n(t) \right] - \lambda_l C_{ml}(t) \end{aligned} \quad (3.18)$$

where ρ_m^s is the static reactivity, ρ_{mn}^F are the dynamical feedback reactivities, and ρ_{mn}^D , $\rho_{mn}^{D_l}$ are the delayed feedback reactivities.

As mentioned above, in the current neutron kinetic model only a single group of delayed neutron precursors $l=1$ is considered and the contributions of ρ_{mn}^D and $\rho_{mn}^{D_l}$ are neglected [12]. Furthermore, only the fundamental and the first modes are considered. Hence, the modal kinetic equations can be written as

$$\begin{aligned} \frac{d}{dt} P_0(t) &= \frac{1}{\Lambda_0} [(\rho_{00}^F - \beta) P_0(t) + \rho_{01}^F P_1(t)] + \lambda C_0 \\ \frac{d}{dt} C_0(t) &= \frac{\beta}{\Lambda_0} P_0(t) - \lambda C_0(t) \end{aligned} \quad (3.19)$$

$$\begin{aligned} \frac{d}{dt} P_1(t) &= \frac{1}{\Lambda_0} [\rho_{10}^F P_0(t) + (\rho_0^s - \beta) P_1(t) + \rho_{11}^F P_1(t)] \\ &+ \lambda C_1 \\ \frac{d}{dt} C_1(t) &= \frac{\beta}{\Lambda_0} P_1(t) - \lambda C_1(t) \end{aligned} \quad (3.20)$$

A comprehensive discussion is given in Appendix B.

The dynamical feedback reactivities, ρ_{mn}^F represent the coupling between the λ -modes and describe the main feedback mechanism between the neutron kinetics and thermal hydraulics via void fraction in the two-phase flow region and fuel temperature. In the framework of the ROM development the approximate calculation [12,68] of the mode feedback reactivities is one of the crucial tasks. In the approximations used in previous work [12], the required reactivities ρ_{mn} were given by $\rho_{mn} \sim \rho_{00} \cdot (\text{weighting factors})_{mn}$; this means that in both cases certain weight factors for terms different from $n = m = 0$ have to be calculated (see section 3.2).

3.1.2 Fuel heat conduction model

The fuel rod heat conduction model in the current reduced order model was completely adopted from Karve et al. [47]. This model is based on the one-dimensional (radial), time-dependent heat conduction equation for the fuel rod and is based on the following assumptions:

- 1) Two axial regions, corresponding to the single and two-phase regions, are considered,
- 2) three distinct radial regions, the fuel pellet, the gap and the clad are modelled in each of the two axial regions,
- 3) azimuthal symmetry for heat conduction in the radial direction is assumed,
- 4) heat conduction in the z-direction is neglected,
- 5) time-dependent, spatially uniform volumetric heat generation is assumed.

These assumptions result in a one-dimensional (radial) time dependent partial differential equation (PDE). By assuming a two-piecewise quadratic spatial approximation for the fuel rod temperature, the PDE can be reduced to a system of ODEs by applying the variation principle. A detailed derivation is presented in [12,47].

In summary, for each channel, four ODEs are developed from the heat conduction PDE. These ODEs are for the two coefficients of each of the two spatially piecewise quadratic representations of the fuel pellet temperature in the single and two-phase regions of the channel. In an explicit index form, these ODEs can be written as

$$\frac{dT_{1,j\phi,l}(t)}{dt} = ll_{1,1,j\phi,l}T_{1,j\phi,l}(t) + ll_{2,1,j\phi,l}T_{2,j\phi,l}(t) + ll_{3,1,j\phi,l} \left[c_q(P_0(t) - \tilde{P}_0) + c_q\xi P_1(t) \right] \quad (3.21)$$

$$\frac{dT_{2,j\phi,l}(t)}{dt} = ll_{1,2,j\phi,l}T_{1,j\phi,l}(t) + ll_{2,2,j\phi,l}T_{2,j\phi,l}(t) + ll_{3,2,j\phi,l} \left[c_q(P_0(t) - \tilde{P}_0) + c_q\xi P_1(t) \right] \quad (3.22)$$

where $\xi = \pm 1$, $j\phi$ stands for single (1ϕ) or two-phase (2ϕ) region, l stands for channel number (1 or 2) and \tilde{P}_0 is the steady state (reference) value of the amplitude function corresponding to the λ -modes. Note that, the final ODEs were derived using the symbolic toolbox of MATLAB. A detailed description is given in Appendix B and a complete derivation is presented in [47].

3.1.3 Thermal hydraulic model

The thermal hydraulic behaviour of the BWR is represented by two heated channels coupled by the neutron kinetics via the mode feedback reactivities and by the recirculation loop (hydraulic coupling). This sub-model is based on the following assumptions:

- 1) The heated channel, which has a constant flow cross section, is divided into two axial regions, the single and the two-phase region.
- 2) All thermal hydraulic values are averaged over the flow cross section.
- 3) The dynamical behaviour of the two-phase region is presented by a drift flux model (DFM) [58-61,69-71] where mechanical non equilibrium is assumed, i.e. difference between the two phase velocities, and a radial non-uniform void distribution is considered. The DFM represents the stability behaviour of the two-phase more accurately than a homogeneous equilibrium model, in particular for high void content.
- 4) The two phases are assumed to be in thermodynamic equilibrium.
- 5) The system pressure is considered to be constant.
- 6) The fluid in both axial regions and the downcomer is assumed to be incompressible.
- 7) Around the closed flow path, mechanical energy terms are very small compared with the thermal energy terms. Consequently, the kinetic energy, potential energy, pressure gradient and friction dissipation are neglected in the energy balance.
- 8) The PDEs (three-dimensional mass, momentum and energy balance equation) are converted into the final ODEs by applying the weighted residual method in which spatial approximations (spatially quadratic but time-dependent profiles) for the single phase enthalpy [12,47] and the two-phase quality are used (is equivalent to a coarse grained axial discretization).
- 9) The downcomer (constant flow cross section) region is considered to be a single phase region.
- 10) All physical processes which are connected with energy increase and energy decrease are neglected in the downcomer. Consequently the core inlet sub-cooling is a boundary condition which is nearly realized by the nuclear power plants (predicted by RAMONA5).
- 11) The pump head due to the recirculation pumps is considered to be constant ($\Delta P_{head} = const$)

Figure 3.2 depicts a schematic sketch of the thermal hydraulic model including the recirculation loop. The sub-model consists of three parts. These are the two heated

channels and the downcomer section. The common lower plenum and the common upper plenum are only shown to indicate that all channels are coupled hydraulically.

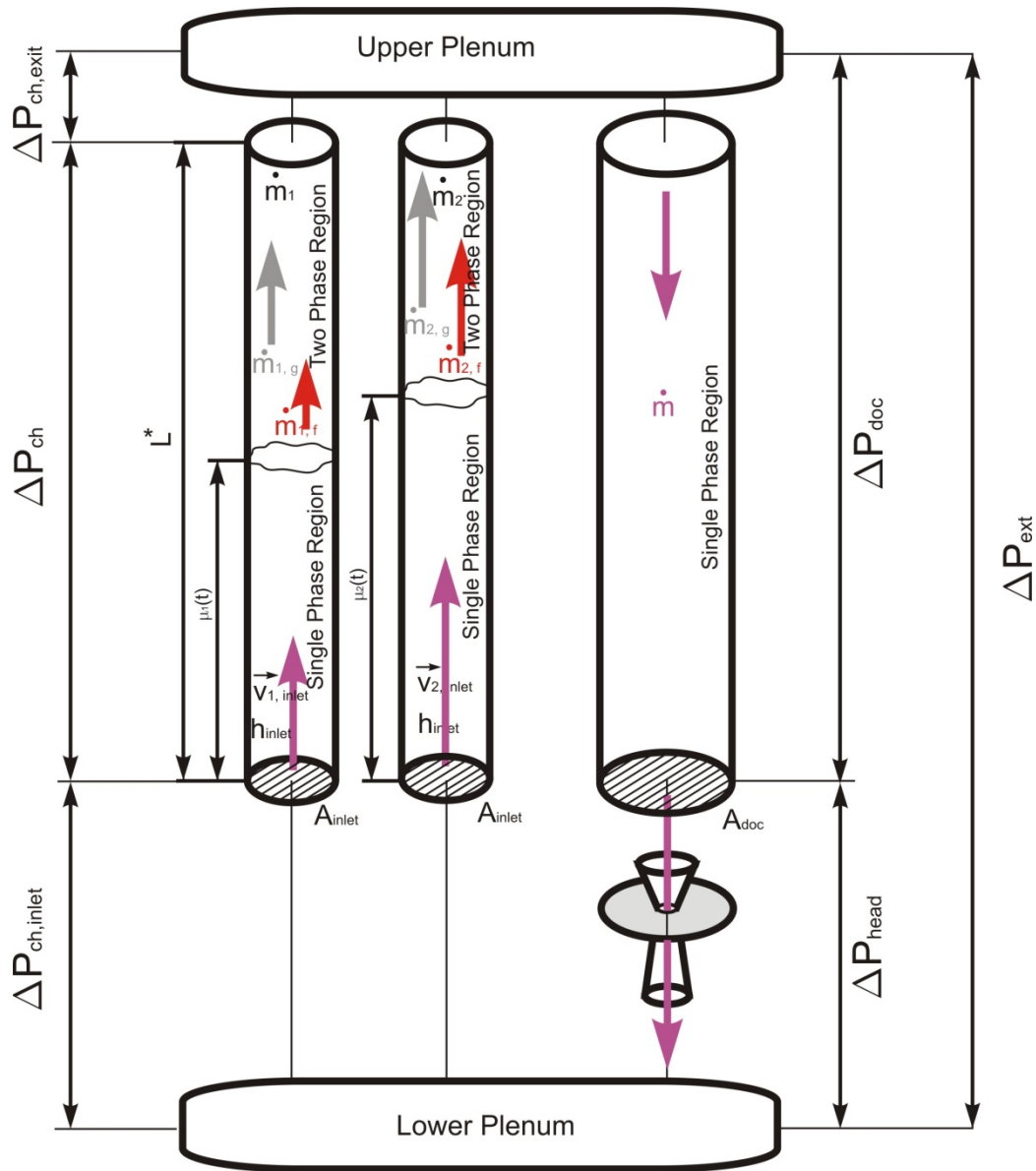


Figure 3.2: Schematic sketch of the thermal hydraulic two-channel model including outer loop section.

The coolant enters the core channel i inlet (single phase region) with the inlet velocities $v_{i,inlet}$ and the inlet enthalpy h_{inlet} and the heat is released by nuclear fissions in the fuel, conducted to the coolant. At a certain axial level (boiling boundary $\mu(t)$), where the coolant reaches the saturation state, the coolant starts to boil. Above the boiling boundary (two-phase region), the coolant is a mixture of water and steam. Because of the thermodynamic equilibrium between the two phases, the heat generated in the fuel is completely used for steam production.

Single phase region [12,47,69-74]

The single phase region extends from the channel inlet to the boiling boundary $\mu(t)$. As mentioned above the dynamical behaviour within this region is represented by the three conservation laws (mass, energy and momentum) for the liquid phase. In order to convert the energy balance from a PDE into an ODE, a time-dependent, spatially quadratic distribution

$$h(z,t) \approx h_{inlet} + a_1(t)z + a_2(t)z^2 \quad (3.23)$$

for the enthalpy is introduced [47] and the weighted residual procedure is applied. Thereby, it will be integrated from the channel inlet to the boiling boundary. As a result, the ODEs

$$\frac{d}{dt}a_1(t) = -2v_{inlet}(t)a_2(t) + \frac{6}{\mu} \left[N_\rho \cdot N_r \cdot N_{pch,1\Phi}(t) - v_{inlet}(t)a_1(t) \right] \quad (3.24)$$

$$\frac{d}{dt}a_2(t) = -\frac{6}{\mu^2} \left[N_\rho \cdot N_r \cdot N_{pch,1\Phi}(t) - v_{inlet}(t)a_1(t) \right] \quad (3.25)$$

for the time dependent functions $a_1(t)$ and $a_2(t)$ of the quadratic distribution (3.23) are obtained. $a_1(t)$ and $a_2(t)$ are the state variables of the single phase region. A detailed derivation is presented in Appendix B.

Two phase region [10-15]

The two phase region extends from the boiling boundary $\mu(t)$ to the channel exit. As mentioned above the dynamical behaviour within this region is represented by a drift flux model which is based on four conservation laws [58-61,69-76], i.e. the continuity equation of the gas phase and the three conservation laws (mass, energy and momentum) for the two phase mixture. In the current work, the density wave phenomenon plays a dominant role so that the mass transport problem was transformed into the void propagation formulation [75,76].

As mentioned above (for the conversion from PDE's into ODE's), the flow quality $x(z,t)$ in the two phase region will be described by a time dependent, spatially quadratic distribution

$$x(z,t) \approx N_\rho N_r \left[s_1(t)[z - \mu(t)] + s_2(t)[z - \mu(t)]^2 \right] \quad (3.26)$$

analogous to the enthalpy distribution in the single phase region [12]. The ODEs can be obtained by applying the weighted residuals method with the weight functions $wg = 1$ and $wg = z$. Thereby, it will be integrated from the boiling boundary to the channel exit. The final ODE's can be written as

$$\frac{ds_1}{dt} = \frac{1}{ff_5(t)} \left[ff_1(t) \frac{d\mu(t)}{dt} + ff_2(t) \frac{dv_{inlet}(t)}{dt} \right] + \frac{1}{ff_5(t)} \left[ff_3(t) \frac{dN_{pch,2\Phi}(t)}{dt} + ff_4(t) \right] \quad (3.27)$$

$$\frac{ds_2}{dt} = \frac{1}{ff_{10}(t)} \left[ff_6(t) \frac{d\mu(t)}{dt} + ff_7(t) \frac{dv_{inlet}(t)}{dt} \right] + \frac{1}{ff_{10}(t)} \left[ff_8(t) \frac{dN_{pch,2\Phi}(t)}{dt} + ff_9(t) \right]. \quad (3.28)$$

A detailed derivation is presented in Appendix B.

Channel inlet velocity

The channel inlet velocity $v_{n,inlet}(t)$ of the n -th heated channel is a further state variable of the ROM. In order to get the final ODEs for the channel inlet velocities, the momentum equations of all considered regions have to be integrated over the closed loop

$$\begin{aligned} 0 &= \oint \frac{\partial p}{\partial z} dz \\ 0 &= \int_0^1 \frac{\partial p_{h_ch}}{\partial z} dz + \int_1^0 \frac{\partial p_{recirc}}{\partial z} dz \\ &= \underbrace{\Delta P_{inlet}^* + \Delta P_{ch}^* + P_{exit}^*}_{\Delta P_{ext}^*}, \end{aligned} \quad (3.29)$$

where ΔP_{inlet}^* and P_{exit}^* are the channel inlet and channel exit pressure drops and ΔP_{ch}^* is the pressure drop over the heated channel. ΔP_{ch}^* with $\Delta P_{ch}^* = \Delta P_{1\Phi}^* + \Delta P_{2\Phi}^*$ is the sum of the single phase $\Delta P_{1\Phi}^*$ and two phase $\Delta P_{2\Phi}^*$ pressure drops. In the PSI-Illinois-ROM, the second integral of (3.29) was set equal to the steady state external pressure drop DP_{ext} . In this case, the closed loop integration can be written as

$$\Delta P_{n,inlet}^* + \Delta P_{n,1\Phi}^* + \Delta P_{n,2\Phi}^* + \Delta P_{n,exit}^* = \Delta P_{ext}^* \quad (3.30)$$

In the PSI-Illinois-ROM, the final ODE for the inlet channel velocity of the n -th heated channel can be derived from equation (3.30). The result can be written as ([12])

$$\frac{d}{dt} v_{n,inlet}(t) = \frac{1}{ff_{n,14}(t)} \left[ff_{n,11}(t) \frac{d\mu_n(t)}{dt} + ff_{n,12}(t) \frac{dN_{n,pch}(t)}{dt} + ff_{n,13}(t) \right]. \quad (3.31)$$

The derivation of the final ODE for the channel inlet velocity, where the recirculation loop is included, is discussed in section 3.3.

3.2 Mode feedback reactivity calculation

3.2.1 Calculation of the mode feedback reactivity in the ROM

In this section two different methods to calculate the void and fuel temperature mode feedback reactivity coefficients are compared. The first of them is the original method used in the PSI-Illinois ROM [12,46,63]. The second method has been developed at UPV Valencia (Spain) in cooperation with the TU Dresden (Germany) during this work [68].

As presented in section 3.1.1, the mode feedback reactivity is defined as

$$\rho_{mn}^F = \frac{\langle \bar{\Psi}_m | [\delta \hat{F} - \delta \hat{L}] | \bar{\Psi}_n \rangle}{\langle \bar{\Psi}_m | \hat{F}_0 | \bar{\Psi}_n \rangle} = \rho_{mn}^{F,Void} + \rho_{mn}^{F,Doppler} \quad (3.32)$$

and can be split to a sum of the mode void feedback reactivity $\rho_{mn}^{F,Void}$ and the mode Doppler feedback reactivity $\rho_{mn}^{F,Doppler}$. Thereby $\rho_{mn}^{F,Void}$ and $\rho_{mn}^{F,Doppler}$ are defined separately as

$$\rho_{mn}^{F,Void} = \frac{\langle \bar{\Psi}_m | \left(\frac{\partial \hat{F}}{\partial \alpha} - \frac{\partial \hat{L}}{\partial \alpha} \right) \delta \alpha | \bar{\Psi}_n \rangle}{\langle \bar{\Psi}_m | \hat{F}_0 | \bar{\Psi}_n \rangle} \quad (3.33)$$

and

$$\rho_{mn}^{F,Doppler} = \frac{\langle \bar{\Psi}_m | \left(\frac{\partial \hat{F}}{\partial T} - \frac{\partial \hat{L}}{\partial T} \right) \delta T | \bar{\Psi}_n \rangle}{\langle \bar{\Psi}_m | \hat{F}_0 | \bar{\Psi}_n \rangle} . \quad (3.34)$$

For generalization, the mode feedback reactivity $\rho_{mn}^{F,X}$ due to the effect X with $X = void, Doppler$ will be defined as

$$\rho_{mn}^{F,X} = \frac{\langle \bar{\Psi}_m | \left(\frac{\partial \hat{F}}{\partial X} - \frac{\partial \hat{L}}{\partial X} \right) \delta X | \bar{\Psi}_n \rangle}{\langle \bar{\Psi}_m | \hat{F}_0 | \bar{\Psi}_n \rangle} . \quad (3.35)$$

The idea of the original method is, first, to express the mode feedback reactivity in terms of the fundamental mode feedback reactivity $\rho_{00}^{F,X}$ and second, to approximate the fundamental mode void feedback reactivity by a linear dependence around its steady state value in terms of the void fraction perturbation and to approximate the fundamental mode Doppler feedback reactivity by a linear dependence around its steady state value in terms of the fuel temperature perturbation, respectively.

In order to take into account the in-phase and out-of-phase oscillation modes, the reactor core is divided into two radial regions r (with $r = 1, 2$) of the same size and

approximately the same steady-state properties. In the following, the contribution of each core region to the feedback reactivity $\rho_{mm}^{F,X,r}$ regarding to the effect X will be calculated. The feedback reactivities $\rho_{mm}^{F,X,r}$ and $\rho_{00}^{F,X,r}$ are defined as

$$\rho_{mm}^{F,X,r} = \frac{\left\langle \bar{\Psi}_m \left| \left(\frac{\partial \hat{F}}{\partial X} - \frac{\partial \hat{L}}{\partial X} \right) \delta X \right| \bar{\Psi}_n \right\rangle^r}{\left\langle \bar{\Psi}_m \left| \hat{F}_0 \right| \bar{\Psi}_n \right\rangle} \quad (3.36)$$

and

$$\rho_{00}^{F,X,r} = \frac{\left\langle \bar{\Psi}_0 \left| \left(\frac{\partial \hat{F}}{\partial X} - \frac{\partial \hat{L}}{\partial X} \right) \delta X \right| \bar{\Psi}_0 \right\rangle^r}{\left\langle \bar{\Psi}_0 \left| \hat{F}_0 \right| \bar{\Psi}_0 \right\rangle} = \frac{\left\langle \bar{\Psi}_0 \left| \left(\frac{\partial \hat{F}}{\partial X} - \frac{\partial \hat{L}}{\partial X} \right) \delta X \right| \bar{\Psi}_0 \right\rangle^r}{F_0} \quad (3.37)$$

where

$$\left\langle \bar{\Psi}_0 \left| \hat{F}_0 \right| \bar{\Psi}_0 \right\rangle = \delta_{00} F_0 = F_0 \quad (3.38)$$

According to the definition of F_0 , F_0^r can be defined as

$$F_0^r = \delta_{00} F_0^r = \left\langle \bar{\Psi}_0 \left| \hat{F}_0 \right| \bar{\Psi}_0 \right\rangle^r \quad (3.39)$$

With the definition (3.39), expression (3.37) can be rewritten as

$$\rho_{00}^{F,X,r} = \frac{\left\langle \bar{\Psi}_0 \left| \left(\frac{\partial \hat{F}}{\partial X} - \frac{\partial \hat{L}}{\partial X} \right) \delta X \right| \bar{\Psi}_0 \right\rangle^r}{F_0^r} \cdot \frac{F_0^r}{\underbrace{F_0^r}_{WD_{00}^r}} = \frac{1}{F_0^r} \cdot \left\langle \bar{\Psi}_0 \left| \left(\frac{\partial \hat{F}}{\partial X} - \frac{\partial \hat{L}}{\partial X} \right) \delta X \right| \bar{\Psi}_0 \right\rangle^r \cdot WD_{00}^r \quad (3.40)$$

where WD_{00}^r is a weight factor. In the next step, the definition (3.36) is multiplied by $\rho_{00}^{F,X,r} / \rho_{00}^{F,X,r}$

$$\rho_{mm}^{F,X,r} = \frac{\left\langle \bar{\Psi}_m \left| \left(\frac{\partial \hat{F}}{\partial X} - \frac{\partial \hat{L}}{\partial X} \right) \delta X \right| \bar{\Psi}_n \right\rangle^r}{\left\langle \bar{\Psi}_m \left| \hat{F}_0 \right| \bar{\Psi}_n \right\rangle} \cdot \frac{\rho_{00}^{F,X,r}}{\rho_{00}^{F,X,r}} \quad (3.41)$$

and then be written as

$$\rho_{mm}^{F,X,r} = \frac{F_0}{F_0^r} \rho_{00}^{F,X,r} \cdot \frac{\left\langle \bar{\Psi}_m \left| \left(\frac{\partial \hat{F}}{\partial X} - \frac{\partial \hat{L}}{\partial X} \right) \delta X \right| \bar{\Psi}_n \right\rangle^r}{\underbrace{\left\langle \bar{\Psi}_0 \left| \left(\frac{\partial \hat{F}}{\partial X} - \frac{\partial \hat{L}}{\partial X} \right) \delta X \right| \bar{\Psi}_0 \right\rangle^r}_{WD_{mm}^r}} \cdot \frac{\left\langle \bar{\Psi}_0 \left| \hat{F}_0 \right| \bar{\Psi}_0 \right\rangle^r}{\left\langle \bar{\Psi}_m \left| \hat{F}_0 \right| \bar{\Psi}_n \right\rangle} = \rho_{00}^{F,X,r} \cdot \frac{WD_{mm}^r}{WD_{00}^r} \quad (3.42)$$

where WD_{mn}^r are the reactivity weight factors. In expression (3.42) the mode feedback reactivity $\rho_{mn}^{F,X,r}$ of region r due to the effect X is expressed by means of $\rho_{00}^{F,X,r}$ and by the weight factor WD_{mn}^r / WD_{00}^r .

It should be emphasized that in a BWR the mode feedback reactivity $\rho_{mn}^{F,X,r}$ has an axial quadratic dependence of the form

$$\rho_{mn}^{F,X,r}(t) \sim \sum_k \left[C_1^{X,r} + C_2^{X,r} \alpha_k^r(t) + C_3^{X,r} (\alpha_k^r)^2(t) \right] \cdot W_k^P \cdot \delta X_k^r(t) \quad , \quad (3.43)$$

where W_k^P is a square power weight factor

$$W_k^P = \frac{P_k^2}{\sum_k P_k^2} \quad (3.44)$$

of the k -th axial node. In the context of the ROM development, the axial dependence of $\rho_{mn}^{F,X,r}$ is ignored and the averaged (weighted) value of region r , see definition (3.36), is used. The reason is that the axial dependence of the reactor power is also ignored in the ROM. Instead of a real axial power profile, an uniform axial power profile represented by the core averaged reactor power is used. Note that, if the real axial power profile including the real axial dependence of $\rho_{mn}^{F,X,r}$ is taken into account in the ROM, the system of equations would become complicated and non-transparent which is a contradiction in the framework of the ROM methodology [43,83]. This simplification can be the reason for the necessity of introducing the artificial factor $fact_{mn}$ (introduced later) used to increase the feedback gain coupling the first and fundamental mode in order to excite the out-of-phase oscillation mode. This was shown by Ginestar et al. [83]. But an independent proof is recommended in a future work.

For the sake of simplicity, a linear dependence around the mean void and mean fuel temperature in terms of the void fraction perturbation and fuel temperature perturbation can be assumed for the void and fuel temperature feedback reactivity. This assumption is reasonable because the amplitudes of the power oscillations generate only small void and fuel temperature oscillations [68]. Thus, it is not necessary to take into account the exact dependence of the mode feedback reactivities on the void and the fuel temperature.

The time dependence of the fundamental mode feedback reactivity is approximated as

$$\rho_{00}^{F,X,r}(t) = C_1^{X,r} \cdot \delta X^r(t) \cdot WD_{00}^r \quad , \quad (3.45)$$

where $C_1^{X,r}$ is artificially defined as the reactivity coefficient of the considered region r respect to the effect X .

After substituting the approximation (3.45) in (3.42) the mode feedback reactivity (related to the region r) due to the effect X can be written as

$$\rho_{mn}^{F,X,r} = C_1^{X,r} \cdot \delta X^r(t) \cdot WD_{mn}^r \quad . \quad (3.46)$$

The expression for the weight factor WD_{mn}^r can be approximated by substituting the perturbations in the production and loss operators by average values [12]. In addition

to that the steady-state production operator is substituted by an average value for the whole reactor core. Then the reactivity weight factor WD_{mn}^r in (3.46) can be written as ([12])

$$WD_{mn}^r = \frac{\langle \tilde{\Psi}_0 | \tilde{\Psi}_0 \rangle^r}{\langle \tilde{\Psi}_m | \tilde{\Psi}_n \rangle} . \quad (3.47)$$

Consequently, the void mode feedback reactivity and the Doppler mode feedback reactivity can be written as

$$\begin{aligned} \rho_{mn}^{F,Void,r}(t) &= C_1^{Void,r} \cdot \delta\alpha^r(t) \cdot WD_{mn}^r = \underbrace{C_1^{Void,r} \cdot WD_{mn}^r}_{C_{mn}^{Void,r}} \cdot (\alpha^r(t) - \alpha_0) \\ &= \underline{\underline{C_{mn}^{Void,r} \cdot \delta\alpha^r(t)}} \end{aligned} \quad (3.48)$$

and

$$\begin{aligned} \rho_{mn}^{F,Doppler,r} &= C_1^{Doppler,r} \cdot \delta T^r(t) \cdot WD_{mn}^r = \underbrace{C_1^{Doppler,r} \cdot WD_{mn}^r}_{C_{mn}^{Doppler,r}} \cdot (T^r(t) - T_0) \\ &= \underline{\underline{C_{mn}^{Doppler,r} \cdot \delta T^r(t)}} \end{aligned} \quad (3.49)$$

respectively. The calculation of the mode feedback reactivities $\rho_{mn}^{F,Void,r}$ and $\rho_{mn}^{F,Doppler,r}$ in the PSI-Illinois-ROM is based on the approximations (3.48) and (3.49) [12].

The second way of computing the mode void feedback reactivity and the mode Doppler feedback reactivity is based on the same concept as described above. The difference is that the mode feedback reactivities $\rho_{mn}^{F,Void,r}$ and $\rho_{mn}^{F,Doppler,r}$ will be calculated with the linear relationship according to

$$\rho_{mn}^{F,Void,r} = C_{mn}^{Void,r} \cdot \delta\alpha^r(t) \quad (3.50)$$

$$\rho_{mn}^{F,Doppler,r} = C_{mn}^{Doppler,r} \cdot \delta T^r(t) . \quad (3.51)$$

They depend on the void and the fuel temperature perturbations and the coefficients $C_{mn}^{Void,r}$ and $C_{mn}^{Doppler,r}$ which are called void and Doppler mode feedback reactivity coefficients. The idea of this method is to avoid the approximation (3.42) and the calculation of the weight factors WD_{mn}^r . The calculation of the mode feedback reactivities $\rho_{mn}^{F,Void,r}$ and $\rho_{mn}^{F,Doppler,r}$ in the current ROM version is based on (3.50) and (3.51).

To summarize, the original way of computing the mode feedback reactivities is based on the approximations (3.48) and (3.49) where the coefficients C_1^{Void} and $C_1^{Doppler}$ and the weight factors WD_{mn}^r have to be calculated before ROM analyses are performed while in the second method, which is based on the approximations (3.50) and (3.51), only the mode feedback reactivity coefficients ($C_{mn}^{Void,r}$ and $C_{mn}^{Doppler,r}$) have to be calculated. The computation of the mode feedback reactivity coefficients $C_{mn}^{Void,r}$ and $C_{mn}^{Doppler,r}$ is explained in the next section.

Finally, according to (3.32), the mode feedback reactivity ρ_{mn}^F of the ROM differential equation system can be calculated as

$$\begin{aligned}
\rho_{mn}^F &= fact_{mn} \sum_{r=1}^2 \left(\rho_{mn}^{F, Void, r} + \rho_{mn}^{F, Doppler, r} \right) \\
&= fact_{mn} \sum_{r=1}^2 \left(C_{mn}^{Void, r} \cdot \delta\alpha^r(t) + C_{mn}^{Doppler, r} \cdot \delta T^r(t) \right) ,
\end{aligned} \tag{3.52}$$

where $fact_{mn}$ with

$$fact_{mn} = \begin{cases} 1 & m = n = 0, 1 \\ fact & m \neq n \end{cases} \tag{3.53}$$

is an artificial factor, introduced as a multiplier of the corresponding feedback reactivity, in order to increase the feedback gain coupling the first and fundamental mode.

3.2.2 Calculation of C_{mn}

In order to calculate the mode reactivity coefficients $C_{mn}^{Void,r}$ and $C_{mn}^{Doppler,r}$ of both core regions $r=1$ and $r=2$, steady state RAMONA runs are necessary. At first, a RAMONA run is performed at the reference OP. Afterwards the corresponding macroscopic cross sections (reference cross sections) were extracted from the RAMONA output file and converted such that the result can be used for solving the steady state λ -Eigenvalue problem (3.3) with the code LAMBDA_REAC. As a result, the eigenvalues $k_n = 1/\lambda_n$ and the corresponding eigenvectors $\bar{\Psi}_n(\vec{r})$ (λ -modes) are calculated [12,44-46,62,63].

Secondly, artificial cross section perturbations corresponding to void and fuel temperature perturbations ($\delta\alpha$ and δT) are imposed on the steady state system and steady state RAMONA runs are performed, respectively. RAMONA provides options to introduce separately artificial cross section perturbations in the void fraction and fuel temperature. In particular, imposed a perturbation on the void fraction involves the void feedback reactivity only and imposing a perturbation on the fuel temperature involves the Doppler feedback reactivity. The perturbed macroscopic cross sections for each artificial effect are then converted to the LAMBDA_REAC-format. Finally, the LAMBDA_REAC code is applied to calculate the mode feedback reactivities $\rho_{mn}^{F,X,r}$ of the effect X ($\delta\alpha$ and δT) and region r , separately [12].

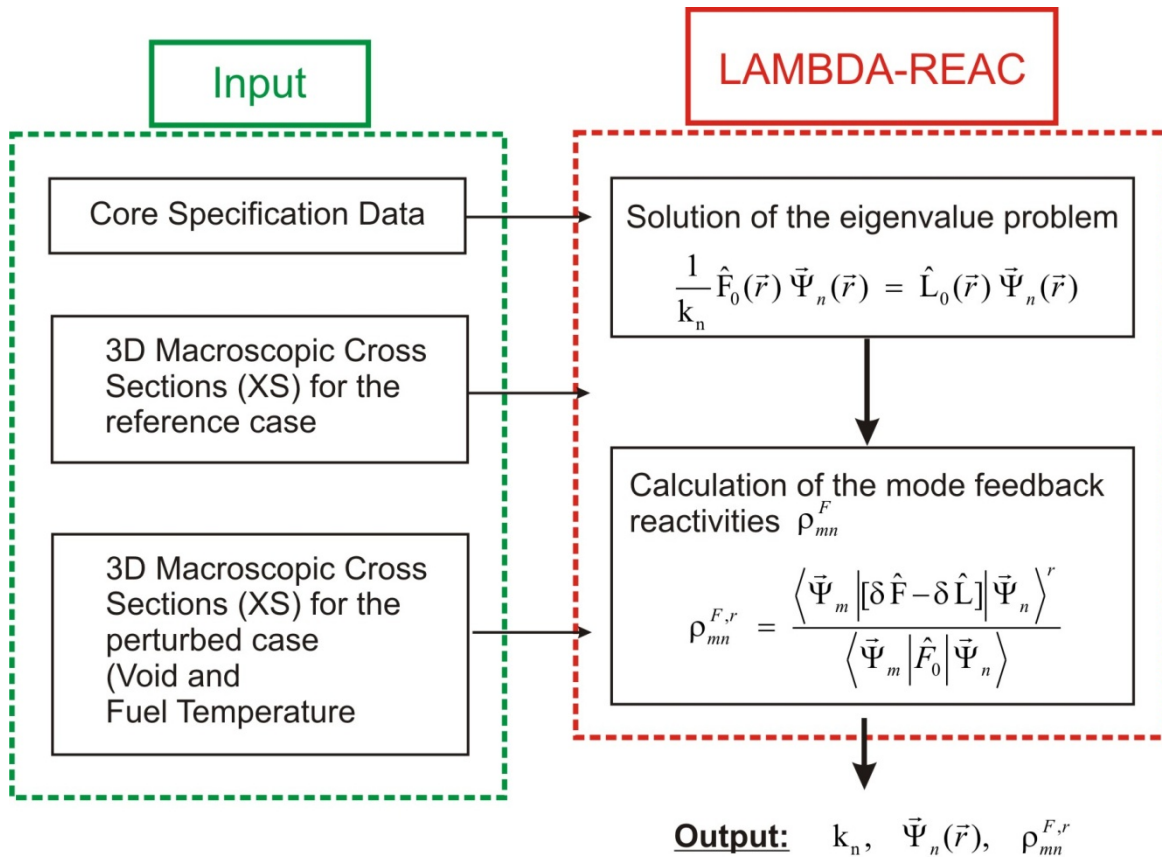


Figure 3.3: Flow-chart of the LAMBDA_REAC code

The mode feedback reactivity coefficients $C_{mn}^{Void,r}$ and $C_{mn}^{Doppler,r}$ can be calculated using the linear approximations (3.50) and (3.51), respectively.

In the following, some results of the original calculation methodology (M1) for $C_{mn}^{Void,r}$ and $C_{mn}^{Doppler,r}$ are compared with the results of the new method (M2) for NPP Leibstadt and NPP Ringhals. The results for $C_{mn}^{Void,r}$ and $C_{mn}^{Doppler,r}$ are summarized in Table 3.1 and Table 3.2.

Table 3.1: Void mode feedback reactivity coefficients in $pcm/\%void$ for NPP Leibstadt (KKL) and NPP Ringhals (KKR)

	KKL M1	KKL M2	KKR M1	KKR M2
$C_{00}^{Void,1}$	-38.2	-37,1	-31.2	-25.4
$C_{00}^{Void,2}$	-38.8	-37.6	-31.3	-25.4
$C_{01}^{Void,1}$	-31.9	-30.8	-28.7	-24.0
$C_{01}^{Void,2}$	31.9	30.8	28.7	24.0
$C_{10}^{Void,1}$	-30.6	-30.4	-28.9	-24.9
$C_{10}^{Void,2}$	30.5	30.2	28.9	24.9
$C_{11}^{Void,1}$	-36.5	-35.8	-31.2	-27.4
$C_{11}^{Void,2}$	-36.2	-35.6	-31.1	-27.3

Table 3.2: Doppler mode feedback reactivity coefficients in pcm/K for NPP Leibstadt (KKL) and NPP Ringhals (KKR)

	KKL M1	KKL M2	KKR M1	KKR M2
$C_{00}^{Doppler,1}$	-1.0	-1.04	-1.17	-1.08
$C_{00}^{Doppler,2}$	-1.0	-1.06	-1.17	-1.08
$C_{01}^{Doppler,1}$	-0.86	-0.86	-1.07	-0.99
$C_{01}^{Doppler,2}$	0.86	0.87	1.07	0.99
$C_{10}^{Doppler,1}$	-0.83	-0.83	-1.08	-1.01
$C_{10}^{Doppler,2}$	0.82	0.83	1.08	1.01
$C_{11}^{Doppler,1}$	-0.99	-0.99	-1.17	-1.09
$C_{11}^{Doppler,2}$	-0.98	-0.98	-1.17	-1.09

According to the technical documentation of the NPP Leibstadt for the begin of cycle 7 (KKLc7rec4) [5,6] the void feedback reactivity coefficient is about $100 \text{ pcm}/\% \text{ void}$ and the Doppler feedback reactivity coefficient is between 2 and $4 \text{ pcm}/K$. The corresponding void feedback reactivity coefficient of the ROM is approximately the sum of the coefficients $C_{00}^{\text{Void},1}$ and $C_{00}^{\text{Void},2}$ for both core regions. The results are $38+38=76 \text{ pcm}/\% \text{ void}$ and $2 \text{ pcm}/K$ for the original method and $37+37=74 \text{ pcm}/\% \text{ void}$ and $2 \text{ pcm}/K$ for the new method.

Table 3.1 and Table 3.2 show that both methods for the calculation of $C_{mn}^{\text{Void},r}$ and $C_{mn}^{\text{Doppler},r}$ provide similar results for both nuclear power plants. This result was expected from the reactor theory point of view. The disadvantage of the original method is that the weight factors WD_{mn}^r and the coefficients $C_1^{\text{Void},r}$ and $C_1^{\text{Doppler},r}$ have to be calculated cumbersome before ROM analyses are performed. This is not necessary in the second method. Here only the mode feedback reactivity coefficients ($C_{mn}^{\text{Void},r}$ and $C_{mn}^{\text{Doppler},r}$) have to be calculated. Consequently, the new calculation methodology for the coefficients $C_{mn}^{\text{Void},r}$ and $C_{mn}^{\text{Doppler},r}$ is qualified for ROM analyses. In addition to that the general effort for the calculation of $C_{mn}^{\text{Void},r}$ and $C_{mn}^{\text{Doppler},r}$ by employing the new method is significantly lower.

3.3 Recirculation loop

3.3.1 The recirculation loop model

The PSI-Illinois-ROM used a fixed total pressure drop $\Delta P_{ext} = const$ with respect to time as a boundary condition (equation(3.55)) [12]. According to

$$\oint \frac{\partial p}{\partial z} dz = 0 = \int_0^1 \frac{\partial p_{h_ch}}{\partial z} dz + \int_1^0 \frac{\partial p_{recirc}}{\partial z} dz \quad (3.54)$$

$$\Rightarrow \quad 0 \approx \int_0^1 \frac{\partial p_{h_ch}}{\partial z} dz - \Delta P_{ext} \quad , \quad (3.55)$$

the outer loop (second integral in (3.54)) was replaced by the boundary condition (first integral represents the pressure drop of the heated channel). This is a reasonable approximation to represent the real stability behaviour in an out-of phase oscillation mode. Note, however, in this case the stability behaviour of the in-phase oscillation mode can not be simulated correctly. Hence, the ROM was extended by a recirculation loop model [23,24].

In the following, a short description of the recirculation loop model is given. In this notation, an asterisk on a variable or parameter indicates the original dimensional quantity, while any quantity without an asterisk is dimensionless.

The mass balance of the downcomer can be written as

$$\frac{\partial}{\partial z} \dot{m}_{tot}^*(t) = 0 \quad (3.56)$$

and the total mass flow $\dot{m}_{tot}^*(t)$

$$\dot{m}_{tot}^*(t) = \sum_n \dot{m}_n^*(t) = -\rho_f^* \left[\sum_n A_{n,inlet}^* V_{n,inlet}^*(t) \right] \quad (3.57)$$

can accordingly be expressed by the sum of the core channel mass flows $\dot{m}_n^*(t)$, because the coolant in all hydraulic regions is considered to be incompressible. Here, n is the channel number and $A_{n,inlet}^*$ is the flow cross section of the n -th heated channel.

The energy balance of the downcomer is reduced to a boundary condition $h_{inlet}^* = h_{doc_inlet}^* = const$ because the energy gain and the energy loss are neglected.

The momentum balance of the downcomer can be written as

$$-\frac{\partial p_{doc}^*}{\partial z^*} = \frac{\partial}{\partial t^*} \left(\frac{\dot{m}_{tot}^*(t)}{A_{doc}^*} \right) + \frac{f_{1\Phi}^*}{2\rho_f^* D_{doc}^*} \left(\frac{\dot{m}_{tot}^*(t)}{A_{doc}^*} \right)^2 + g^* \rho_f^* \quad (3.58)$$

where the term on the left hand side describes the pressure drop in the downcomer, the first term on the right hand side describes the pressure drop due to inertial effects of the coolant, the second term states the downcomer friction and the last term is the

gravity term. A_{doc}^* is the downcomer flow cross section, D_{doc}^* is the hydraulic diameter of the downcomer, \dot{m}_{tot}^* is the total mass flow, ρ_f^* is the liquid density and $f_{1\Phi}^*$ is the single phase friction factor. Substitution (3.57) into (3.58) and transforming into dimensionless form lead to

$$-\frac{\partial P_{doc}}{\partial z} = -A_{ol} \left(\sum_n \frac{\partial}{\partial t} v_{n,inlet}(t) \right) - N_{f1\Phi} A_{ol}^2 D_{ol} \left[\sum_n v_{n,inlet}(t) \right]^2 + Fr^{-1} \quad (3.59)$$

where A_{ol} and D_{ol} are defined as $A_{ol} = A_{inlet}^* / A_{doc}^*$ and $D_{ol} = D_h^* / D_{doc}^*$ (D_h^* hydraulic diameter of the heated channel).

The ODEs for the channel inlet velocities $v_{n,inlet}(t)$ are determined by expression (3.54) in which the pressure drop over the recirculation loop is given by

$$\int_1^0 \frac{\partial P_{recirc}}{\partial z} dz = \int_1^0 \frac{\partial P_{doc}}{\partial z} dz - \Delta P_{head} \quad (3.60)$$

The evaluation of equation (3.54) with expression (3.60) was performed by using the symbolic toolbox of MATLAB. The final ODE for the n -th heated channel can be written as

$$\frac{d}{dt} v_{n,inlet}(t) = A_n(t) - B_n(t) \cdot \left(\sum_n \frac{d}{dt} v_{n,inlet}(t) \right) - B_n(t) N_{f1\Phi} A_{ol} D_{ol} \left(\sum_n v_{n,inlet}(t) \right)^2 \quad (3.61)$$

where $A_n(t)$ is defined as

$$A_n(t) = \frac{1}{ff_{n,14}(t)} \left[ff_{n,11}(t) \frac{d\mu_n(t)}{dt} + ff_{n,12}(t) \frac{dN_{n,pch}(t)}{dt} + ff_{n,13}(t) + \underbrace{1 + Fr \cdot \Delta P_{head}}_{Fr \cdot DP_{ext}} \right] \quad (3.62)$$

and $B_n(t)$ is defined as $B_n(t) = Fr A_{ol} / ff_{n,14}(t)$. The time dependent intermediate terms $ff_{n,11}(t)$, $ff_{n,12}(t)$, $ff_{n,13}(t)$ and $ff_{n,14}(t)$ are calculated in [12]. The time independent terms of (3.60) are included in function $A_n(t)$, where DP_{ext} is the steady state external pressure drop with $DP_{ext} = Fr^{-1} + \Delta P_{head}$, where the downcomer friction is neglected. In the steady state case, the integral (3.60) can be approximated as

$$\int_1^0 \frac{\partial P_{recirc}}{\partial z} dz \approx -Fr^{-1} - \Delta P_{head} = -DP_{ext} \quad (3.63)$$

because the contribution of the downcomer friction is very small in (3.61). In section 3.3.2 will be demonstrated that the effect of the downcomer friction on the thermal-hydraulic stability behaviour is very small. In addition to that the downcomer friction is not considered in RAMONA5. Hence, it can be neglected for BWR stability analyses.

Equation (3.63) relates the steady state external pressure drop to the pump head. In addition to that (as expected) it can be seen that the steady state core inlet velocity $v_{n,inlet,0}$ does not depend on the downcomer flow cross section. This means, $v_{n,inlet,0}$ depends on ΔP_{head} or DP_{ext} only.

As expected, each ODE for $v_{n,inlet}(t)$ is hydraulically coupled because of (3.57) with all the other heated channels. Equation (3.61) is the ODE for the channel inlet velocity $v_{n,inlet}(t)$ of the n -th heated channel.

Due to practical relevance, the ODEs for $v_{n,inlet}(t)$ was written separately for the one- and the two-heated channel cases. The result for the one-heated- channel case is

$$\frac{d}{dt}v_{inlet} = \frac{1}{1+B} \left[A + B N_{f,1\Phi} A_{ol} D_{ol} (v_{inlet})^2 \right] \quad (3.64)$$

and the ODEs for $v_{n,inlet}(t)$ in the two-heated-channel case ($n = 1, 2$) can be written as

$$\begin{aligned} \frac{d}{dt}v_{1,inlet} &= \frac{-A_2 \cdot B_1 + A_1 \cdot B_2 + A_1}{1 + B_1 + B_2} + \frac{B_1 N_{f,1\Phi} A_{ol} D_{ol}}{1 + B_1 + B_2} \left[v_{1,inlet} + v_{2,inlet} \right]^2 \\ \frac{d}{dt}v_{2,inlet} &= \frac{-A_1 \cdot B_2 + A_2 \cdot B_1 + A_2}{1 + B_1 + B_2} + \frac{B_2 N_{f,1\Phi} A_{ol} D_{ol}}{1 + B_1 + B_2} \left[v_{1,inlet} + v_{2,inlet} \right]^2 . \end{aligned} \quad (3.65)$$

According to equation (3.61) (second and third term on the right hand side), $\dot{v}_{n,inlet}(t)$ depends on all heated channels. The inertial term contributes to the mass flow changes of all heated channels. Thus, the inertial term of the downcomer momentum balance describes the impact of all heated channels on the n -th heated channel. From the physical point of view, if the downcomer flow cross section is increased (A_{ol} decreases), the inertial effects of the downcomer mass flow decrease. For $A_{doc} \rightarrow \infty$ the ratio $A_{ol} \rightarrow 0$ which corresponds to the constant external pressure drop boundary condition. In this case ($A_{ol} = 0$), the inertial term in the downcomer momentum balance vanishes and the n -th heated channel is independent of all the other heated channels. This means, the change of the mass flow in the k -th heated channel does not affect the n -th heated channel. Consequently, if the ratio A_{ol} is zero ($A_{ol} = 0$) the inertial effects of the downcomer vanish and (3.61) is reduced to $\dot{v}_{n,inlet} = A_n$ (original ODE) which is the result of expression (3.55) evaluated in [12] (final ODEs for the heated channel inlet velocities presented by Dokhane [12] with $DP_{ext} = Fr^{-1} + \Delta P_{head}$).

3.3.2 The effect of the recirculation loop model on the stability behaviour of a simple thermal-hydraulic one heated channel model

In this subsection, the impact of the recirculation loop of the thermal hydraulic one heated channel model in the HEM limit on the stability boundary (SB) and bifurcation characteristics (BCH) are investigated [23,24]. This sub-model, in the following referred to as TH-model, is a subset of the TUD-ROM. In particular, the TH-model is a set of 5 nonlinear ODE's ((3.24), (3.25), (3.27), (3.28) and (3.64)) for the state variables $a_1(t)$, $a_2(t)$, $s_1(t)$, $s_2(t)$ and $v_{inlet}(t)$. The input parameters of the TH-model are based on the TH-model used originally by Dokhane et al. [12,13] for its validation against experimental data (Saha et al. [77]).

3.3.2.1 Bifurcation analysis using BIFDD

In order to study the impact of the recirculation loop of the TH-model on the SB and BCH, the ratio A_{ol} is varied in small steps (which corresponds to the variation of the downcomer flow cross section A_{doc}^*) and semi-analytical bifurcation analysis is carried out by employing BIFDD. The bifurcation parameter is N_{pch} and the iteration parameter is N_{sub} . By setting $D_{ol} = 0$ downcomer friction is not considered in (3.64). Because of practical relevance the ratio A_{ol} and N_{sub} were varied in the interval $A_{ol} \in [0.0, \dots, 2.0]$ and $N_{sub} \in [0.1, \dots, 4.0]$, respectively. Figure 3.4 shows SB's in the N_{sub} - N_{pch} -parameter space and the corresponding BCH's for different A_{ol} -values.

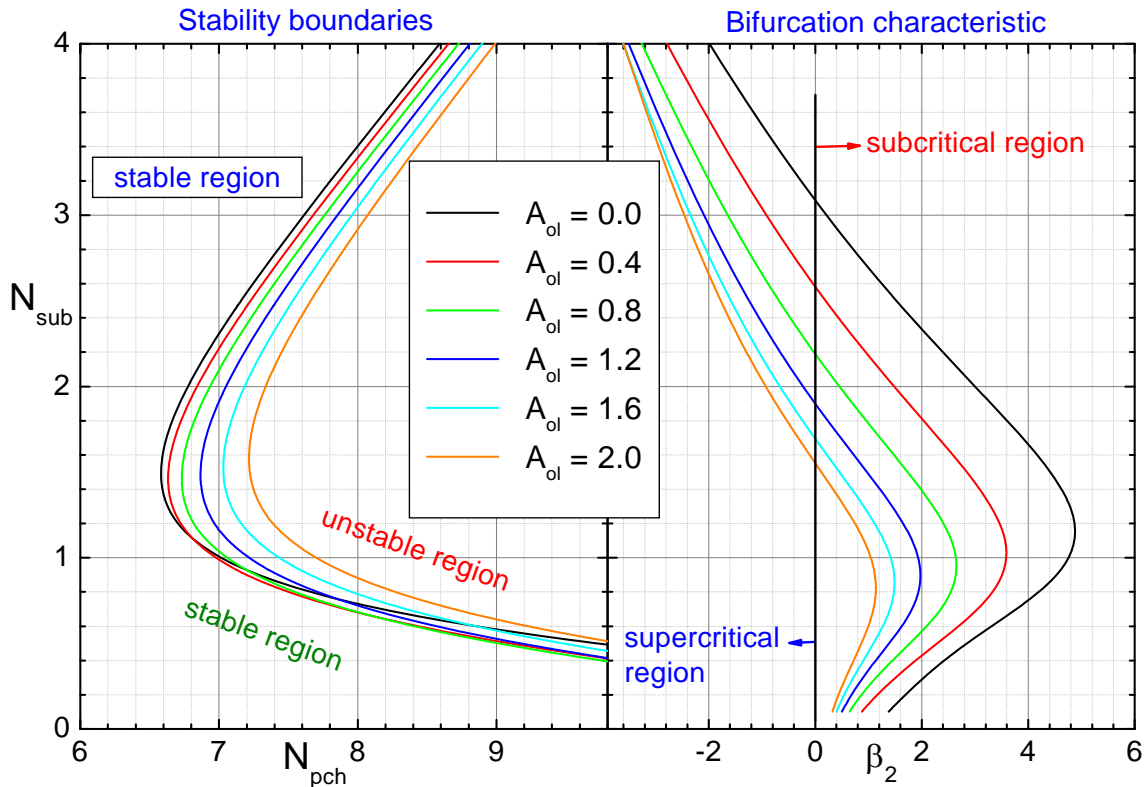


Figure 3.4: Results of the SB's and the corresponding BCH's for different ratios $A_{ol} \in [0.0, \dots, 2.0]$ are presented.

The stability boundaries shift to the right hand side for increasing A_{ol} values. The set of stable fixed points increases in the $N_{sub} - N_{pch}$ -parameter space and thus the system becomes more stable. This behaviour is in line with the well-known **density wave oscillation (DWO) mechanism** [69-74,77,78]: the larger the bypass cross section, the better the boundary condition $DP_{external} = const$ is fulfilled (constant external pressure drop over the channel) and thus self-sustained density wave oscillations can occur. The set of fixed points, where unstable limit cycles exist, decreases for increasing A_{ol} values because the set of subcritical PAH bifurcation points decreases. This fact has safety relevance (in a general sense) because such fixed points may deceptively appear as stable fixed points if the perturbation is sufficiently small. If the disturbance overcomes the critical amplitude, however, the fixed point becomes unstable.

To analyse the influence of the downcomer friction separately, the ratio D_{ol} was varied in $D_{ol} \in [0.0, \dots, 0.14]$ where A_{ol} was set $A_{ol} = 1.2$. Figure 3.5 and Figure 3.6 present the results of the bifurcation analyses for the D_{ol} variation.

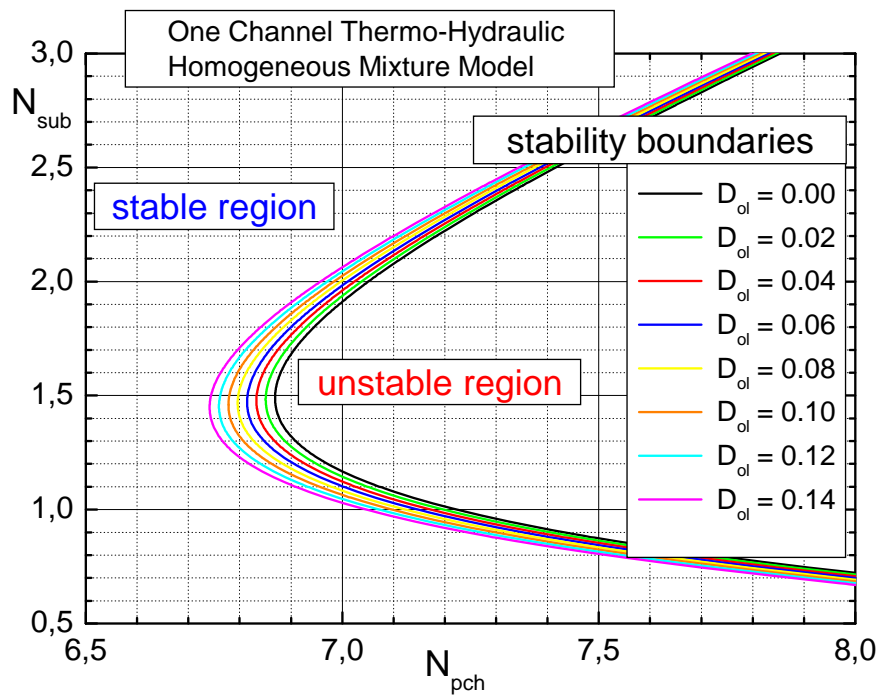


Figure 3.5: Stability boundaries in the $N_{sub} - N_{pch}$ -parameter space for different ratios D_{ol} with $D_{ol} \in [0.0, \dots, 0.14]$.

Figure 3.5 clearly shows that the stability boundaries shift to the left hand side for increasing D_{ol} values. Consequently, the system becomes more unstable. On the other hand, the number of subcritical fixed points decreases for increasing D_{ol} values shown in Figure 3.6. But both figures also show that the stability behaviour of the dynamical system is not significantly sensitive to the D_{ol} variation. Practical values of D_{ol} are within the interval $D_{ol} \in [0.02, \dots, 0.04]$. As shown in Figure 3.5, the effect of D_{ol} -deviations is small. Thus, the downcomer friction can be neglected in further investigations.

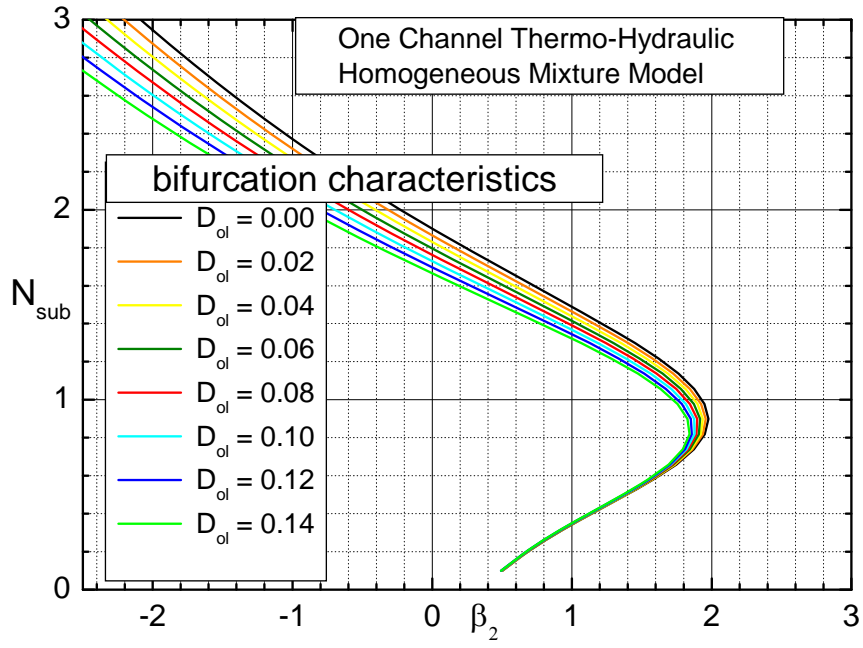


Figure 3.6: Poincaré-Andronov-Hopf bifurcation characteristics in the $N_{sub} - \beta_2$ -parameter space for different ratios D_{ol} with $D_{ol} \in [0.0, \dots, 0.14]$.

3.3.2.2 Numerical integration

The semi-analytical bifurcation analysis is valid only in the vicinity of the SB. Hence, to obtain information about of the stability behaviour beyond the local bifurcation findings, numerical integration of the set of the ODEs is necessary. In addition to that, the predictions of the semi-analytical bifurcation analysis can be confirmed independently by employing numerical integration. To this end, the ODEs are integrated (in the time domain) in the MATLAB environment, where a Runge-Kutta method was used.

The aim of this section is to show the numerical integration method by means of the thermal-hydraulic one heated channel model in a close neighbourhood of two points, defined in Figure 3.7, respectively.

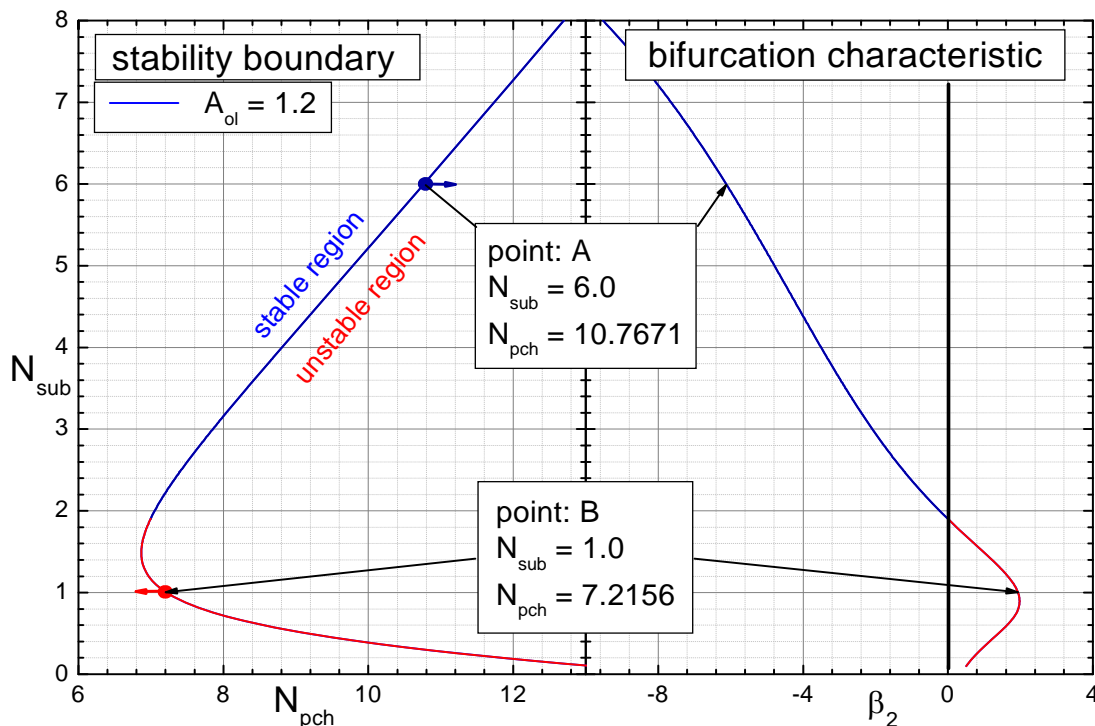


Figure 3.7: Definition of two points, A and B on the SB for $A_{ol} = 1.2$. In point A supercritical PAH-B are predicted. In point B subcritical PAH-B are predicted.

Numerical integration results with parameter configurations corresponding to point A and B are presented in the following.

Analysis at point A:

On the left hand side of point A, stable fixed points are predicted. For the analysis in this region the phase change number was changed from the critical value $N_{pch} = 10.7671$ to $N_{pch} = 10.7$ and a perturbation in the inlet velocity δv_{inlet} was introduced to the system (steady state). Figure 3.8 presents the time evolution of v_{inlet} . It is clearly shown that the system is stable.

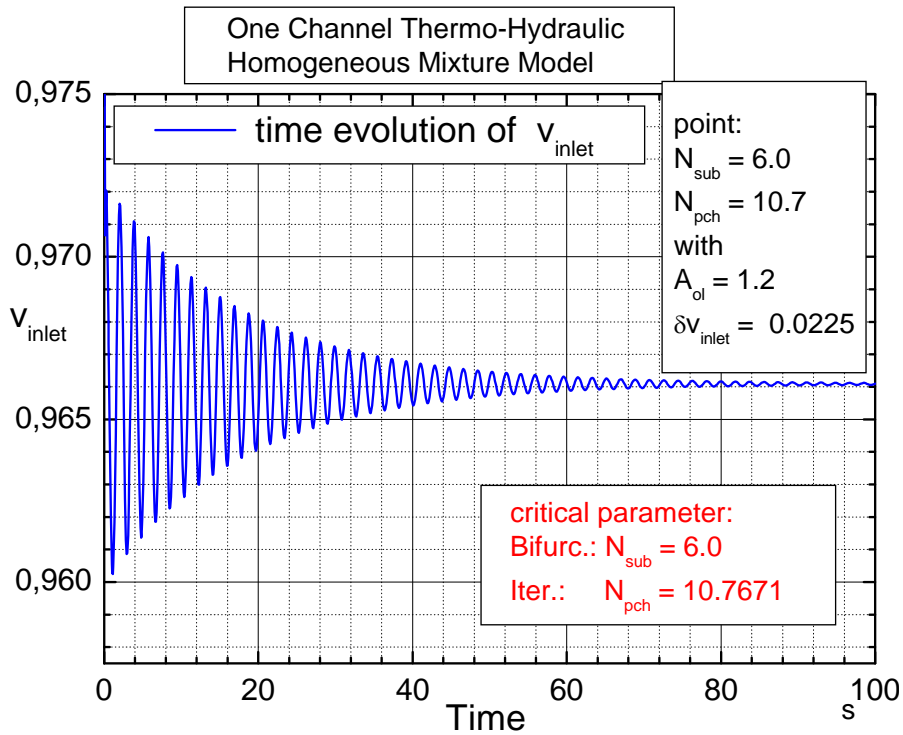


Figure 3.8: Time evolution of v_{inlet} . The system is stable.

On the right hand side of the SB, stable limit cycles of the dynamical system are predicted. In order to confirm this prediction, N_{pch} was changed from the critical value $N_{pch} = 10.7671$ to $N_{pch} = 10.78$ and the same perturbation amplitude δv_{inlet} was imposed on the system. As shown in Figure 3.9, the existence of a stable periodic solution is confirmed by numerical integration at this point.

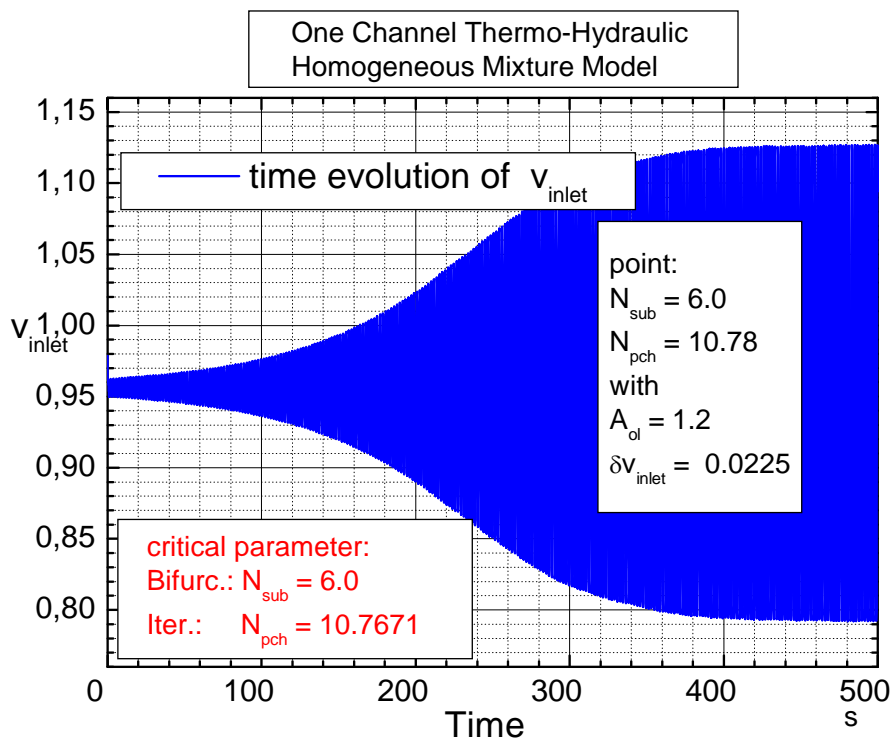


Figure 3.9: Time evolution of v_{inlet} (stable periodic solution).

Analysis at point B:

A subcritical bifurcation is predicted at point B. Consequently, unstable limit cycles are expected in the stable region close to point B. The numerical integration was carried out in the linear stable region at $N_{pch} = 7.2151$. At first, a small perturbation ($\delta v_{inlet} = 0.01$) is imposed on the system and numerical integration is carried out. The result is shown in Figure 3.10. In the second step, a six times larger perturbation amplitude ($\delta v_{inlet} = 0.06$) was imposed on the system. The result is shown in Figure 3.11.

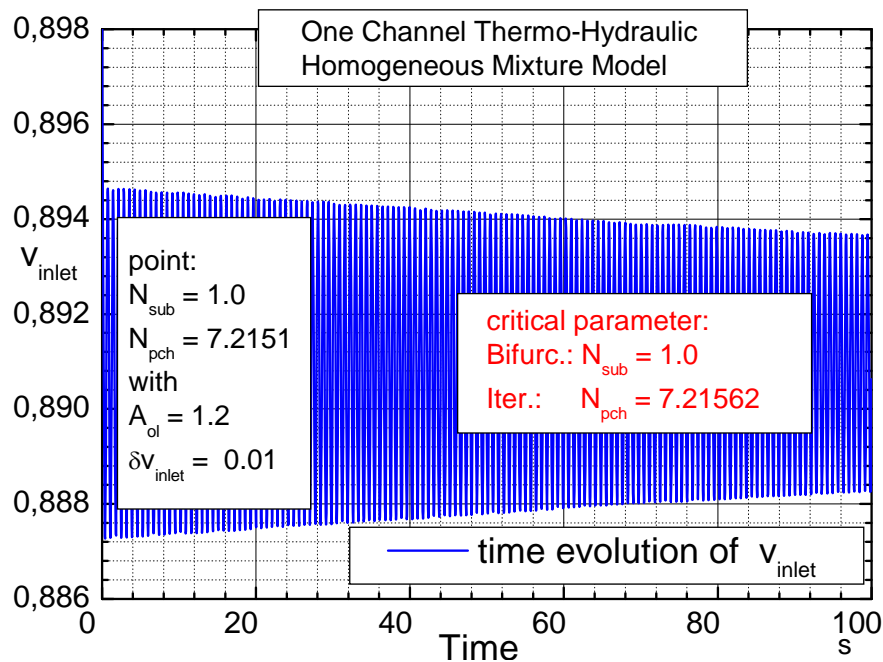


Figure 3.10: Time evolution of v_{inlet} . The system is stable for the relative small perturbation amplitude $\delta v_{inlet} = 0.01$.

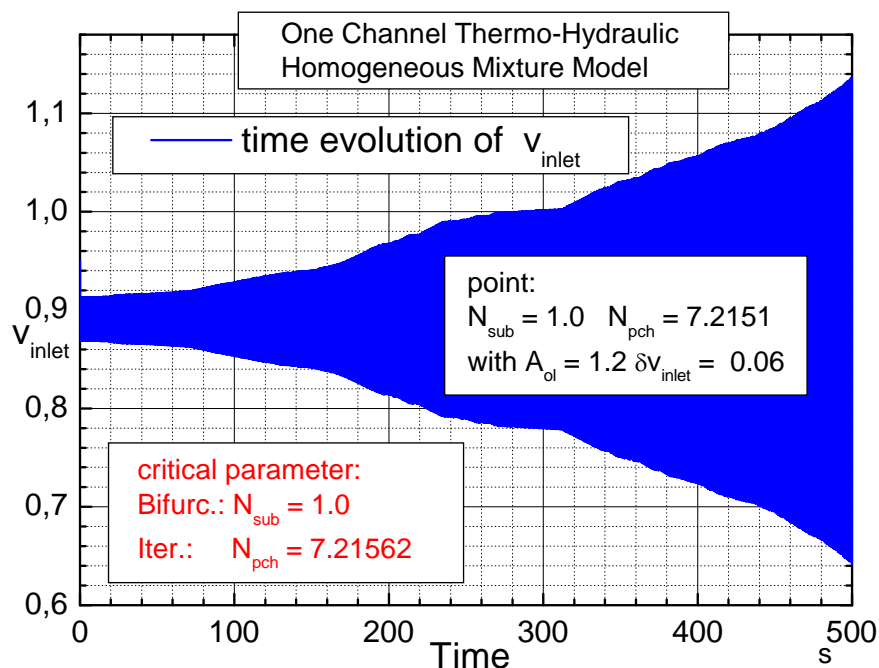


Figure 3.11: Time evolution of v_{inlet} . The system is unstable for the relative large perturbation amplitude of $\delta v_{inlet} = 0.06$.

The results of the numerical integration at the point B confirm the prediction of the semi-analytical bifurcation analysis. Roughly speaking, the system is stable for sufficient small perturbations and unstable for sufficient large perturbations.

On the right hand side of point B the system is unstable. The results of the numerical integration carried out in this region are not presented here.

3.3.2.3 Summary

The study of the impact of the recirculation loop on the SB and PAH-B was carried out by variation of the downcomer flow cross section. The results show clearly that the stability behaviour of the thermal hydraulic one heated channel model is very sensitive to variations of the downcomer flow cross section. The larger the downcomer flow cross section the more unstable the system is. If the downcomer flow cross section is infinitely large, the boundary condition of a constant external pressure drop will be fulfilled.

The dominant term in the momentum balance of the downcomer is the inertial term. In contrast, the friction term in this balance equation do not have a significant impact on the thermal-hydraulic stability characteristics. This result is in line with the RAMONA5 model in which downcomer-friction is not taken into account. Hence, downcomer friction will be neglected in all further analyses.

Additionally, numerical integration of the TH-model was carried out in the close region of two points located on the SB. The dynamical behaviour predicted by the semi-analytical bifurcation analysis could be confirmed independently by the numerical integration.

3.3.3 The effect of the recirculation loop model on the stability behaviour of the ROM (coupled model)

In the framework of this investigation, the impact of the recirculation loop on both in-phase and out-of-phase oscillation mode of the ROM based on NPP Leibstadt cycle 7 record #4 (KKLc7_rec4 [5,6,79]) data is analysed. To this end, semi-analytical bifurcation analysis with BIFDD is performed. Besides, a modified BIFDD version is employed to examine the set of fixed points where the complex conjugated eigenvalues with the second largest real parts are zero.

In the scope of this analysis, the following definitions are made:

- eigenvalue or pair of complex conjugated eigenvalues (λ_1) of the Jacobian matrix of the ROM differential equation system with the largest real part: $\text{Re}(\lambda_1) > \text{Re}(\lambda_i) \quad \forall \lambda_i$ with $i \neq 1$ or $|\text{Re}(\lambda_1)| < |\text{Re}(\lambda_i)| \quad \forall \lambda_i$ with $i \neq 1$
- eigenvalue or pair of complex conjugated eigenvalues (λ_2) with the second largest real part: $\text{Re}(\lambda_1) > \text{Re}(\lambda_2) > \text{Re}(\lambda_i) \quad \forall \lambda_i$ with $i \neq 1, 2$ or $|\text{Re}(\lambda_1)| < |\text{Re}(\lambda_2)| < |\text{Re}(\lambda_i)| \quad \forall \lambda_i$ with $i \neq 1, 2$
- The eigenvectors \vec{p}_{in} and \vec{p}_{out} of the linearized BWR system (ROM) correspond to specific eigenstates which are referred to as in-phase oscillation mode and out-of-phase oscillation mode, respectively. The eigenvalues corresponding to \vec{p}_{in} and \vec{p}_{out} are λ_{in} and λ_{out} . As will be shown later, λ_{out} and λ_{in} are the eigenvalues with the largest and second largest real parts for the reference OP of KKLc7rec4.

Before continuing, the general solution of the linearized system of the dynamical system (2.1) in section 2.2 is discussed (also presented in Appendix A). In order to linearize the dynamical system (2.1) at the steady state solution \vec{X}_0 , the Ansatz

$$\vec{X}(t) = \vec{X}_0 + \delta\vec{X}(t) \quad (3.66)$$

is substituted in (2.1) and a Taylor-expansion is applied

$$\begin{aligned} \underbrace{\frac{d}{dt}\vec{X}_0}_{=0} + \frac{d}{dt}\delta\vec{X} &= F(\vec{X}_0 + \delta\vec{X}, \gamma_0) \\ &= \underbrace{F(\vec{X}_0, \gamma_0)}_{=0} + \underbrace{D_x F(\vec{X}_0, \gamma_0)}_J \underbrace{[\vec{X} - \vec{X}_0]}_{=\delta\vec{X}} + \underbrace{0(\|\delta\vec{X}\|^2)}_{\approx 0} \end{aligned} \quad (3.67)$$

where the linear term is taken into account, only. The result is

$$\frac{d}{dt}\delta\vec{X} = J\delta\vec{X} \quad (3.68)$$

where J is the Jacobian matrix defined as

$$J = \begin{pmatrix} \frac{\partial F_1}{\partial x_1} & \dots & \frac{\partial F_1}{\partial x_n} \\ \vdots & \ddots & \vdots \\ \frac{\partial F_n}{\partial x_1} & \dots & \frac{\partial F_n}{\partial x_n} \end{pmatrix} . \quad (3.69)$$

Equation (3.68) is the linearized system of (2.1) at \vec{X}_0 . The solution of equation (3.68) can be written as

$$\delta \vec{X}(t) = e^{Jt} \delta \vec{X}_0 . \quad (3.70)$$

Roughly speaking, the solution (3.70) describes the time evolution of the small perturbation $\delta \vec{X}$ which is imposed on the steady state \vec{X}_0 at $t=t_0=0$ with $\delta \vec{X}(t=t_0) = \delta \vec{X}_0$. According to equation (3.70), the time evolution of $\delta \vec{X}$ only depends on J . In turn, J depends on the parameter vector γ .

In order to evaluate (3.70), the linear transformation

$$\delta \vec{X}(t) = P \vec{U}(t) \quad (3.71)$$

is performed such that the Jacobian matrix can be transformed into the Jordan normal form. To this end, the eigenvalue problem

$$J \vec{p}_i = \lambda_i \vec{p}_i \quad (3.72)$$

has to be solved, where \vec{p}_i are the eigenvectors with their corresponding eigenvalues λ_i of the Jacobian matrix. The transformation matrix P can according to $P = [\vec{p}_1, \dots, \vec{p}_i, \dots, \vec{p}_n]$ be written in terms of the eigenvectors \vec{p}_i . In other words, the columns of P are the eigenvectors \vec{p}_i of the Jacobian matrix.

In the linear system (3.68) the vector $\delta \vec{X}$ is substituted by Ansatz (3.71) and the final equation is multiplied by P^{-1} from the left hand side. The result can be written as

$$\frac{d}{dt} \vec{U} = P^{-1} J P \vec{U} = D \vec{U} , \quad (3.73)$$

where D

$$D = P^{-1} J P = \begin{pmatrix} \lambda_1 & \dots & \dots & 0 \\ \vdots & \ddots & & \vdots \\ \vdots & \begin{pmatrix} a_i & b_i \\ -b_i & a_i \end{pmatrix} & & \vdots \\ \vdots & & \ddots & \vdots \\ 0 & \dots & \dots & \lambda_n \end{pmatrix} \quad (3.74)$$

is the Jacobian matrix transformed into the Jordan normal form. If all eigenvalues of J are real and distinct, the matrix D will have a diagonal form.

The solution of (3.73) can be written as

$$\vec{U}(t) = e^{D(t-t_0)} U_0 , \quad (3.75)$$

where $\delta \vec{X}_0 = P \vec{U}_0$. The inverse transformation gives

$$\delta \vec{X} = P \vec{U}(t) = P e^{D(t-t_0)} U_0 = P e^{D(t-t_0)} P^{-1} \delta \vec{X}_0 . \quad (3.76)$$

The general solution of the linearized system (3.68) can be written as

$$\begin{aligned} \vec{X}(t) &= \vec{X}_0 + \sum_{i=1}^n c_i \vec{P}_i e^{\lambda_i t} \\ \begin{pmatrix} x_1(t) \\ \vdots \\ x_n(t) \end{pmatrix} &= \begin{pmatrix} x_{01}(t) \\ \vdots \\ x_{0n}(t) \end{pmatrix} + \sum_{i=1}^n c_i \begin{pmatrix} p_{i1} \\ \vdots \\ p_{in} \end{pmatrix} e^{\lambda_i t} , \end{aligned} \quad (3.77)$$

where the constants c_i can be calculated from the initial conditions.

As can be seen in (3.77), the stability behaviour of the linearized system in the vicinity of \vec{X}_0 depends on the real parts of the eigenvalues λ_i of J with $\lambda_i = \lambda_i(\gamma)$. According to (3.77) all components $x_i(t)$ of the general solution contain all eigenvalues λ_i of J . This means, if there is at least one pair of complex conjugate eigenvalues with a positive real part, the system will be unstable. If all eigenvalues have strictly negative real parts, the system will be stable. When a selected control parameter is changed and the eigenvalue with the largest real part becomes zero, bifurcation analyses as explained in sections 2.2 and 2.3 are necessary.

3.3.3.1 Bifurcation analysis using BIFDD

The selection of the reference OP and the procedure to calculate the ROM (the artificial factor *fact* is *fact* = 5) input is presented in section 4.2. In the scope of the bifurcation analysis, N_{sub} and DP_{ext} are defined to be the iteration and bifurcation parameters, respectively, and the downcomer friction is neglected. In order to study the effect of the recirculation loop on the BWR stability behaviour, the ratio A_{ol} was varied. Thereby, a change of $A_{ol} = A_{inlet}^* / A_{doc}^*$ corresponds to a change of the downcomer flow cross section A_{doc}^* . For calculation of ratio A_{ol} from the RAMONA5 model, the flow cross section of downcomer 2 (DC2, see [32]) was taken into account. The result is $A_{ol} = 12.68$ and is considered to be the reference value for this analysis.

At first, the bifurcation analysis is carried out for $A_{ol} = 12.68$. The stability boundary is shown in Figure 3.12. The analysis has shown that the pair of complex conjugate eigenvalues with the largest real part corresponds to the out-of-phase oscillation mode ($\lambda_1 = \lambda_{out}$ with $\text{Re}(\lambda_1) > \text{Re}(\lambda_i) \quad \forall \lambda_i, i \neq 1$). For this parameter configuration, all the other eigenvalues have strictly negative real parts. This means, only the out-of-phase mode is excited at operational points for which $\text{Re}(\lambda_1) > 0$ (linear unstable region).

The bifurcation characteristics are presented in Figure 3.13 and show that β_2 is always positive ($\beta_2 > 0$). This means, unstable periodical solutions are predicted in the linear stable region close to the stability boundary. Figure 3.14 show the SB trans-

formed into the power flow map where the 112% rod-line and the exclusion region for cycle 7 are included.

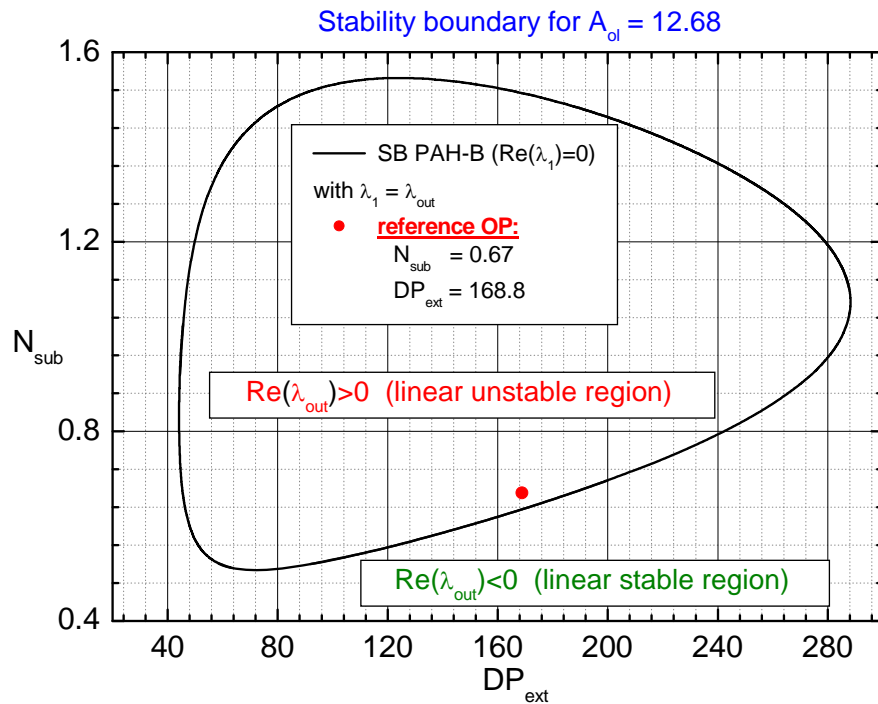


Figure 3.12: Stability boundary for $A_{ol} = 12.68$.

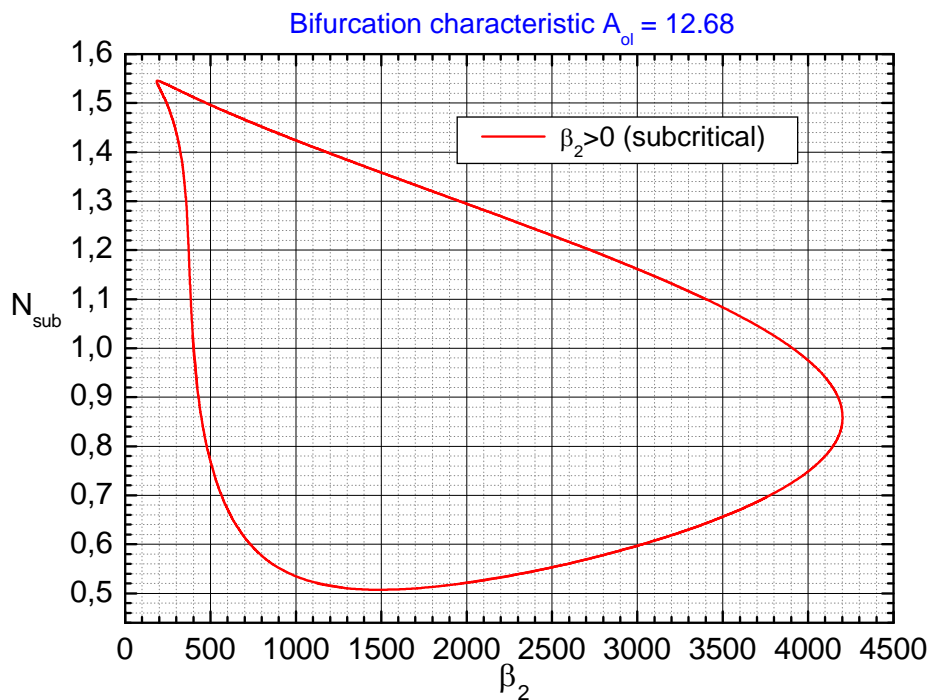


Figure 3.13: Bifurcation characteristics for $A_{ol} = 12.68$.

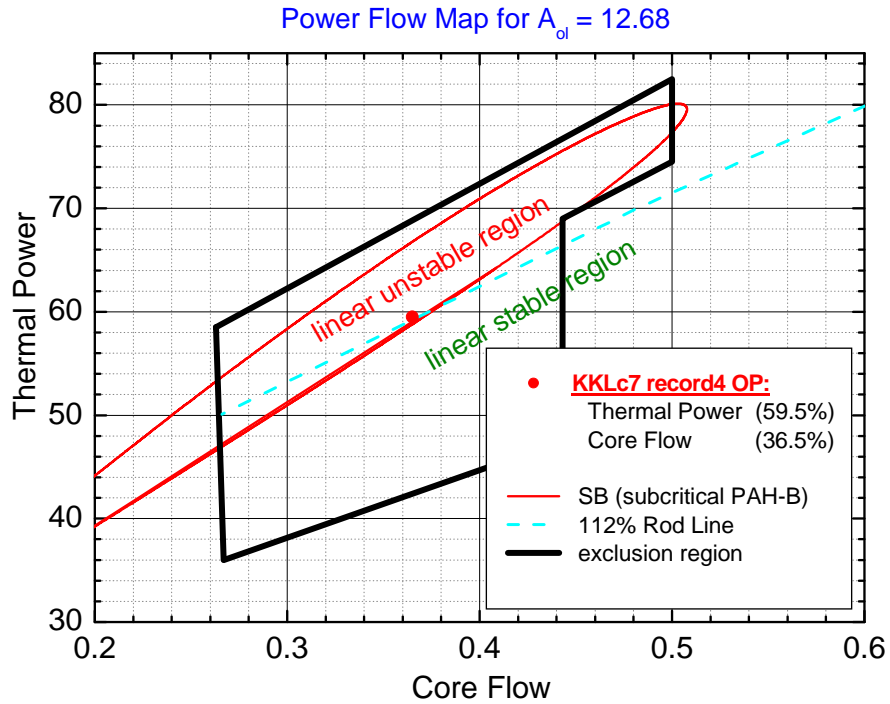


Figure 3.14: SB transformed into the power flow map.

Secondly, the ratio A_{ol} was changed to $A_{ol} = 6.75$ and bifurcation analysis has been carried out. The analysis has shown (Figure 3.15) that there is a small region close to the reference OP where the in-phase mode is excited ($Re(\lambda_{in}) > 0$) for $A_{ol} = 6.75$. But at the reference OP, only the out-of-phase mode is excited, because $Re(\lambda_{out}) > 0$ and $Re(\lambda_{in}) < 0$ with $\lambda_2 = \lambda_{in}$. The SB and the nature of the PAH-B have not changed.

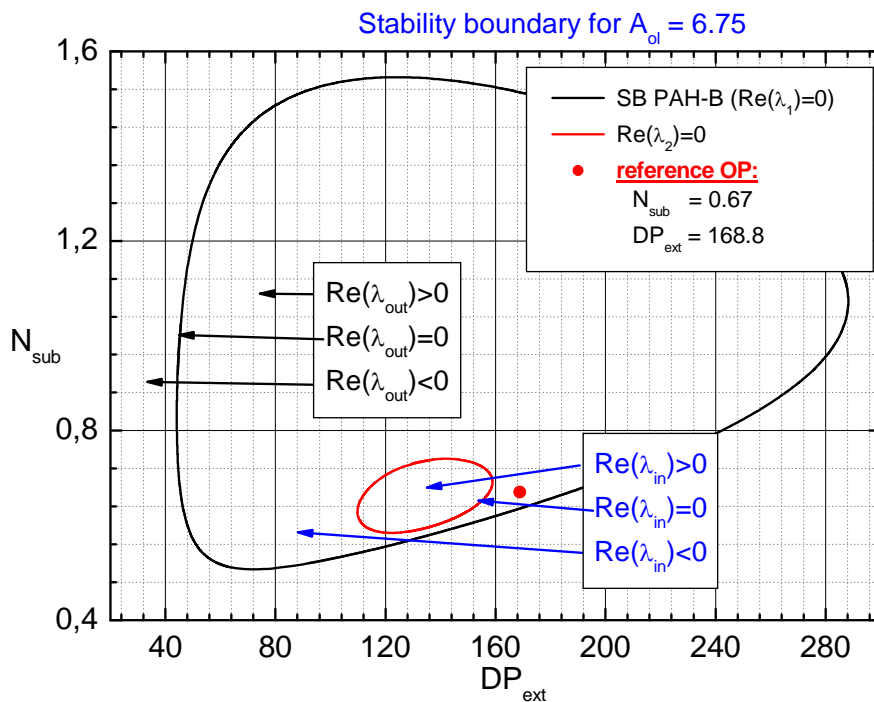


Figure 3.15: Stability boundary for $A_{ol} = 6.75$. The bifurcation characteristics are unchanged.

Furthermore, bifurcation analyses for the ratios $A_{ol} = 6.00$ and $A_{ol} = 4.00$ have been performed, respectively. The stability boundaries for both cases are presented in Figure 3.16 and Figure 3.17, respectively. The nature of the PAH-B for $A_{ol} = 4$ and $A_{ol} = 12.68$ is shown in Figure 3.18.

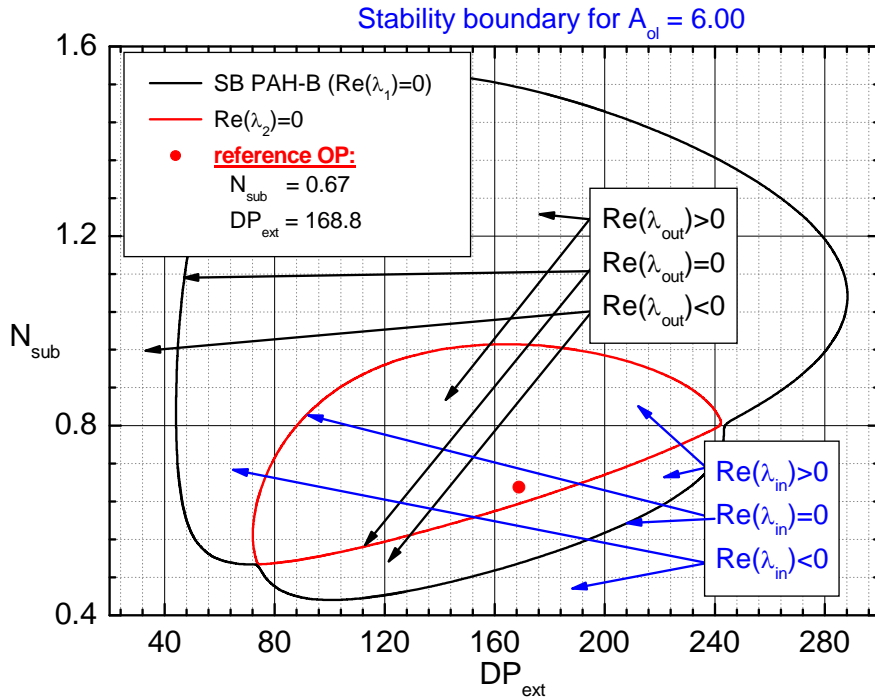


Figure 3.16: Stability boundary for $A_{ol} = 6.00$.

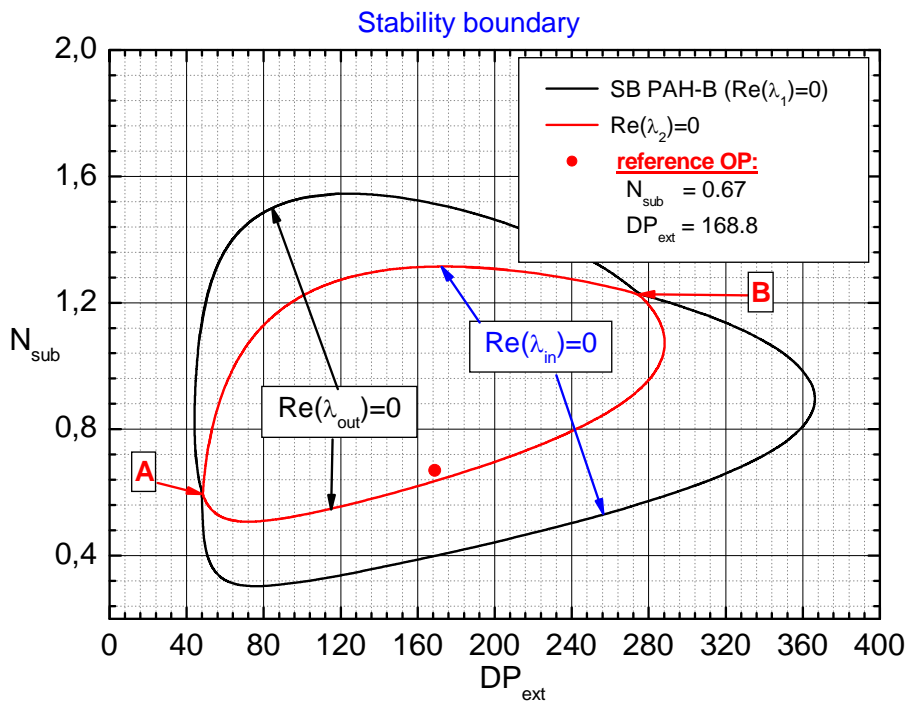


Figure 3.17: Stability boundary for $A_{ol} = 4.00$.

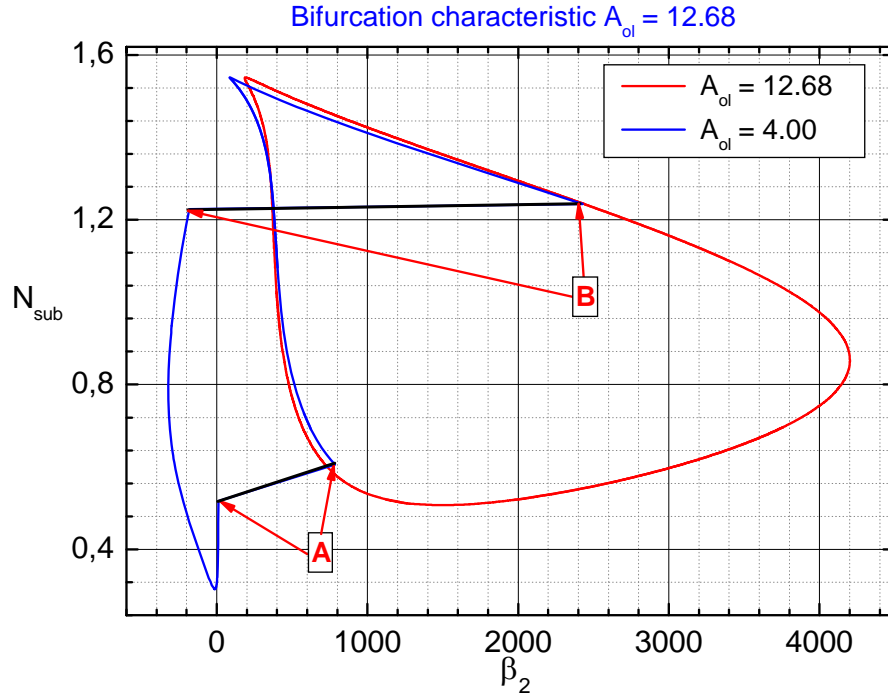


Figure 3.18: Nature of the PAH-B for the reference case and $A_{ol} = 4.00$.

The bifurcation analysis has shown that the downcomer flow cross section variation does not have an effect on the out-of-phase oscillation mode because the A_{ol} variation does not change the locations of operational points where $\text{Re}(\lambda_{out}) = 0$, in the $N_{sub} - DP_{ext}$ -parameter map. On the other hand, the A_{ol} (A_{doc}) variation has a significant effect on the in-phase oscillation mode. If A_{ol} is decreased (A_{doc} will be increased), the set of fixed points for which the in-phase mode is excited, will grow. In other words, if the downcomer flow cross section is increased, the region where $\text{Re}(\lambda_{in}) \geq 0$ (in the $N_{sub} - DP_{ext}$ -parameter space) is growing.

Furthermore, as can be seen in Figure 3.15, Figure 3.16 and Figure 3.17 the real part of the pair of complex conjugated eigenvalues associated with the in-phase oscillation mode is passing the real part of the pair of complex conjugated eigenvalues associated with the out-of-phase oscillation mode with increasing downcomer flow cross section ($A_{ol} \rightarrow$ decreasing). E.g. such crossing points are depicted in Figure 3.17, point A and B. The effect of passing real parts of both pairs of complex conjugated eigenvalues associated with the in- and out-of-phase oscillation modes on the bifurcation characteristics are presented in Figure 3.18. In point A and B the bifurcation characteristics are changing significantly. If $\text{Re}(\lambda_{in}) > \text{Re}(\lambda_{out})$, $\beta_2 < 0$ and if $\text{Re}(\lambda_{out}) > \text{Re}(\lambda_{in})$, $\beta_2 > 0$.

3.3.3.2 Numerical integration

Numerical integration was performed at the reference OP for different A_{ol} ratios $A_{ol} = [12.68, 8.0, 7.0, 6.0]$. The transient was initiated by introducing perturbations in the channel inlet velocities with opposite sign (an in-phase oscillation is triggered).

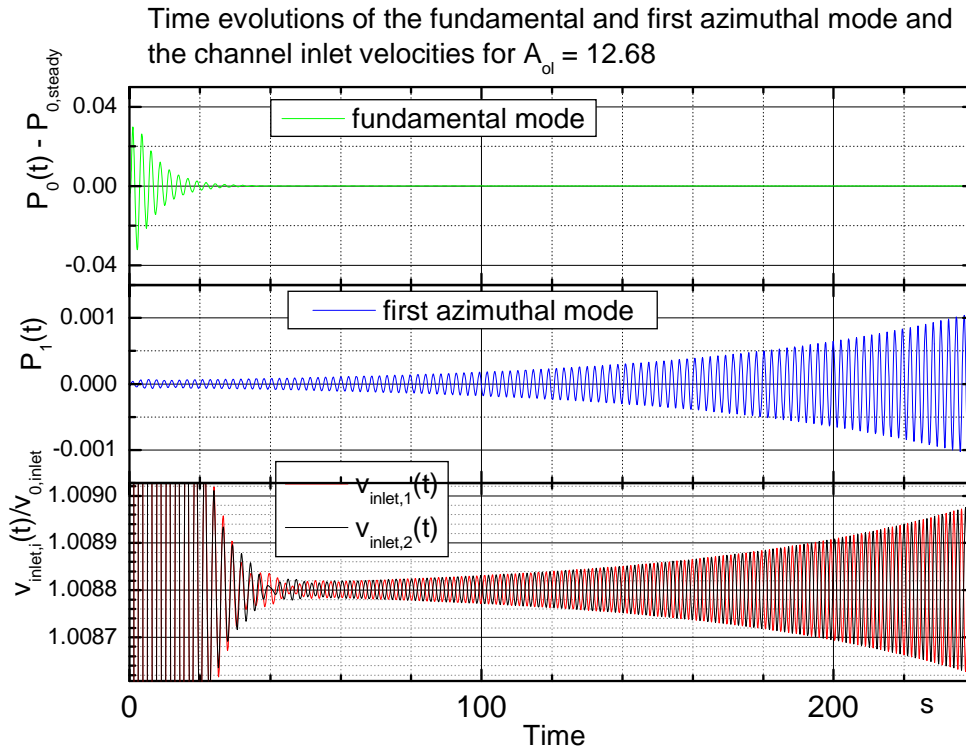


Figure 3.19: Numerical integration for $A_{ol} = 12.68$.

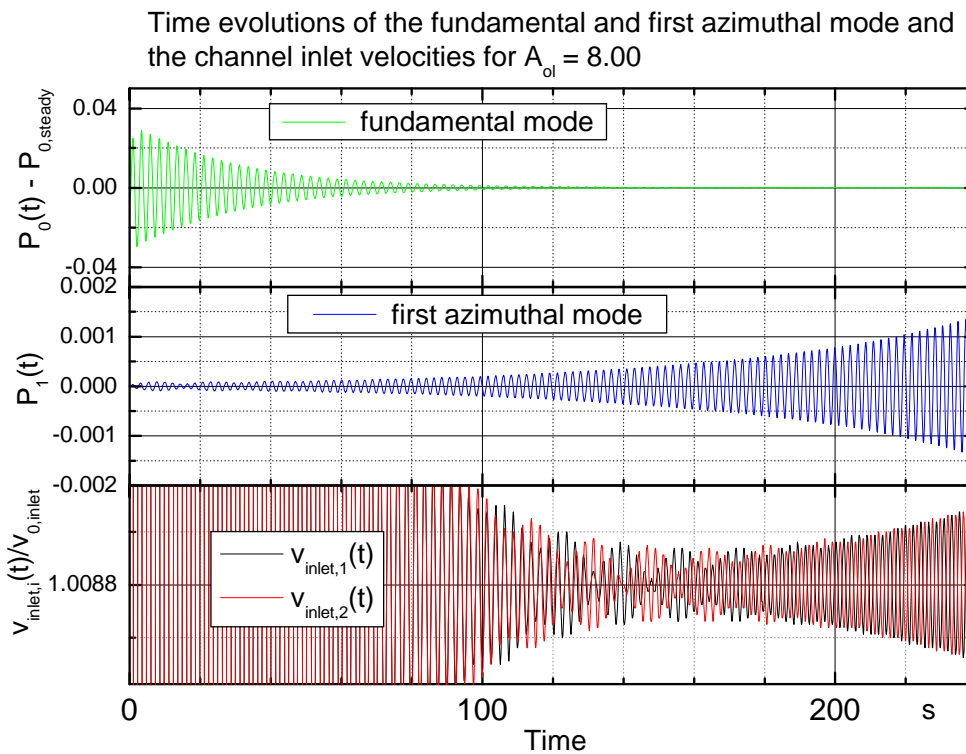


Figure 3.20: Numerical integration for $A_{ol} = 8.00$.

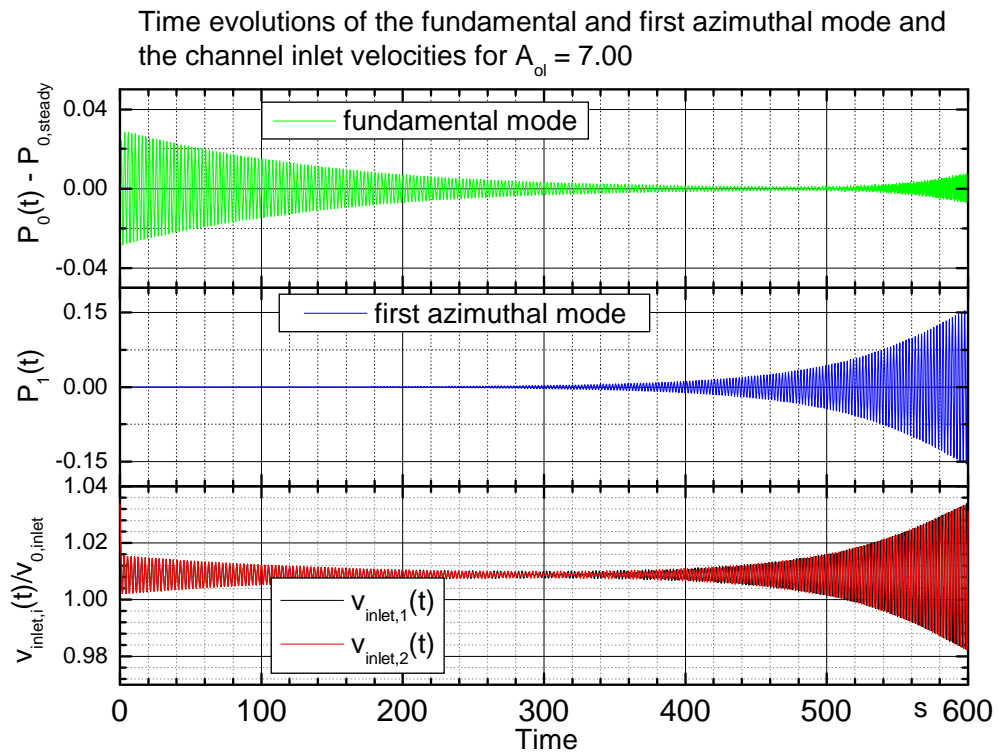


Figure 3.21: Numerical integration for $A_{ol} = 7.00$.

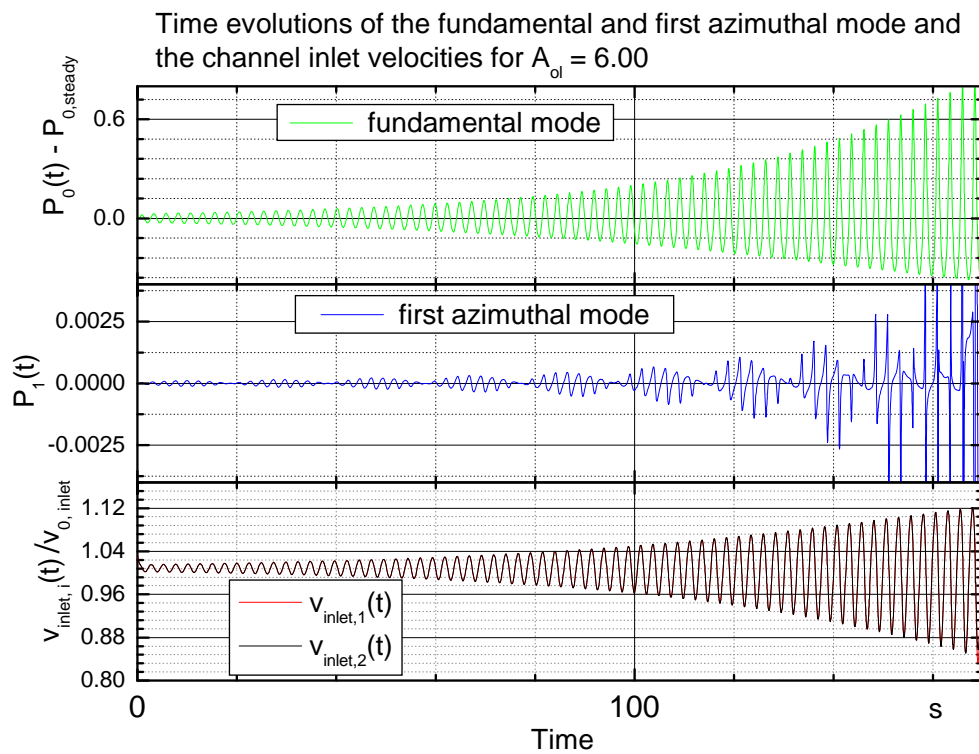


Figure 3.22: Numerical integration for $A_{ol} = 6.00$.

The numerical integrations for different downcomer flow cross section confirm the prediction of the bifurcation analyses.

3.3.3.3 RAMONA5 analysis

In the following subsection, RAMONA5 analyses are performed at the reference OP (but with $h_{sub} = 120 \text{ kJ/kg}$) where the downcomer flow cross section (DC2) is varied. The reference value of A_{doc}^* is $A_{doc}^* = 0.25 \text{ m}^2$. The transient is initiated by imposing a sinusoidal control rod perturbation into the steady state system (additional information about the KKL-RAMONA5 model and the locations of the LPRM's is given in section 4.1).

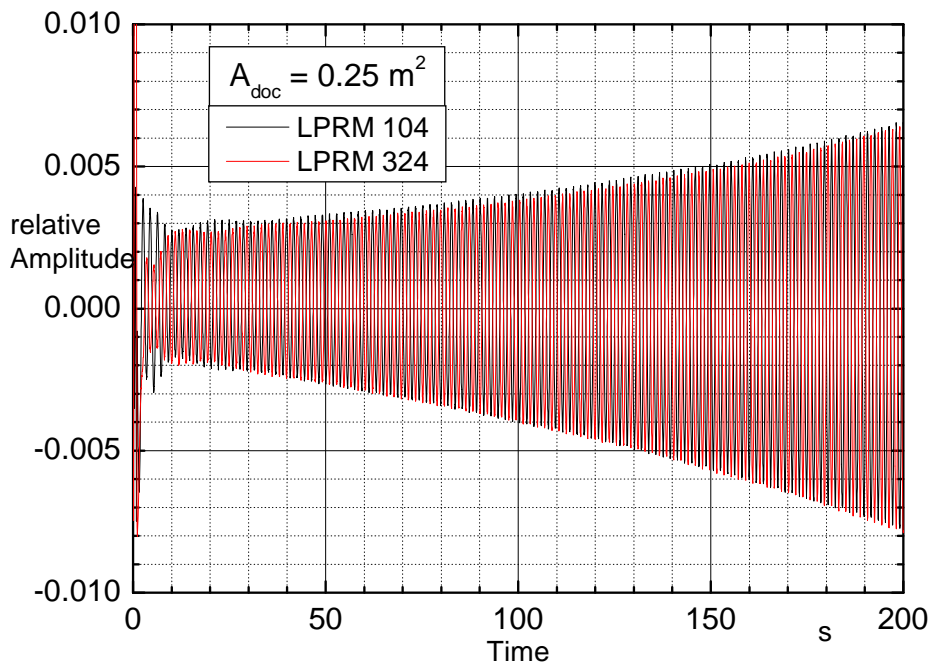


Figure 3.23: Signals (relative amplitudes) of LPRM 10 and 32 in the fourth level respectively. The global power oscillation is strong decaying.

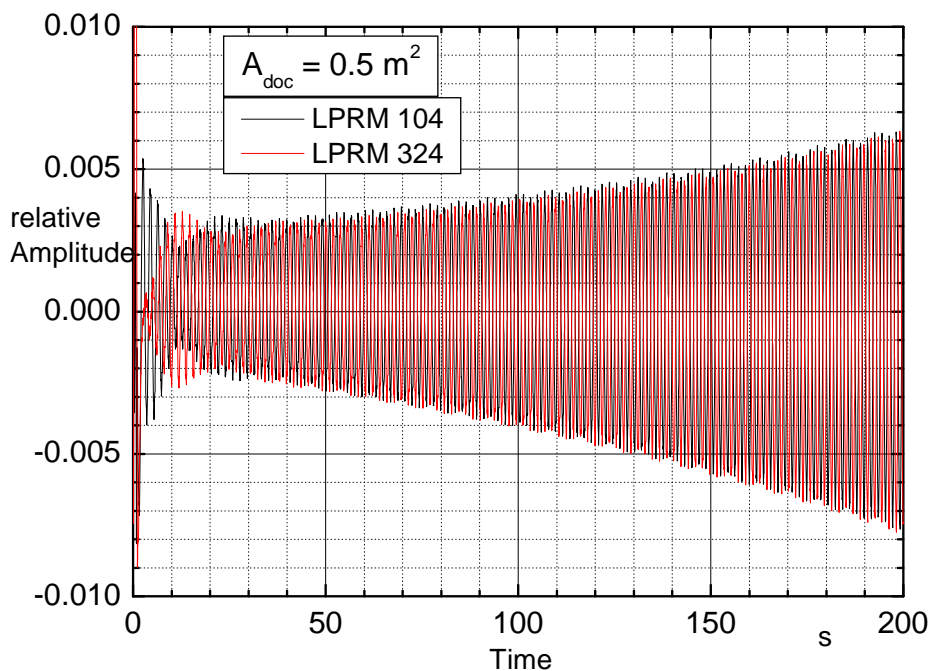


Figure 3.24: Signals (relative amplitudes) of LPRM 10 and 32 in the fourth level respectively. The global power oscillation is decaying.

Figure 3.23 to Figure 3.26 show results where A_{doc}^* was varied in the interval $A_{doc}^* = [0.25, \dots, 1.0] m^2$. It can be seen, the larger the downcomer flow cross section the slower the decay of the in-phase oscillation mode is, while the out-of-phase oscillation mode is not affected.

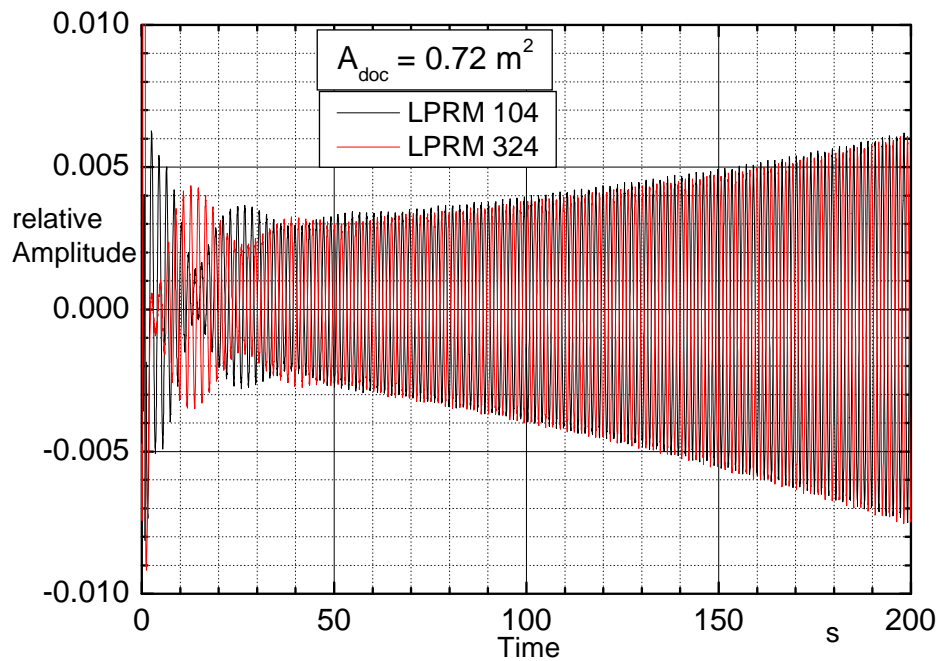


Figure 3.25: Signals (relative amplitudes) of LPRM 10 and 32 in the fourth level respectively. This figure clearly show that the global power oscillation is decaying not so strong as in Figure 3.24 and Figure 3.25.

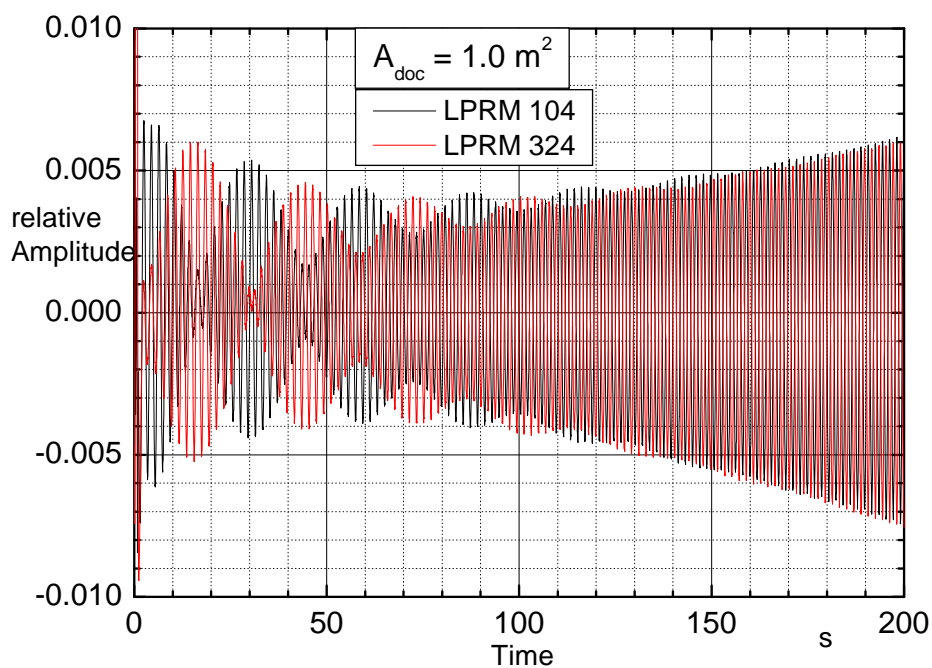


Figure 3.26: Signals (relative amplitudes) of LPRM 10 and 32 in the fourth level respectively.

From the first 80 seconds (Figure 3.26), it can be seen that the global and regional power oscillations are superposed. When the amplitudes of the global power oscillations become small enough, the regional power oscillation will dominate. The nature of the regional power oscillation, however, is not affected.

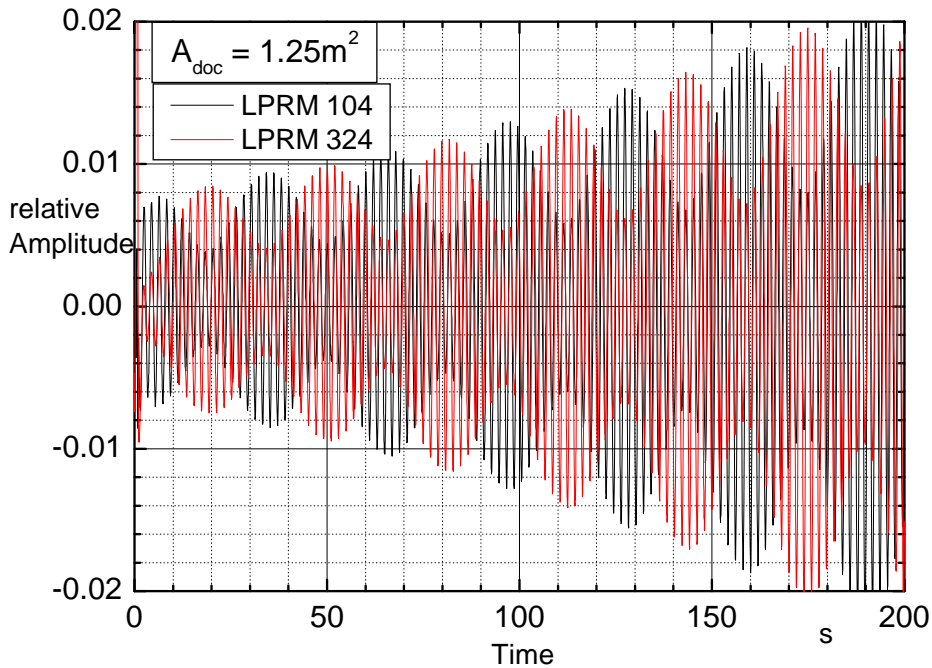


Figure 3.27: Signals (relative amplitudes) of LPRM 10 and 32 in the fourth level respectively. The global oscillation is unstable

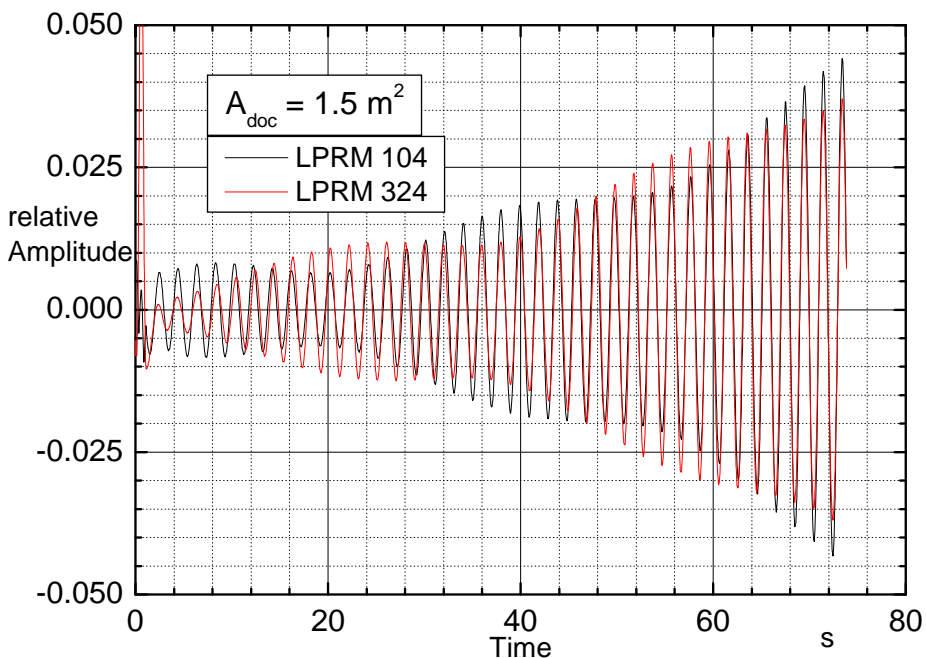


Figure 3.28: Signals (relative amplitudes) of LPRM 10 and 32 in the fourth level respectively. The global oscillation is unstable.

In Figure 3.27 and Figure 3.28 show that the growing regional power oscillation is superposed by a growing global power oscillation. The larger the downcomer flow cross section, the more unstable the global power oscillation is.

The analysis of the downcomer flow cross section variation with the system code RAMONA5 has shown that A_{doc} has a strong impact on the stability property of the in-phase oscillation mode while the stability behaviour of the out-of-phase oscillation mode is not affected. This result is consistent with the result of the ROM analysis.

3.3.3.4 Physical interpretation

In the following, the momentum balance (3.58) of the recirculation loop and the final ODE's (3.65) for the channel inlet velocities are taken into account. Thereby the out-of-phase oscillation mode (\bar{p}_{out}) and the in-phase oscillation mode (\bar{p}_{in}) are considered separately. The goal is to show that the out-of-phase oscillation mode is independent of the downcomer flow cross section while the in-phase oscillation mode depends on it. In other words, it will be shown that the out-of-phase eigenstate \bar{p}_{out} is approximately (if downcomer friction is neglected) independent of A_{doc} . In this case, $\text{Re}(\lambda_{out})$ will not change significantly under A_{doc} variations.

The out-of-phase mode (out-of-phase eigenstate, see definition in section 3.3.3) is characterized by thermal-hydraulic and heat conduction properties that have opposite sign in both channels. In particular, if both channels are identical, the derivatives of the inlet channel mass flows (\dot{m}_1^* and \dot{m}_2^*) respect to time have opposite sign $\ddot{m}_1^* = -\ddot{m}_2^*$ and thus the total mass flow is constant $\dot{m}_{tot}^*(t) = const$ in relation (3.57). Consequently, the inertial term (first term on the right hand side) in the momentum balance (3.58) vanishes for $\dot{m}_{tot}^*(t) = const$ (downcomer friction is not considered) and thus the downcomer pressure drop only depend on the gravity term which is a constant. Hence, for the out-of-phase oscillation mode, the momentum balance (3.58) is independent of A_{doc} . In this case, the integral (3.60) is constant and is equal to the steady state external pressure drop

$$\int_1^0 \frac{\partial p_{recirc}}{\partial z} dz = \int_1^0 \frac{\partial P_{doc}}{\partial z} dz - \Delta P_{head} = Fr^{-1} + \Delta P_{head} = DP_{extern} \quad . \quad (3.78)$$

The final ODEs are then reduced to the form of $\dot{v}_{n,inlet}(t) = A_n(t)$ (where $A_n(t)$ is defined in (3.62)). Function $A_n(t)$ is independent of the downcomer flow cross section. Hence, the variation of A_{doc} has none effect on the out-of-phase oscillation mode because due to $\dot{m}_{tot}^*(t) = const$ the downcomer momentum balance becomes independent of A_{doc} and thus the integral (3.60) is equal to the steady state external pressure drop. As a conclusion, the stability properties of the out-of-phase oscillation mode (or out-of-phase eigenstate) are independent of the downcomer flow cross section. This is consistent with the RAMONA5 and ROM results.

The in-phase oscillation mode (in-phase eigenstate) is characterized by thermal-hydraulic and heat conduction properties that have the same sign in both channels. In particular, the derivatives of the inlet channel mass flows (\dot{m}_1^* and \dot{m}_2^*) respect to

time have the same sign and thus the total core mass flow is not constant with respect to time. Hence, the downcomer momentum balance (3.58) depends on A_{doc} . Consequently, the final ODEs (3.65) for the channel inlet velocities depend on A_{doc} (see definition of $B_n(t)$). Consequently, the in-phase oscillation mode depends on A_{doc} . From the coupled system (3.61), it can be deduced that, the more A_{ol} will be increased (A_{doc} is decreased) the more of the momentum of the n -th channel is transferred to the downcomer which has (according to the RAMONA5 and ROM results) a stabilizing effect for the in-phase oscillation mode.

3.3.3.5 Conclusions

This analysis has shown that the recirculation loop has a significant impact on the stability properties of the in-phase oscillation mode, while the out-of-phase oscillation mode is not affected. The larger the downcomer flow cross section, the more unstable the in-phase oscillation mode is. The limit $A_{ol} = 0$ corresponds to the constant external pressure drop boundary condition. Consequently, BWR stability analysis should always be performed including the recirculation loop. It should be emphasized that the stability properties for the reference OP of KKLc7rec4 can only be reproduced correctly by the ROM if the correct downcomer flow cross section of the RAMONA5 model (DC2) is used. In this case, ROM and RAMONA5 results are consistent.

In other words, the new ROM, where the recirculation loop is implemented, simulates correctly the oscillation mode: the out-of-phase oscillation is excited and the in-phase mode is decaying. As mentioned in the introduction of the thesis, the original ROM was not able to correctly predict the oscillation mode. Responsible for the correct simulation of the oscillation mode is the **implemented recirculation loop model**, in which the downcomer flow cross section of the RAMONA5 (DC2) model is used as input parameter, and the **increased artificial factor** $fact_m = 5$ with $m \neq n$.

3.4 Subcooled boiling

3.4.1 The modified profile fit model

As mentioned in section 3.1.3, the two phase region of the thermal-hydraulic model of the ROM is represented by a Drift-Flux-model where thermodynamic equilibrium between the two phases is considered. In real two phase flow systems, however, there is a region between the single- and two-phase regions where thermodynamic equilibrium between the two phases does not exist. The liquid phase is subcooled, but local boiling from the heated surface appears. The void fraction of this region is not taken into account by the current thermal-hydraulic model of the ROM. Hence the void fraction axially integrated over the two-phase flow region $\alpha_{2\phi}$ is underestimated in the current ROM version.

Note that, the void fraction is the dominant feedback parameter coupling the neutron kinetics with the thermal hydraulics. The feedback gain, the void profile and the channel pressure drops determine the thermal-hydraulic state. Hence, it is obvious to extend the reduced order model by a model which takes into account the subcooled boiling phenomenon in order to simulate the BWR stability behaviour more realistic. The questions to be answered in this section are:

- is it necessary to take into account the subcooled boiling phenomenon in the ROM and,
- which model for describing the subcooled boiling phenomenon is appropriate.

It can be proved that the ROM must be extended by a third region where a mechanistic model describes the thermodynamic non-equilibrium between the two phases and the void generation on the heated surface. Such a model extension requires extremely large effort. Therefore, in the scope of this work, the effect of the subcooled boiling on the BWR stability behaviour has been approximately estimated by a modified profile fit model (Levy, 1966 [27]).

Before describing the subcooled boiling model used in this analysis, a short summary of the subcooled boiling phenomenon will be given [27,69-74]. In general subcooled boiling is characterized by the fact that the mean enthalpy $\langle h \rangle^*$ of the liquid phase is less than saturation ($\langle h \rangle^* < h_{sat}^*$), but local boiling from the heated surface appears. The bubbles removed from the heated surface are travelling through the subcooled liquid and are collapsing because of condensation processes. One part of the power is transferred into the subcooled liquid while the rest is invested in steam production. Consequently, besides the appearance of the additional void fraction α_{scool} , the heat transfer conditions are changed in the subcooled boiling region.

Figure 3.29 shows a sketch of a typical void profile in a vertical (z-direction) heated pipe during a forced coolant convection. The subcooled liquid is entering the channel inlet with the inlet enthalpy h_{inlet}^* and the inlet velocity v_{inlet}^* and is heated along the z-direction. While travelling through the channel the mean coolant enthalpy $\langle h \rangle^*$ is in-

creasing. The region between the channel inlet and level $z^* = \mu_{voidage}^*$ is called the single phase region.

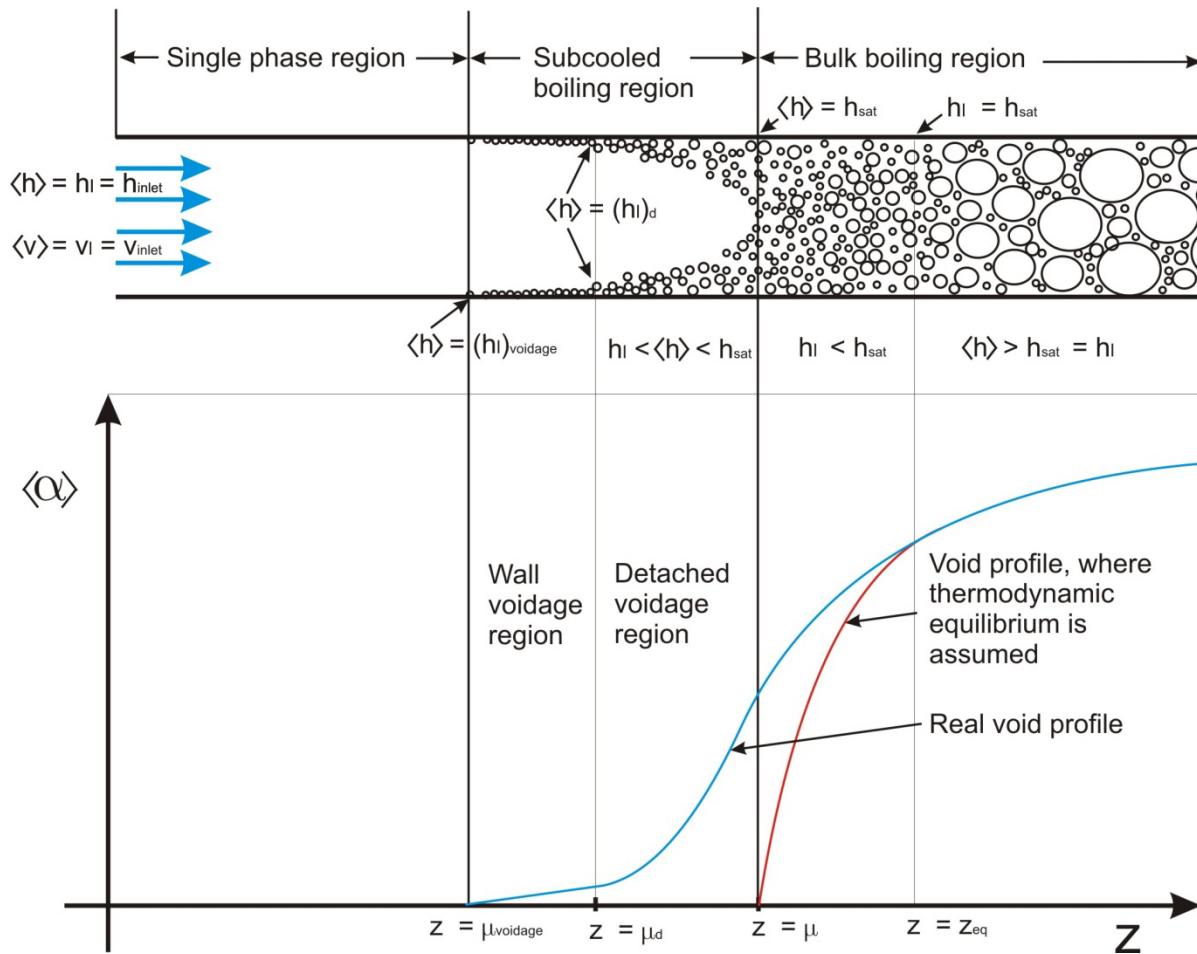


Figure 3.29: Typical axial void profile of forced coolant in a heated pipe [27,69-74].

At level $z^* = \mu_{voidage}^*$, characterized by $\langle h \rangle^* = (h_l^*)_{voidage}$, the first vapour bubbles appear and from $z^* = \mu_{voidage}^*$ to $z^* = \mu_d^*$ more and more bubbles are forming on the heated wall. This region, commonly denoted as the wall voidage region, is characterized by the fact that the forces (for example the buoyant force) exerted on the vapour bubbles are smaller than the forces (for example the surface tension force) maintaining the bubbles on the wall. Consequently, the vapour bubbles remain in contact with the wall in this region.

At level $z^* = \mu_d^*$ with $\langle h \rangle^* = (h_l^*)_d$, called void departure point, the vapour bubble size is large enough to leave the surface and the vapour volumetric fraction rise significantly. The region between $z^* = \mu_d^*$ and $z^* = \mu^*$, also termed detached voidage region, is characterized by a mean enthalpy lower than saturation $h_l^* < \langle h \rangle^* < h_{sat}^*$.

At location $z^* = \mu^*$ the mean enthalpy is at saturation but the liquid enthalpy is less than saturation $h_l^* < \langle h \rangle^* = h_{sat}^*$. Due to this fact, in this region and also in the detached voidage region heat exchange processes between the two phases occur such that thermodynamic equilibrium does not exist.

The liquid phase reaches the saturation state at level $z^* = z_{eq}^*$. Above this location thermodynamic equilibrium between the two phases is nearly realized. Heat transferred into the coolant is completely invested in steam generation.

The subcooled boiling model is based on the following assumptions:

- 1) Wall voidage is not taken into account so that the subcooled boiling region is defined to be the detached voidage region plus the region between $z^* = \mu^*$ and $z^* = z_{eq}^*$.
- 2) The heat transfer conditions in the subcooled boiling region are considered to be the same as the heat transfer condition in the single phase region
- 3) For the determination of the void departure point μ_d^* , the criteria of Saha and Zuber (1974) [69-74,77] are applied
- 4) The drift flux relation [27,69-74] between the volumetric void fraction and the flow quality is used

The profile fit model used in the current analysis is based on Levy's (1966) [27] relationship

$$x_{scool}(z, t) = x_{eq}(z, t) - x_d e^{\left(\frac{x_{eq}(z, t)}{x_d} - 1\right)} \quad (3.79)$$

relating the thermodynamic equilibrium quality x_{eq} to the "true" flow quality x_{scool} . Here, x_{eq} is defined as

$$x_{eq}(z, t) = \frac{\langle h(z, t) \rangle^* - h_{sat}^*}{\Delta h_{fg}^*} \quad (3.80)$$

Expression (3.80) is the heat balance where thermodynamic equilibrium is assumed and the quality x_d at the void departure point μ_d^* is defined as

$$x_d(t) = -\frac{h_{sat}^* - \langle h(\mu_d, t) \rangle^*}{\Delta h_{fg}^*}, \quad (3.81)$$

where $\langle h(\mu_d, t) \rangle^*$ is the coolant mean enthalpy at μ_d^* (below μ_d^* the volumetric void fraction is approximately zero). Because $x_{eq}(\mu_d) = x_d$, then $x_{scool}(\mu_d) = 0$ [27,73]. On the other hand, as the "true" flow quality x_{scool} increases and becomes large enough $x_{scool} \gg x_d$ and positive, where non-thermodynamic equilibrium stop to exist, then $x_{scool} \rightarrow x_{eq}$.

For the description of subcooled boiling in the ROM using the profile fit model (3.79), the values x_d and x_{eq} which are defined in (3.80) and (3.81), have to be estimated. As mentioned in assumption 3), for the determination of the mean enthalpy $\langle h(\mu_d, t) \rangle^*$ at the void departure point, the criteria of Saha and Zuber (1974)

$$-\frac{h_{sat}^* - \langle h(\mu_d, t) \rangle^*}{\Delta h_{fg}^*} = 0.0022 \cdot \frac{D_h^* q^* c_{pl}^*}{k_f^* \cdot \Delta h_{fg}^*} \quad (3.82)$$

are applied [72,73], where c_{pl}^* is the specific heat capacity of liquid water. The criteria (3.82) can be rewritten in terms of dimensionless numbers, the phase change number $N_{pch,1\Phi}$ and the single phase conversion number $N_{cov,1\Phi}$

$$\begin{aligned}
 x_d(t) &= \frac{-N_{pch,1\Phi}(t)}{N_{cov,1\Phi}} \cdot 0.0022 \cdot \frac{D_h^* q_{1\Phi}''(t) c_{pl}^*}{k_f^* \cdot \Delta h_{fg}^*} \cdot \frac{N_{cov,1\Phi}}{N_{pch,1\Phi}(t)} \\
 x_d(t) &= \frac{-N_{pch,1\Phi}(t)}{N_{cov,1\Phi}} \cdot 0.0022 \cdot \frac{D_h^* q_{1\Phi}''(t) c_{pl}^*}{k_f^* \cdot \Delta h_{fg}^*} \cdot \frac{h_{\infty,1\Phi}^* T_0^* \xi_h^* L^* \Delta \rho^*}{A_{inlet}^* \Delta h_{fg}^* v_0^* \rho_g^* \rho_f^*} \\
 x_d(t) &= \frac{-N_{pch,1\Phi}(t)}{N_{cov,1\Phi}} \cdot 0.0022 \cdot \frac{D_h^* c_{pl}^* h_{\infty,1\Phi}^* T_0^*}{k_f^* \cdot \Delta h_{fg}^*} \\
 x_d(t) &= \frac{-N_{pch,1\Phi}(t) \cdot C_d}{N_{cov,1\Phi}} \\
 \text{where } C_d &= \frac{0.0022}{N_{cov,1\Phi}} \cdot \frac{D_h^* h_{\infty,1\Phi}^* T_0^* c_{pl}^*}{k_f^* \cdot \Delta h_{fg}^*} .
 \end{aligned} \tag{3.83}$$

The dimensionless parameter $N_{pch,1\Phi}$ and $N_{cov,1\Phi}$ are defined as

$$\begin{aligned}
 N_{pch,1\Phi} &= \frac{q_{1\Phi}'' \xi_h^* L^* \Delta \rho^*}{A_{inlet}^* \Delta h_{fg}^* v_0^* \rho_g^* \rho_f^*}, & N_{cov,1\Phi} &= \frac{h_{\infty,1\Phi}^* T_0^* \xi_h^* L^* \Delta \rho^*}{A_{inlet}^* \Delta h_{fg}^* v_0^* \rho_g^* \rho_f^*} \\
 \text{where } N_r &= \frac{\rho_f^*}{\Delta \rho^*} \quad \text{and} \quad N_\rho = \frac{\rho_g^*}{\rho_f^*},
 \end{aligned} \tag{3.84}$$

where T_0^* is the saturation temperature of the liquid phase.

In order to calculate the thermodynamic equilibrium quality x_{eq} , the mean enthalpy $\langle h \rangle^*$ along the flow channel should be determined. In the current analysis $\langle h \rangle^*$ is expressed by the quadratic enthalpy profile

$$\langle h(z,t) \rangle = \frac{\langle h(z,t) \rangle^*}{\Delta h_{fg}^*} \equiv h(z,t) = a_2(t) \cdot z^2 + a_1(t) \cdot z + h_{inlet} \quad , \tag{3.85}$$

used for converting the original energy balance (PDE) to an ordinary differential equation by applying the weighed residual method. Substituting (3.85) into (3.80) yields

$$\begin{aligned}
 x_{eq}(z,t) &= \frac{\langle h(z,t) \rangle^* - h_{sat}^*}{\Delta h_{fg}^*} = \frac{\langle h(z,t) \rangle^*}{\Delta h_{fg}^*} - \frac{h_{sat}^*}{\Delta h_{fg}^*} = a_2(t) \cdot z^2 + a_1(t) \cdot z + h_{inlet} - \frac{h_{sat}^*}{\Delta h_{fg}^*} \\
 x_{eq}(z,t) &= a_2(t) \cdot z^2 + a_1(t) \cdot z + \underbrace{\frac{h_{inlet}^*}{\Delta h_{fg}^*} - \frac{h_{sat}^*}{\Delta h_{fg}^*}}_{-N_{sub} N_r N_\rho} \\
 &= a_2(t) \cdot z^2 + a_1(t) \cdot z - N_{sub} N_r N_\rho \quad ,
 \end{aligned} \tag{3.86}$$

where the definition of the subcooling number N_{sub}

$$N_{sub} = \frac{h_{sat}^* - h_{inlet}^*}{\Delta h_{fg}^*} \frac{\Delta \rho^*}{\rho_g^*} = \frac{h_{sat}^* - h_{inlet}^*}{\Delta h_{fg}^*} \frac{\Delta \rho^*}{\rho_g^*} \cdot \frac{\rho_f^*}{\rho_f^*} \quad (3.87)$$

$$N_{sub} = \frac{h_{sat}^* - h_{inlet}^*}{\Delta h_{fg}^*} \frac{1}{N_r N_\rho}$$

is used.

The point of bubble departure μ_d is the level at which the coolant mean enthalpy is equal to $\langle h(\mu_d, t) \rangle^*$. Hence, μ_d can be obtained by applying the boundary condition $h(\mu_d, t) = \langle h(\mu_d, t) \rangle$ in the quadratic enthalpy profile (3.85). Accordingly (as shown in section 3.1.3), the bulk boiling boundary μ is determined by the boundary condition $h(\mu, t) = \langle h(\mu, t) \rangle = h_{sat}$. The results for μ_d and μ are

$$\mu_d = \frac{2 \Delta h_{id}}{a_1 + \sqrt{a_1^2 + 4a_2 \Delta h_{id}}} \quad \text{and} \quad (3.88)$$

$$\mu = \frac{2 N_r N_\rho N_{sub}}{a_1 + \sqrt{a_1^2 + 4a_2 N_r N_\rho N_{sub}}} ,$$

where Δh_{id} is defined as $\Delta h_{id} = \langle h(\mu_d, t) \rangle - h_{inlet}$ and can be rewritten as $\Delta h_{id} = N_r N_\rho N_{sub} + x_d$.

Finally, the axial void profile $\alpha_{scool} = \alpha_{scool}(z)$ can be calculated using the drift flux relation [27,69-74]

$$\alpha_{scool}(z, t) = \frac{1}{C_0} \left[\alpha_{hom}(z, t) - V_{gj} \cdot \alpha_{corr}(z, t) \right] , \quad (3.89)$$

where

$$\alpha_{hom}(z, t) = \frac{x_{scool}(z, t) N_r}{x_{scool}(z, t) + N_r N_\rho} \quad (3.90)$$

is the relation for mechanical equilibrium conditions and

$$\alpha_{corr}(z, t) = \frac{x_{scool}(z, t) N_r}{(x_{scool}(z, t) + N_r N_\rho) \cdot (C_0 j(z, t) + V_{gj})} \quad (3.91)$$

can be assumed as a correction term which takes into account the mechanical non-equilibrium between the two phases.

3.4.2 Analysis with the TH-model

The first analysis with the included subcooled boiling model was performed with the simple thermal-hydraulic one heated channel model (TH-model, see subsection 3.3.2). The aim is to analyse the differences between the axial void profiles provided by the original two-phase flow model (so-called bulk boiling model) and the subcooled boiling model. The investigation is performed for thermal-hydraulic conditions which are relevant for BWR stability analysis.

The axial void profiles have been calculated by employing the numerical integration code, where only steady state calculations have been performed (see section 2.4 and Figure 2.7). At first, this analysis has been carried out at the selected reference OP. This OP is characterized by

$$\begin{aligned}
 P^* &= 12.1 \text{ bar} \\
 \dot{m}_{tot}^* &= 0.5 \text{ kg / s} \\
 \dot{Q}^* &= 50.0 \text{ kW} \\
 N_{sub} &= 1.0 \text{ .}
 \end{aligned}
 \tag{3.92}$$

Furthermore, the axial void profiles have been calculated for five different OPs, where the system pressure P^* and the total coolant mass flow \dot{m}_{tot}^* are fixed and the power and core inlet subcooling have been varied as shown in Table 3.3.

Table 3.3: Variation of the power and core inlet subcooling

N_{sub}	\dot{Q}^* (kW)
1	50 (ref.OP)
2	50
3	50
1	40
1	30
1	20

The results of this analysis are presented in the following (from Figure 3.30 to Figure 3.35).

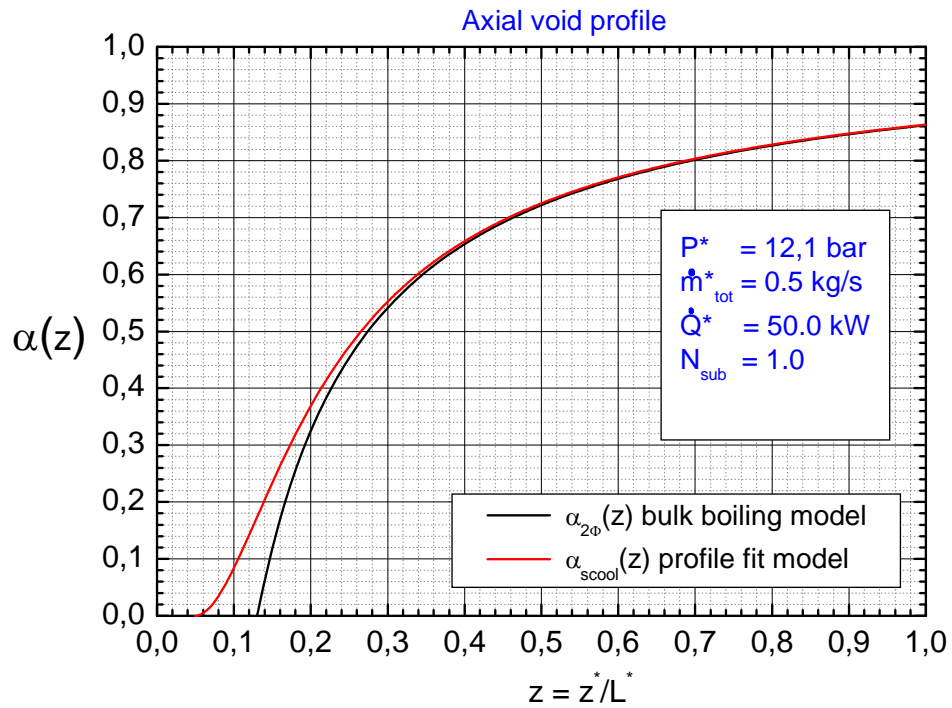


Figure 3.30: Comparison of the axial void profiles calculated by the bulk boiling model and the subcooled boiling model for the reference OP.

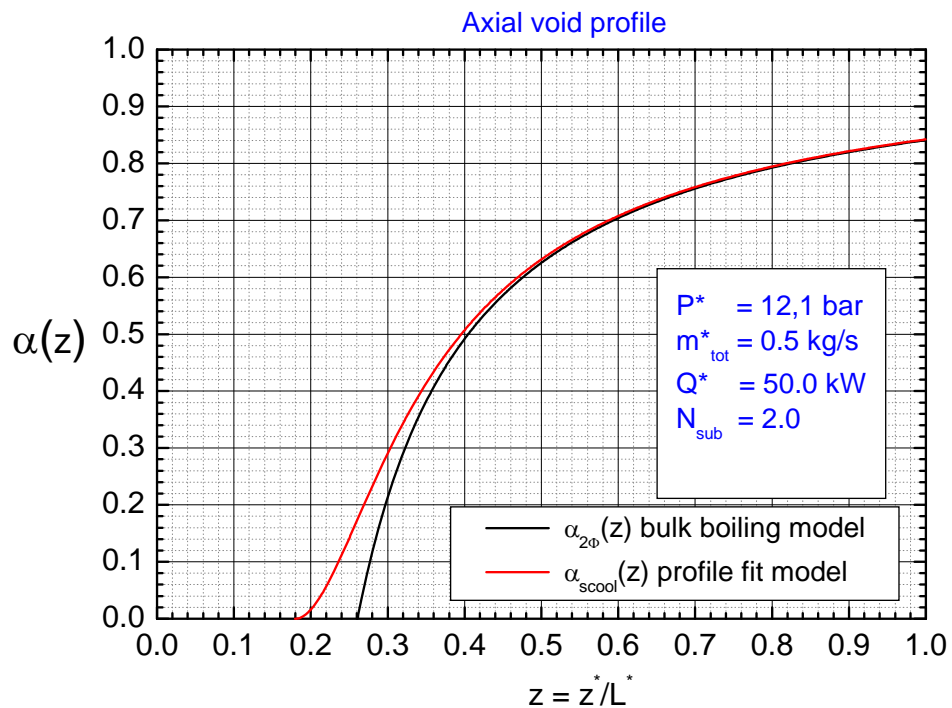


Figure 3.31: Comparison of the axial void profiles calculated by the bulk boiling model and the subcooled boiling model for $N_{\text{sub}} = 2.0$.

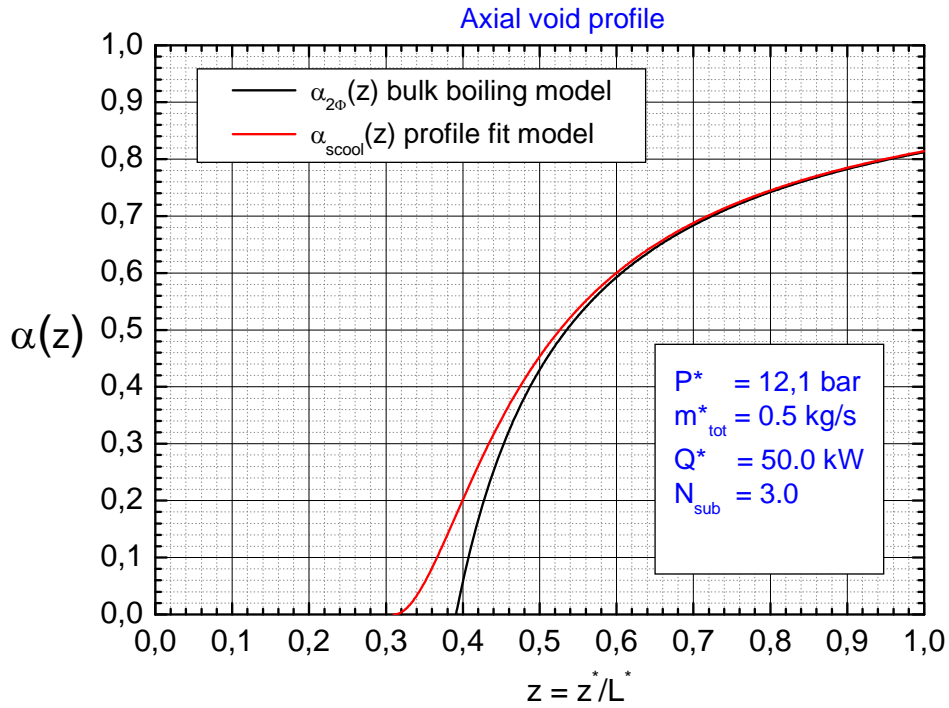


Figure 3.32: Comparison of the axial void profiles calculated by the bulk boiling model and the subcooled boiling model for $N_{\text{sub}} = 3.0$.

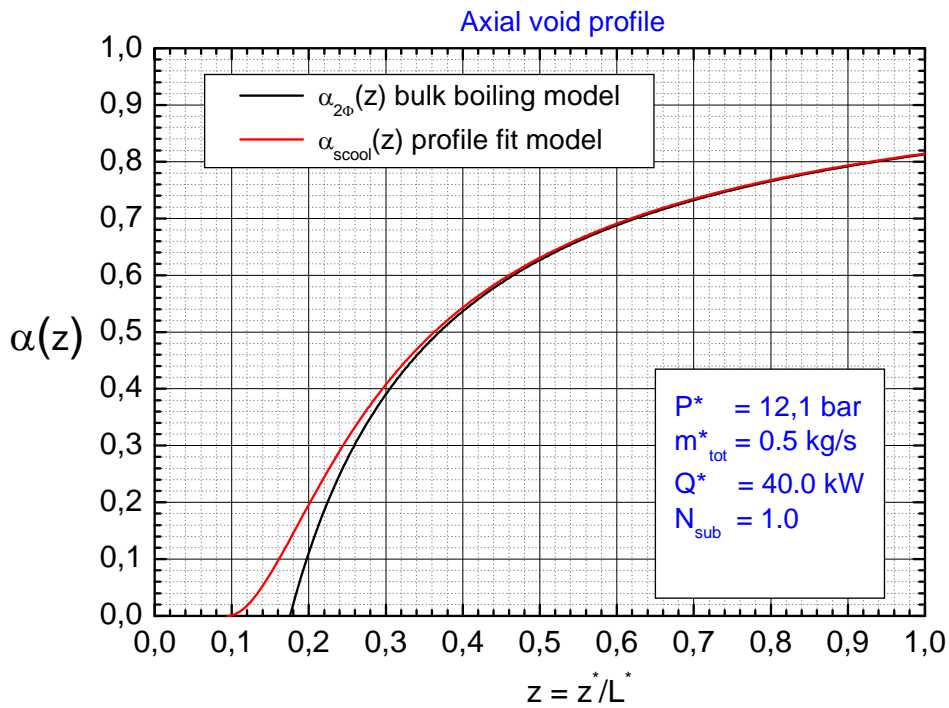


Figure 3.33: Comparison of the axial void profiles calculated by the bulk boiling model and the subcooled boiling model for $\dot{Q}^* = 40.0 \text{ kW}$.

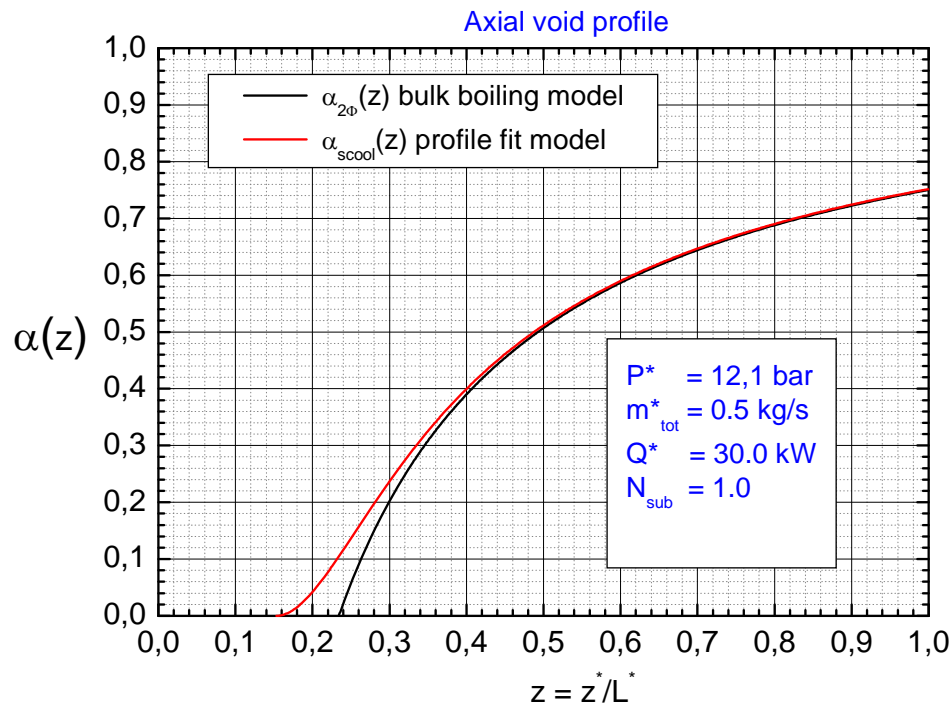


Figure 3.34: Comparison of the axial void profiles calculated by the bulk boiling model and the subcooled boiling model for $\dot{Q}^* = 30.0 \text{ kW}$.

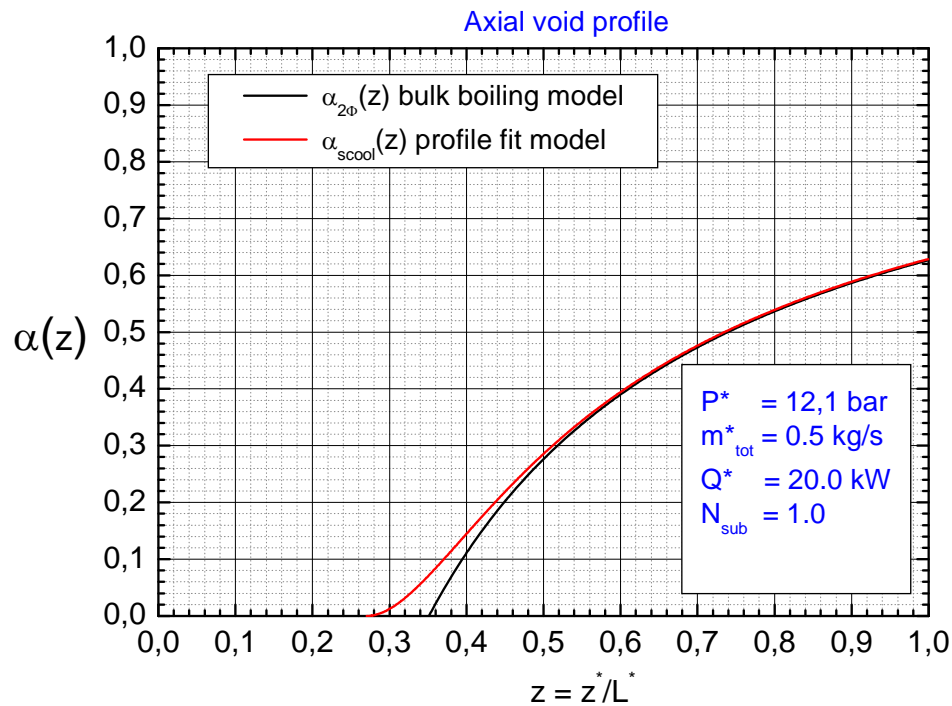


Figure 3.35: Comparison of the axial void profiles calculated by the bulk boiling model and the subcooled boiling model for $\dot{Q}^* = 20.0 \text{ kW}$.

In order to quantify the differences between the calculated axial void profiles of the bulk boiling model and the subcooled boiling model, the mean void fraction of the channel ($\alpha_{2\Phi}^{tot}$ and α_{scool}^{tot}) and the mean void fraction of the two phase region ($\langle \alpha_{2\Phi} \rangle$)

und $\langle \alpha_{scool} \rangle$) are calculated for all OP's presented in Table 3.3. These quantities are defined as

$$\alpha_{2\Phi}^{tot} = \frac{\int_0^1 \alpha_{2\Phi}(z) dz}{\int_0^1 dz} = \int_{\mu}^1 \alpha_{2\Phi}(z) dz \quad (3.93)$$

$$\alpha_{scool}^{tot} = \frac{\int_0^1 \alpha_{scool}(z) dz}{\int_0^1 dz} = \int_{\mu_d}^1 \alpha_{scool}(z) dz \quad (3.94)$$

$$\langle \alpha_{2\Phi} \rangle = \frac{\int_{\mu}^1 \alpha_{2\Phi}(z) dz}{\int_{\mu}^1 dz} \quad (3.95)$$

and

$$\langle \alpha_{scool} \rangle = \frac{\int_{\mu_d}^1 \alpha_{scool}(z) dz}{\int_{\mu_d}^1 dz} , \quad (3.96)$$

which can be used to calculate the relative deviation $\delta\alpha^{tot}$ and $\delta\langle\alpha\rangle$ according to

$$\delta\alpha^{tot} = \frac{\alpha_{scool}^{tot} - \alpha_{2\Phi}^{tot}}{\alpha_{scool}^{tot}} \quad (3.97)$$

$$\delta\langle\alpha\rangle = \frac{\langle\alpha_{scool}\rangle - \langle\alpha_{2\Phi}\rangle}{\langle\alpha_{scool}\rangle} . \quad (3.98)$$

The results for the mean void fractions and the relative deviations are summarized in Table 3.4 and Table 3.5.

Table 3.4: Mean void fractions and the corresponding relative deviations

N_{sub}	$\alpha_{2\Phi}^{tot}$	$\langle\alpha_{2\Phi}\rangle$	α_{scool}^{tot}	$\langle\alpha_{scool}\rangle$	$\delta\alpha^{tot}$	$\delta\langle\alpha\rangle$
1	0.59017	0.67841	0.60626	0.6375	0.02654	0.06418
2	0.47914	0.64793	0.49508	0.60335	0.03220	0.07389
3	0.37133	0.60968	0.38708	0.56089	0.04069	0.08698

Table 3.5: Mean void fractions and the corresponding relative deviations

\dot{Q}^* (kW)	$\alpha_{2\Phi}^{tot}$	$\langle \alpha_{2\Phi} \rangle$	α_{scool}^{tot}	$\langle \alpha_{scool} \rangle$	$\delta\alpha^{tot}$	$\delta\langle \alpha \rangle$
20.0	0.26713	0.41169	0.27523	0.37707	0.02943	0.09182
30.0	0.41011	0.53537	0.42120	0.49723	0.02633	0.07670
40.0	0.50360	0.61070	0.51704	0.57088	0.02599	0.06975

The results show that the relative deviations $\delta\alpha^{tot}$ of the channel mean void fractions are less than 4.1% for operational points relevant for BWR stability analyses.

3.4.3 Analysis with the ROM for KKLc7rec4

As will be described in more details in section 4.2.1, the axial power profile in the ROM is approximated by a uniform axial profile. In contrast to this the real axial power profiles of real BWR systems are typically bottom peaked. Ignoring the true axial power profile leads to deviations between the axial void profiles calculated with RAMONA5 and ROM, where the system pressure, the core inlet subcooling, the core inlet mass flow and the core averaged power of the RAMONA5 model are used as ROM input. The aim of this section is to compare the effect of the use of the uniform axial power profile in the ROM with the effect of neglecting subcooled boiling on the axial void profiles.

The present ROM investigation is performed for KKLc7rec4. The goal is to estimate the deviation between the axial void profile calculated by RAMONA5 and ROM (without adjustment of the axial void profile, explained in 4.2.1). For this purpose, the steady state calculations with RAMONA5 and ROM have been performed for the selected reference OP and afterwards the resulting axial void profiles have been evaluated. Note that for this analysis the correct core inlet subcooling, core averaged power, system pressure and core inlet mass flow that are obtained from the RAMONA5 model, are used as input for the ROM.

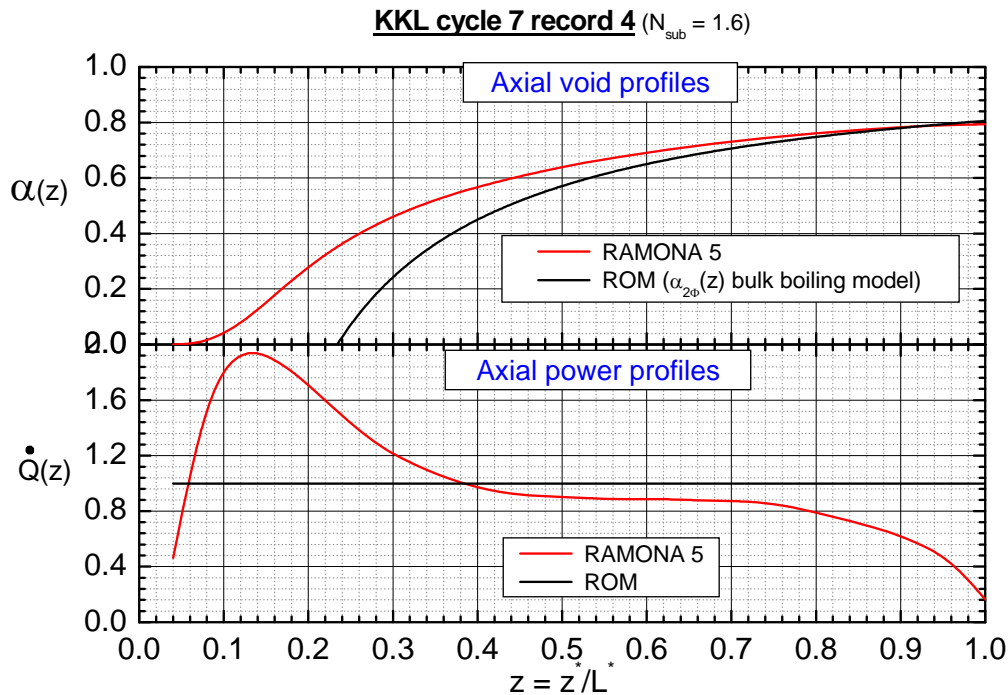


Figure 3.36: Comparison of the axial power profiles and the corresponding axial void profiles of RAMONA5 and ROM for the reference OP.

Figure 3.36 shows the significant deviation between the axial void profiles due the use of different axial power profiles in RAMONA5 and ROM while the core inlet subcooling, the core averaged power, the system pressure and the core inlet mass flow

are equal in both models. The channel averaged void fractions and the corresponding relative deviations between both axial void profiles are calculated as

$$\alpha_{RAMONA5}^{tot} = \frac{\int_0^1 \alpha_{RAMONA5}(z) dz}{\int_0^1 dz} = 0.535 \quad (3.99)$$

$$\alpha_{2\Phi}^{tot} = \frac{\int_0^1 \alpha_{2\Phi}(z) dz}{\int_0^1 dz} = 0.442 \quad (3.100)$$

and

$$\delta\alpha^{tot} = \frac{\alpha_{RAMONA5}^{tot} - \alpha_{2\Phi}^{tot}}{\alpha_{RAMONA5}^{tot}} \quad (3.101)$$

$$\underline{\underline{\delta\alpha^{tot} = 0.174}} \quad .$$

Similar analyses have been performed for NPP Ringhals and NPP Brunsbüttel. It turned out that the use of a uniform axial power profile, instead of the real one (NPP Leibstadt, NPP Ringhals and NPP Brunsbüttel) induces deviations between axial void profiles calculated by RAMONA5 and ROM in the order of magnitude of about 16% (16% to 19%). In contrast to that the neglecting of subcooled boiling leads to a relative deviation of about 5% (without adjustment of the axial void profile, described in subsection 4.2.1). It is repeatedly emphasized that the large discrepancy will exist only, if the axial void profile of the ROM hasn't been adjusted. As will be shown in subsection 4.2.1, after applying the adjustment procedure for the axial void profile of the ROM, the deviation between the channel averaged void fraction calculated by RAMONA5 and ROM (original two phase flow model) are less than 1% (see Figure 4.20). Consequently, from the thermal-hydraulic point of view and in the framework of the thesis analysis approach, the considering of the subcooled boiling phenomenon is not necessary.

4 BWR Stability Analyses for NPP Leibstadt

In order to gather stability data for the beginning of cycle 7 of the NPP Leibstadt (KKL) a stability test was performed on September 6th 1990 [5,6,79]. In this test, while the neutron flux was oscillating out-of-phase, both rotational and counter-phase oscillatory patterns (this means that the symmetry line orientation which divides the core into two halves during azimuthal out-of-phase oscillations was not fixed but oscillating or rotating) were observed. The time evolution of the averaged core thermal power during the stability test (record #4 and record #5) is shown in Figure 4.1 [5,6,79].

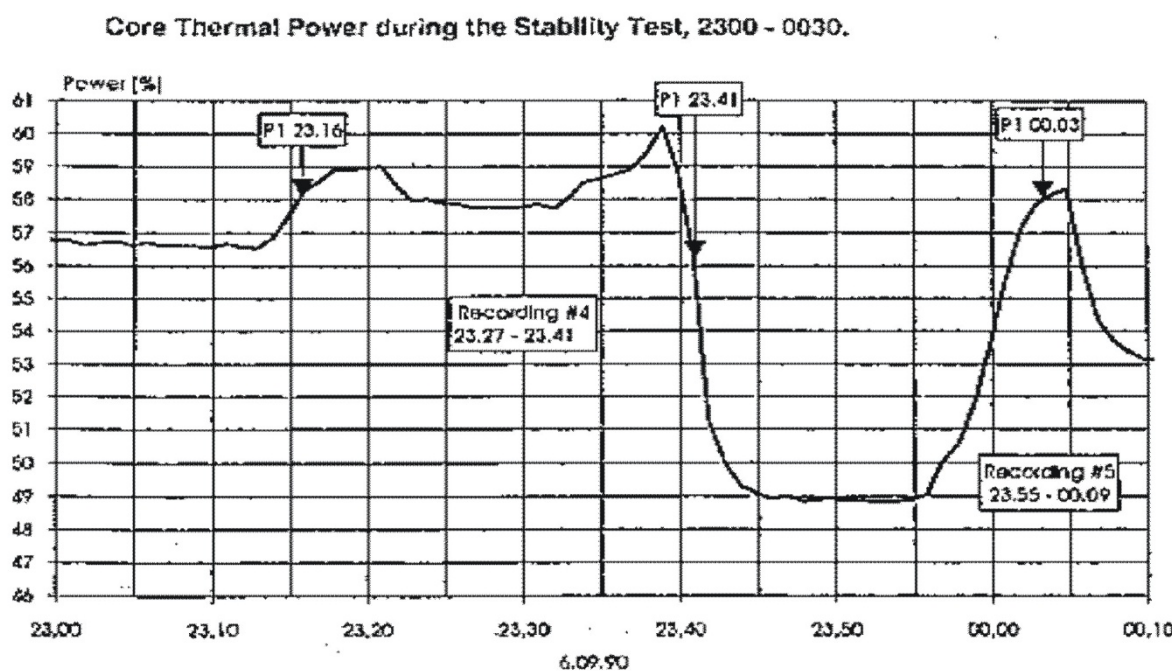


Figure 4.1: Core thermal power during the stability test (record 4 and record 5) [5,6,79].

The test was initiated by pulling out control rods. The onset of un-damped regional power oscillations occurred at approximately 57% power (100% Power = 3138MW) and 36.5% coolant mass flow (100% mass flow = 11151 kg/s). Further increase in power to 59% at 23:38 caused the oscillations to grow to approximately 30% peak-to-average on several LPRM. In order to suppress the growing power oscillation, the core thermal power was then reduced to 49% power by inserting control rods. After about ten minutes, the stability test for the previous operational point was repeated. Enhanced oscillation amplitudes were observed for this point, again. The oscillations were then suppressed by reinserting control rods and the stability test was terminated. The time evolution of the LPRM 19 of record #4 is presented in Figure 4.2. More details of this test are given in [5,6,79]. The locations of the LPRM's are presented in Figure 4.10 of subsection 4.1.2.

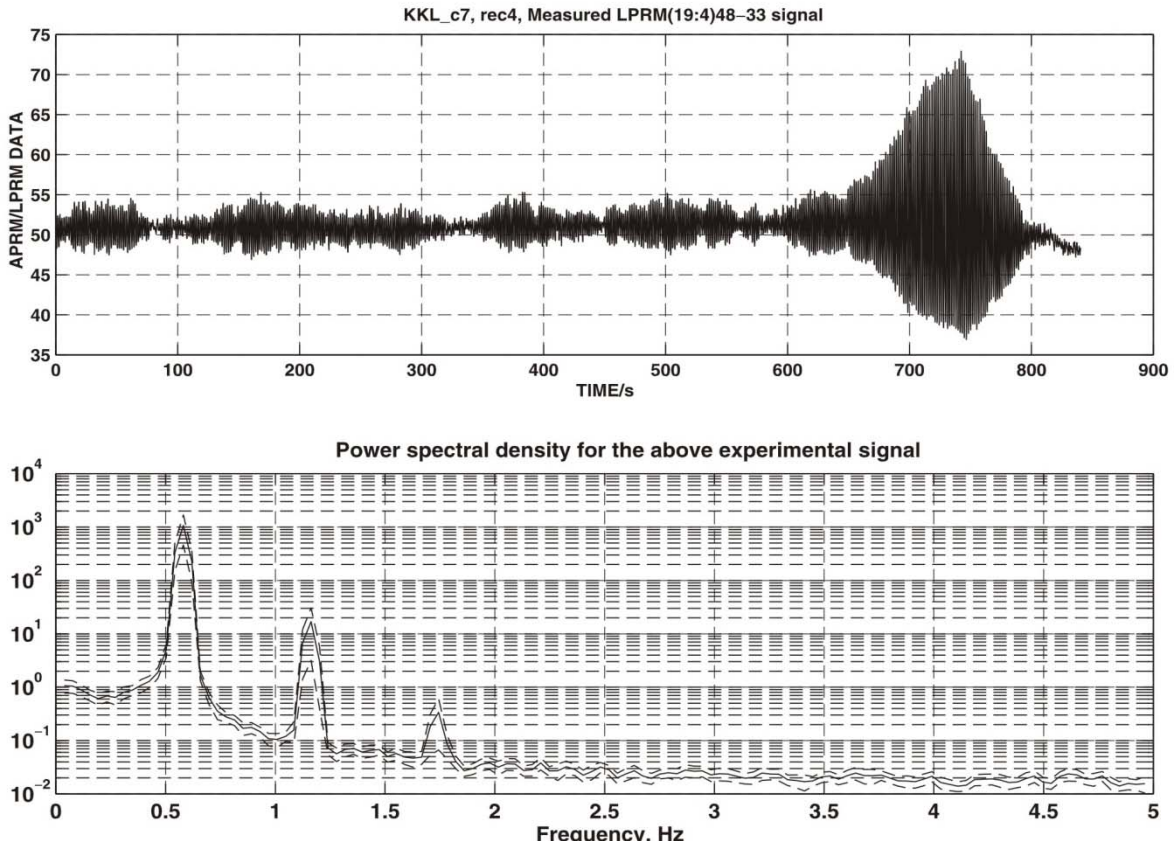


Figure 4.2: Measured LPRM signal and its corresponding power spectral density [5,6,79].

The regional power oscillations appear in records #4 and #5 of the stability test. Figure 4.3 shows the signals of LPRM 9 and LPRM 31 of record #4.

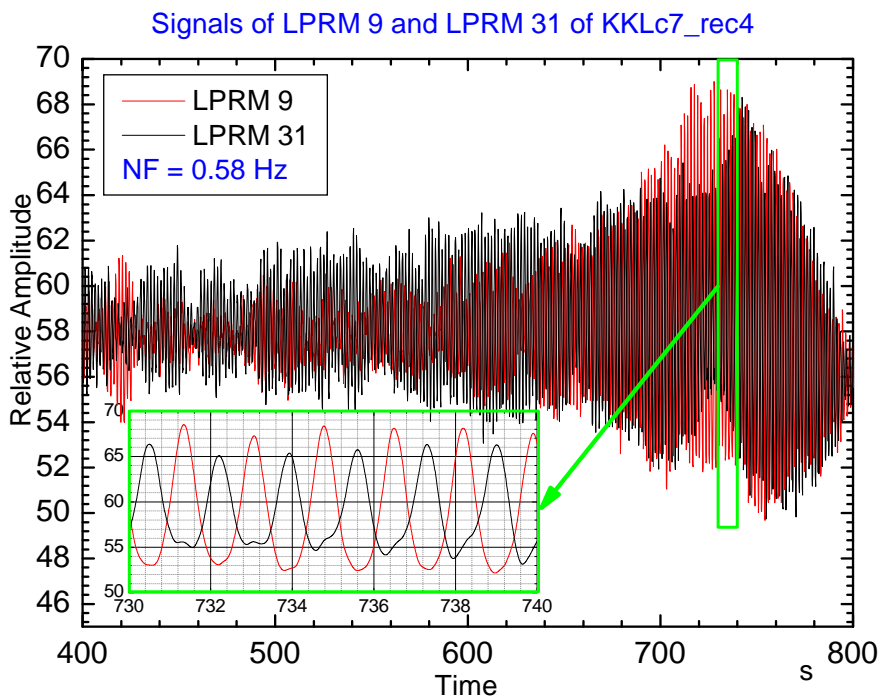


Figure 4.3: Time evolution of the LPRM signals, measured in KKLc7_rec4.

As a result of the stability test, a growing regional power oscillation with a natural frequency of 0.58 Hz ($NF^* = 0.58s^{-1}$) is occurring in the considered operational point. Furthermore, the power spectral density shows the higher harmonics of the oscillation which indicates the nonlinear character of the oscillation, such as a stable limit cycle.

In the scope of this work, the nonlinear stability analysis is based on data which corresponds to record #4. These parameters are input values of the system code RAMONA given in [5,6,79]. The operational point of record #4 is given by

$$\begin{aligned}
 \text{Power} &= 59.5\% \quad (1867.11 \text{ MW}) \\
 \text{Flow} &= 36.5\% \quad (4072.12 \text{ kg/s}) \\
 \text{Subcooling} &= 104.0 \text{ kJ/kg} \\
 \text{Pressure} &= 69.74 \text{ bar}
 \end{aligned}
 \tag{4.1}$$

It should be emphasized that, in order to represent with RAMONA5 the real stability behaviour of the selected operational point a code tuning was necessary. In particular the channel inlet loss coefficients, the channel wall friction, the slip correlation coefficients, the coolant bypass fraction and the core inlet subcooling were modified in the known uncertainty region.

Figure 4.4 shows the control rod positions and the corresponding numbers of fuel elements in a quarter core. This configuration is composed symmetrically around $x = 8, y = 8$.

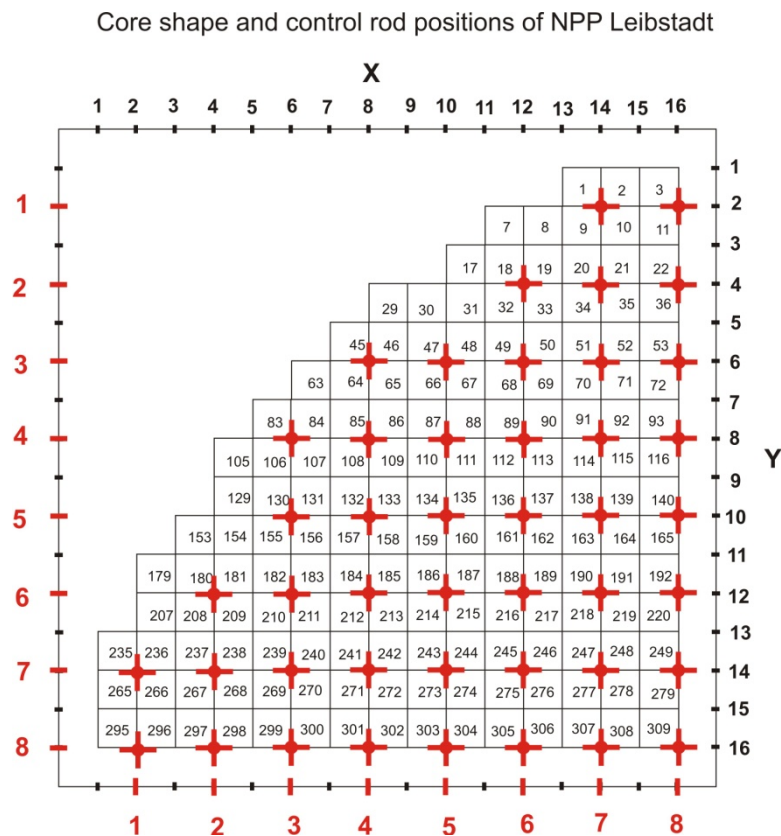


Figure 4.4: Control rod positions of a quarter core.

The control rod configuration of the entire core is shown below (Figure 4.5).

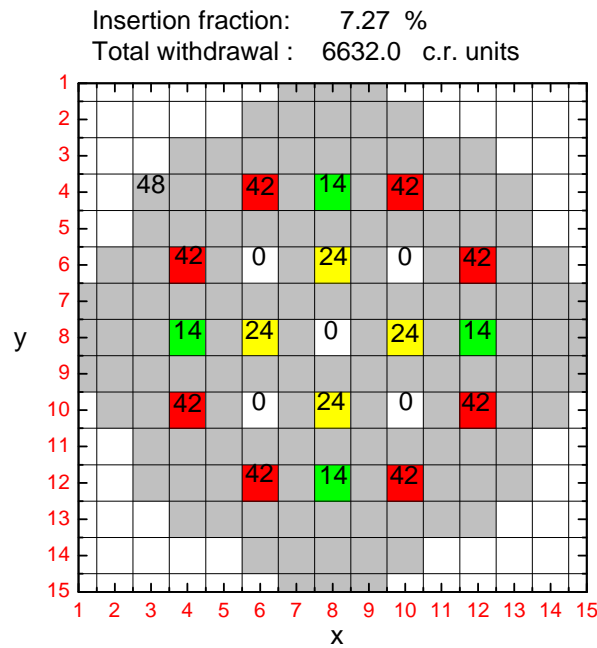


Figure 4.5: Control rod configuration used in RAMONA5 for KKL cycle 7 record 4 in units of notches. 1 notch = 7.62 cm. 48 notches means the control rod is complete out (withdrawed) of the core and 0 means the control rod is complete inside (inserted) the core.

To analyse the stability behaviour of the operational point, an initial perturbation is imposed on the system by two control rods (see Figure 4.6) and the LPRM/APRM histories are calculated. Thereby a sinusoidal control rod movement is introduced.

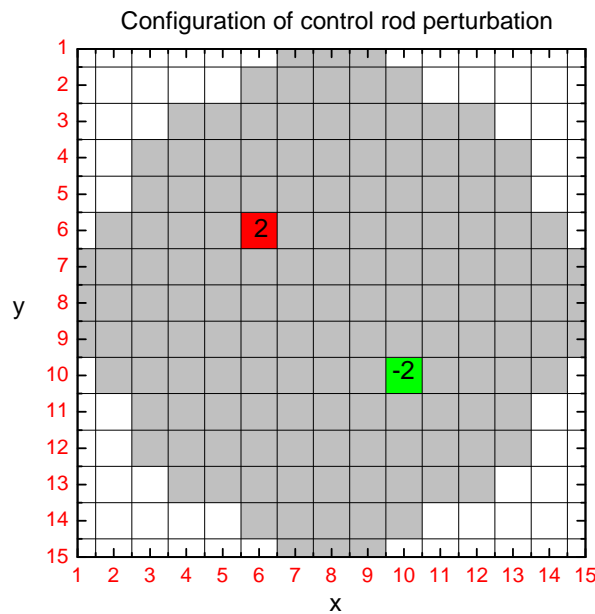


Figure 4.6: Configuration of the control rod perturbation. The amplitude is given in units of axial RAMONA-nodes. The opposite sign (and colour) indicates that the initial amplitude of the perturbation has an opposite direction.

For the present nonlinear BWR stability analyses the operational point given in (4.1) is defined to be the reference OP but the core inlet subcooling is modified to a value of $125.0 \cdot 10^3 \text{ kJ/kg}$.

4.1 RAMONA5 analysis at the reference OP

4.1.1 Steady state analysis

As mentioned in the previously, in the first step of the nonlinear stability analysis with RAMONA5, the steady state distributions will be evaluated and prepared for the ROM input calculation. Furthermore, in general, before stability analysis with RAMONA5 can be conducted, selected steady state distributions such as the axial power and axial void profiles, which are generated by RAMONA5 will be compared with the corresponding PRESTO-2 results. PRESTO-2 is a comprehensive validated core simulator. The total values should not differ more than 10 % [79]. This check is not shown in the scope of the thesis. Instead of that it will be indicated that all steady state results of RAMONA5 and PRESTO-2 are consistent within the assumed 10 % error region. In this section only selected steady state results most significant for the BWR stability behaviour are presented.

Figure 4.7 and Figure 4.8 show the radial power distribution, axially averaged. As can be seen, the specific control rod configuration which is depicted in Figure 4.5 influences the radial power in such away that the radial power distribution has a bowl form convenient for generating out of phase power oscillations.

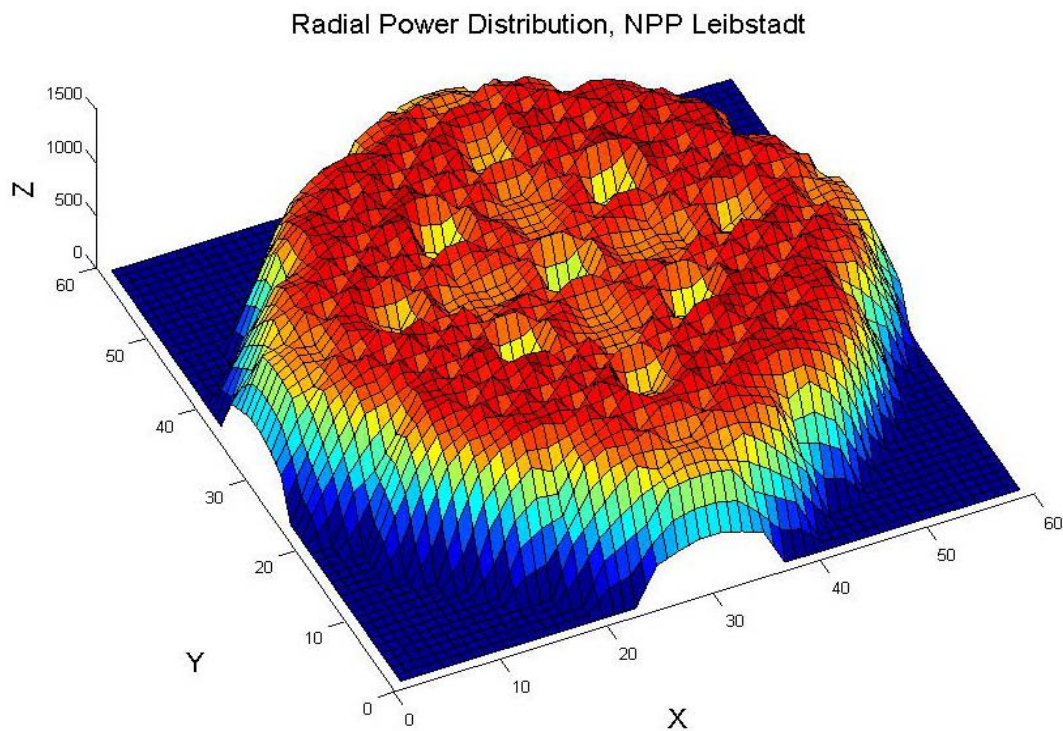


Figure 4.7: Three dimensional radial power distribution axially averaged for NPP Leibstadt (reference OP). The Z-Axis corresponds to the relative power ($\cdot 10^{-1}$).

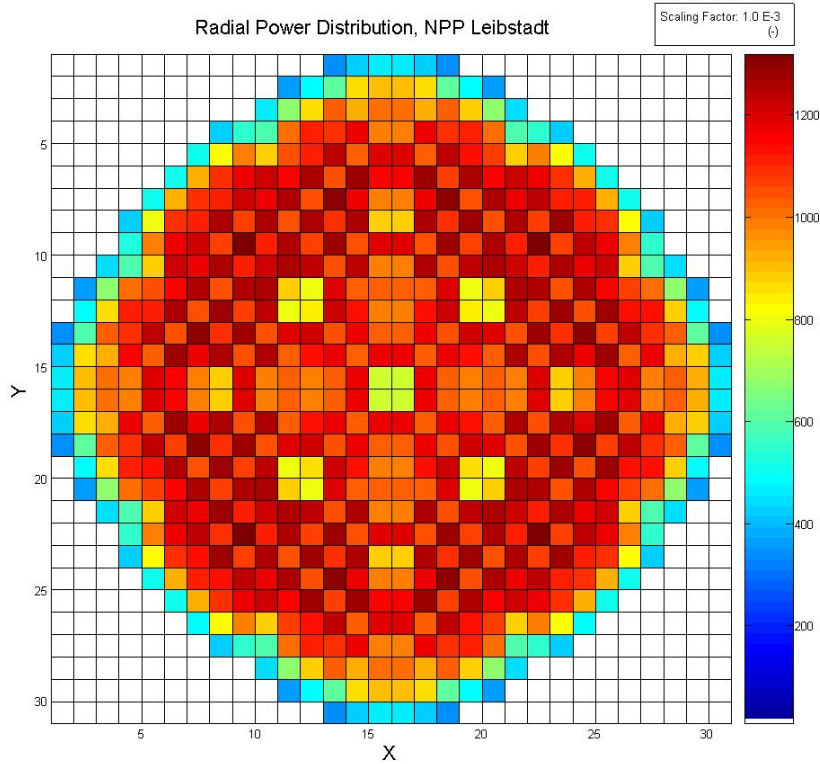


Figure 4.8: Radial power distribution axially averaged for NPP Leibstadt (reference OP).

Figure 4.9 shows the axial profile of the relative power, radially averaged, and the corresponding axial void profile calculated by RAMONA 5.2-5 for the reference OP.

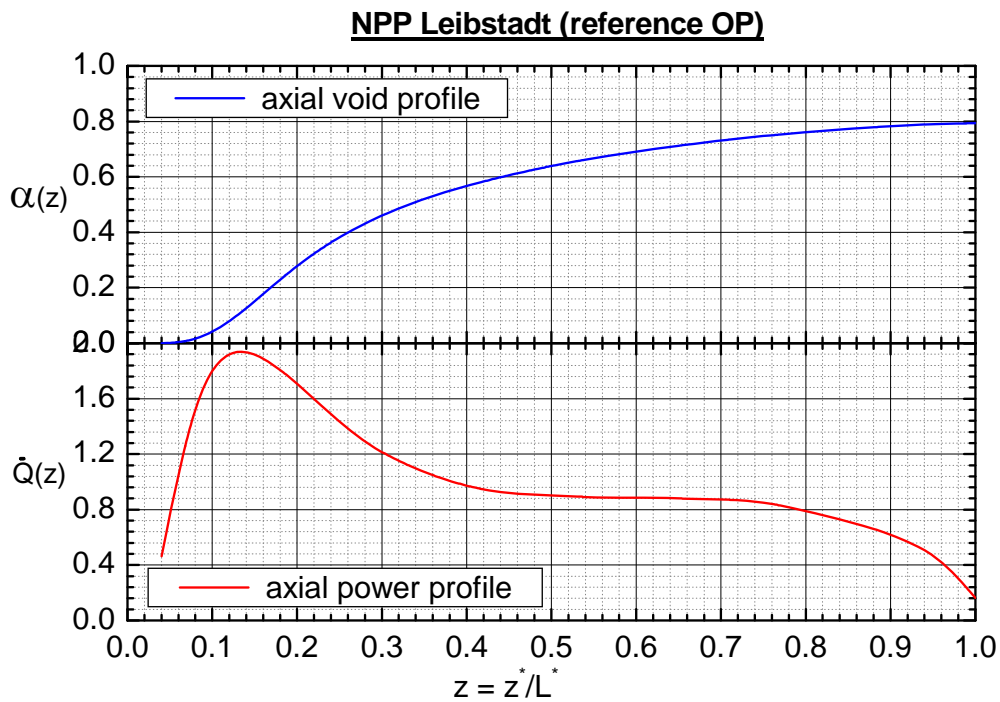


Figure 4.9: Axial power and axial void profile, radially averaged, respectively.

The power peak in the lower part of the channel is mainly caused by the moderation characteristics of neutrons in the single phase region where the coolant has a higher density respect to the upper parts of the channel. The higher the coolant density (mixture density!) the more efficient the neutron moderation is and the higher is the neutron density and accordingly the more energy will be deposited in the coolant (more elastic and inelastic collision of neutrons with the target material). The axial power profile (Figure 4.9) is reflected by the axial void profile for a given coolant mass flow and a fixed parameter configuration.

4.1.2 Transient analysis

The transient behaviour is initiated by introducing a 2 node sinusoidal control rod movement resulting in a perturbation of the state variables of the BWR system. The signals of the LPRM 9 (10) and 26 (32) of the fourth level which are located in different core half's are selected for the evaluation of the transient behaviour. Note that, RAMONA predicts a fixed symmetry line. The core shape, symmetry line and the locations of the LPRM detectors of the fourth level are presented in the next figure.

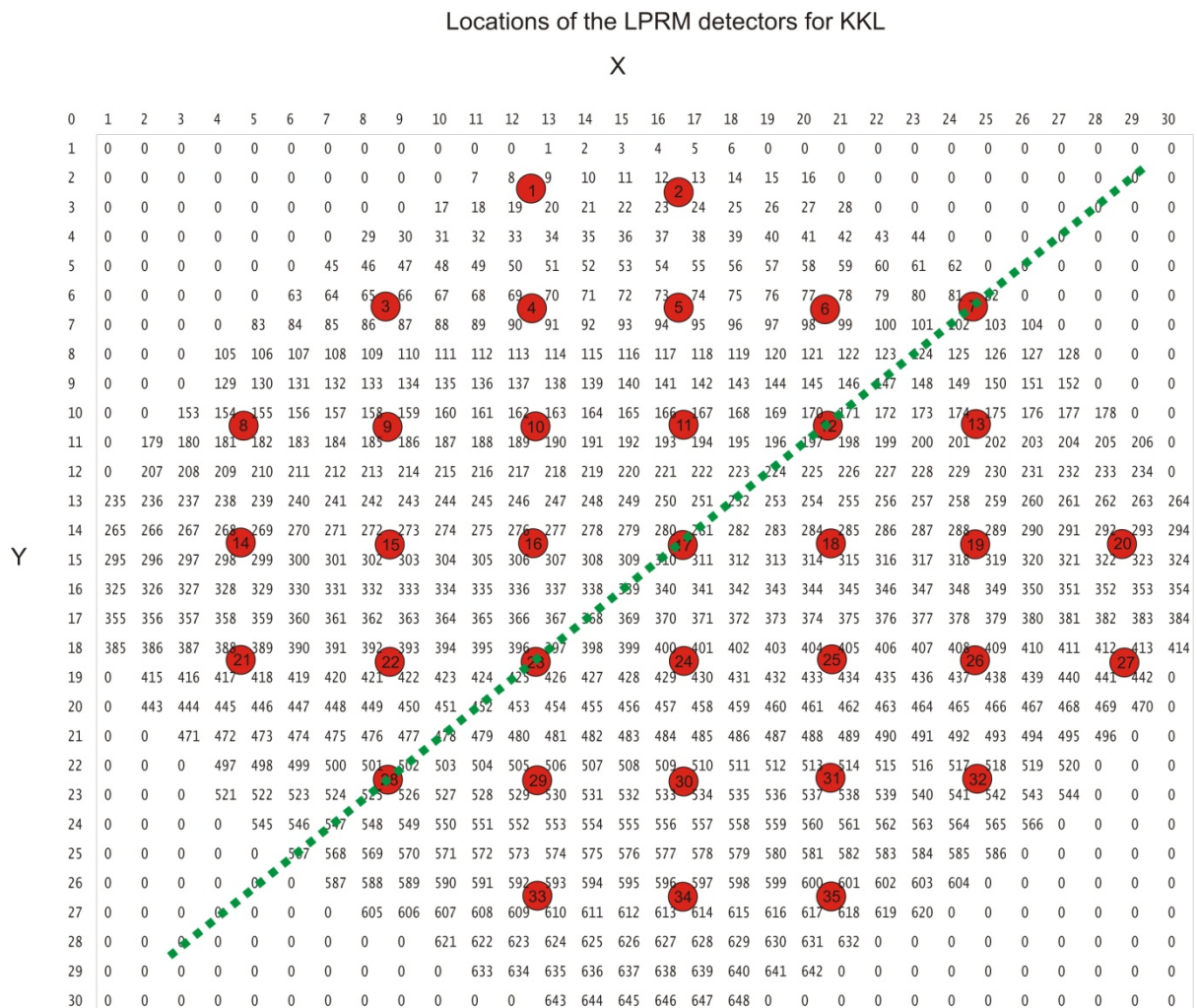


Figure 4.10: Locations of the LPRM detectors for KKLc7_rec4. The LPRM detectors 9 and 26 are located in different core half's.

Figure 4.11 shows the time evolution of the LPRM signals 9 and 26. As can be seen, an increasing out of phase power oscillation is occurring at the reference OP. The frequency of the oscillation is $NF^* = 0.537s^{-1}$. All RAMONA5 investigations for the reference OP and its close neighbourhood have shown that the out of phase power oscillation will not discharge into a stable limit cycle. It should be emphasized that the existence of a stable limit cycle cannot be verified by RAMONA5 **and** measurement results but its existence must not be excluded because as shown in the power spectral density of LPRM 26 (Figure 4.12) the higher harmonics occurs. If a limit cycle with large amplitudes exists (from the mathematical point of view), the RAMONA5 integration can be interrupted before reaching the limit cycle when specific termination conditions are satisfied.

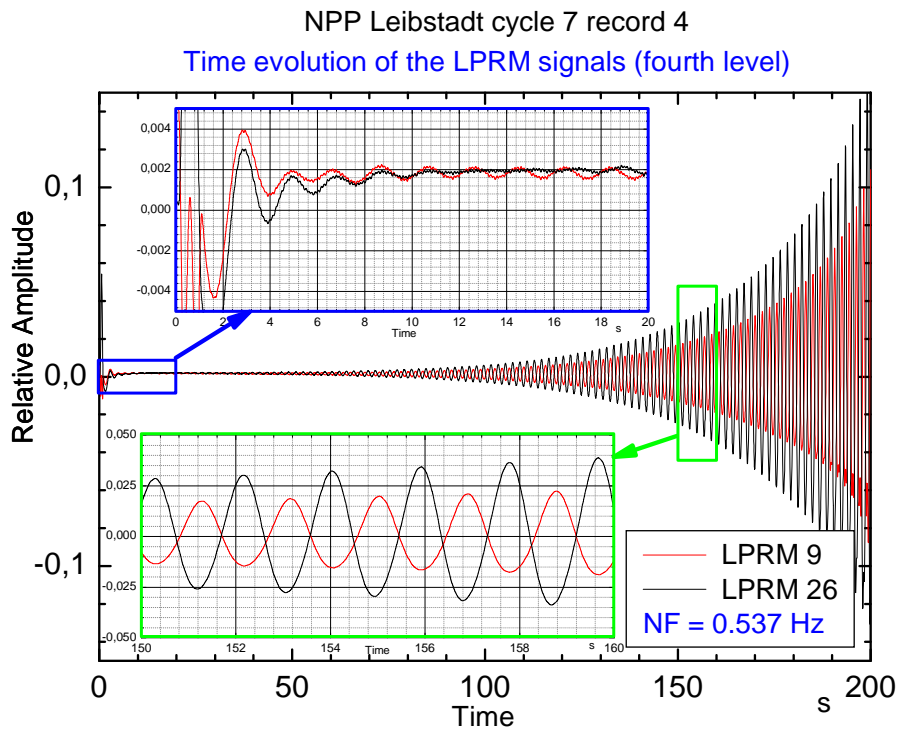


Figure 4.11: RAMONA5 result for the reference OP. The relative amplitudes of signals are shown for LPRM 9 and LPRM 26. Both LPRM signals have a phase shift of π .

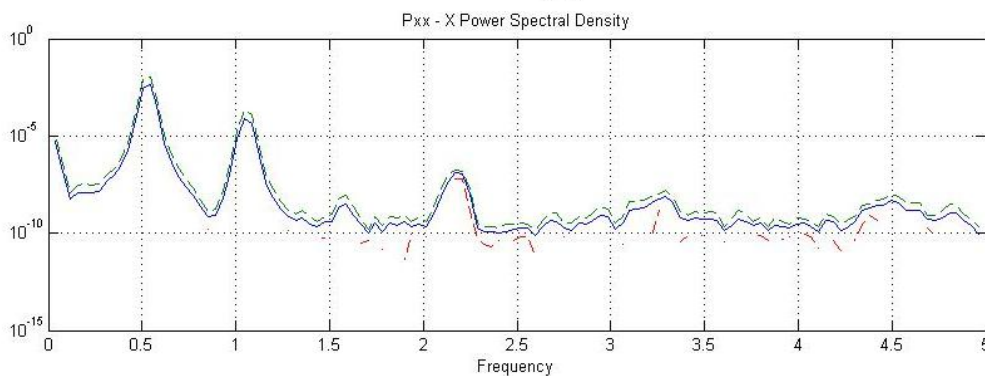


Figure 4.12: Power spectral density corresponding to LPRM 26 of the fourth level.

In order to demonstrate the essential stability properties corresponding to the reference OP more clear, the core inlet subcooling was reduced from $h_{sub} = 125 \text{ kJ/kg}$ to $h_{sub} = 120 \text{ kJ/kg}$ (where $h_{sub} = h_{sat} - h_{inlet}$) which is legitimate because the latter value is located within the uncertainty region.

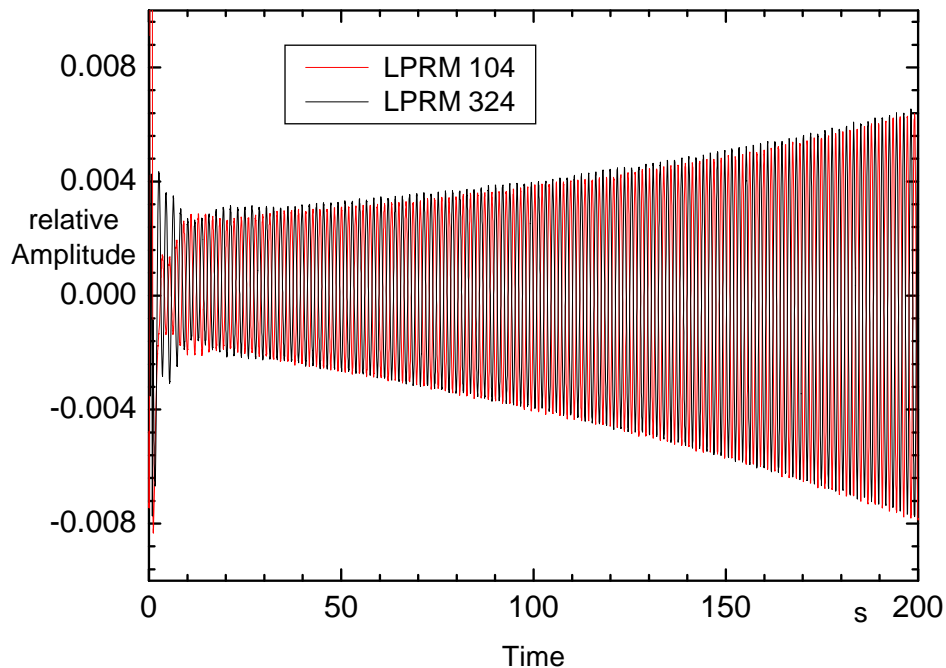


Figure 4.13: Signals are shown (relative amplitudes) of LPRM 10 and 32 in the fourth level respectively.

As shown in Figure 4.13, the increasing rate of the oscillation for $h_{sub} = 120 \text{ kJ/kg}$ is smaller than for the reference case. Figure 4.14 depicts clearly a phase shift of π between both LPRM-signals.

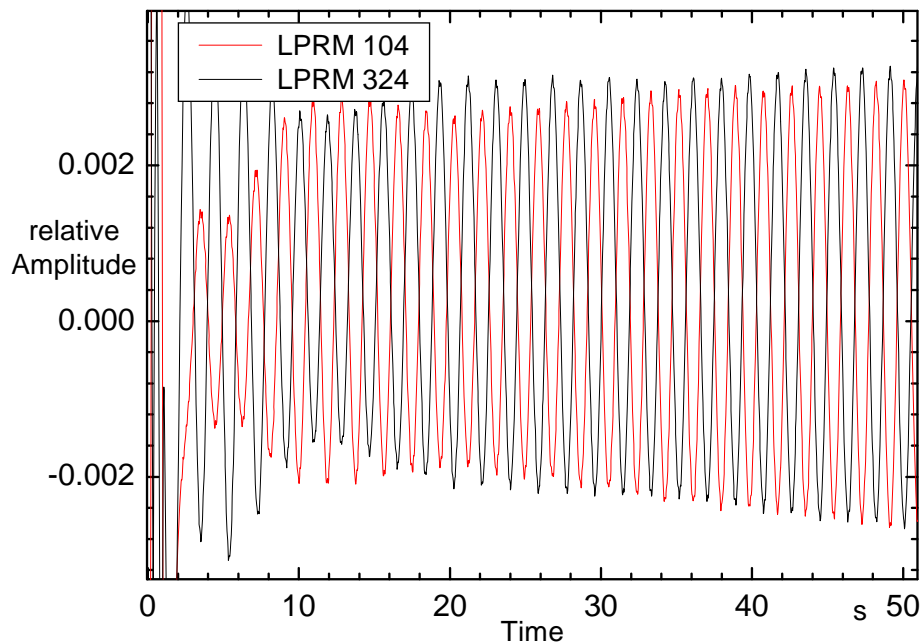


Figure 4.14: In this figure are shown the signals of LPRM 10 and 32 in the fourth level (relative amplitudes). The signals have a phase shift of π .

During an out-of-phase power oscillation the power and the total mass flow, averaged over the whole core, are approximately constant. These characteristics are shown in the next two figures. After twenty seconds, numerical noise only occur.

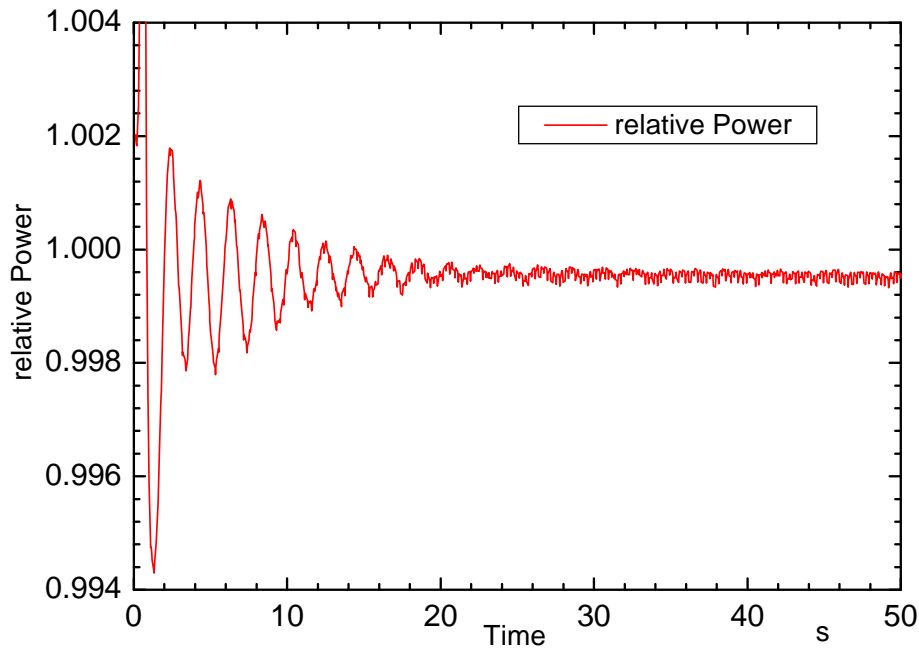


Figure 4.15: The relative power, averaged over all nodes is shown.

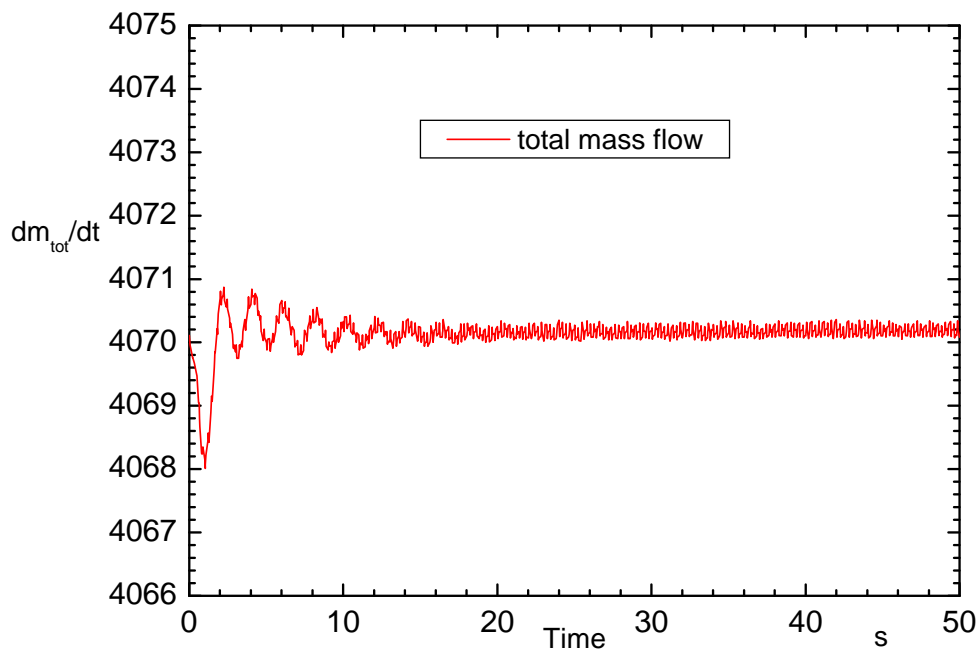


Figure 4.16: The total mass flow in the reactor core is presented.

4.2 Calculation of the ROM input parameters

As stated in section 2.6 all ROM inputs are calculated from the specific RAMONA5 model and its steady state solution corresponding to the reference OP. To this end, a steady state RAMONA5 run for the reference OP is necessary. Afterwards the new calculation methodology for the ROM input parameters is applied. Thereby the demand is that the ROM should provide the correct steady state values at the reference OP. Most essential quantities are the mode feedback reactivity coefficients, the core inlet mass flow, the axial void profile and the channel pressure drops along the closed flow path.

In the scope of this section, at first, the adjustment of the axial void profile is explained (section 4.2.1). Thereby the pressure loss coefficients as well as the core inlet subcooling corresponding to the axial void profile are calculated. Secondly, the calculation of the mode-feedback reactivity coefficients (section 3.2.2), the estimation of the drift flux parameters V_{gj} and C_0 (section 4.2.2) and the calculation of the ROM pressure drops (section 4.2.3) are presented.

4.2.1 Adjustment of the axial void profile

In addition to the core inlet mass flow, the core inlet subcooling and the system pressure, the most essential factor for determining the axial void profile is the axial power profile. In the actual reduced order model (as an approximation) a uniform axial power profile is assumed. But the real axial power profile is bottom peaked. Typical axial peaking factors are around 1.8 for NPP Leibstadt, NPP Ringhals and NPP Brunsbüttel. This deviation between the real power profile and the approximated power profile lead to a deviation between the real and calculated axial void profiles when the core inlet mass flow and the core inlet subcooling are equal for both models. Figure 3.36 (in subsection 3.4.3) and Figure 4.17 show a comparison of the axial power and void profiles calculated by RAMONA5 and ROM for NPP Leibstadt and NPP Brunsbüttel. Thereby the system pressure, the core inlet mass flow, the core inlet subcooling and the core averaged power of RAMONA5 are used as ROM input. But due to the different axial power profiles, the axial void profiles are different significantly. This discrepancy is shown quantitatively in subsection 3.4.3 for KKLc7_rec4-OP.

In the scope of the new calculation procedure of the ROM input parameters, the axial void profile will be adjusted in such a way that the resulting axial void profile of the ROM is similar to that one of RAMONA5. Thereby selected ROM input parameters such as the pressure loss coefficients and the core inlet subcooling of the ROM will be adjusted in an appropriate manner.

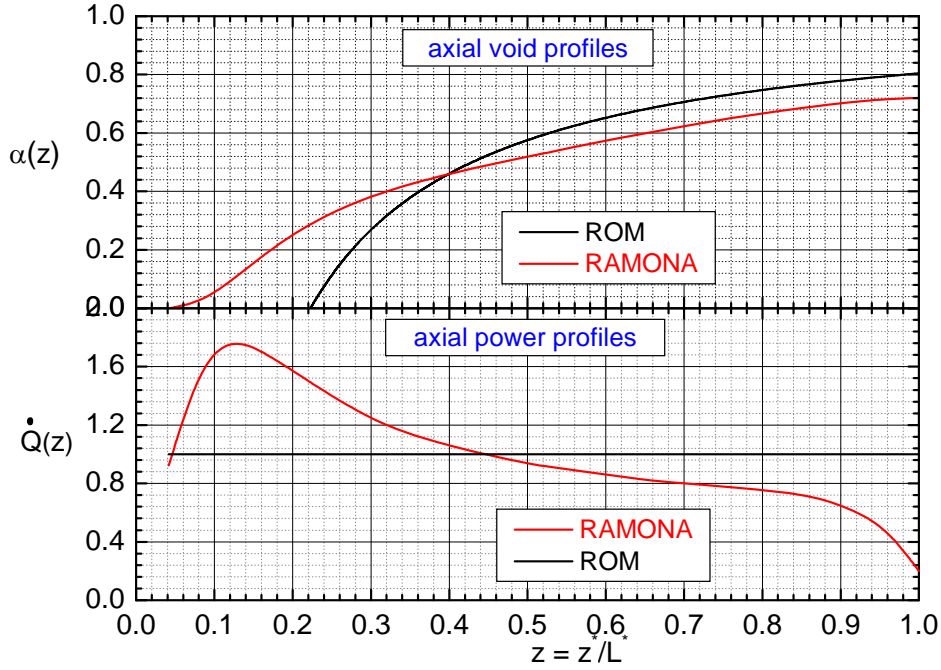


Figure 4.17: Comparison of the axial void and power profiles, calculated by the system code RAMONA5 and the ROM, where the core averaged inlet mass flow, the core inlet subcooling and the core averaged power of RAMONA5 were used as ROM input. (NPP Brunsbüttel)

Due to the bottom peak occurring in a real BWR system, the boiling boundary is shifted downwards in comparison with the boiling boundary predicted by the ROM. In order to represent the true axial void profile this shift can be corrected by changing the subcooling number N_{sub} . This can be derived from the single phase energy balance. The steady state energy balance along the thermal-hydraulic channel can be described by

$$\rho_l^* v_{inlet}^*(t^*) \frac{\partial h^*(z^*, t^*)}{\partial z^*} = \dot{q}^{m*}(z^*, t^*) \quad (4.2)$$

If a uniform axial power profile is used in the ROM, the power density \dot{q}^{m*} is constant along the heated channel. Further, it is assumed that all the power along the channel is transferred into the coolant as heat (without heat loss). Thus \dot{q}^{m*} can be expressed as

$$\dot{q}^{m*} = \frac{\dot{Q}^*}{A^* L^*} \quad (4.3)$$

where \dot{Q}^* is the core averaged power calculated from the real axial power profile and A^* is the coolant flow cross section. The axial enthalpy profile can be obtained according to

$$\int_0^{z^*} dz^* \frac{\partial h^*(z^*)}{\partial z^*} = \int_0^{z^*} dz^* \frac{\dot{q}^{m*}}{\rho_l^* v_{inlet}^*} \quad (4.4)$$

$$h^*(z^*) - \underbrace{h^*(0)}_{h_{inlet}^*} = \frac{\dot{q}^{**}}{\rho_l v_{inlet}^*} z^* \quad (4.5)$$

$$h^*(z^*) = h_{inlet}^* + \frac{\dot{q}^{**}}{\rho_l v_{inlet}^*} z^* \quad (4.6)$$

by integrating (4.2) from the channel inlet to z^* . According to (4.4), if \dot{q}^{**} is constant (as assumed in the ROM), the enthalpy profile will have a linear dependence along the heated channel.

Finally (4.6) can be converted into

$$h^*(z^*) = N_r N_\rho \Delta h_{fg}^* \left(N_{pch} \frac{z^*}{L^*} - N_{sub} \right) + h_{sat}^* \quad (4.7)$$

which is written in terms of dimensionless numbers N_r , N_ρ , N_{pch} and N_{sub} . From this follows the channel exit enthalpy as

$$h_{exit}^* = h^*(z^* = L^*) = N_r N_\rho \Delta h_{fg}^* (N_{pch} - N_{sub}) + h_{sat}^* \quad (4.8)$$

In the above relations, the phase change number was rewritten as

$$N_{pch} = \frac{\overbrace{\dot{q}^{**}}}{\underbrace{\rho_f^* v_0^* A_{inlet}^*}_{\dot{m}_{tot}^*} \Delta h_{fg}^* \rho_g^*} = \frac{\dot{Q}^* \Delta \rho^*}{\dot{m}_{tot}^* \Delta h_{fg}^* \rho_g^*} \quad (4.9)$$

If the boundary condition $h(\mu, t) = \langle h(\mu, t) \rangle = h_{sat}$ is used in (4.4) an expression for the boiling boundary

$$\mu^* = \rho_l v_{inlet}^* \frac{h_{sat}^* - h_{inlet}^*}{\dot{q}^{**}} \quad (4.10)$$

$$\mu^* = \frac{N_{sub} L^*}{N_{pch}}$$

$$\mu = \frac{N_{sub}}{N_{pch}} \quad (4.11)$$

is found. It can be seen, there exists an infinite ensemble of N_{sub} and N_{pch} for the same location μ where the coolant starts to boil. However, N_{pch} is fixed because the core inlet mass flow \dot{m}_{tot}^* and the core averaged power \dot{Q}^* are based on RAMONA5. In order to simulate the boiling boundary which is given by RAMONA5 the subcooling number N_{sub} must be adjusted. The order of magnitude of N_{pch} for the KKLc7_rec4-OP is around $N_{pch} = 6.5$, for example. As can be seen in Figure 4.20 the boiling boundary μ of this OP has the order of magnitude of $\mu = 0.1$. According to relation (4.11), the subcooling number can be estimated as $N_{sub} = \mu \cdot N_{pch} = 0.65$. This is the expected order of magnitude for N_{sub} for the KKLc7_rec4-OP.

To summarize, equation (4.11) is the result of the assumption that the power has a uniform axial power profile within the heated channel. The dimensionless number

N_{sub} belongs to a specific axial power profile of the considered thermal-hydraulic state. This means, when the same thermal hydraulic state is represented by two different thermal-hydraulic models where different axial power profiles are used, the corresponding subcooling numbers are not comparable.

In order to adjust the axial void profile, a special calculation procedure for the subcooling number, the pressure loss coefficients K_{inlet} , K_{exit} , $N_{f,1\Phi}$, $N_{f,2\Phi}$ and for the steady state values α_0 (mean void fraction of the two phase region) and T_{avg0} (mean fuel temperature) has been developed and is applied in the present work. These parameters are adjusted in such a way that the axial void profile and the pressure drops of the closed flow path of the ROM becomes similar to that one of RAMONA5 for the reference OP. Note that, the pressure loss coefficients and the values of α_0 and T_{avg0} cannot be calculated directly from the RAMONA5 model and its steady state solution because of the different calculation methodologies applied in both codes. Instead of the pressure loss coefficients, the corresponding physical pressure drops will be calculated from the RAMONA5 output (shown in section 4.2.3), for example.

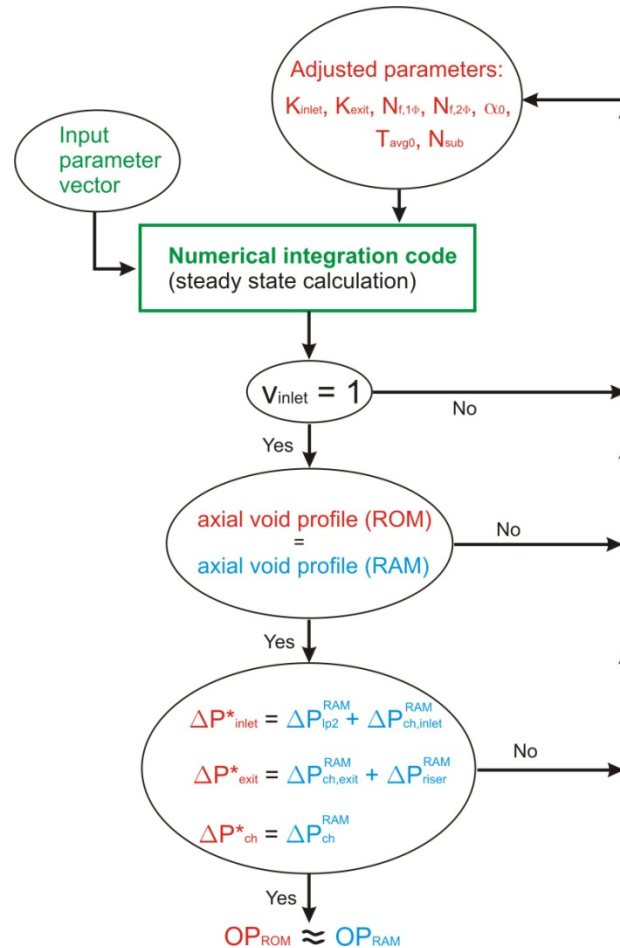


Figure 4.18: Flow-chart of the adjustment procedure for the axial void profile and the pressure drops of the ROM.

In Figure 4.18 is shown a flow-chart of the adjustment procedure, where the axial void profile and pressure drops of the ROM will be adapted by adjusting N_{sub} , K_{inlet} , K_{exit} , $N_{f,1\Phi}$, $N_{f,2\Phi}$, α_0 and T_{avg0} and then performing steady state calculations of the

ROM equation system. The steady state calculations of the ROM equation system will be repeated iteratively. In each iteration step, these parameters will be changed in such a way that the axial power profile and pressure loss coefficients become more and more similar to that ones of RAMONA5 for the considered operational point while preserving the correct core inlet mass flow.

4.2.2 Estimation of the drift-flux parameters V_{gj}^* and C_0

The local drift-flux velocity v_{gj}^* is defined as

$$v_{gj}^* = v_g^* - j^* \quad , \quad (4.12)$$

where v_g is the velocity of the gas phase and j is the centre of volume velocity and can be written as

$$j^* = \alpha^* v_g^* + (1 - \alpha^*) v_l^* \quad . \quad (4.13)$$

In expression (4.13), α is the volumetric void fraction and v_l is the liquid velocity (an asterix indicates a dimensional value). The drift flux velocity V_{gj}^* used in the ROM is called accurately the void-weighted averaged local drift velocity [69-76] and is defined as

$$V_{gj}^* = \frac{\langle \alpha^* v_{gj}^* \rangle}{\langle \alpha^* \rangle} \quad , \quad (4.14)$$

where the brackets indicates an area averaging. Accordant to (4.14), the distribution parameter C_0 is defined as

$$C_0 = \frac{\langle \alpha^* j^* \rangle}{\langle \alpha^* \rangle \langle j^* \rangle} \quad . \quad (4.15)$$

Depending on the flow regime, there exist several correlations and models recommended for the calculation of V_{gj}^* and C_0 which are based on extensive experimental database [75,76]. For the purpose of the present reduced order model, these two parameters are assumed to be independent of flow regimes, especially the void fraction. Based on this assumption, both parameters can be written as

$$C_0 = 1.2 - 0.2 \sqrt{\frac{\rho_g^*}{\rho_l^*}} \quad (4.16)$$

$$V_{gj}^* = C_{dr} \left(\frac{\sigma g^* \Delta \rho^*}{\rho_l^{*2}} \right)^{0.25} \quad (4.17)$$

where C_{dr} is a parameter which can be used for an adjustment by the user [52,69]. For example, as described in [69] (Chapter 3.5.2), for the churn-turbulent flow, the constant C_{dr} is around 1.42. In this case, the void-weighted averaged local drift ve-

locity is $V_{gj}^* = 0.173 \text{ m/s}$ and the distribution parameter is $C_0 = 1.156$. The corresponding dimensionless value of V_{gj}^* is $V_{gj} = V_{gj}^* / v_0^* = 0.326$.

An assessment of V_{gj}^* by employing RAMONA5 and using definition (4.14) result in $V_{gj}^* = 0.33 \text{ m/s}$ which corresponds to $V_{gj} = 0.62$. In this case, the constant C_{dr} is around 2.7. A sensitivity study, where the values of V_{gj}^* and C_0 have been assessed, was performed for NPP Leibstadt and NPP Ringhals. All results of V_{gj}^* are between $(0.25 - 0.4) \text{ m/s}$. From the results of the sensitivity study can be concluded, the values of V_{gj}^* and C_0 can be tuned legitimately in the interval $V_{gj}^* \in [0.2, \dots, 0.5] \text{ m/s}$ and $C_0 \in [1.0, \dots, 1.2]$.

4.2.3 Calculation of the ROM pressure drops

As discussed in section 3.3, in the PSI-Illinois-ROM, only the pressure drop over the reactor core ΔP_c^{RAM} , given by the RAMONA model, was taken into account. In particular, ΔP_c^{RAM} is extracted from the specific RAMONA5 model and is used by the PSI-Illinois-ROM as external pressure drop $\Delta P_{ext}^* = \Delta P_c^{RAM}$. Besides, ΔP_{ext}^* is assumed to be constant [12,47]. The core pressure drop can be subdivided according to

$$\Delta P_c^{RAM} = \Delta P_{ch,inlet}^{RAM} + \Delta P_{ch}^{RAM} + P_{ch,exit}^{RAM} \quad (4.18)$$

the sum of the channel inlet pressure drop $\Delta P_{ch,inlet}^{RAM}$, the channel pressure drop ΔP_{ch}^{RAM} (single phase plus two phase pressure drop) and the exit pressure drop $\Delta P_{ch,exit}^{RAM}$.

When the core pressure drop is used as external pressure drop in the ROM, the ROM pressure drops have to satisfy

$$\Delta P_{ch}^* = \Delta P_{ch}^{RAM} \quad (4.19)$$

$$\Delta P_{inlet}^* = \Delta P_{ch,inlet}^{RAM} \quad (4.20)$$

$$\Delta P_{exit}^* = \Delta P_{ch,exit}^{RAM} \quad (4.21)$$

at the reference OP.

In order to simulate the stability behaviour more realistic, the TUD-ROM was extended by a recirculation loop model [23,24]. In addition to that all pressure drops along the closed flow path are taken into account. Figure 4.19 shows the most relevant pressure drops of the RAMONA5 model.

The pressure drop over the lower plenum 1 and the steam dome are very small and can be neglected. For example, the lower plenum1 pressure drop is four orders of magnitude smaller than other pressure drops considered for the nonlinear stability analyses.

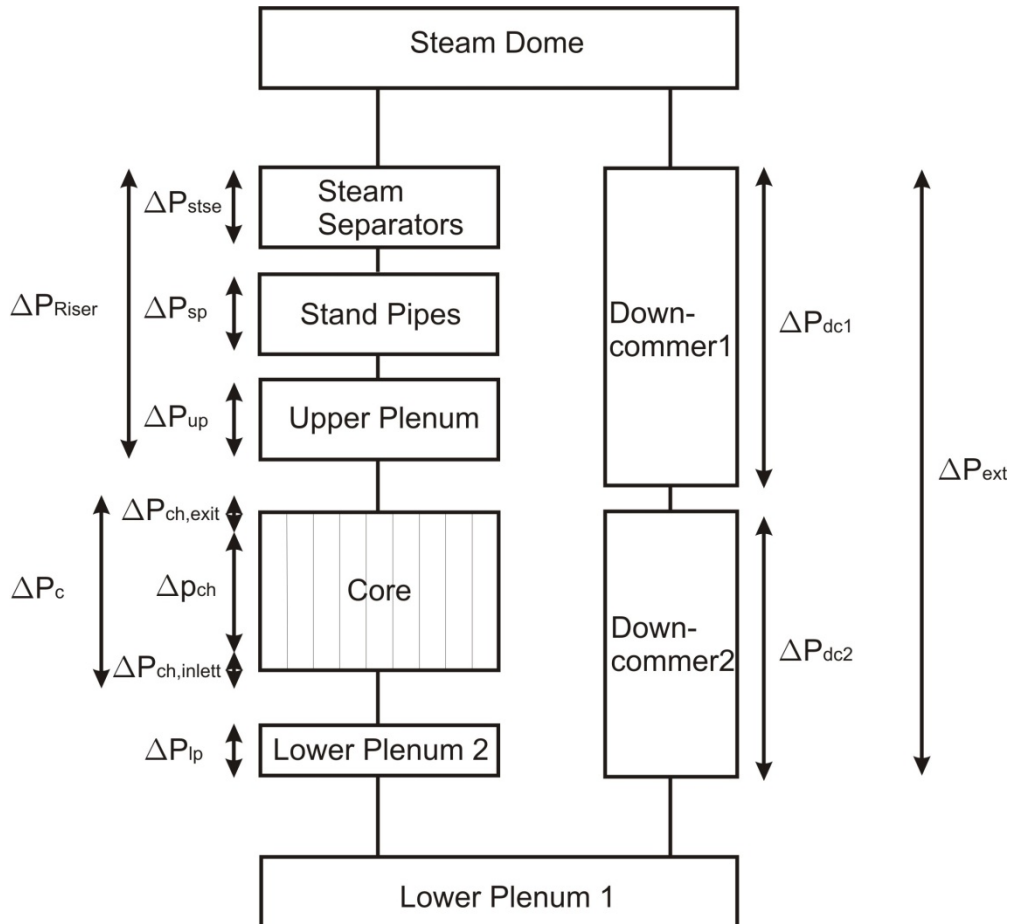


Figure 4.19: Schematic sketch of the components considered in RAMONA5.

The pressure drop along the closed flow path is satisfying the boundary condition

$$\oint \frac{\partial p}{\partial z} dz = 0 \quad . \quad (4.22)$$

According to the thermal-hydraulic model shown in Figure 4.19, the boundary condition (4.22) can be expressed as

$$0 = \int_0^1 \frac{\partial p_{h_ch}}{\partial z} dz + \int_1^0 \frac{\partial p_{recirc}}{\partial z} dz \quad (4.23)$$

$$0 = \underbrace{\Delta P_{lp2}^{RAM} + \underbrace{\Delta P_{ch,inlett}^{RAM} + \Delta P_{ch}^{RAM} + \Delta P_{ch,exit}^{RAM}}_{\Delta P_c^{RAM}} + \underbrace{\Delta P_{up}^{RAM} + \Delta P_{sp}^{RAM} + \Delta P_{stse}^{RAM}}_{\Delta P_{riser}^{RAM}}}_{\int_0^1 \frac{\partial p_{h_ch}}{\partial z} dz} + \underbrace{(\Delta P_{dc1}^{RAM} + \Delta P_{dc2}^{RAM})}_{\int_1^0 \frac{\partial p_{recirc}}{\partial z} dz}, \quad (4.24)$$

where the first integral in (4.23) describes the pressure drops along the upward flow and the second integral the pressure drops along the downward flow. Therefore the external pressure drop can be written as

$$\Delta P_{ext} = \int_0^1 \frac{\partial p_{h_ch}}{\partial z} dz = \int_1^0 \frac{\partial p_{recirc}}{\partial z} dz \quad . \quad (4.25)$$

As mentioned previously, the pressure drops provided by the RAMONA5 (at the reference OP) are presented in Appendix F. It should be pointed out that $\Delta P_{ch,exit}^{RAM}$, $\Delta P_{ch,inlet}^{RAM}$ and ΔP_{ch}^{RAM} are not printed in the output file and thus were calculated separately. $\Delta P_{ch,inlet}^{RAM}$ and $\Delta P_{ch,exit}^{RAM}$ can be calculated by relation

$$\Delta P_{ch,inlet}^{RAM} = \frac{1}{2} k_{inlet} \frac{G^{*2}}{\rho_l^*} \quad \text{with} \quad G^* = \frac{\dot{m}_{tot}^*}{A_{tot}^*} \quad (4.26)$$

and

$$\Delta P_{ch,exit}^{RAM} = \frac{1}{2} k_{exit} \frac{G^{*2}}{\rho_l^*} \Phi_{local}^2, \quad (4.27)$$

where k_{inlet} and k_{exit} are defined in the RAMONA5 input and Φ_{local}^2 is a two phase multiplier for irreversible local losses. In the RAMONA5 model, Φ_{local}^2 is defined as

$$\Phi_{local}^2 = 1 + CRT(2) \cdot x_{exit} \cdot \left(\frac{\rho_l^*}{\rho_g^*} - 1 \right), \quad (4.28)$$

where x_{exit} is the exit quality and $CRT(2)$ is a constant provided by the user.

Figure 3.2, presented in subsection 3.1.3, depicts the most relevant thermal-hydraulic components of the ROM including the pressure drops along the closed loop. According to Figure 3.2 the boundary condition (4.22) for the simplified BWR model can be written as

$$0 = \int_0^1 \frac{\partial p_{h_ch}}{\partial z} dz + \int_1^0 \frac{\partial p_{recirc}}{\partial z} dz \quad (4.29)$$

$$0 = \overbrace{\Delta P_{inlet}^* + \Delta P_{ch}^* + P_{exit}^*} + \overbrace{(-\Delta P_{doc}^* - \Delta P_{head}^*)}.$$

For a steady state forced circulation flow, the second integral in expression (4.29) can be written in dimensionless form as

$$DP_{ext} \equiv \Delta P_{ext} = Fr^{-1} + \Delta P_{head}, \quad (4.30)$$

where DP_{ext} is the steady state external pressure drop. In the steady state case, all time dependent terms in ΔP_{doc}^* are zero (friction in the recirculation loop is neglected) [23,24]. It can be seen in the steady state expression (4.30), natural circulation occurs, when the pump head becomes zero. Thus natural circulation will appear in operational points for which relation (4.30) becomes $DP_{ext} \equiv \Delta P_{ext} \leq Fr^{-1}$ (downcomer friction is ignored).

In addition to the void generation, the pressure drops over the closed flow path are of paramount importance for the thermal-hydraulic stability properties and thus for stability behaviour of the whole nuclear reactor system. Therefore, the pressure drops of the ROM should be simulated as close as possible to the RAMONA pressure drops. To this end, the following relations should be satisfied by the ROM at steady state conditions at the reference OP:

$$\Delta P_{ch}^* = \Delta P_{ch}^{RAM} \quad (4.31)$$

$$\Delta P_{inlet}^* = \Delta P_{lp2}^{RAM} + \Delta P_{ch,inlet}^{RAM} \quad (4.32)$$

$$\Delta P_{exit}^* = \Delta P_{ch,exit}^{RAM} + \Delta P_{riser}^{RAM} \quad (4.33)$$

The channel inlet and exit pressure drops in the ROM can be calculated by

$$\Delta P_{inlet}^* = K_{inlet} \cdot v_{inlet}^2 \cdot \rho_l^* v_0^{*2} \quad (4.34)$$

and

$$\Delta P_{exit}^* = K_{exit} \cdot \rho_m \cdot v_m^2 \cdot \rho_l^* v_0^{*2} \quad , \quad (4.35)$$

where v_{inlet} is the dimensionless inlet velocity, K_{inlet} and K_{exit} are the channel inlet and exit pressure loss coefficients of the ROM, v_0^* is the dimensional reference channel inlet velocity, ρ_m is the dimensionless mixture density and v_m is the corresponding dimensionless mixture velocity. Practically, the pressure loss coefficients can be adjusted (adjustment procedure, see Figure 4.18) in such a way that the channel inlet and channel exit pressure drops are satisfying relation (4.32) and (4.33) under steady state conditions (at the reference OP). The satisfaction of (4.31) can be realized by a tuning of the single phase $N_{f,1\Phi}$ and two phase friction $N_{f,2\Phi}$ numbers occurring in the single phase and two phase momentum equation [12,47]. Finally, the pressure drops which have to be satisfied by the ROM were estimated accordant to (4.31), (4.32), (4.33). The effect of spacer friction is included in the ROM-coefficients $N_{f,1\Phi}$ and $N_{f,2\Phi}$ [12].

4.2.4 Summary of the ROM input calculation for NPP Leibstadt

All design parameters of the ROM have been calculated from the specific KKL-RAMONA5 model at the reference OP. The operating parameters are estimated from the steady state solution provided by RAMONA5 at this OP. In order to simulate the correct steady state conditions with the ROM, a new calculation procedure for the input values was applied. The thermal-hydraulic state of the reference OP will be simulated correctly by the ROM when its axial void profile and its pressure drops along the closed flow path are calculated close to the reference case.

Furthermore, the evaluation of the time histories of the LPRM signals, resulting from the first RAMONA5 analysis, reveals the orientation of the symmetry line, which divides the core in region 1 and region 2. This is the symmetry line presented in Figure 4.10. In contrast to the RAMONA5 result, the measured LPRM signals show an un-fixed symmetry line [5]. As a result of the first RAMONA5 transient analysis, core region 1 and core region 2 are determined which is necessary for the application of the C_{mm} -calculation procedure.

As can be seen in Table 4.1, the values of the heated channel pressure drops simulated by the ROM are close to the reference values provided by RAMONA5. The comparison of the axial void profile (radially averaged), calculated by RAMONA5,

with the axial void profile, provided by the ROM, is presented in Figure 4.20. The largest deviation between both axial void profiles occurs in the region where sub-cooled boiling exists. Thereby the deviation of the total volumetric void fraction is less than 1%.

Table 4.1: This table contains the pressure drops provided by the RAMONA5 output and that one calculated by the ROM (KKLc7_rec4-OP). The steady state external pressure drop DP_{ext}^* provided by the RAMONA5 output is a ROM input parameter while the channel inlet pressure drop $\Delta P_{ch,inlet}^*$, the channel pressure drop (single and two phase pressure drop) ΔP_{ch}^* and the channel exit (outlet) pressure drop $\Delta P_{ch,exit}^*$ are adjusted by tuning of K_{inlet} , K_{exit} , $N_{f,1\Phi}$ and $N_{f,2\Phi}$.

Pressure drop	RAMONA5	ROM
$\Delta P_{ch,inlet}^*$	$-1.654 \cdot 10^4 Pa$	$-1.641 \cdot 10^4 Pa$
ΔP_{ch}^*	$-2.777 \cdot 10^4 Pa$	$-2.763 \cdot 10^4 Pa$
$\Delta P_{ch,exit}^*$	$-2.956 \cdot 10^4 Pa$	$-2.984 \cdot 10^4 Pa$
DP_{ext}^*	$-7.387 \cdot 10^4 Pa$	$-7.387 \cdot 10^4 Pa$

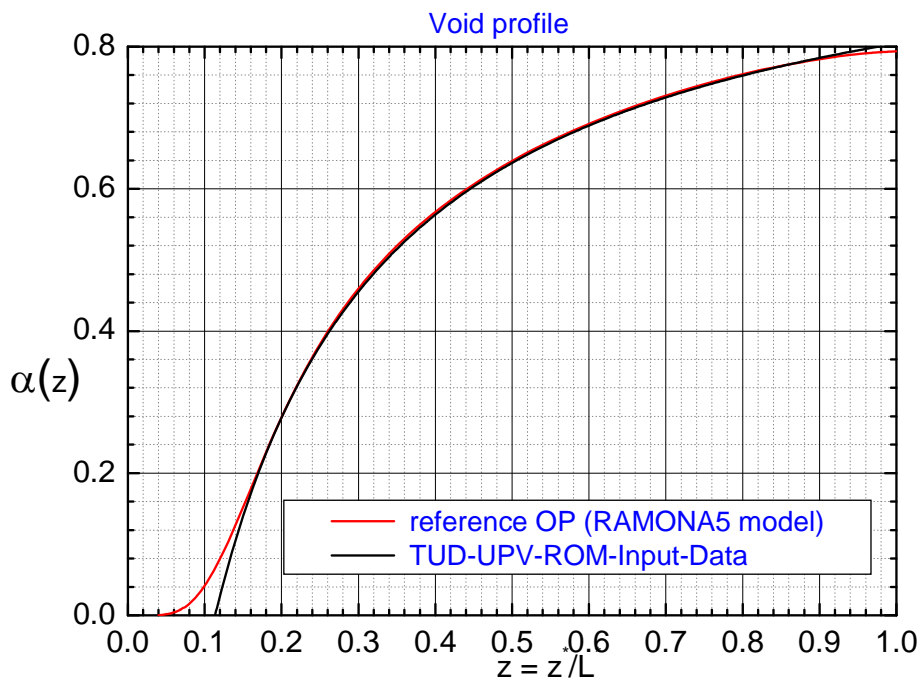


Figure 4.20: Comparison of the axial void profile (radially averaged) calculated by RAMONA5 with the axial void profile provided by the ROM.

The drift flux parameters used as input values are $V_{gj} = 0.35$ and $C_0 = 1.02$.

4.3 Local nonlinear stability analysis

4.3.1 Numerical integration at the reference OP

After calculation of all ROM input data from the RAMONA5 model and its steady state solution at the reference OP, the transient behaviour is analysed by employing the numerical integration code. To this end, the transient is initiated by introducing small perturbations in the inlet velocities where the perturbation amplitudes have the same sign (in-phase oscillation is triggered).

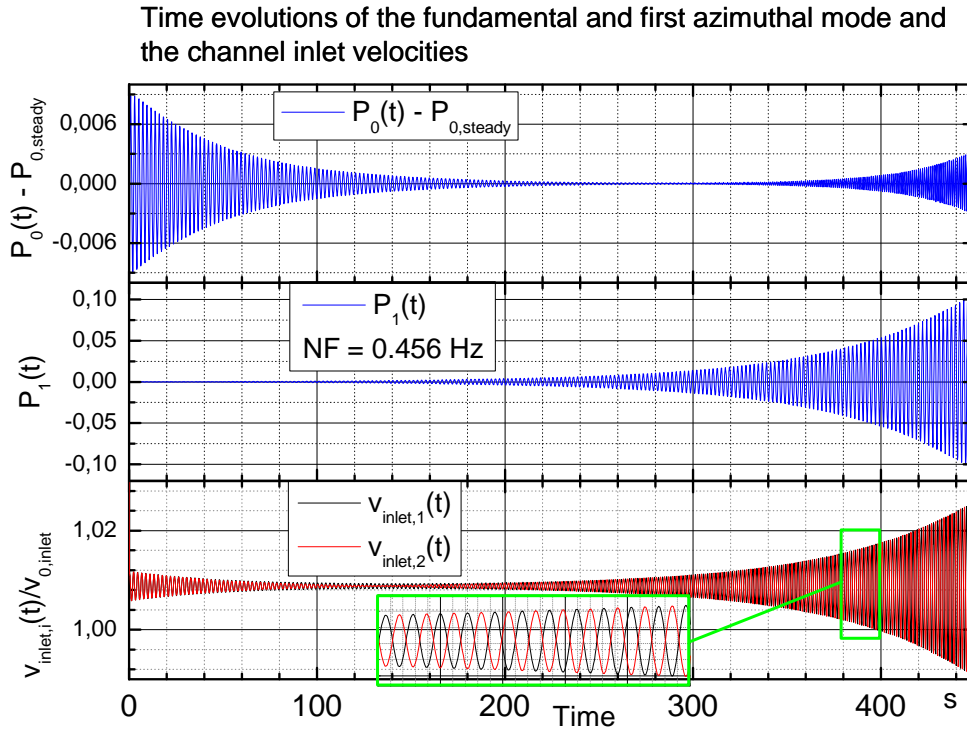


Figure 4.21: Time evolutions of the fundamental $P_0(t)$ and first azimuthal mode $P_1(t)$ and the channel inlet velocities $v_{1,inlet}(t)$ and $v_{2,inlet}(t)$.

The time evolution of the fundamental mode $P_0(t)$, the first azimuthal mode $P_1(t)$ and the channel inlet velocities $v_{1,inlet}(t)$ and $v_{2,inlet}(t)$ are shown in Figure 4.21. It can be seen that the amplitudes of the fundamental mode oscillation are decaying for the first 250 s and then increasing while the first azimuthal mode oscillation is increasing continuously, after the perturbation was imposed on the system. Thus, the prediction of the RAMONA5 investigation at the reference OP could be verified by the ROM. This means, an increasing out of phase power oscillation is occurring at the reference OP because the first azimuthal mode is excited. It should be emphasized that, in order to excite the first azimuthal mode, the artificial factor *fact* was increased [12,42,43] in the scope of the ROM-input calculation. The oscillation frequency predicted by the ROM is $NF^* = 0.457s^{-1}$.

The behaviour of the fundamental mode oscillation (decaying for the first 250 s and then increasing) can be explained by the solution of a linearized system where each component of the solution depends on each eigenvalue of the Jacobian matrix (see

subsection 3.3.3 and Appendix A). This means, if there is at least one pair of complex conjugated eigenvalues with a real part larger than zero, all components of the solution will diverge asymptotically in an oscillatory manner [12,56].

4.3.2 Bifurcation analysis

Bifurcation analysis is performed in this section. To this end, at first, semi-analytical bifurcation analysis with the bifurcation code BIFDD is carried out. As a result, the stability properties of fixed points and periodical solutions are examined in an appropriated parameter map. Secondly, numerical integration is carried for independent confirmation of the results of the bifurcation analysis and for the nonlinear analysis more far away from the SB. In the scope of the numerical integration of the ROM equation system the time evolution of all phase space variables are calculated.

4.3.2.1 Semi-analytical bifurcation analysis

In this subsection, semi-analytical bifurcation analysis of the ROM equation system with the bifurcation code BIFDD is performed. To this end, the subcooling number N_{sub} and the steady state external pressure drop DP_{ext} are selected to be the bifurcation and iteration parameters. This means, the stability boundary (SB) will be calculated in the $N_{sub} - DP_{ext}$ -operating plane and is referred to the reference OP. A variation of DP_{ext} corresponds to a movement on the rod-line which crosses the reference OP while the 3D-distributions will not be affected. Thus the stability properties of operational points along the rod-line and its close neighbourhood are analysed. The stability boundary and the bifurcation characteristics are shown in Figure 4.22.

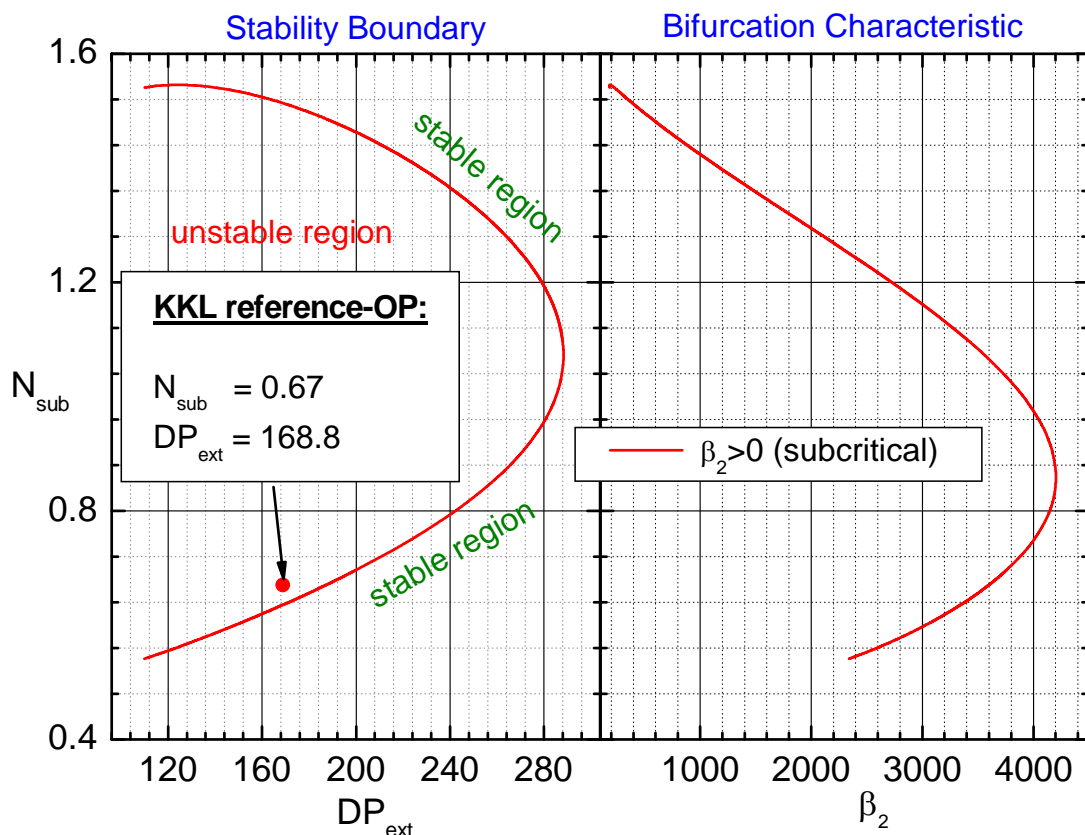


Figure 4.22: Stability boundary and the bifurcation characteristics for the reference OP. The SB is defined as the set of fixed points where the Hopf conditions are fulfilled.

As explained in section 2.3, the stability boundary is defined as the set of fixed points for which the Hopf conditions are fulfilled. Roughly speaking, this means, in each of these fixed points a limit cycle is “born” and exists either in the linear stable or (linear) unstable region. The stability characteristics of the limit cycle are determined by the Floquet parameter β_2 . The stability boundary and the bifurcation characteristics, depicted in Figure 4.22, are plotted only in the region which is reasonable from the physical point of view. The ROM results becomes doubtfully for DP_{ext} less than $DP_{ext} = 110$.

As expected, the reference OP is located in the linear unstable region close to the SB. This result was predicted by the RAMONA5 analysis as well as by numerical integration (see section 4.4.1 and 4.4.2) of the ROM equation system. In Figure 4.23 is depicted the SB projected into the power flow map where the dimensionless power and core inlet mass flow are scaled to nominal conditions. Hence, the vertical axis corresponds to the relative thermal core power and the horizontal axis corresponds to the relative core inlet mass flow.

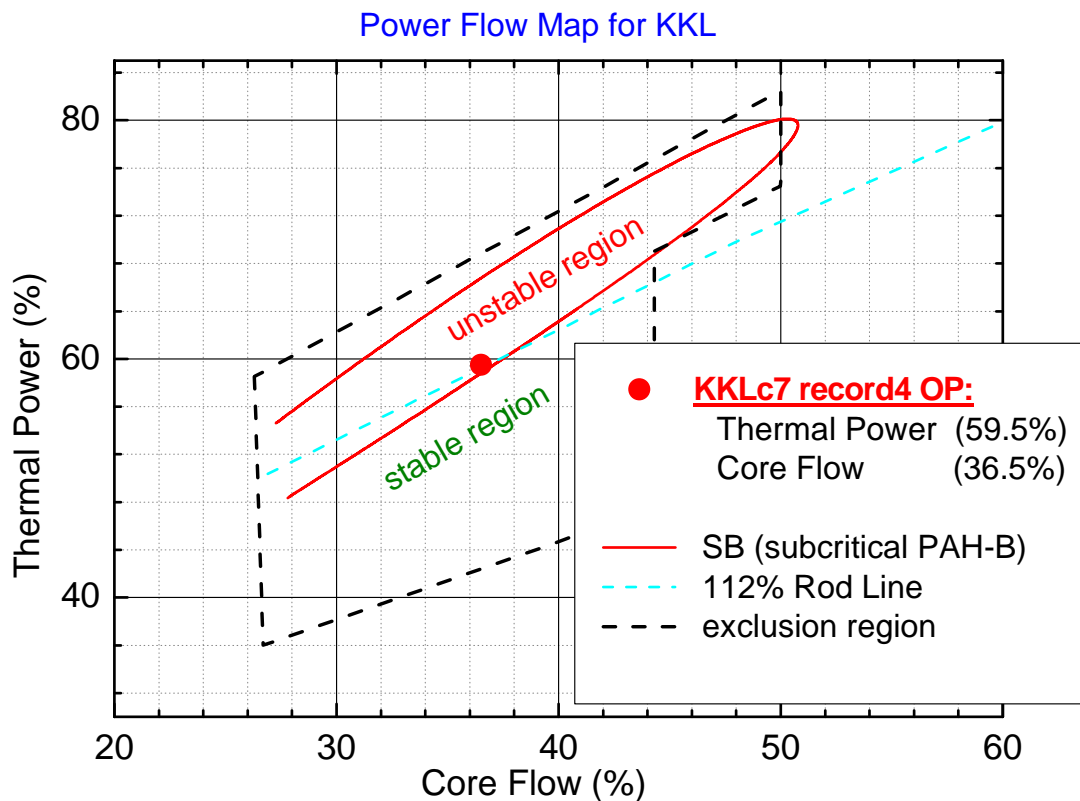


Figure 4.23: SB “transformed” into the power-flow map.

Unstable periodical solutions (unstable limit cycle) close to the KKLc7_rec4-OP are predicted by the semi-analytical bifurcation analysis. These solutions are located in the linear stable region close to the stability boundary. This means, in this region co-exist stable fixed points and unstable limit cycles.

4.3.2.2 Numerical integration

Semi-analytical bifurcation analysis is only valid in the vicinity of the critical bifurcation parameter (SB) in the parameter space and in the close neighbourhood of the singular fixed point in the phase space. In order to get information of the stability behaviour beyond the local bifurcation findings numerical integration of the set of the ODEs is necessary. In addition to that the predictions of the semi-analytical bifurcation analysis can be confirmed independently.

The results of the local numerical integration for selected parameters confirm the prediction of the bifurcation analysis. The forgoing bifurcation analysis forecasts the existence of unstable periodical solutions, which are born in the subcritical Hopf-bifurcation point, in the stable region. Hence, fixed points located in the stable region were selected to carry out numerical integration.

Figure 4.24 shows the SB in the close neighbourhood of the reference OP (zoomed in). In addition to that this figure shows the parameters for which the numerical integration is performed to confirm the existence of an unstable periodical solution.

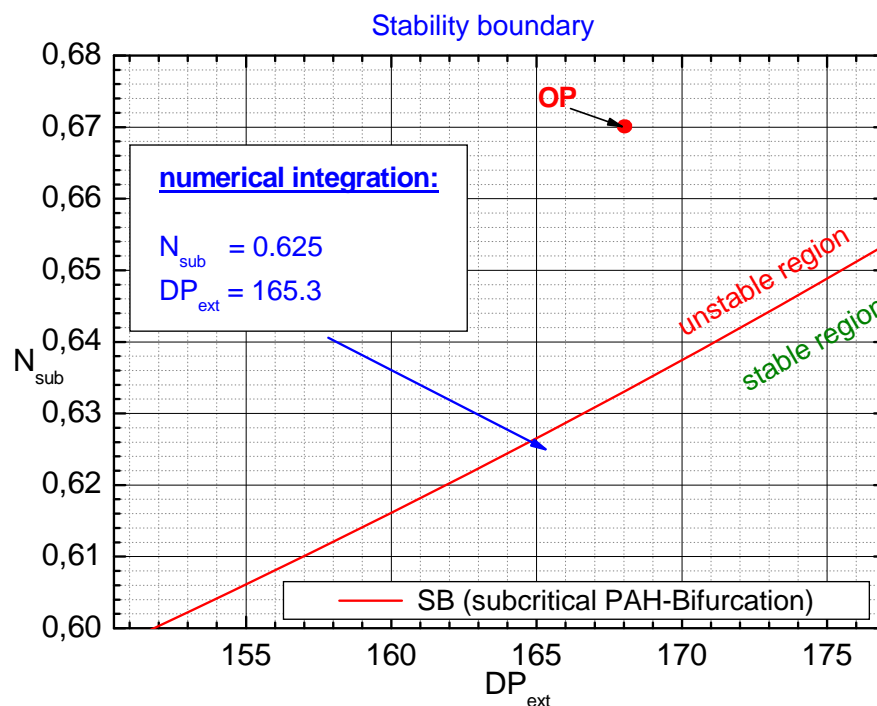


Figure 4.24: SB and the point for which the unstable limit cycle is verified by numerical integration

In order to verify the existence of the unstable limit cycle, perturbations of different amplitudes are imposed on the system. This means, according to $\vec{X}(t) = \vec{X}_0 + \delta\vec{X}(t)$, the steady state solution \vec{X}_0 is perturbed by different perturbation amplitudes $\delta\vec{X}(t)$ and the transient behaviour of the system state $\vec{X}(t)$ is calculated by numerical integration of the ROM equation system. If a sufficient small perturbation is imposed on the system, the state variables will return to the steady state solution. But if a sufficient large perturbation is imposed on the system, the state variables will diverge in

an oscillatory manner. As shown in Figure 4.25, the results of the numerical integration method confirm locally the prediction of the bifurcation analysis.

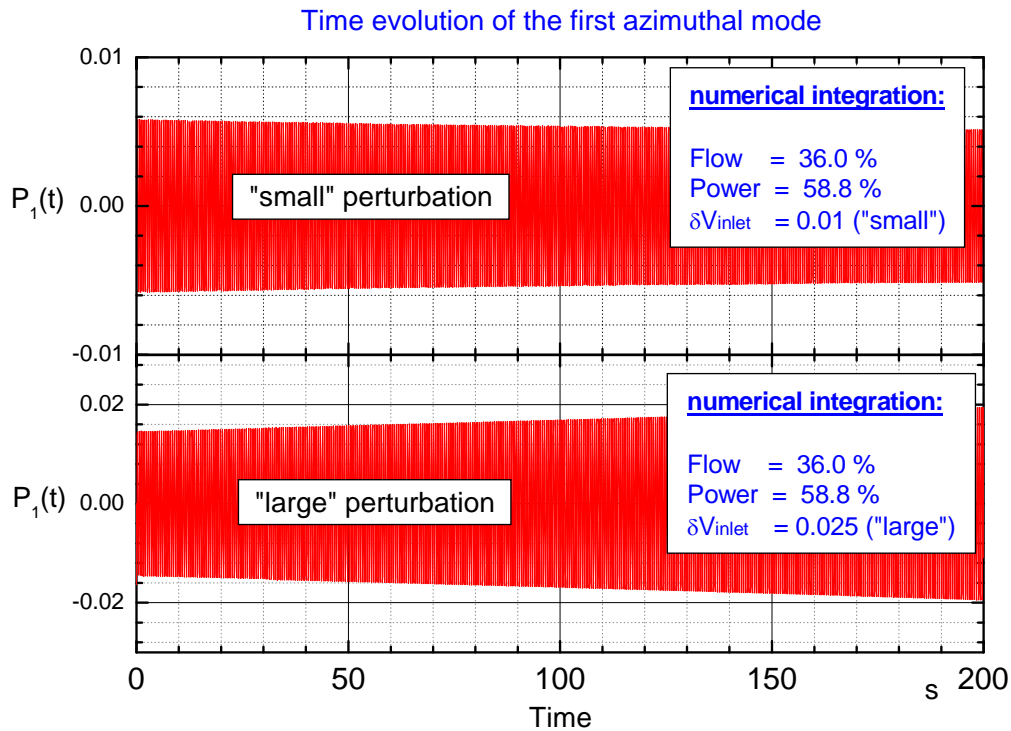


Figure 4.25: Numerical integration is carried out in an operational point where an unstable periodical solution is predicted. The transient was initiated by imposing perturbations of the core inlet mass flow (small $\delta v_{inlet} = 0.01$, large $\delta v_{inlet} = 0.025$).

4.3.2.3 Summary

Stability and bifurcation analysis with the ROM for the reference OP were performed by employing the bifurcation code BIFDD. The SBs and nature of the PAH-Bs are determined and visualized in appropriated two-dimensional parameter spaces. In particular, the subcooling number N_{sub} and the steady state external pressure drop DP_{ext} are selected to be the iteration and bifurcation parameters. Thereby, the variation of DP_{ext} corresponds to a movement along the rod-line which crosses the reference OP. Hence, the stability properties of operational points along the rod-line are analyzed.

Unstable periodical solutions (unstable limit cycle) close to the KKLc7_rec4-OP are predicted by the semi-analytical bifurcation analysis. These solutions are located in the linear stable region close to the stability boundary. This means, in this region **co-exist stable fixed points and unstable limit cycles**. As mentioned previously, the asymptotic decay ratio (linear stability indicator) is less than 1 ($DR < 1$) in this region. A linear stability analysis is not capable to examine the stability properties of limit cycles.

4.4 Comparative study with RAMONA5 and ROM: Local consideration

In this section, a comparative study with RAMONA5 and ROM is performed in the parameter space spanned by the core inlet subcooling and the steady state pressure drop. The goal of this investigation is to study the dependence of the stability behaviour regarding variations in the core inlet subcooling and the steady state pressure drop, respectively. As a result, the relative location of the reference OP respect to the stability boundary will be obtained. The terminology “local consideration” means that the comparative study is applied for operational points located in the neighbourhood of the reference OP and only in the phase space region near the singular fixed point.

4.4.1 Variation of the core inlet subcooling

The effect of the core inlet subcooling variation on the stability behaviour is considered next. To this end, RAMONA5 and ROM analyses were made in a parallel manner. Thereby the core inlet subcooling was varied in small steps and the transient behaviour was investigated.

4.4.1.1 RAMONA results

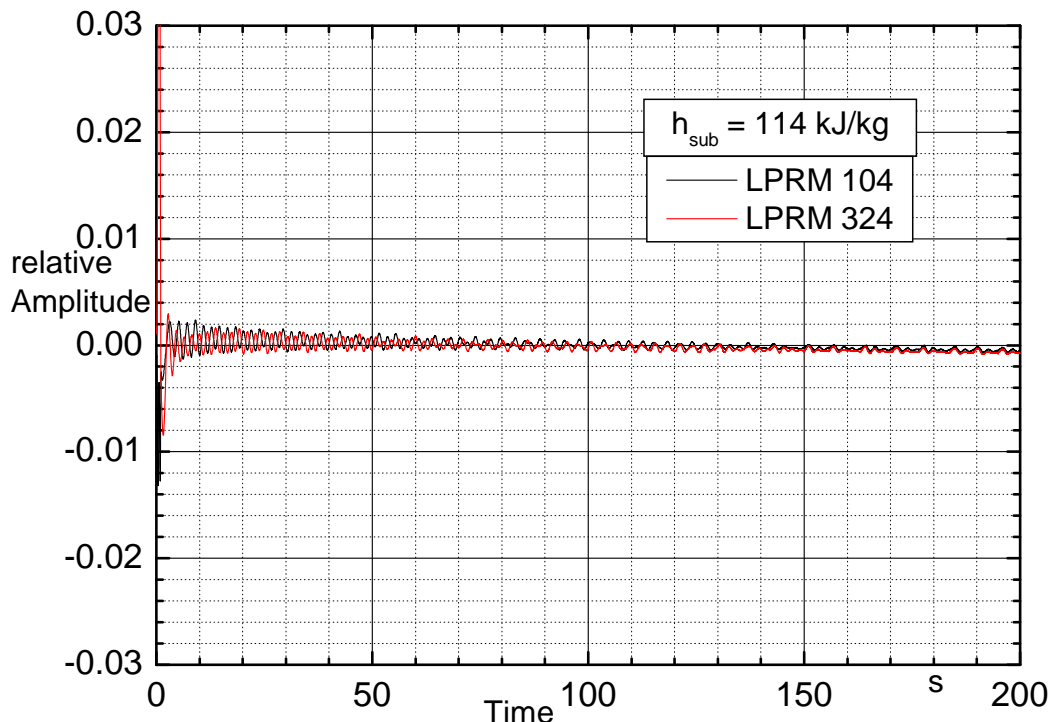


Figure 4.26: Signals (relative amplitudes) of LPRM 10 and 32 in the fourth level respectively. The regional oscillation is decaying. Consequently, the BWR system is stable in that operational point. (KKL)

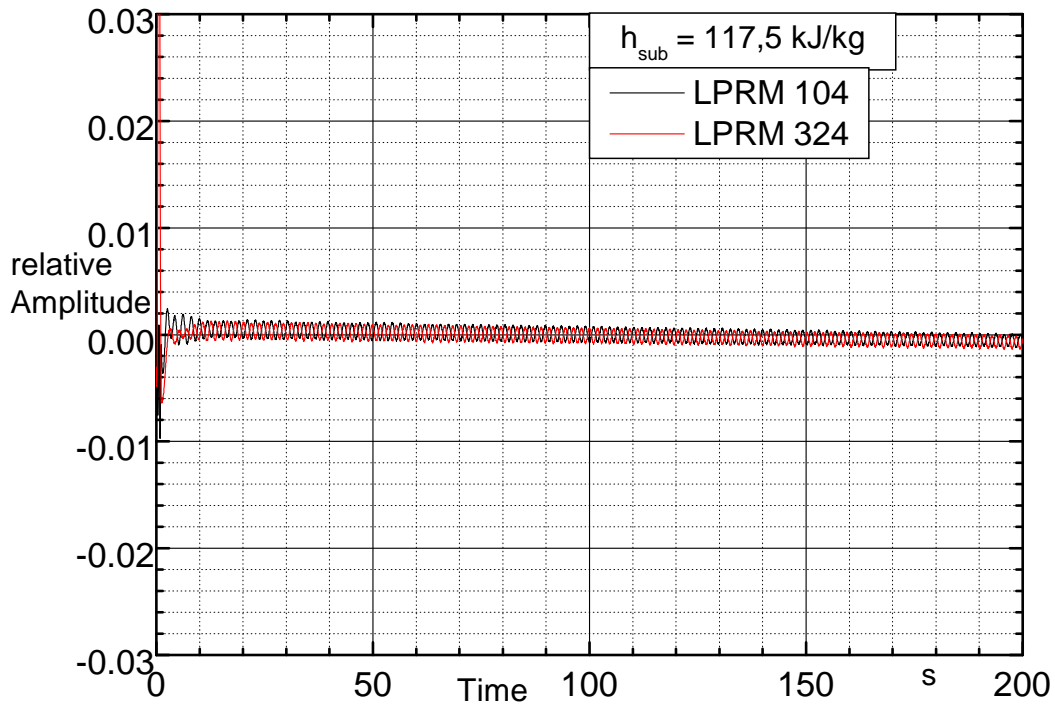


Figure 4.27: Signals (relative amplitudes) of LPRM 10 and 32 in the fourth level respectively. The regional oscillation is decaying slowly. (KKL)

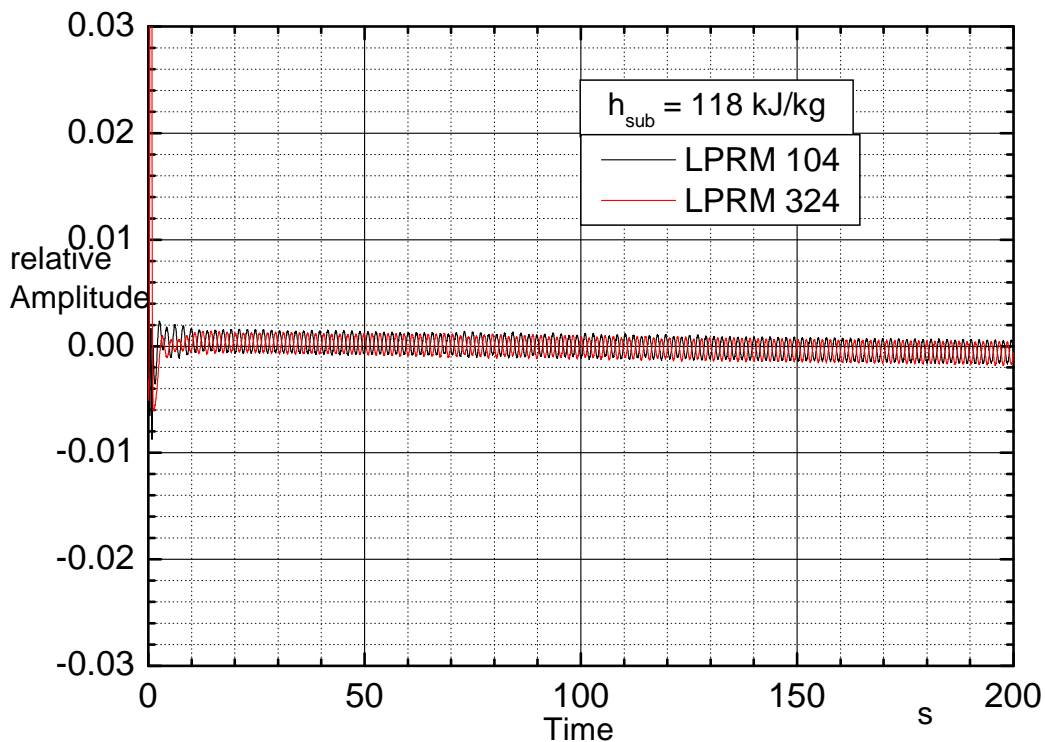


Figure 4.28: Signals (relative amplitudes) of LPRM 10 and 32 in the fourth level respectively. It seems, the oscillation amplitudes are remaining constant. (KKL)

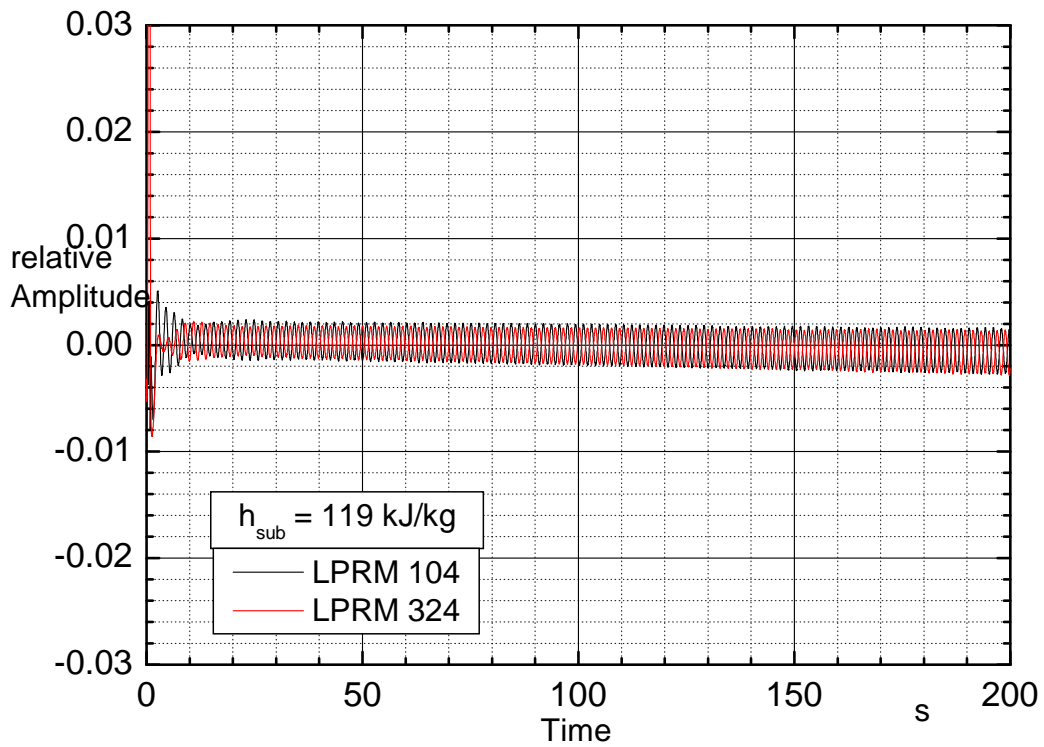


Figure 4.29: Signals (relative amplitudes) of LPRM 10 and 32 in the fourth level respectively. The oscillation amplitudes are increasing slowly. (KKL)

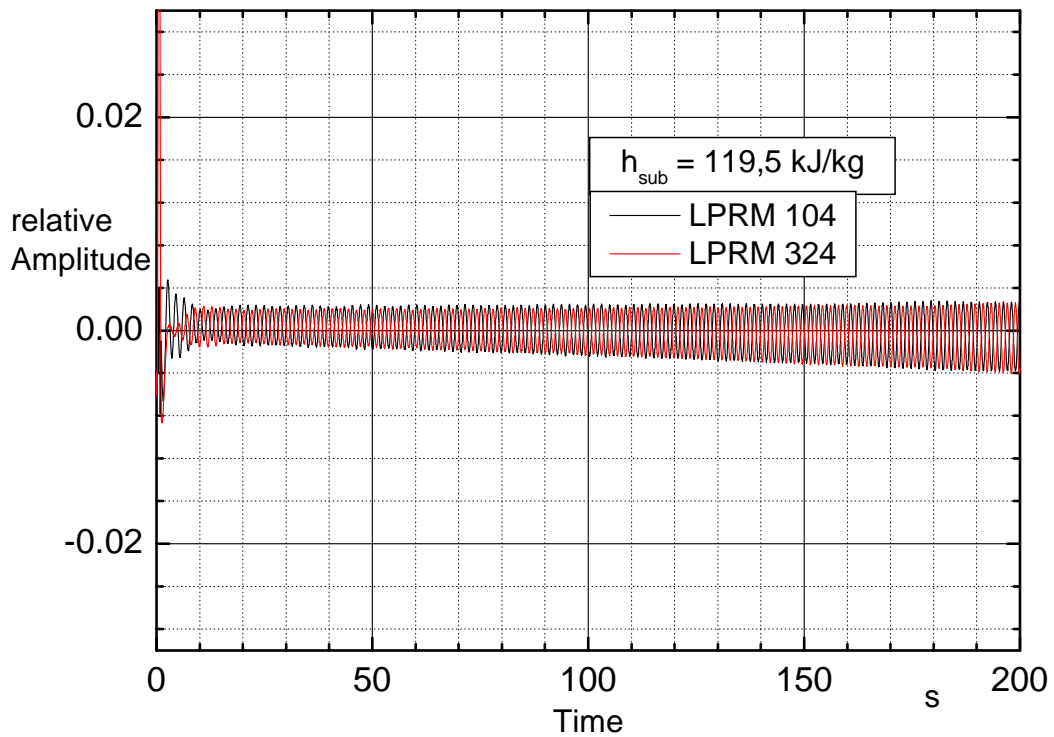


Figure 4.30: Signals (relative amplitudes) of LPRM 10 and 32 in the fourth level respectively. The oscillation amplitudes are increasing. (KKL)

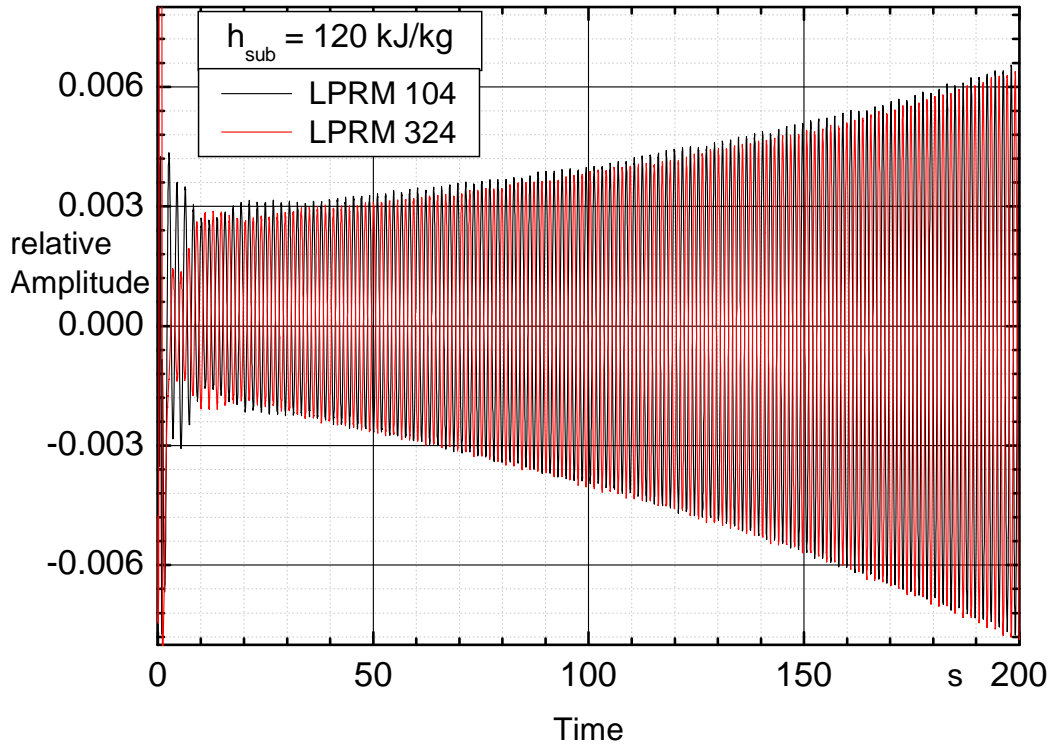


Figure 4.31: Signals (relative amplitudes) of LPRM 10 and 32 in the fourth level respectively. (KKL)

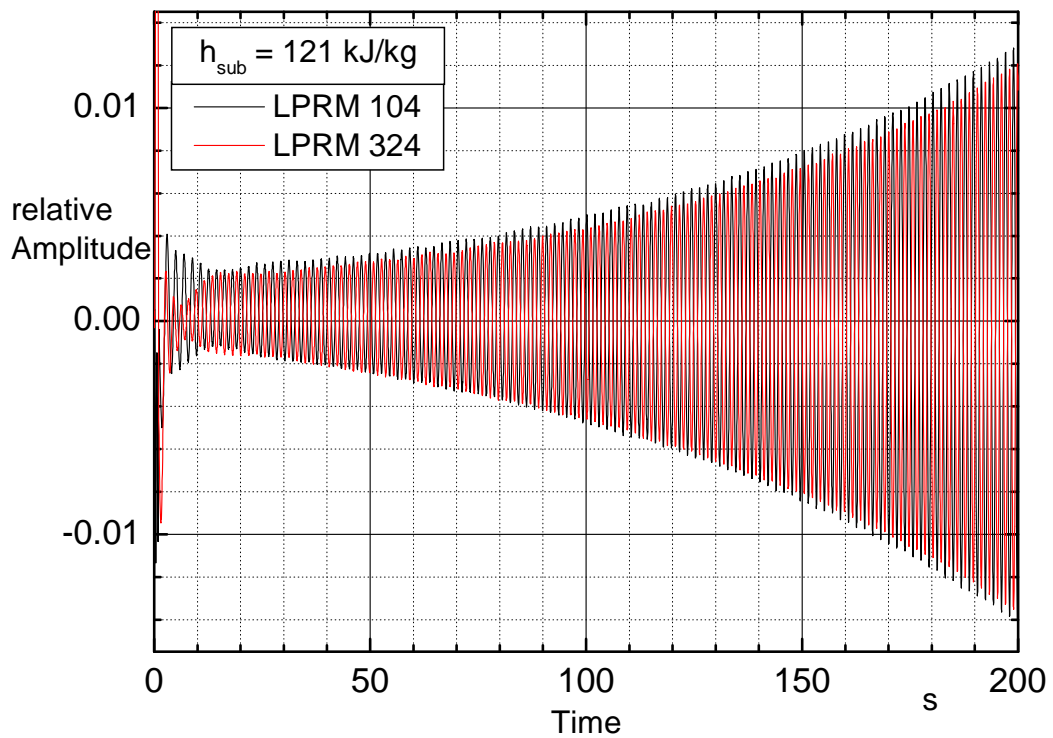


Figure 4.32: Signals (relative amplitudes) of LPRM 10 and 32 in the fourth level respectively. (KKL)

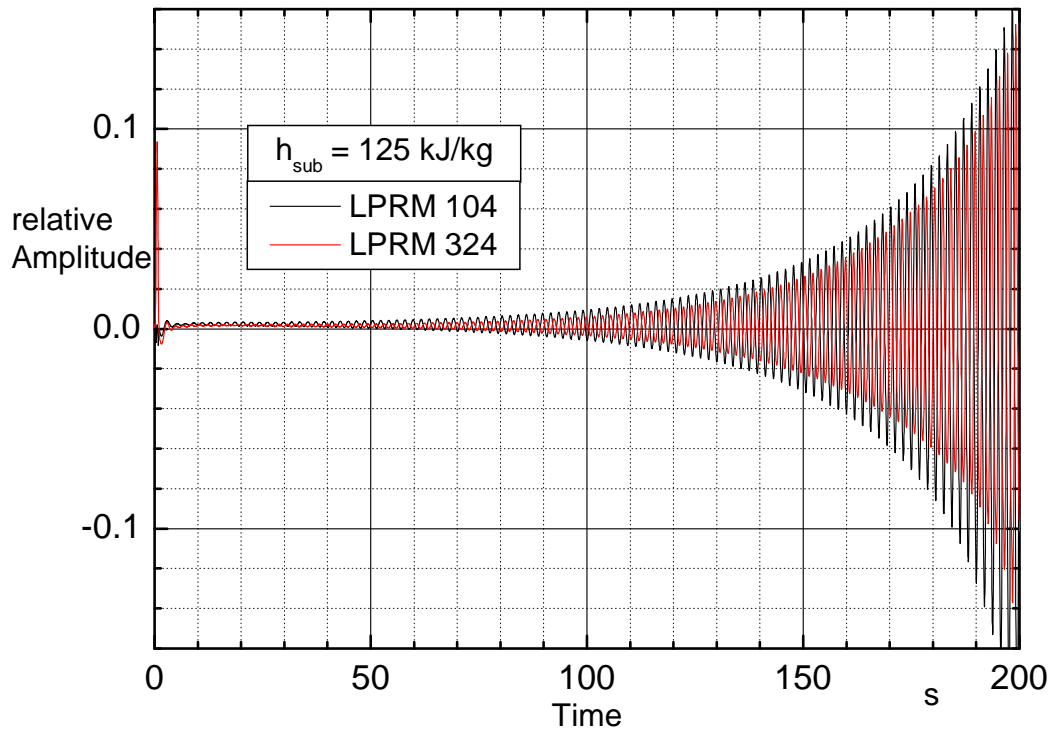


Figure 4.33: Signals (relative amplitudes) of LPRM 10 and 32 in the fourth level respectively. (KKL)

The RAMONA5 investigation has shown the more the core inlet subcooling will be increased the larger the increasing rate of the oscillation amplitudes are. Besides, the analysis reveals the location of the stability boundary where the oscillation amplitudes are neither decaying nor non-decaying after imposing a perturbation on the steady state system. According to this, the stability boundary is located between $h_{sub} = 117.5 \text{ kJ/kg}$ and $h_{sub} = 119.0 \text{ kJ/kg}$. Below the stability boundary, it can be stated, the lower the core inlet subcooling the more stable the system is.

4.4.1.2 ROM results

The ROM-results for the core inlet subcooling variation study are shown in Figure 4.34. For this analysis, only the first azimuthal mode is evaluated.

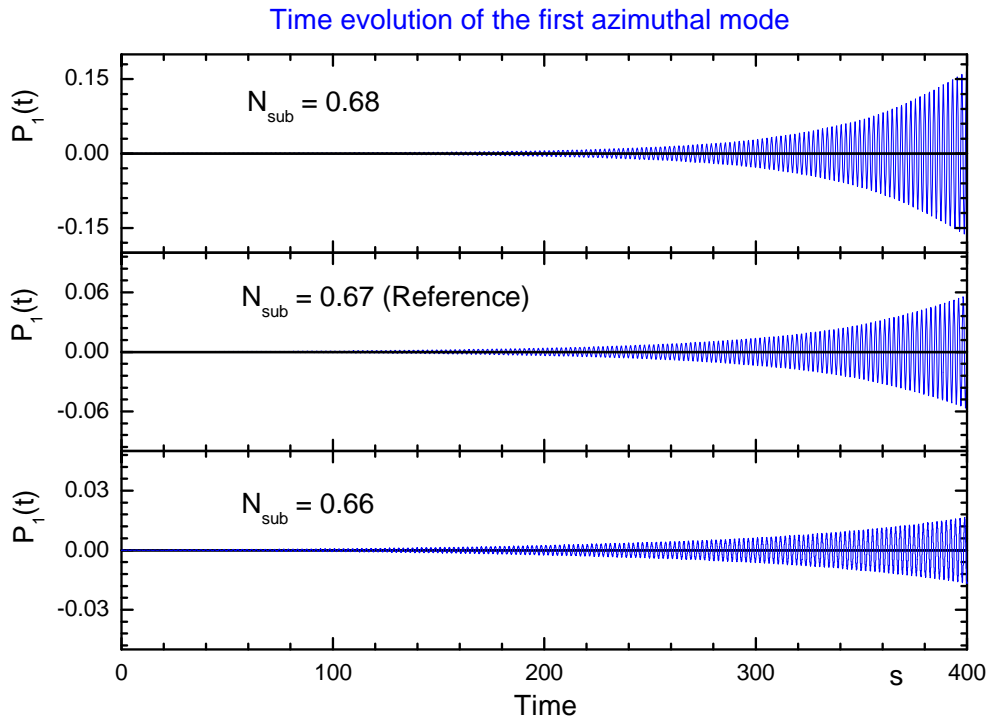


Figure 4.34: Time evolution of the first azimuthal mode for different core inlet subcoolings.

As can be seen, the prediction of the system code RAMONA5 can be verified qualitatively by the simplified BWR model.

4.4.2 Variation of the steady state external pressure drop

The effect of the steady state external pressure drop on the stability behaviour is considered in this section. To this end, RAMONA5 and ROM analyses were performed, where the steady state external pressure drop was varied in small steps. For each iteration step, the transient behaviour was investigated. In the scope of the RAMONA5 analysis, the core inlet mass flow was varied instead of DP_{ext} (the core inlet mass flow is proportional to DP_{ext}) because DP_{ext} cannot be varied directly in RAMONA5.

4.4.2.1 RAMONA results

In the framework of the present RAMONA5 investigation the core inlet mass flow was varied about $\pm 5\%$. In Table 4.2 the core inlet mass flows and the corresponding steady state external pressure drops (steady state RAMONA5 results) for which the transient behaviour was analysed are presented.

Table 4.2: Core inlet mass flow and the corresponding steady state external pressure drop

\dot{m}_{tot} (kg/s)	DP_{ext}^* ($10^4 Pa$)	$DP_{ext} = \frac{DP_{ext}^*}{\rho_f^* V_0^*}$
3870.00	7.1075	162.42
3970.00	7.2470	165.60
4070.12 (reference)	7.3870	168.82
4105.00	7.4358	169.90
4120.00	7.4570	170.40
4140.00	7.4850	171.00
4170.00	7.5268	172.00
4270.00	7.6665	175.00

The results of the RAMONA5 investigation have shown, the lower the core inlet mass flow the more unstable the system is. For $\dot{m}_{tot} = 3870 kg/s$ the increasing rate of the oscillation amplitudes are significant larger than the increasing rate for $\dot{m}_{tot} = 3970 kg/s$ or for $\dot{m}_{tot} = 4070 kg/s$ (reference). On the other hand, if the critical mass flow (corresponds to the stability boundary) which divides the stable region from the unstable one, is passed, the system becomes more stable, when the core inlet mass flow will be increased. For example, for $\dot{m}_{tot} = 4270 kg/s$ (+5%) the system is stable (oscillation amplitudes are decaying), while for $\dot{m}_{tot} = 4170 kg/s$ the system is

still unstable (oscillation amplitudes are increasing with time). Hence, the stability boundary could be located between these both values.

Time evolution of the LPRM signals

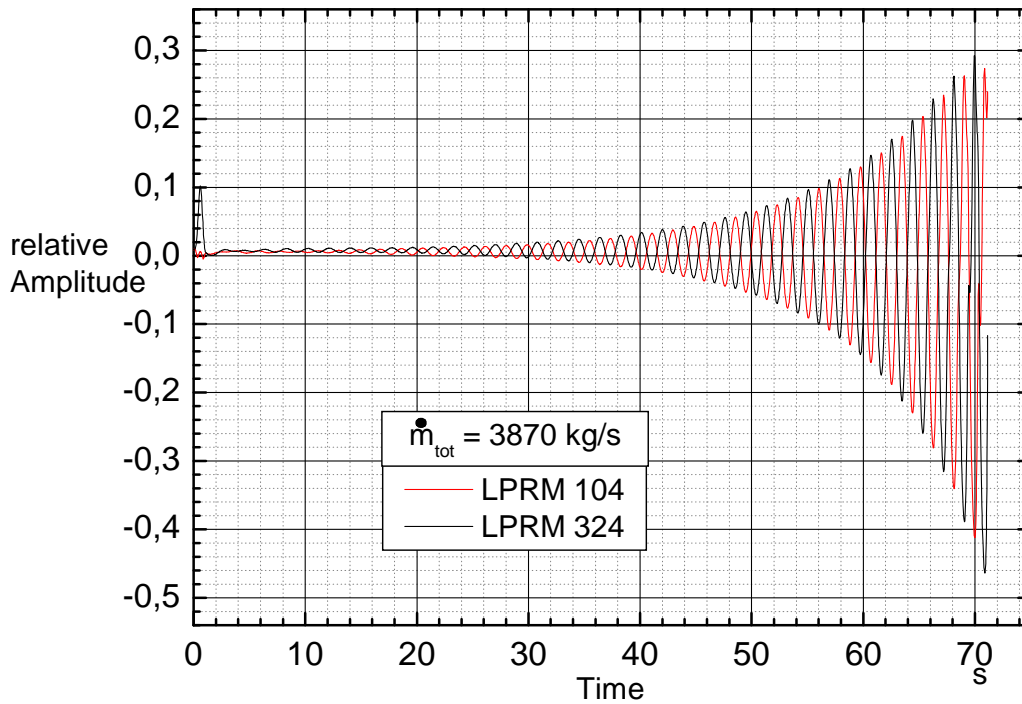


Figure 4.35: Signals (relative amplitudes) of LPRM 10 and 32 in the fourth level respectively. The calculation was interrupted after about 70 s. (KKL)

Time evolution of the LPRM signals

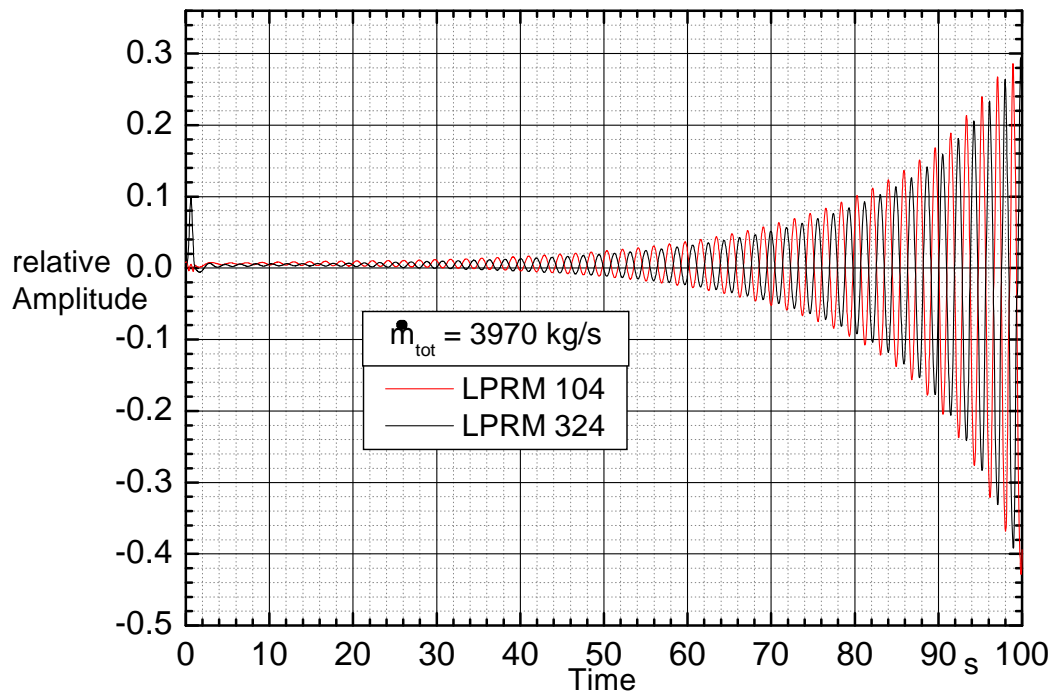


Figure 4.36: Signals (relative amplitudes) of LPRM 10 and 32 in the fourth level respectively. It can be seen, that the increasing rate of the foregoing figure is larger then in the present one. (KKL)

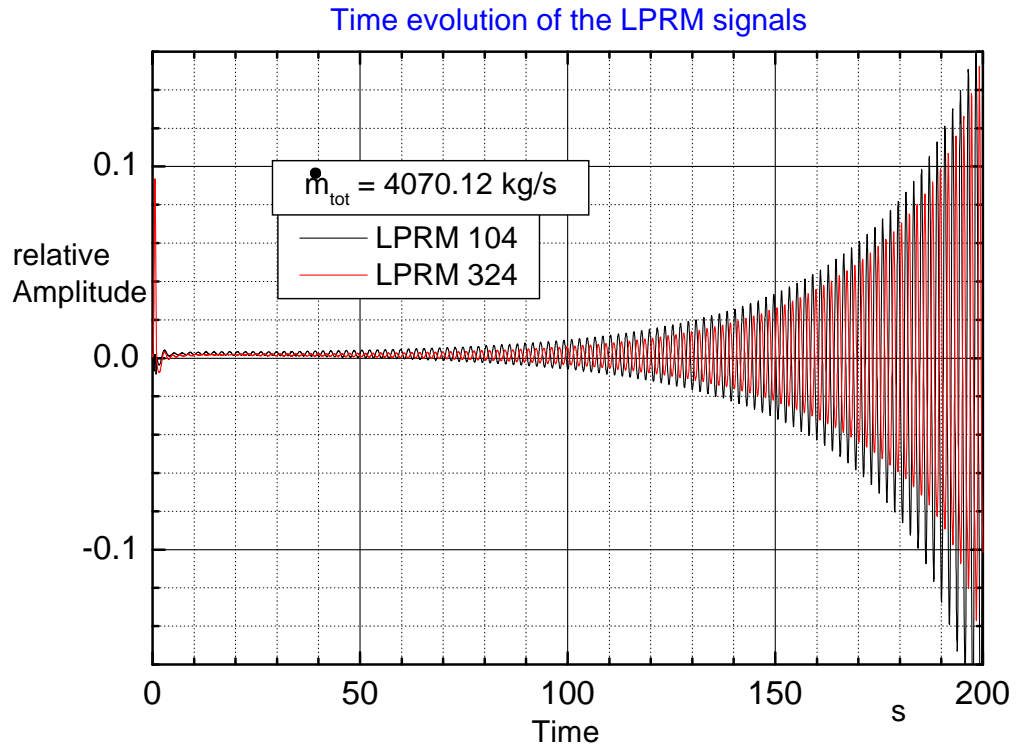


Figure 4.37: Signals (relative amplitudes) of LPRM 10 and 32 in the fourth level respectively. (KKLc7_rec4-OP)

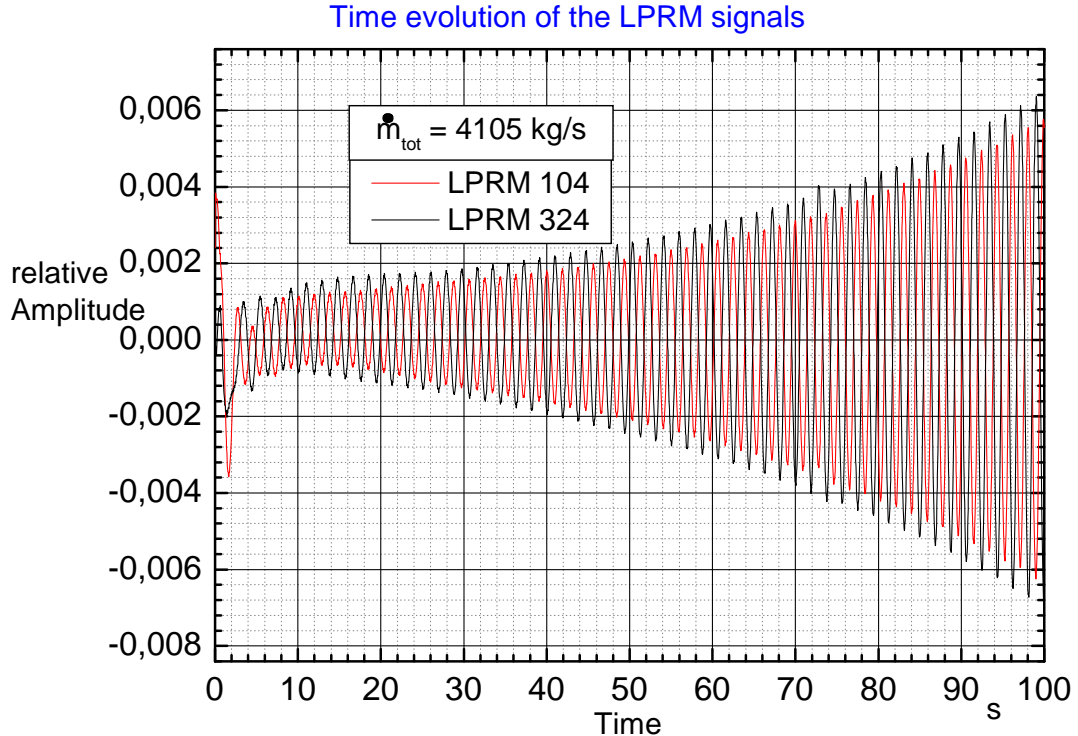


Figure 4.38: Signals (relative amplitudes) of LPRM 10 and 32 in the fourth level respectively. (KKL)

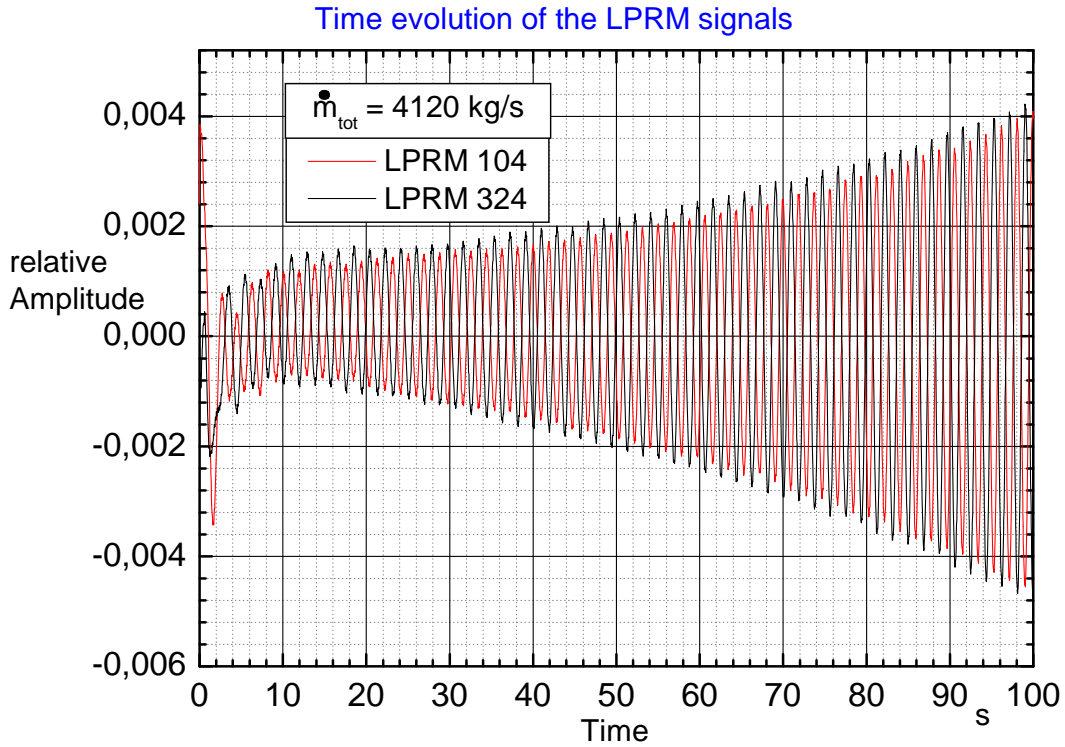


Figure 4.39: Signals (relative amplitudes) of LPRM 10 and 32 in the fourth level respectively. (KKL)

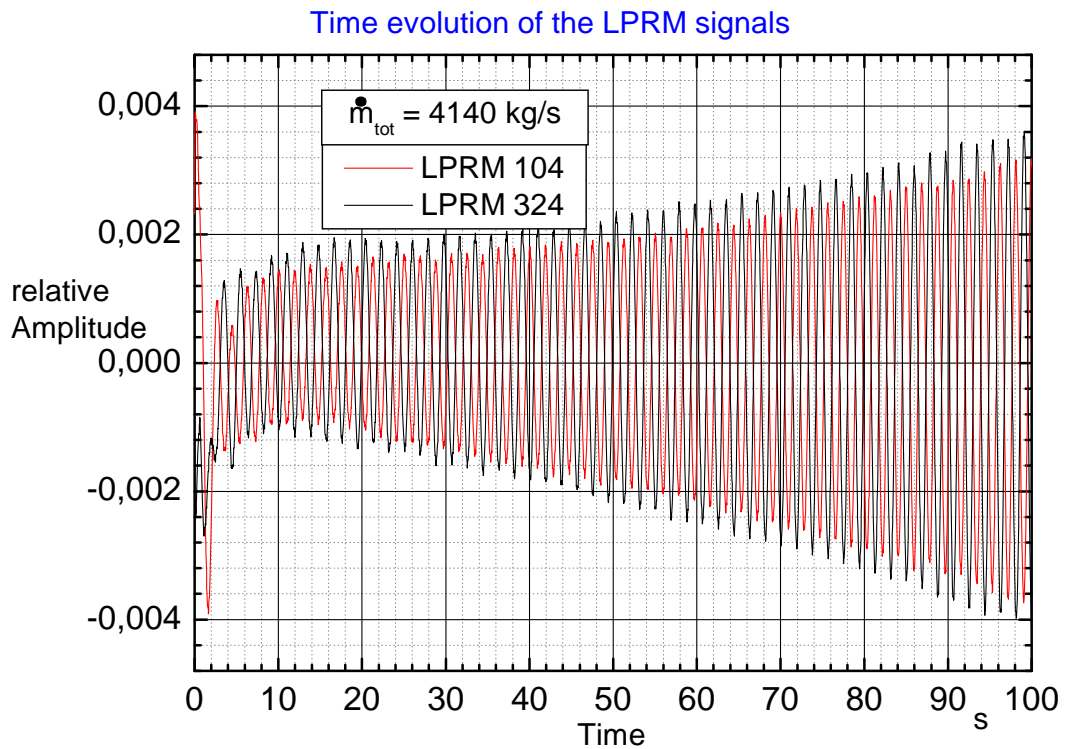


Figure 4.40: Signals (relative amplitudes) of LPRM 10 and 32 in the fourth level respectively. (KKL)

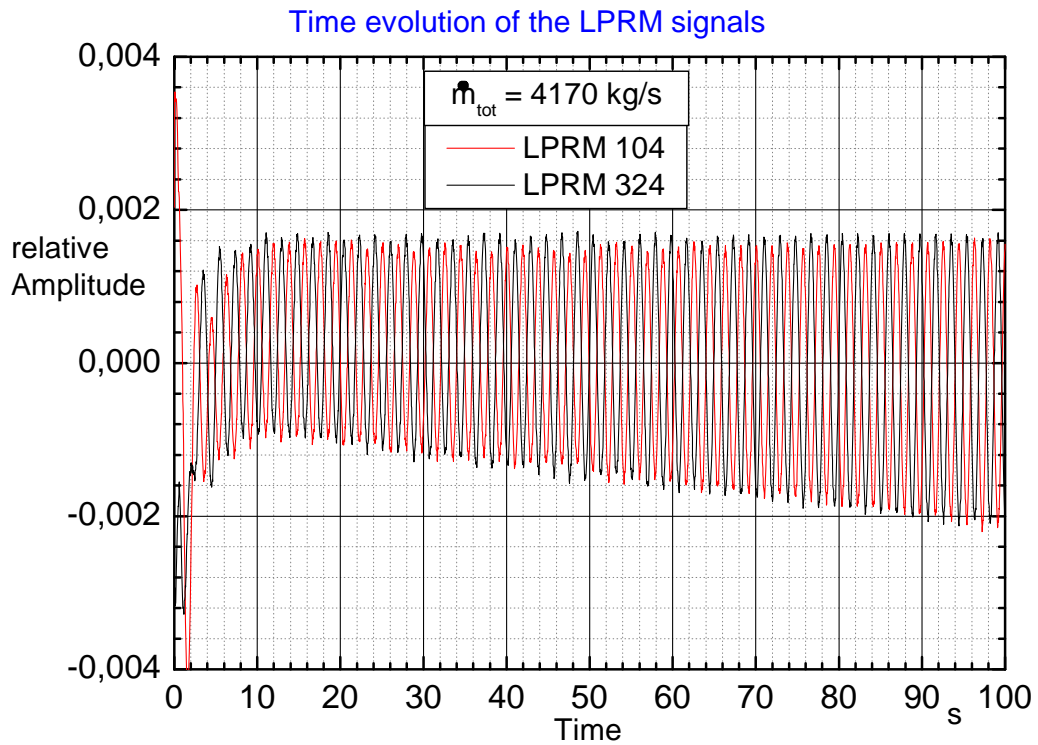


Figure 4.41: Signals (relative amplitudes) of LPRM 10 and 32 in the fourth level respectively. (KKL)

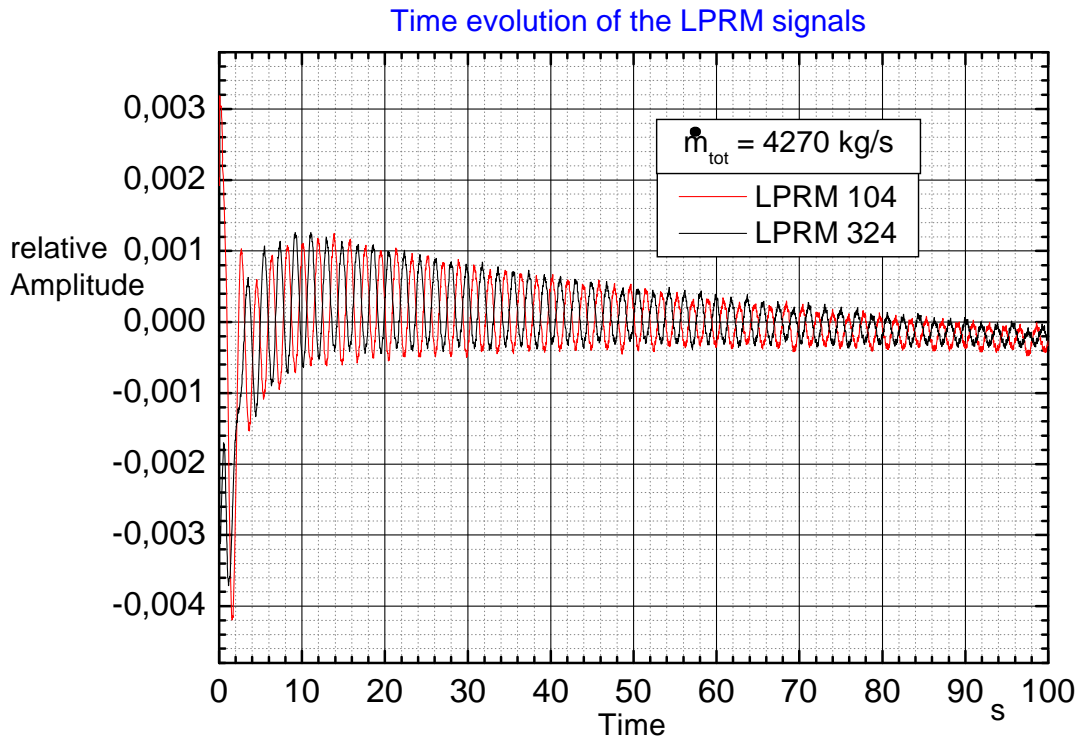


Figure 4.42: Signals (relative amplitudes) of LPRM 10 and 32 in the fourth level respectively. For this core inlet mass flow, the system is stable. (KKL)

4.4.2.2 ROM results

In the scope of this analysis the steady state external pressure DP_{ext} drop was varied, which corresponds to a mass flow variation.

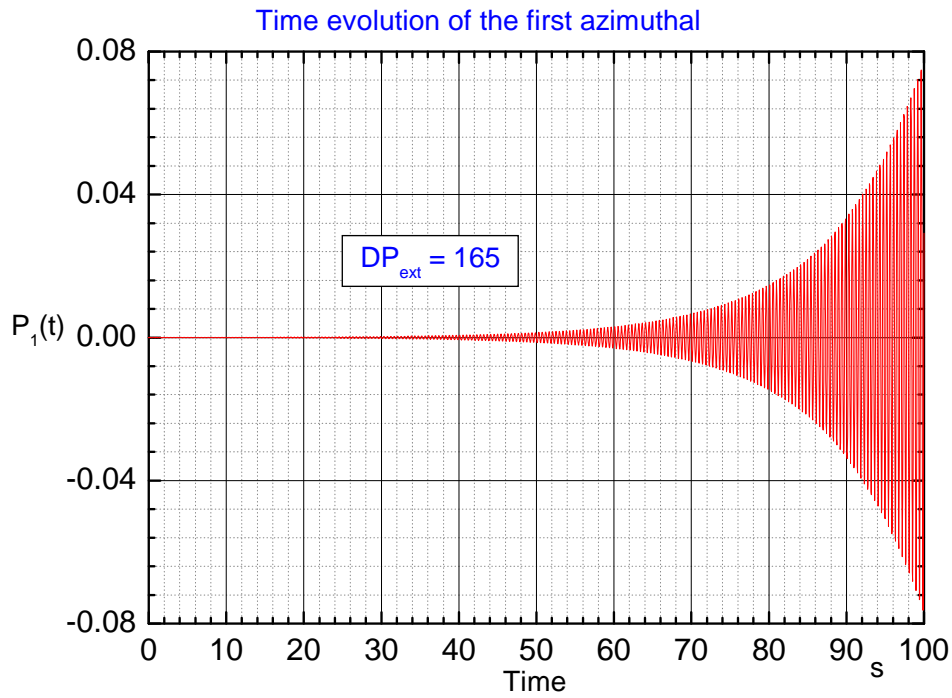


Figure 4.43: Time evolution of the first azimuthal mode.

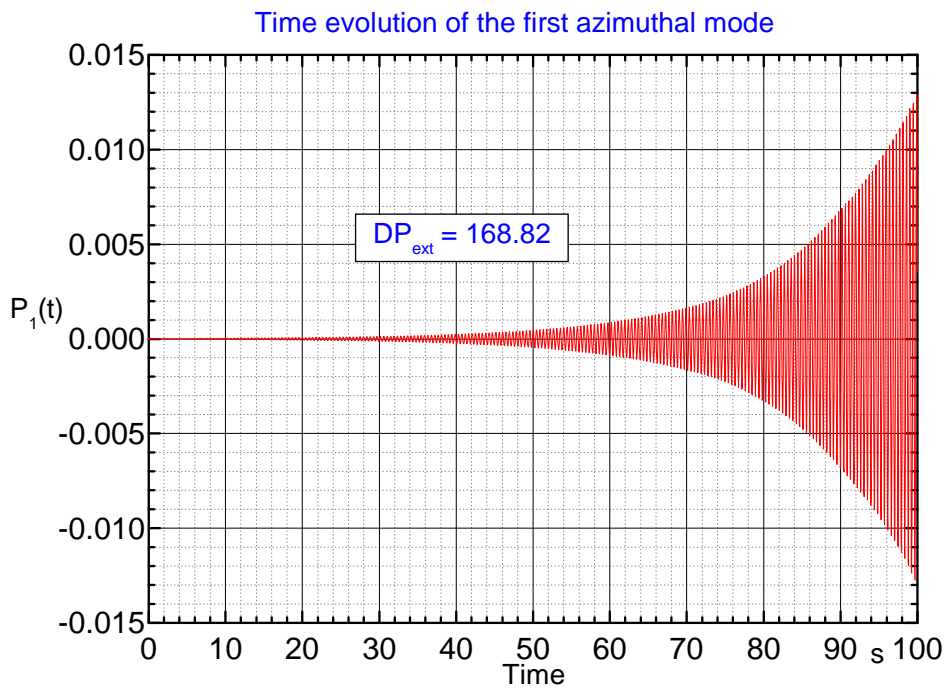


Figure 4.44: Time evolution of the first azimuthal mode.

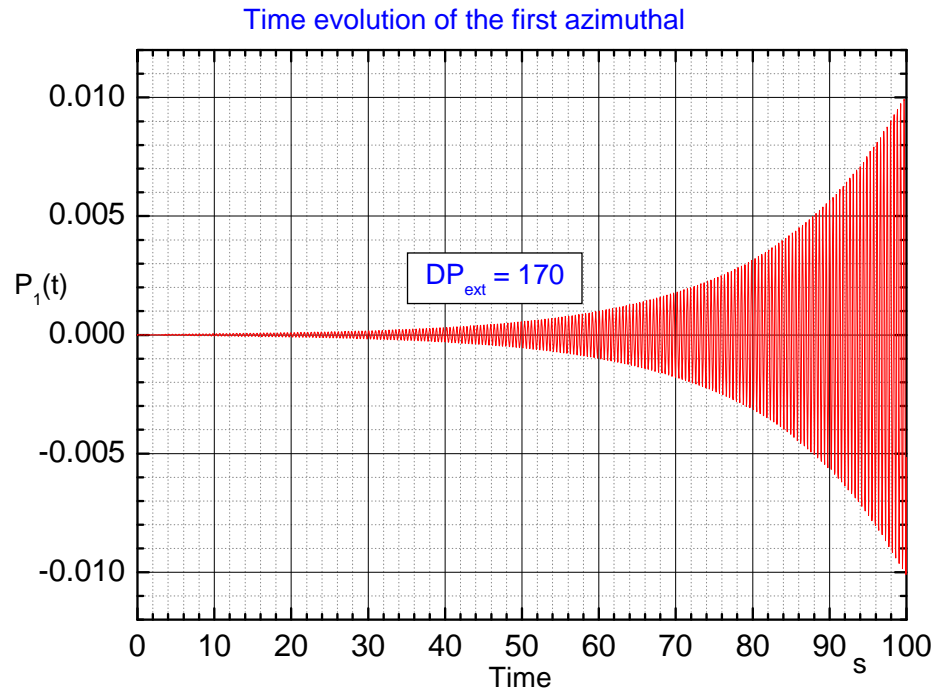


Figure 4.45: Time evolution of the first azimuthal mode. (KKL)

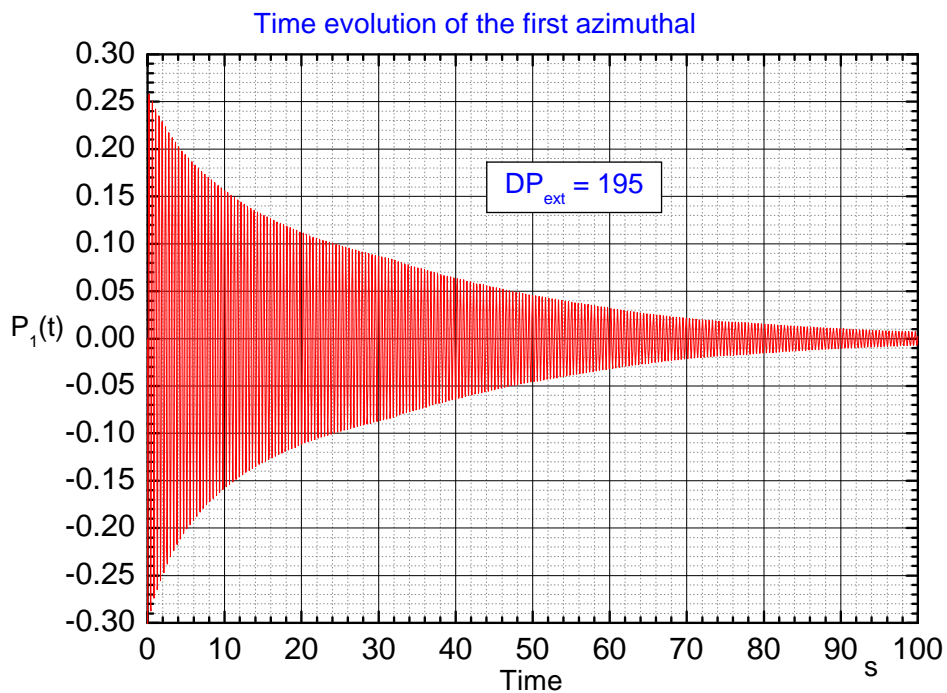


Figure 4.46: Time evolution of the first azimuthal mode. This OP is stable. (KKL)

The ROM analysis has shown, the lower DP_{ext} the more unstable the system is. Thereby the stability boundary could be located between $DP_{ext} = 170$ and $DP_{ext} = 195$.

4.4.3 Conclusion

To summarize, the TUD-ROM can reproduce the stability behaviour, predicted by RAMONA5, in the close neighbourhood of the reference operational point. The TUD-ROM and RAMONA5 predict the following behaviour:

- the higher the core inlet subcooling the more unstable the system is
- the lower the mass flow the more unstable the system is

It can be concluded that the reference OP is located close to the stability boundary. On the one hand the system becomes stable when the core inlet subcooling will be decreased about -5% and on the other hand the system becomes stable when the core inlet mass flow will be increased about +5%. As a final conclusion, the dependence of the BWR stability behaviour on variation of the core inlet subcooling and the steady state external pressure drop has shown that the results of RAMONA5 and ROM are consistent. The location of the reference OP respect to the stability boundary can also be simulated correctly by the TUD-ROM (see diagram on the right hand side of Figure 1.3).

4.5 Global nonlinear stability analysis

Previous ROM analyses have shown that the bifurcation analyses using BIFDD and the numerical integration method provides (locally in the origin of the dynamical system in the vicinity of the control parameter $\gamma_{k,c}$ whereby index k is ignored in the following discussion) consistent results. Further analyses at the reference OP and its neighbourhood, whereby numerical integration is carried out for a time period of 800 s revealed the existence of stable limit cycles (global consideration). The result of the time integration at the reference OP using the numerical integration code is shown in Figure 4.47.

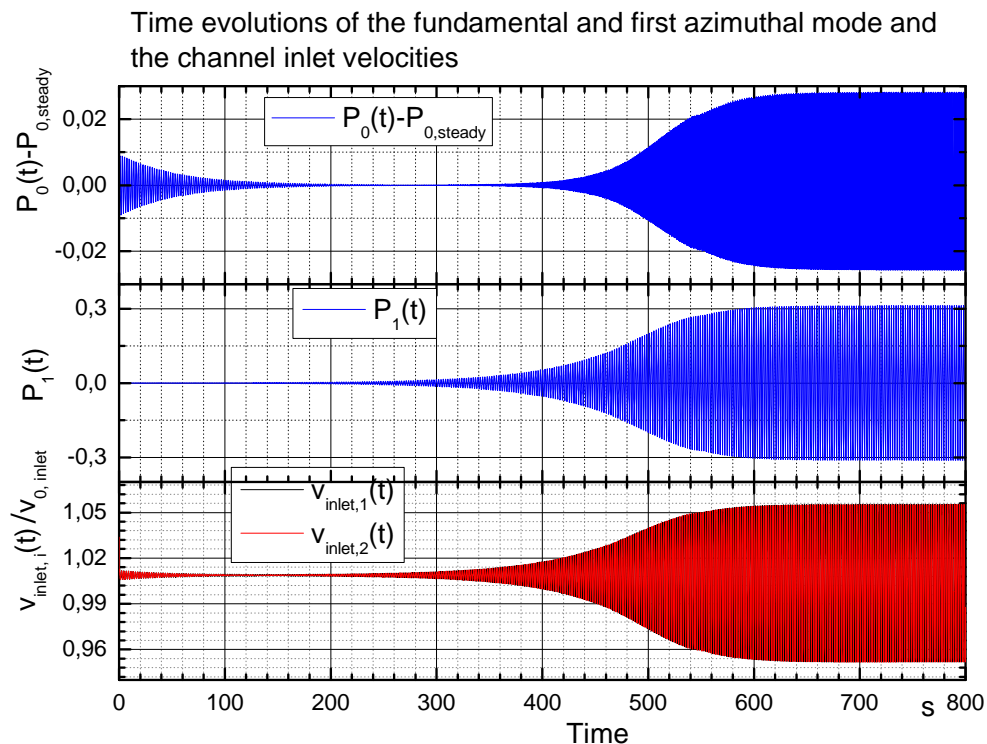


Figure 4.47: Result of the numerical integration at the reference OP where a long time integration is carried out (reference OP of KKLc7rec4).

The (cursory) conclusion is: The existence of a stable limit cycle in the linear unstable region is inconsistent with the result of the bifurcation analysis which delivers subcritical Hopf bifurcations. Hence, unstable limit cycles are predicted in the linear stable region for this analysis case. In order to understand this behaviour, more in depth considerations are necessary.

The above analysis reveals that the system behaviour cannot be examined only by local considerations such as semi-analytical bifurcation analysis using BIFDD. The coexistence of a subcritical bifurcation point (where an unstable limit cycle is born) and stable limit cycles in the linear unstable region could be a unique indicator for a possible existence of global bifurcation. In contrast to the Hopf bifurcation, global bifurcations involve large regions of the phase space rather than just the neighbourhood of a singular fixed point. Thus, in the scope of the present work, the post-

bifurcation state can only be determined through numerical integration of the ROM equations. For this purpose, the amplitudes of the limit cycles vs. the core inlet subcooling will be determined by numerical integration. Thereby, all the other parameters are fixed. The results are plotted in Figure 4.48 and Figure 4.49. The diagram shown in these figures is also known as bifurcation diagram. In particular, the global behaviour in the close neighbourhood of the stability boundary will be analysed.

The subcooling number N_{sub} is varied between 0.9 and 0.6 and the stable limit cycle amplitudes of the first azimuthal mode $A(P_1)$ are determined. Table 4.3, Figure 4.48 and Figure 4.49 summarises results of this analysis.

Table 4.3: This table summarises the limit cycle amplitudes $A(P_1)$ for different core inlet subcoolings.

N_{sub}	$A(P_1)$
0.9	0.707
0.8	0.585
0.75	0.49688
0.7	0.3845
0.67	0.29038
0.64	0.14917
0.639	0.148
0.638	0.143
0.637	0.135
0.636	0.129
0.635	0.11076
0.634	0.096
0.633	0.087
0.6325	0.081
0.631	0.06
0.63	0.049

The results show, that limit cycle amplitudes $A(P_1)$ decreases with decreasing core inlet subcooling. Below the critical value $N_{sub,c} \approx 0.63547$ (the Hopf conditions are fulfilled at $N_{sub,c}$) stable limit cycles still exist (see Figure 4.49). This means, **stable and unstable limit cycles** coexist in the linear stable region. The coexistence of stable and unstable limit cycles for $N_{sub} < N_{sub,c}$ is verified by numerical integration for $N_{sub} = 0.632$ by imposing different perturbation amplitudes on the system. A sufficient small perturbation leads to a stable behaviour. But when a sufficient large perturba-

tion is imposed on the system, the state variables are attracted by the limit cycle. This is presented in Figure 4.50.

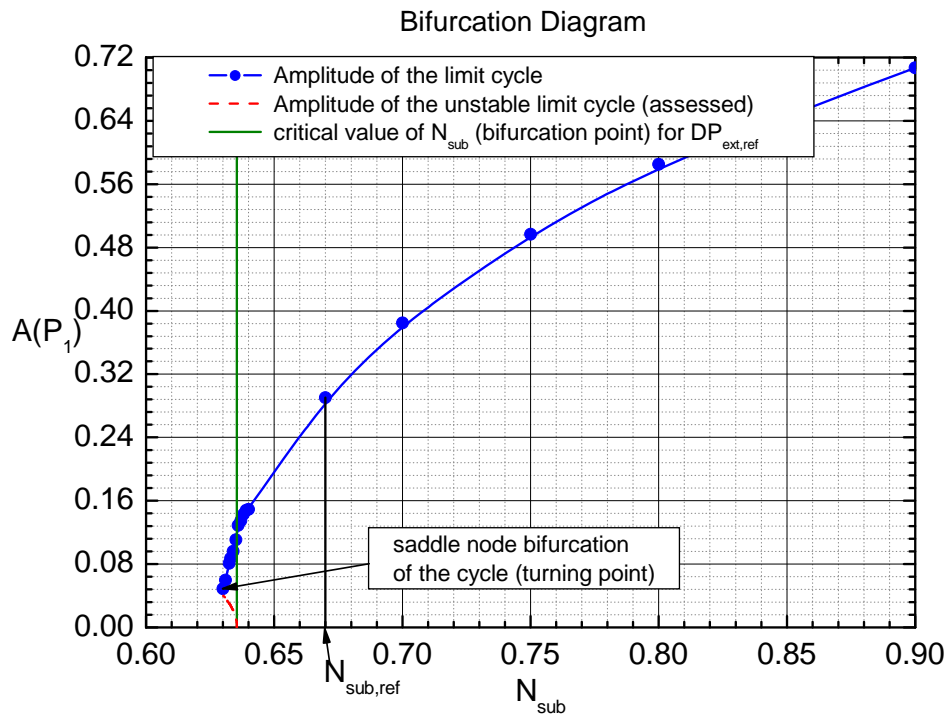


Figure 4.48: The results of the numerical integration are plotted as bifurcation diagram, where N_{sub} is the bifurcation parameter and $DP_{ext} = DP_{ext,ref}$.

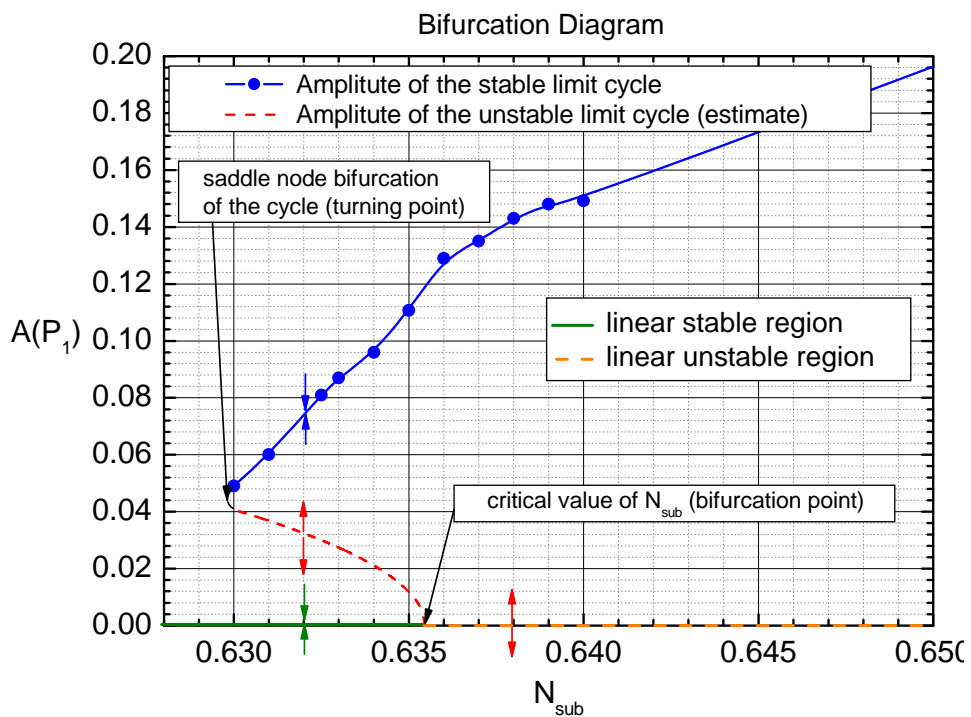


Figure 4.49: ("Zoom in" of Figure 4.48) The function of the amplitudes of the unstable limit cycle is an assessment only, not a calculated one.

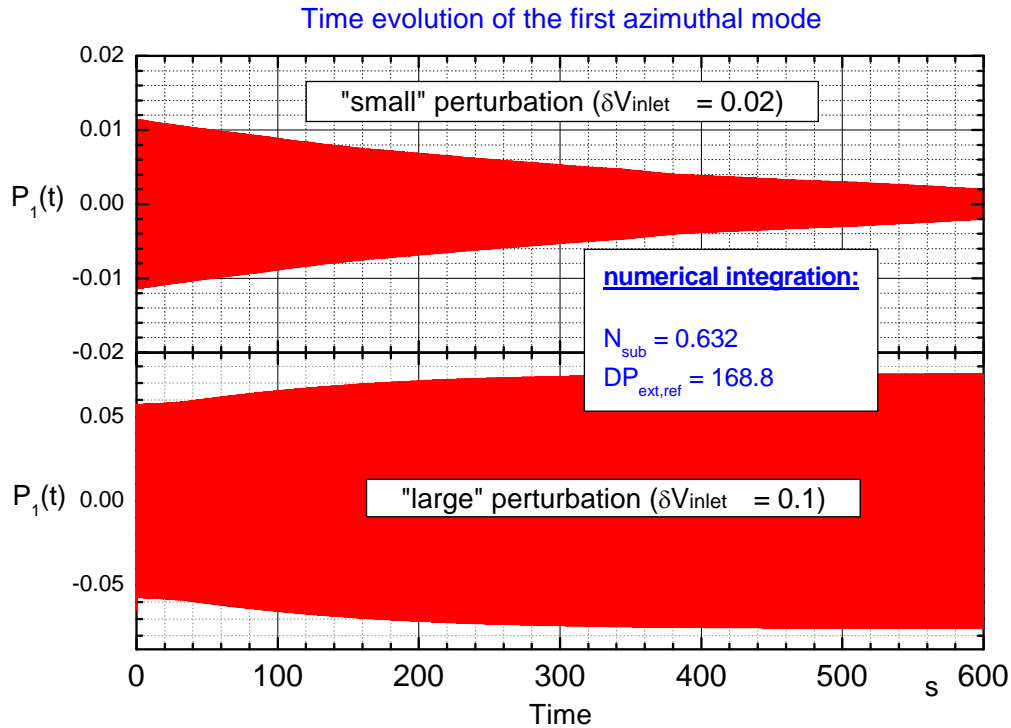


Figure 4.50: This figure shows the results of numerical integration for $N_{sub} = 0.632$ and $DP_{ext} = DP_{ext,ref}$, where a sufficient small $\delta v_{inlet} = 0.02$ and large $\delta v_{inlet} = 0.1$ perturbation is imposed on the system. When a small perturbation is imposed on the system, the state variables are returning to the steady state solution (origin of the dynamical system). When a large perturbation is imposed on the system, the state variables are attracted by the limit cycle.

The amplitudes of the unstable limit cycle correspond to the boundary which separates the basin of attraction of the singular fixed point and of the stable limit cycle.

The analysis has shown that stable and unstable limit cycles do not exist for core inlet subcooling less than $N_{sub} < 0.63$. Hence, there is a critical core inlet subcooling $N_{sub,t}$, where the two limit cycles coalesce and annihilate. Due to (numerical) convergence problems of numerical integration, $N_{sub,t}$ cannot be calculated exactly. The estimated value of $N_{sub,t}$ is $N_{sub,t} \approx 0.63$. From this result, it can be concluded that in $N_{sub,t}$ there is a saddle-node bifurcation of a cycle. This bifurcation type belongs to the class of global bifurcations and is also referred to as turning point or fold bifurcation.

Theoretical example for a saddle-node bifurcation of a cycle

Before considering an example for a saddle-node bifurcation of a cycle, a general remark is given to normal forms. Normal forms of bifurcations are simplified system of equations that approximates the dynamics of the system in the vicinity of the bifurcation point. After the application of simplification techniques (such as the centre manifold reduction, where the n -dimensional system is reduced to a two-dimensional system, when the Hopf-conditions are fulfilled), the resulting equation system can be transformed into a specific normal form associated with this type of bifurcation. Hence, in order to understand the above phenomenon, it is sufficient to analysis the specific normal form of the bifurcation.

In the following, the normal form for a generic Hopf bifurcation of fixed points

$$\begin{aligned}\frac{dx}{dt} &= \dot{x} = \gamma x - \omega y + (ax - by)(x^2 + y^2) \\ \frac{dy}{dt} &= \dot{y} = \omega x + \gamma y + (bx + ay)(x^2 + y^2)\end{aligned}\quad (4.36)$$

is taken into account. This normal form is frequently discussed in many text books [17-20] and thus is not repeated in all details here. The equation system (4.36) is extended (by higher order terms) in such a way that the resulting system becomes

$$\begin{aligned}\frac{dx}{dt} &= \dot{x} = \gamma x - \omega y + (ax - by)(x^2 + y^2) - cx(x^2 + y^2)^2 \\ \frac{dy}{dt} &= \dot{y} = \omega x + \gamma y + (bx + ay)(x^2 + y^2) - cy(x^2 + y^2)^2\end{aligned}\quad (4.37)$$

In (4.37) γ with $\gamma \in \mathbb{R}$ is the control parameter, a , b and c are coefficients and ω is the constant angular frequency. In the first step, the eigenvalues of the Jacobian matrix

$$J(\gamma) = \begin{bmatrix} \frac{d\dot{x}}{dx} & \frac{d\dot{x}}{dy} \\ \frac{d\dot{y}}{dx} & \frac{d\dot{y}}{dy} \end{bmatrix}\quad (4.38)$$

are calculated. The Jacobian matrix elements of (4.37) are

$$\begin{aligned}\frac{d\dot{x}}{dx} &= \gamma + a(x^2 + y^2) + 2x(ax - by) - c(x^2 + y^2)^2 - 4cx^2(x^2 + y^2) \\ \frac{d\dot{x}}{dy} &= -\omega - b(x^2 + y^2) + 2y(ax - by) - 4cxy(x^2 + y^2) \\ \frac{d\dot{y}}{dx} &= \omega + b(x^2 + y^2) + 2x(ax + by) - 4cxy(x^2 + y^2) \\ \frac{d\dot{y}}{dy} &= \gamma + a(x^2 + y^2) + 2y(ax + by) - c(x^2 + y^2)^2 - 4cy^2(x^2 + y^2)\end{aligned}\quad (4.39)$$

In the origin ($x = 0, y = 0$) the Jacobian matrix of (4.37) is reduced to

$$J = \begin{bmatrix} \gamma & -\omega \\ \omega & \gamma \end{bmatrix} \quad (4.40)$$

and the corresponding eigenvalues are $\lambda_{1/2} = \gamma \pm i\omega$. This result is equal to that one of the system (4.36). Furthermore, the third Hopf-condition

$$\frac{d\lambda_{1/2}}{d\gamma} \neq 0 \quad \text{with} \quad \frac{d\lambda_{1/2}}{d\gamma} = 1 \quad (4.41)$$

is also fulfilled. Hence, the system (4.37) satisfies the Hopf conditions in the origin at $\gamma = \gamma_c = 0$.

In order to analyse the global characteristics of (4.37), this system is transformed into its polar form. To this end, the polar coordinates

$$\begin{aligned} x &= r \cos \theta \\ y &= r \sin \theta \end{aligned} \quad (4.42)$$

are introduced and substituted in (4.37). The resulting equation system can be expressed as

$$\dot{\vec{X}} = F(\vec{X}, \gamma) = \begin{pmatrix} \dot{r} \\ \dot{\theta} \end{pmatrix} = \begin{pmatrix} \gamma r + ar^3 - cr^5 \\ \omega + br^2 \end{pmatrix}. \quad (4.43)$$

There is no loss in generality in assuming that the coefficients a and c are $a = c = 1$ and $b = 0$ (the case $a = c = -1$ and $b = 0$ is not considered for KKLc7_rec4 because in this case a supercritical Hopf bifurcation occurs in the origin). In this case, the equation system (4.43) can be rewritten as

$$\begin{pmatrix} \dot{r} \\ \dot{\theta} \end{pmatrix} = \begin{pmatrix} \gamma r + r^3 - r^5 \\ \omega \end{pmatrix} = \begin{pmatrix} F_r \\ F_\theta \end{pmatrix}, \quad (4.44)$$

where both state variables \dot{r} and $\dot{\theta}$ are now decoupled. The radial function F_r corresponds to the one-dimensional normal form of a subcritical pitchfork bifurcation of fixed points but with the difference that the higher order term $-r^5$ is included.

The global system behaviour of (4.44) only depends on the radial function F_r because function F_θ describes the rotation of the r -axis around the origin with the constant angular frequency ω . Hence, in order to examine the dynamics of (4.44), it is only necessary to evaluate the one dimensional problem $\dot{r} = F_r$. It will be demonstrated that the problem $\dot{r} = F_r$ undergoes a saddle-node bifurcation of fixed points. As a consequence, the two-dimensional system (4.44) undergoes a saddle-node bifurcation of cycles (global bifurcation).

The steady state solution of $\dot{r} = F_r$ is determined by solving

$$\dot{r} = 0 = F_r = \gamma r + r^3 - r^5 = r(\gamma + r^2 - r^4) \quad (4.45)$$

The solution r_0 of (4.45) can be written as

$$r_{01} = 0 \quad \forall \gamma \in \mathbb{R} \quad (4.46)$$

$$r_{02/03} = \pm \frac{1}{2} \sqrt{2 + 2\sqrt{1 + 4\gamma}} \quad \forall \gamma \in \left[-\frac{1}{4}, \dots, \infty\right) \quad (4.47)$$

$$r_{04/05} = \pm \frac{1}{2} \sqrt{2 - 2\sqrt{1 + 4\gamma}} \quad \forall \gamma \in \left[-\frac{1}{4}, \dots, 0\right] . \quad (4.48)$$

In order to examine the stability properties of the steady state solution r_0 , the first derivative of F_r respect to r (dF_r/dr) is determined for all γ . If $dF_r(r_0)/dr < 0$, the system is locally stable, and if $dF_r(r_0)/dr > 0$, the system is locally unstable. The result of dF_r/dr can be written as

$$\frac{dF_r}{dr} = \gamma + 3r^2 - 5r^4. \quad (4.49)$$

To evaluate the derivative dF_r/dr for all steady state solutions separately, the steady state solutions (4.46), (4.47) and (4.48) are substituted in (4.49) and the results are plotted in Figure 4.51. The steady state solutions r_0 vs γ are shown in Figure 4.52 (bifurcation diagram).

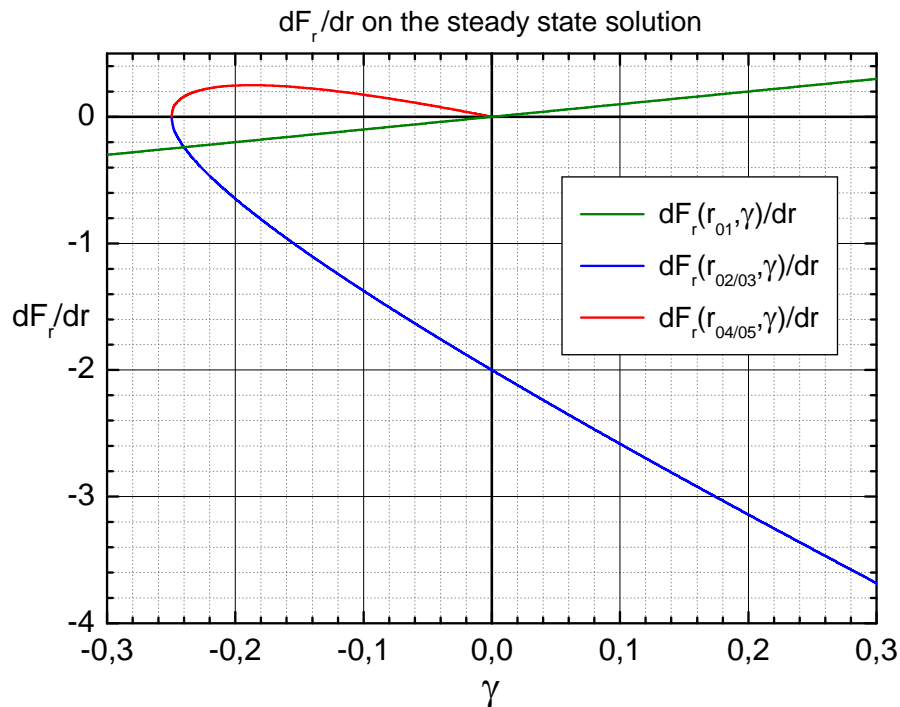


Figure 4.51: Evaluation of the derivative dF_r/dr .

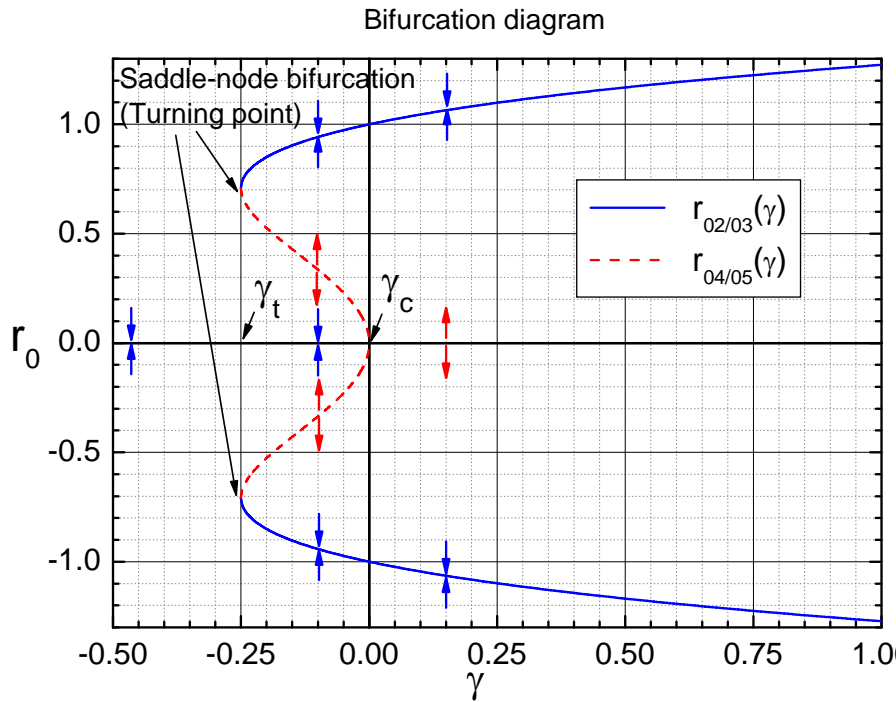


Figure 4.52: Bifurcation diagram

The steady state solution r_{01} exists for all $\gamma \in \mathbb{R}$ and is locally stable for $\gamma < 0$ and locally unstable for $\gamma > 0$. In the two-dimensional system (4.37), this solution corresponds to the fixed point solution, existing for all $\gamma \in \mathbb{R}$. The solutions $r_{02/03}$ only exist for $\gamma > -0.25$ and are locally stable in their domain because of $dF_r(r_{02/03})/dr < 0$. The solutions $r_{04/05}$ are only defined for $[-0.25 < \gamma < 0]$ and are locally unstable because $dF_r(r_{04/05})/dr > 0$. But at the saddle points $(\gamma_t = -0.25; r_{02} = r_{04} = 1/2 \cdot \sqrt{2})$ and $(\gamma_t = -0.25; r_{03} = r_{05} = -1/2 \cdot \sqrt{2})$, where $r_{02/03}$ and $r_{04/05}$ are coalescing and annihilating) the solutions $r_{02/03}$ and $r_{04/05}$ are neither locally stable nor locally unstable. As depicted in Figure 4.53 the solutions $r_{02/03}$ and $r_{04/05}$ corresponds to periodical solutions of the two-dimensional system (4.37). Note that, roughly speaking, $r_{02/03}$ and $r_{04/05}$ are rotating around the origin with ω .

To summarize, for small r the bifurcation diagram looks just like the subcritical pitchfork bifurcation case (occurring in equation $\dot{r} = \gamma r + r^3$ at $\gamma = \gamma_c = 0$): the origin is locally stable for $\gamma < 0$ and two backward-bending branches of unstable fixed points bifurcate from the origin when $\gamma = \gamma_c = 0$. But in contrast to the subcritical pitchfork bifurcation case, the unstable branches turn around and become stable at $\gamma = \gamma_t = 0$ where $\gamma_t < 0$. This behaviour is effected by the r^5 term in (4.44) (higher order terms in (4.37)). The stable branches $r_{02/03}$ exist for $\gamma > \gamma_t$.

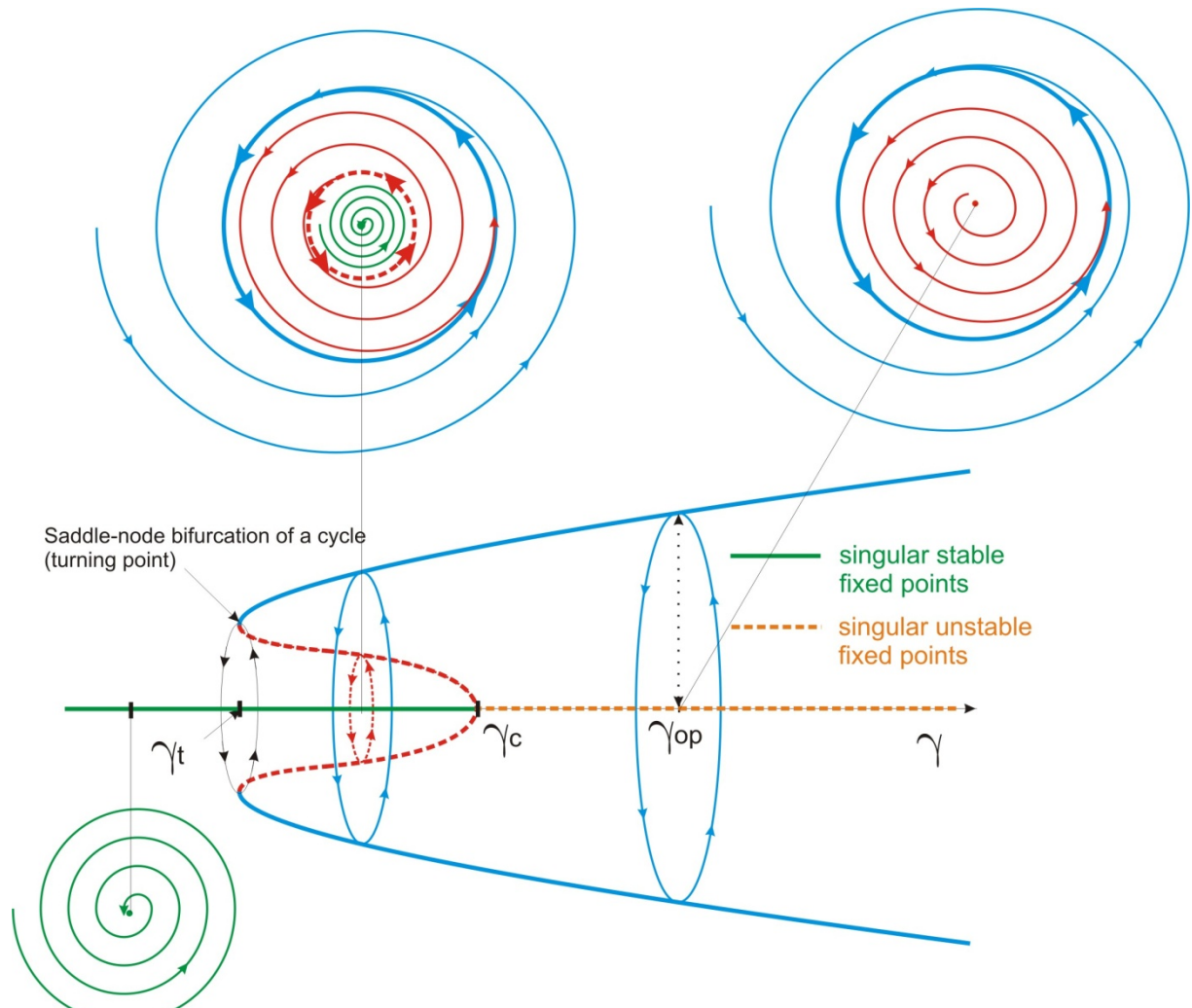


Figure 4.53: This figure depicts a bifurcation diagram of a saddle-node bifurcation of a cycle and the corresponding radial phase portraits.

In the above analysis, it was helpful to analyse only the one-dimensional (radial) system $\dot{r} = F_r$ of the two dimensional system (4.44). As demonstrated above, this system undergoes a saddle-node bifurcation of fixed points at $\gamma = \gamma_t = -1/4$, where a stable and an unstable branch of fixed points occur. Returning to the two-dimensional system (4.44), these fixed points correspond to circular limit cycles. The global behaviour of (4.37) is summarized in Figure 4.53 (there is depicted the bifurcation diagram and the corresponding radial phase portraits).

From the above analysis, the following conclusions can be made:

- 1) The bifurcation at $\gamma = \gamma_t = -1/4$ is a saddle-node bifurcation of a cycle. In this point, a stable and an unstable periodical solution (circular limit cycle) are born (“out the clear blue sky”). As depicted in Figure 4.53, the phase portrait is changing significantly when passing γ_t .
- 2) In the range $\gamma_t < \gamma < \gamma_c = 0$, two qualitatively different stable states coexist, namely the origin (fixed point solutions) and the stable limit cycle. Both states are separated by an unstable limit cycle (see phase portrait in Figure 4.53). In

other words, due to the saddle-node bifurcation at $\gamma = \gamma_t = -1/4$, a stable and an unstable limit cycle coexist with stable fixed points within the parameter range $\gamma_t < \gamma < \gamma_c$. One consequence is that the origin is stable to “small” perturbations, but not to “large” ones. In this sense the origin is locally stable, but not globally stable.

- 3) From the stability analysis point of view, a saddle-node bifurcation is operational safety significant, if the amplitude of the stable limit cycle is sufficient large. Supposing the system is in the state $r = 0$ (origin), and the control parameter γ is slowly increased. As long as $\gamma < \gamma_c$ the state remains at the origin. But at $\gamma = \gamma_c = 0$ the origin loses stability and thus the slightest “nudge” will cause the state to jump to the limit cycle. In this case, the state will start to oscillate when reaching $\gamma = \gamma_c = 0$ and the oscillations are growing as long as they will be attracted by the stable limit cycle. With further increase of γ , the state moves out along the limit cycle solution. But if γ is now reduced, the state remains on the stable limit cycle oscillation, even when γ is decreased below $\gamma_c = 0$. The system will return to the origin when the control parameter γ is reduced below γ_t . These characteristics (called hysteresis) can be considered as a loss of reversibility as the control parameter is varied.
- 4) The system behaviour of (4.37) near the origin is similar to the behaviour of a system which undergoes a subcritical Hopf bifurcation at $\gamma = \gamma_c$. In particular, in the origin the Jacobian matrix elements of (4.37) are equal to that one of (4.36). Hence, the corresponding eigenvalues of both systems are equal too.

Summary

Previous ROM analyses for KKLc7_rec4 (local nonlinear stability analysis) have shown that the bifurcation analyses and the numerical integration method provide consistent results only in the Hopf bifurcation points γ_c (local consistency) and their close neighbourhoods. In order to study the global character of the nonlinear system, numerical integration is necessary. For this purpose, numerical integration of the ROM equation system have been carried out, where N_{sub} was varied in the range $[0.62, \dots, 0.9]$. The analyses have shown that in the range $N_{sub,t} < N_{sub} < 0.9$ ($N_{sub,t} = 0.63$) stable limit cycles exist, even though the bifurcation analysis predicts only unstable limit cycles for $N_{sub} < N_{sub,c}$ ($N_{sub,c}$ is the critical bifurcation parameter, for which the Hopf conditions are fulfilled). Hence, at the reference OP the state variables will also be attracted by the limit cycle. In addition to that, for $N_{sub} \in [N_{sub,t}, \dots, N_{sub,c}]$ with $N_{sub,t} < N_{sub,c}$ stable fixed point solution, unstable periodical solution and stable periodical solution coexist. Below $N_{sub,t}$, only stable fixed point solution exist.

One would think that the predictions of BIFDD and the results of the numerical integration are inconsistent. Note that, BIFDD is based on local methods. Thus the stability investigation using BIFDD is concentrated only in the origin of the system close to the critical parameter γ_c (see Figure 4.54).

In the scope of this section it was shown that the nonlinear stability behaviour predicted by the ROM for KKLc7_rec4 can be explained by the existence of a saddle-node bifurcation of cycles. The main (general) characteristics of a system which experienced a saddle-node bifurcation of cycles are deduced from the normal form of this bifurcation type. It was shown that in the origin ($r=0$) of a dynamical system which undergoes a saddle-node bifurcation at γ_t , the Hopf conditions are (locally) fulfilled at $\gamma = \gamma_c = 0$. This satisfies the local prediction of BIFDD for KKLc7_rec4. Furthermore, the coexistence of stable fixed point solution, unstable periodical solution and stable periodical solution for $\gamma_t < \gamma < \gamma_c$ can be explained. These characteristics are summarized in Figure 4.54.

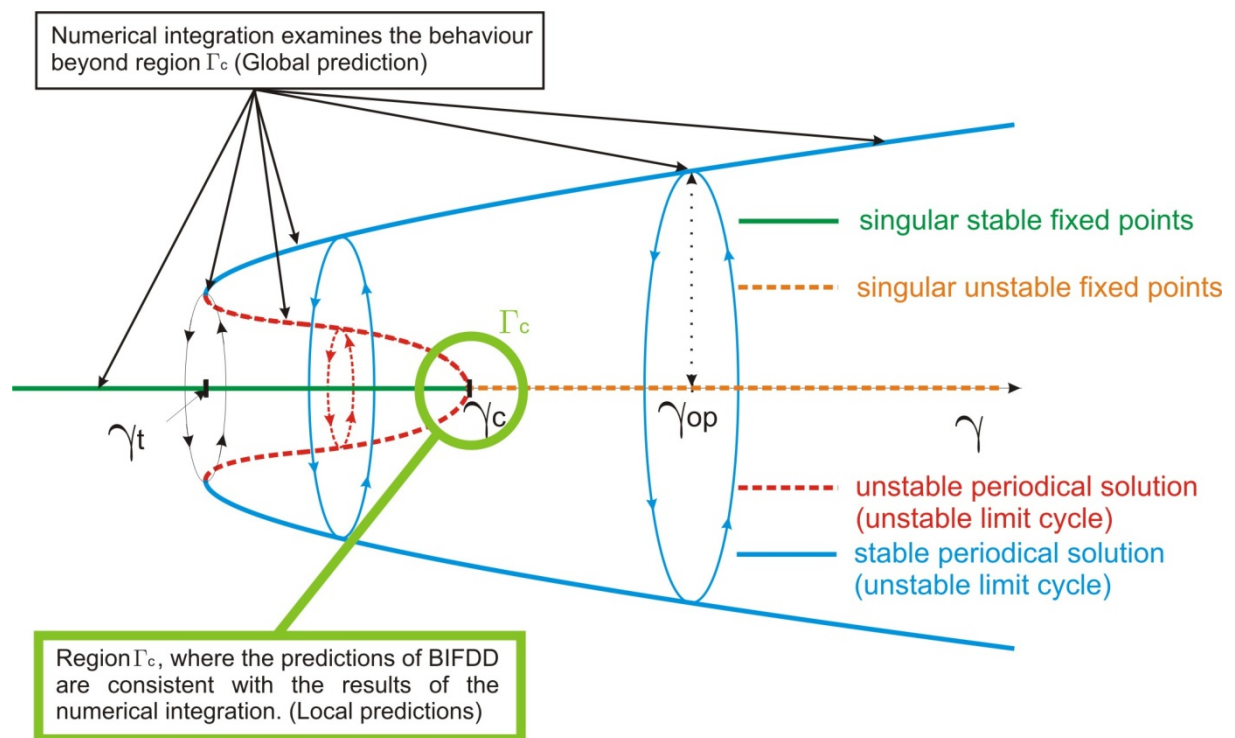


Figure 4.54: Summary of the main characteristics of a system, which undergoes a saddle-node bifurcation of cycles. The results of BIFDD are only valid locally in the close neighbourhood of the origin of the system close to γ_c (region Γ_c). The global character of the nonlinear system can only be examined by numerical integration.

As a final conclusion, the nonlinear behaviour of the ROM for the KKLc4_rec4 case fulfils the main characteristics of a system, which undergoes a saddle node bifurcation of cycles, where the coefficients a and c of (4.37) (or (4.43)) are positive.

4.6 Stability boundary in the $N_{sub} - DP_{ext}$ -parameter space and its relation to the $N_{sub} - N_{pch}$ -parameter space

This section is devoted to reveal the relation of the stability boundary, calculated in the $N_{sub} - DP_{ext}$ -parameter space, to the $N_{sub} - N_{pch}$ -parameter space. To this end, the analysis starts with a brief review of the meaning of the $N_{sub} - N_{pch}$ -parameter space. The $N_{sub} - N_{pch}$ -parameter space represents thermal hydraulic states within the heated flow channel [69]. When one or more system parameters are varied, the corresponding change of the thermal-hydraulic conditions of a BWR system can be visualized in this parameter space. In particular, in a BWR there is a functional dependence between N_{sub} and N_{pch} because of the coupling of the neutron kinetics, the fuel rod dynamics and the thermal-hydraulics. This dependence (between N_{sub} and N_{pch}) should be taken into account when the bifurcation analysis is carried out in the $N_{sub} - N_{pch}$ -parameter space.

This section is organized in three parts. In the first part, the physical meaning of the SB calculated in the $N_{sub} - N_{pch}$ -parameter space is discussed. In the second Part, the relation of the SB calculated in the $N_{sub} - DP_{ext}$ -parameter space to the SB calculated in the $N_{sub} - N_{pch}$ -parameter space is shown. The last part of this section is an extension of the second part. The ROM-input used for this analysis is close to that of KKLc7_rec4.

4.6.1 Part1:

The location of the reference OP in the $N_{sub} - N_{pch}$ -parameter space is presented in Figure 4.55. The diagonal line (where $N_{pch} = N_{sub}$) separates single phase states from two phase states.

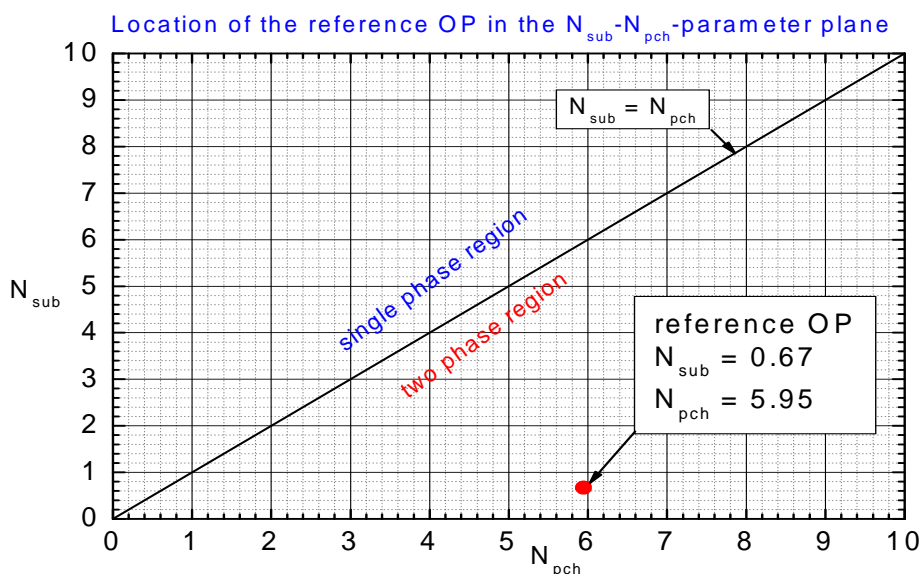


Figure 4.55: Location of the reference OP (KKL) in the $N_{sub} - N_{pch}$ -parameter plane.

As stated above, the phase change number is a function of the subcooling number $N_{pch} = N_{pch}(N_{sub})$ (coupled neutron kinetic – thermal-hydraulic system). This curve $N_{pch} = N_{pch}(N_{sub})$ (see Figure 4.56) describes the change of the thermal hydraulic state (of the reference OP in the $N_{sub} - N_{pch}$ -parameter plane) depending on N_{sub} while all the other parameters are kept constant. The curve $N_{pch}(N_{sub})$ was calculated by applying the numerical integration code. Thereby, steady state calculations were performed where N_{sub} was varied in small steps.

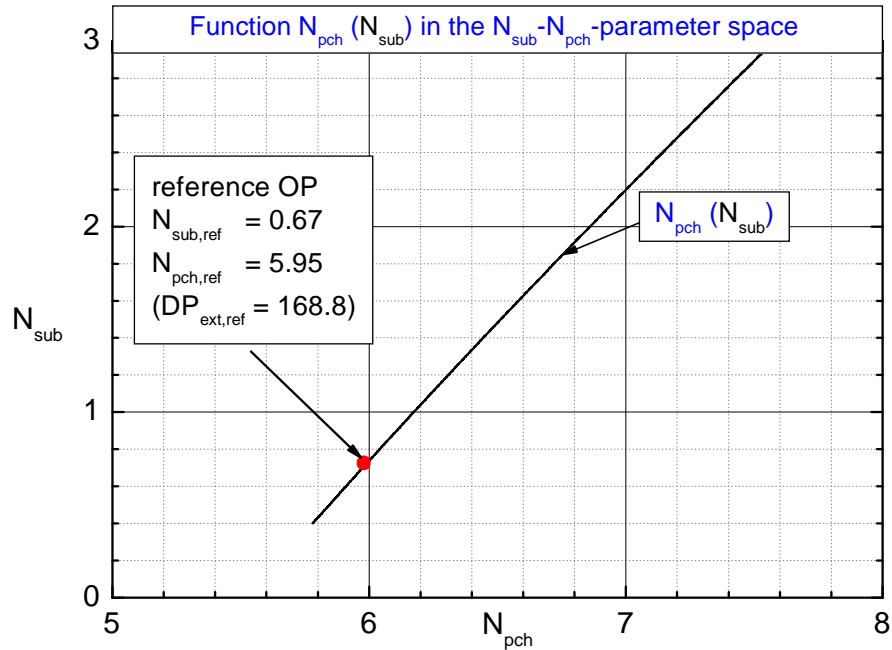


Figure 4.56: The curve $N_{pch}(N_{sub})$ in the $N_{sub} - N_{pch}$ -parameter plane.

Bifurcation analysis in the $N_{sub} - N_{pch}$ -parameter plane is conducted in the following. In Figure 4.57 are presented the stability boundary and the curve $N_{pch}(N_{sub})$.

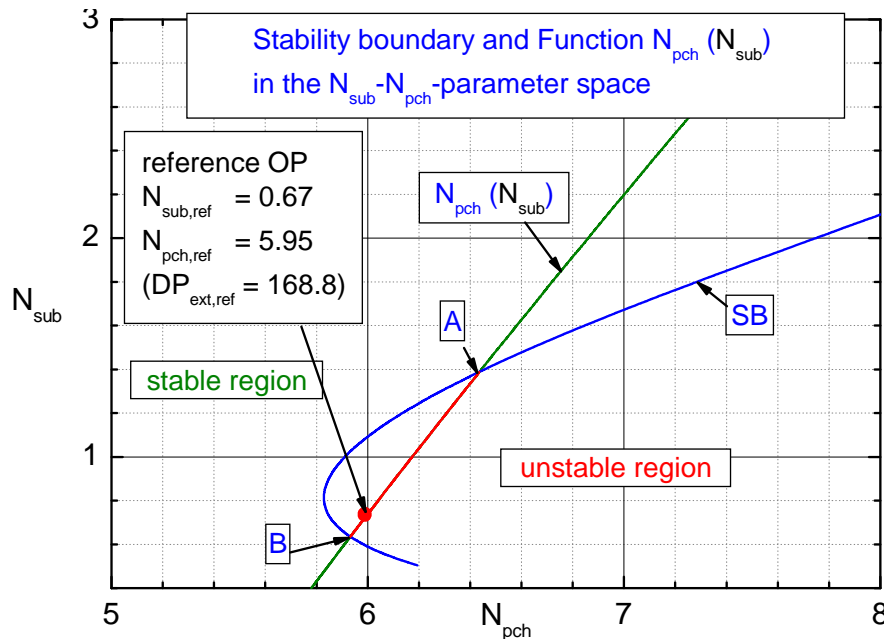


Figure 4.57: Result of the bifurcation analysis performed in the $N_{sub} - N_{pch}$ -parameter plane.

Note that, in the $N_{sub} - N_{pch}$ -parameter space, operational points only exist on the curve $N_{pch}(N_{sub})$ for a fixed parameter configuration of a BWR. Hence, the bifurcation analysis, performed in the $N_{sub} - N_{pch}$ -parameter space, provides information about the stability properties of fixed points located on the curve $N_{pch}(N_{sub})$ (for the nuclear coupled thermal-hydraulic system).

The results of the bifurcation analysis, presented in Figure 4.57, show that all operational points, located on the curve $N_{pch}(N_{sub})$ between A and B (red section), are unstable fixed points. All the other OPs which are located on $N_{pch}(N_{sub})$ are stable fixed points.

In the scope of this approach, the following conclusions are valid:

- The bifurcation analysis carried out in the $N_{sub} - N_{pch}$ -parameter space reveals the stability characteristics of all fixed points which are located on the curve $N_{pch}(N_{sub})$.
- In order to interpret the results of the bifurcation analysis performed in the $N_{sub} - N_{pch}$ -parameter space, the stability boundary should be plotted in conjunction with $N_{pch}(N_{sub})$. This means, the stability boundary plotted without $N_{pch}(N_{sub})$ makes no sense.

4.6.2 Part 2:

The same analysis is carried out for $DP_{ext} = 180$ ($DP_{ext,ref} = 168.8$). The results are plotted in Figure 4.58 and Figure 4.59. As can be seen, the variation of DP_{ext} causes a shift of $N_{pch}(N_{sub})$ and of the SB in N_{pch} -direction, respectively. Thereby, the shift has the same sign but the sensitivities regarding DP_{ext} -variations are different (is explained in detail in part 3 of this section).

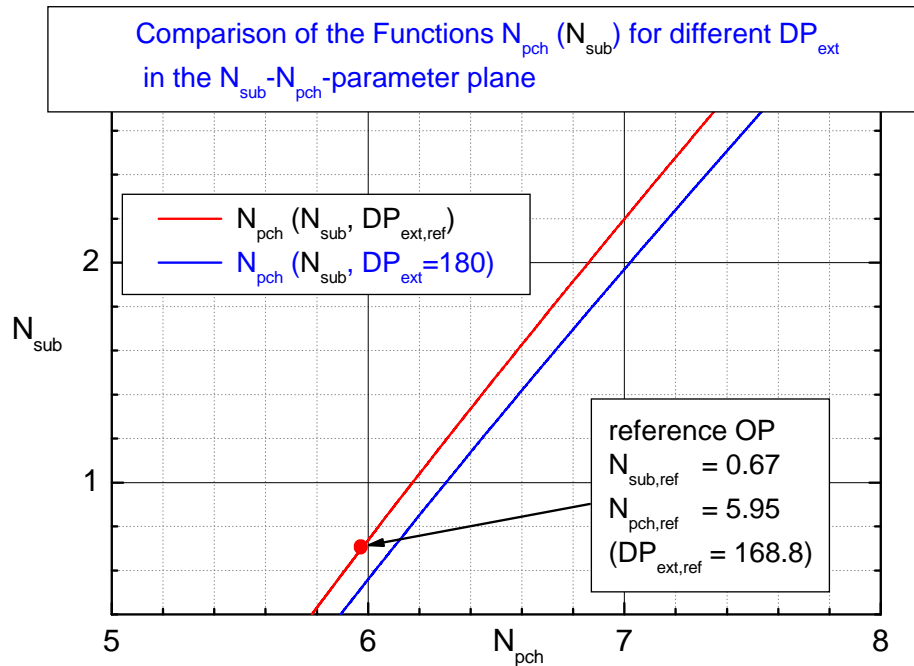


Figure 4.58: Comparison of the curves $N_{pch}(N_{sub})$ for two different external pressure drops, the reference pressure drop and $DP_{ext} = 180$.

In Figure 4.59 are shown the stability boundaries and their corresponding curves $N_{pch}^{DP_{ext,ref}}(N_{sub})$ and $N_{pch}^{DP_{ext}=180}(N_{sub})$. The SB (in the following referred to as $N_{pch}^{SB}(N_{sub})$) and the curve $N_{pch}(N_{sub})$ are moving in N_{pch} -direction, when DP_{ext} will be varied. The derivatives

$$\frac{d}{d DP_{ext}} N_{pch}(N_{sub}) \quad (4.50)$$

and

$$\frac{d}{d DP_{ext}} N_{pch}^{SB}(N_{sub}) \quad (4.51)$$

with

$$\frac{d}{d DP_{ext}} N_{pch}(N_{sub}) \neq \frac{d}{d DP_{ext}} N_{pch}^{SB}(N_{sub}) \quad (4.52)$$

represent the sensitivity of the curves $N_{pch}(N_{sub})$ and $N_{pch}^{SB}(N_{sub})$ regarding DP_{ext} variations. Relation (4.52) means, the number of unstable fixed points is changing, when DP_{ext} is varied. Roughly speaking, under DP_{ext} variation, the stability boundary

and function $N_{pch}(N_{sub})$ are moving with different “velocities” in the $N_{sub} - N_{pch}$ -parameter space. The change of the length of the red section corresponds to a change of the number of unstable fixed points.

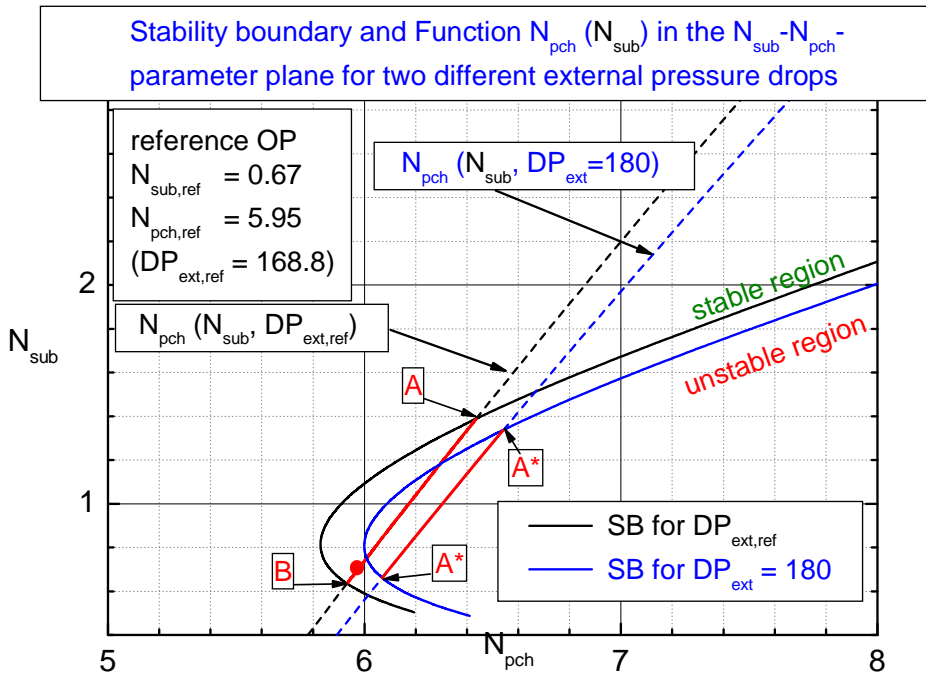


Figure 4.59: Comparison of the SB and the curve $N_{pch}(N_{sub})$ for two different external pressure drops, the reference pressure drop and $DP_{ext} = 180$.

Function $N_{pch}^{DP_{ext,ref}}(N_{sub})$ and $N_{pch}^{DP_{ext}=180}(N_{sub})$ can be transformed into the $N_{sub} - DP_{ext}$ -parameter space (Figure 4.60).

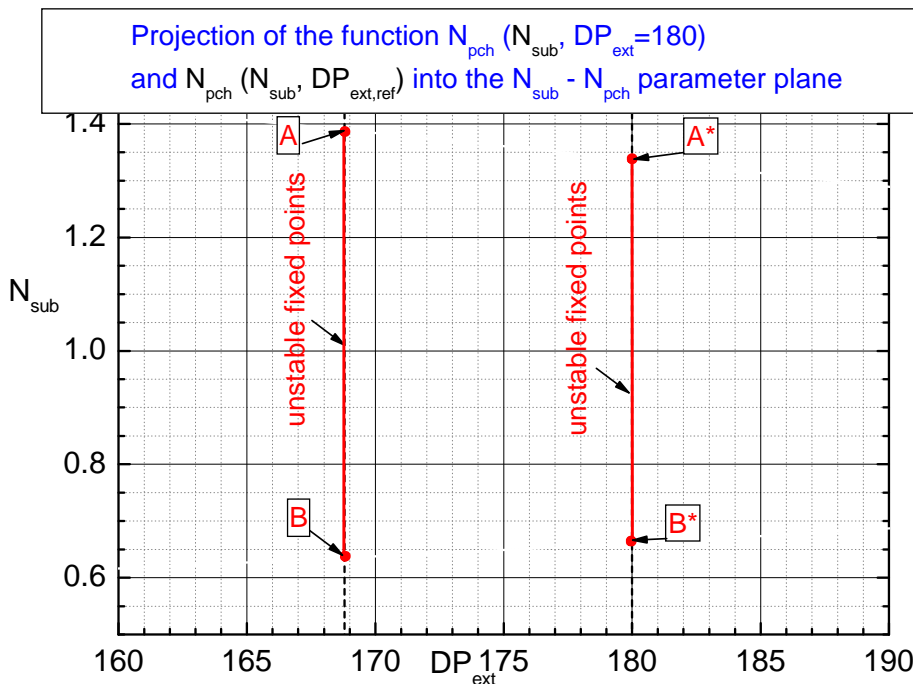


Figure 4.60: Projection of the curves $N_{pch}^{DP_{ext,ref}}(N_{sub})$ and $N_{pch}^{DP_{ext}=180}(N_{sub})$ into the $N_{sub} - DP_{ext}$ -parameter space.

In Figure 4.61 are plotted the curves $N_{pch}^{DP_{ext,ref}}(N_{sub})$ and $N_{pch}^{DP_{ext}=180}(N_{sub})$ including the stability boundary calculated in the $N_{sub} - DP_{ext}$ -parameter space (see section 4.3). In this map, both curves are straight lines which are parallel to the N_{sub} -axis. As postulated, the points A, A*, B and B* are located on the stability boundary (black line) which was calculated in the $N_{sub} - DP_{ext}$ -parameter space.

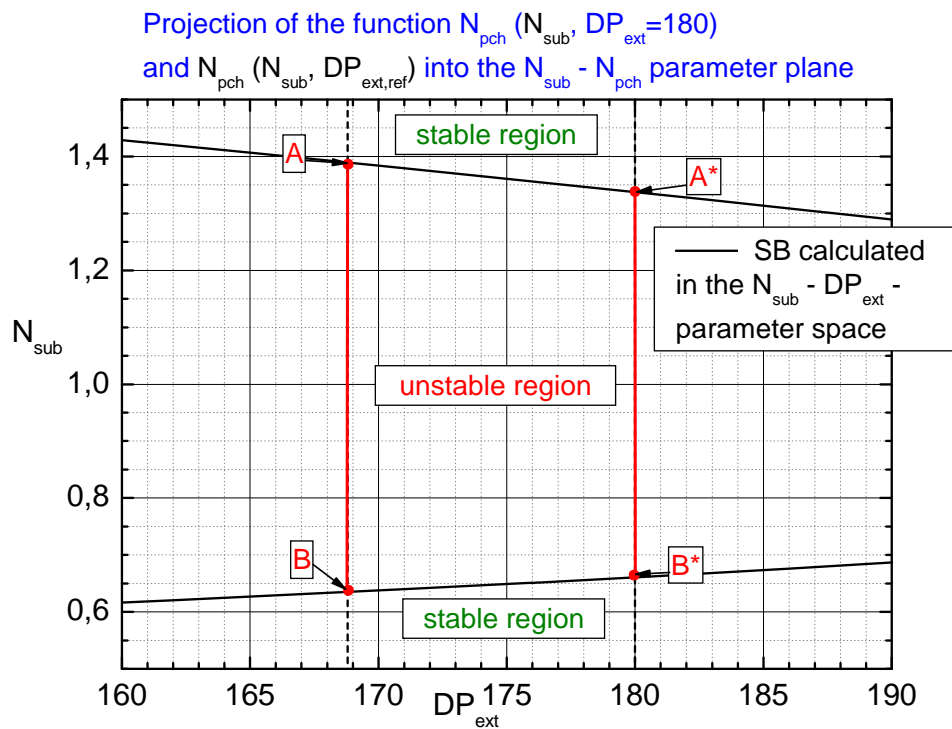


Figure 4.61: Projection of the two curves $N_{pch}^{DP_{ext,ref}}(N_{sub})$ and $N_{pch}^{DP_{ext}=180}(N_{sub})$ into the $N_{sub} - DP_{ext}$ -parameter space and the stability boundary calculated in the $N_{sub} - DP_{ext}$ -parameter space.

4.6.3 Part 3:

The described procedure was applied for further selected external pressure drops that are depicted in Figure 4.62.

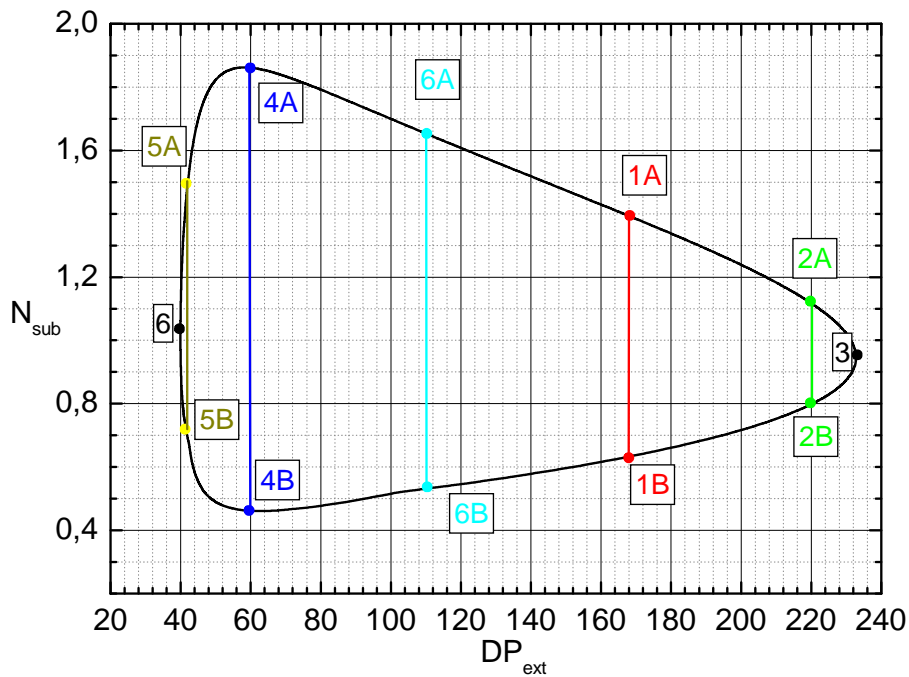


Figure 4.62: Stability boundary calculated in the $N_{sub} - DP_{ext}$ -parameter space. This map shows the locations of the selected DP_{ext} for which the bifurcation analysis will be carried out in the $N_{sub} - N_{pch}$ -parameter space.

The SB depicted in Figure 4.62 was then „transformed“ (projection onto) into the $N_{sub} - N_{pch}$ -parameter space (see Figure 4.63).

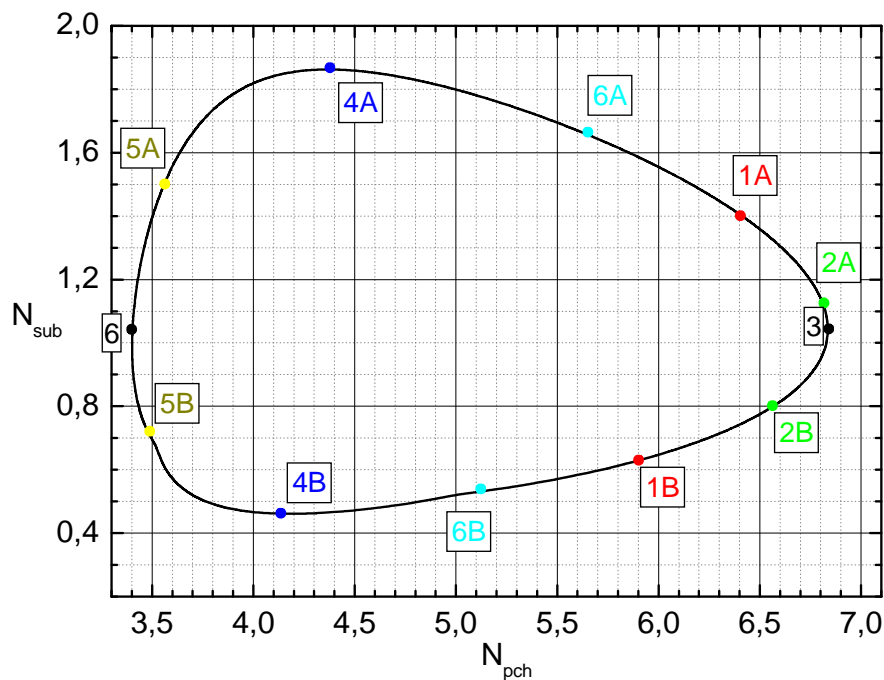


Figure 4.63: Stability boundary **calculated** in the $N_{sub} - DP_{ext}$ -parameter space and **“transformed”** into the $N_{sub} - N_{pch}$ -parameter space.

For all of these selected steady state external pressure drops (depicted in Figure 4.62), bifurcation analysis was performed in the $N_{sub} - N_{pch}$ -parameter plane. The results are presented in Figure 4.64 and Figure 4.65.

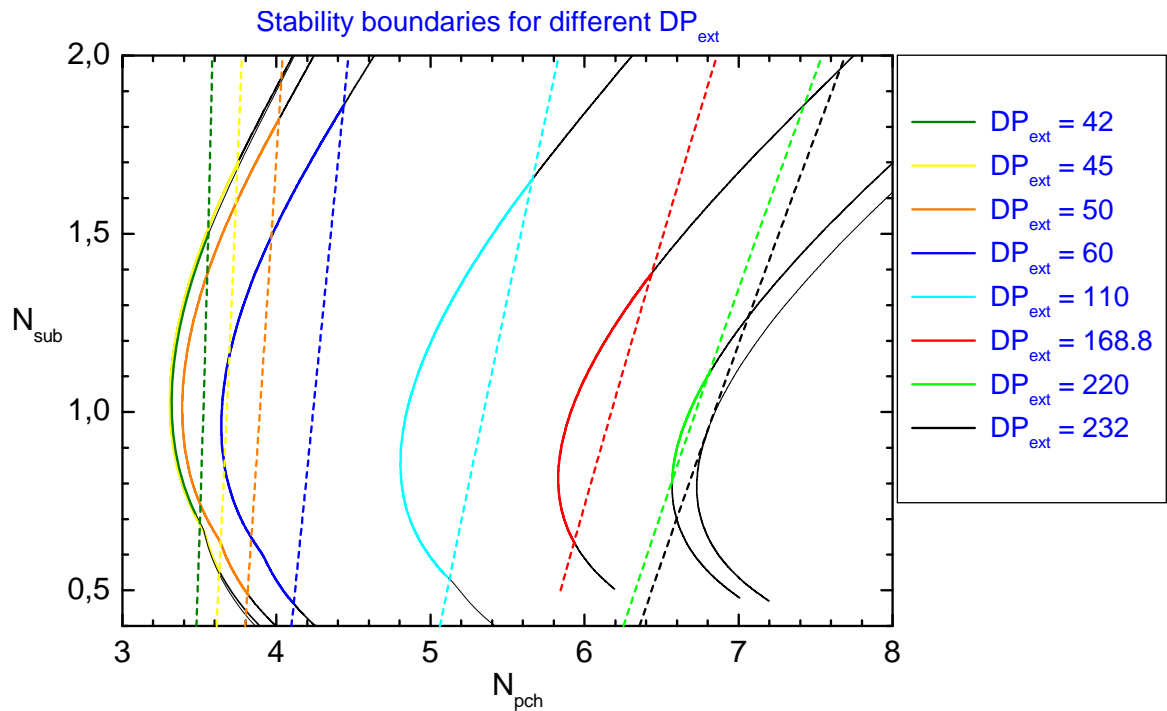


Figure 4.64: Stability boundaries, calculated in the $N_{sub} - N_{pch}$ -parameter space, and the curves $N_{pch}(N_{sub})$ for different external pressure drops are shown.

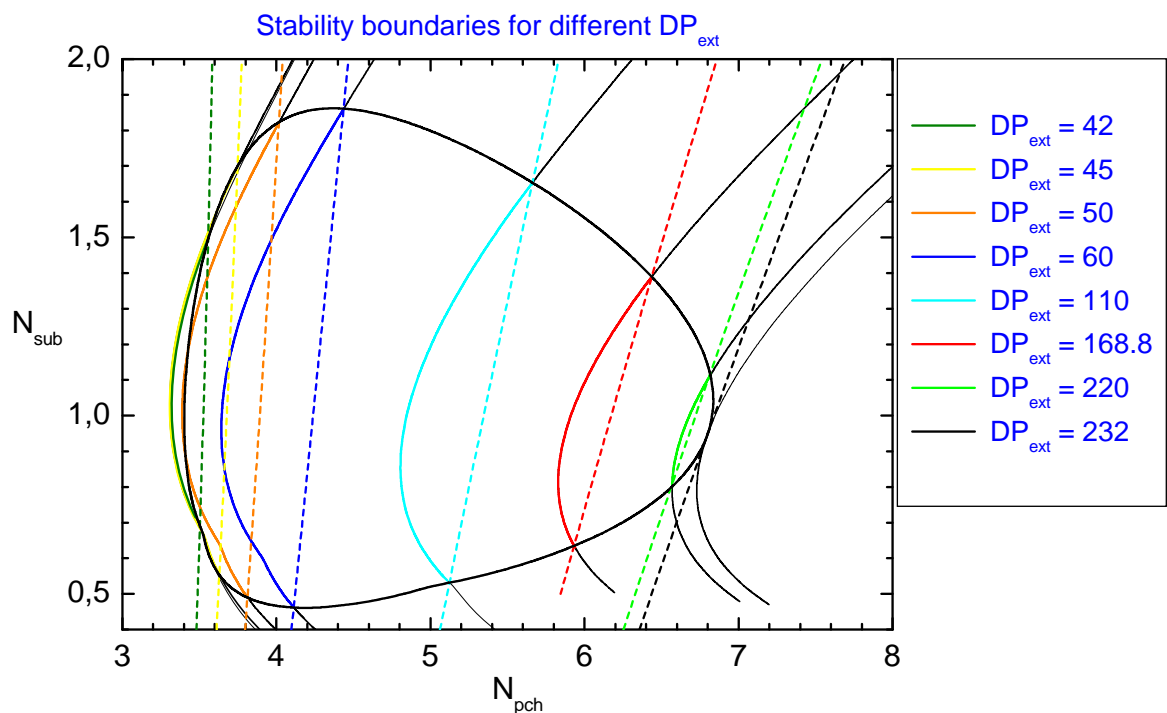


Figure 4.65: Comparison of the stability boundaries calculated in the $N_{sub} - N_{pch}$ -parameter space for different external pressure drops and the stability boundary **calculated** in the $N_{sub} - DP_{ext}$ -parameter space and “**transformed**” into the $N_{sub} - N_{pch}$ -parameter space.

Figure 4.65 depicts the stability boundaries calculated in the $N_{sub} - N_{pch}$ -parameter space and the stability boundary calculated in the $N_{sub} - DP_{ext}$ -parameter space but transformed into the $N_{sub} - N_{pch}$ -parameter space. From this result, it can be concluded that under variation of DP_{ext} , the relative movement of $N_{pch}(N_{sub})$ and $N_{pch}^{SB}(N_{sub})$ is responsible for the shape of the SB calculated in the $N_{sub} - DP_{ext}$ -parameter plane.

If DP_{ext} is increased in small steps, the stability boundary will cross the curve $N_{pch}(N_{sub})$ for a certain value of DP_{ext} (point 3 in Figure 4.63). In this case, the curve $N_{pch}(N_{sub})$ is tangent to the stability boundary at $DP_{ext} = 232$. The same behaviour is observed at $DP_{ext} \approx 39$. These characteristics are caused by a change of the sensitivities of the stability boundaries and their curves $N_{pch}(N_{sub})$ under DP_{ext} -variation. In order to explain the sensitivities of $N_{pch}^{SB}(N_{sub})$ and $N_{pch}(N_{sub})$, the slopes of the curves $N_{pch}^{SB, N_{sub}=0.95}(DP_{ext})$ and $N_{pch}^{N_{sub}=0.95}(DP_{ext})$ along DP_{ext} are taken into account (Figure 4.66) for example.

The curve $N_{pch}^{SB, N_{sub}=0.95}(DP_{ext})$ describes the change of the critical value of the phase change number (where the Hopf-conditions are fulfilled) depending on DP_{ext} , while $N_{sub} = 0.95$ is fixed.

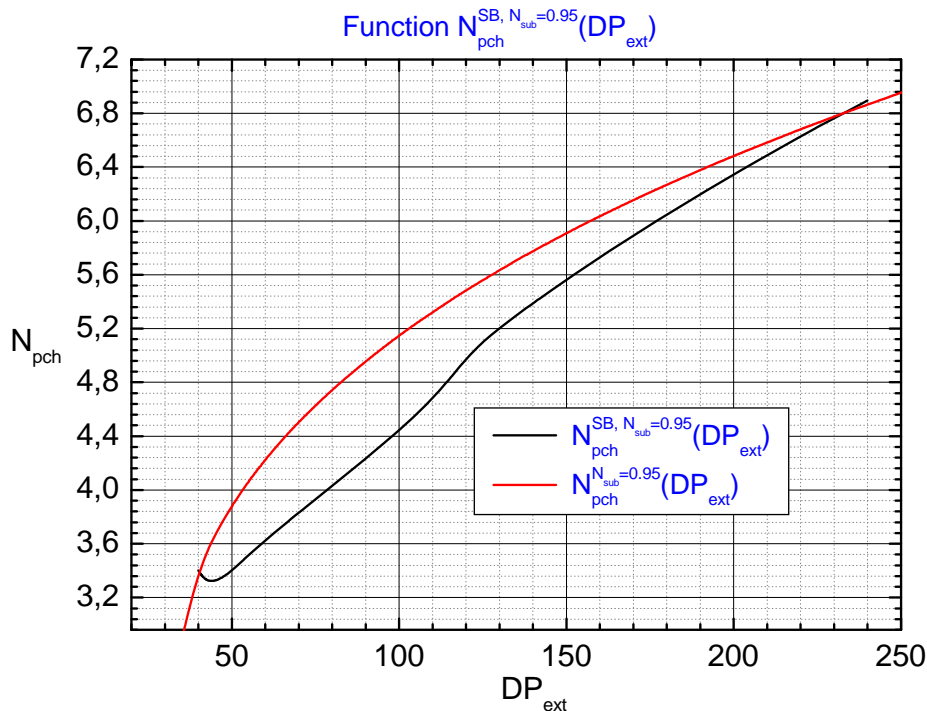


Figure 4.66: This figure shows the critical values of the phase change number depending on DP_{ext} (called $N_{pch}^{SB, N_{sub}=0.95}(DP_{ext})$) and the curve $N_{pch}^{N_{sub}=0.95}(DP_{ext})$. Thereby, $N_{sub} = 0.95$ is fixed. The result of $N_{pch}^{SB, N_{sub}=0.95}(DP_{ext})$ below $DP_{ext} < 45$ is not valid and not clear!

Figure 4.66 demonstrates that the derivative (4.51) of the curve $N_{pch}^{SB, N_{sub}=0.95}(DP_{ext})$ is approximately constant for all DP_{ext} . Consequently, the sensitivity of the stability boundary remains approximately constant regarding DP_{ext} variations.

The slope of the curve $N_{pch}^{N_{sub}=0.95}(DP_{ext})$ changes significantly with increasing DP_{ext} . The slopes of the curves at $DP_{ext} = 50$ and $DP_{ext} = 200$ were estimated as

$$\frac{d}{d DP_{ext}} N_{pch}^{N_{sub}=0.95}(DP_{ext} = 50) = 61.54 \cdot 10^{-3} \quad (4.53)$$

$$\frac{d}{d DP_{ext}} N_{pch}^{SB, N_{sub}=0.95}(DP_{ext} = 50) = 21.09 \cdot 10^{-3} \quad (4.54)$$

$$\frac{d}{d DP_{ext}} N_{pch}^{N_{sub}=0.95}(DP_{ext} = 200) = 9.8 \cdot 10^{-3} \quad (4.55)$$

$$\frac{d}{d DP_{ext}} N_{pch}^{SB, N_{sub}=0.95}(DP_{ext} = 200) = 13.556 \cdot 10^{-3} \quad (4.56)$$

The slopes at the both coordinates correspond to the sensitivity of the SB and the function $N_{pch}(N_{sub})$ regarding DP_{ext} variations. Because of

$$\frac{d}{d DP_{ext}} N_{pch}^{N_{sub}=0.95}(DP_{ext} = 50) > \frac{d}{d DP_{ext}} N_{pch}^{SB, N_{sub}=0.95}(DP_{ext} = 50) \quad (4.57)$$

the curve $N_{pch}(N_{sub})$ has passed the stability boundary. The comparison at $DP_{ext} = 200$ yields

$$\frac{d}{d DP_{ext}} N_{pch}^{N_{sub}=0.95}(DP_{ext} = 200) < \frac{d}{d DP_{ext}} N_{pch}^{SB, N_{sub}=0.95}(DP_{ext} = 200) \quad (4.58)$$

Relation (4.58) is responsible that the stability boundary is passing the curve $N_{pch}(N_{sub})$.

4.6.4 Conclusions

- The bifurcation analysis in the $N_{sub} - DP_{ext}$ -parameter plane yields information about the stability properties of fixed points along the rod line and their corresponding operational conditions in the power flow map. The use of N_{sub} and DP_{ext} for the bifurcation analysis is more general because three parameters are varied implicitly $\rightarrow N_{sub}$, DP_{ext} and N_{pch} . In other words, N_{pch} is a function of N_{sub} and DP_{ext} .
- The bifurcation analysis in the $N_{sub} - N_{pch}$ -parameter plane yields information about the stability properties of fixed points along the curve $N_{pch}(N_{sub})$ and its corresponding thermal hydraulic states.
- The slopes of the curves $N_{pch}^{N_{sub}=0.95}(DP_{ext})$ and $N_{pch}^{SB, N_{sub}=0.95}(DP_{ext})$ (Figure 4.66) describe the sensitivities of function $N_{pch}(N_{sub})$ and the stability boundary $N_{pch}^{SB}(N_{sub})$ regarding DP_{ext} -variations. In addition to that they describe the relative movement between $N_{pch}(N_{sub})$ and $N_{pch}^{SB}(N_{sub})$ under variation of DP_{ext} .
- Under variation of DP_{ext} , the relative movement between $N_{pch}(N_{sub})$ and $N_{pch}^{SB}(N_{sub})$ is responsible for the shape of the SB calculated in the $N_{sub} - DP_{ext}$ -parameter plane.

- The shape of the stability boundary which was calculated in the $N_{sub} - DP_{ext}$ -parameter space, can be explained by bifurcation analyses carried out in the $N_{sub} - N_{pch}$ -parameter space for different DP_{ext} .

As described in the previous sections, the ROM-input is based on the selected operational point. Accordingly, the stability boundary (SB) which was calculated in the $N_{sub} - DP_{ext}$ -operating plane, is related to the reference operational point with its specific steady state 3D parameter distributions. The ROM predictions are only valid in the neighbourhood of the reference OP. Hence, it makes no sense to consider the predicted stability characteristics of fixed points which are located too far away from the reference point. Because in such points the 3D parameter distributions are completely different from the considered reference OP and thus the stability behaviour may be different as predicted by the ROM. The crucial question is: how large is the area of validity of the ROM predictions for a considered reference OP?

5 Summary and conclusions

The thesis is devoted to nonlinear BWR stability analysis of operational points for which measurement data are available from stability tests. In the context of the thesis, a novel approach to nonlinear BWR stability analysis has been developed. This approach can be summarized as follows:

- Sophisticated integral BWR (system) codes and simplified BWR models (ROM) are used as complementary tools to examine the stability characteristics of fixed points and periodic solutions of the nonlinear differential equations describing the stability behaviour of a BWR loop.
- The intention is:
 - to identify the stability properties of certain **operational points (OP)** by performing ROM analysis. The ROM analysis provides an overview about types of instabilities which have to be expected in certain parameter spaces.
 - to apply the system code RAMONA5 for a detailed stability investigation in these operational points and their neighbourhoods. In particular, the nonlinear phenomena revealed by the ROM analysis will be analysed in detail.
- Because the ROM analysis reveals an overview about the solution types existing in certain parameter regions and due to the flexible application of certain methods to the ROM (e.g. variation of specific algorithms for the numerical integration, application of methods from nonlinear dynamics), the results of the ROM can help to get a better understanding of the results of the system code.

The novel approach to nonlinear BWR stability analysis improves the reliability of the BWR stability analysis significantly.

In the scope of the ROM analyses two independent techniques are employed. These are the semi-analytical bifurcation analysis with the bifurcation code BIFDD and the numerical integration of the system of the ROM differential equations. Bifurcation analysis with BIFDD determines the stability properties of fixed points and periodical solutions (correspond to limit cycle). For independent confirmation of these results, the ROM system will be solved directly by numerical integration for selected parameters.

The ROM applied in this thesis, the TUD-ROM, was originally developed at PSI in collaboration with the University of Illinois (PSI-Illinois-ROM). The objective of the ROM development is to develop a model as simple as possible from the mathematical and numerical point of view while preserving the physics of the BWR stability behaviour. Hence, the partial differential equations (PDE) describing the BWR will be converted into ordinary differential equations (ODE). The system of ODEs includes all spatial effects in an approximated (spatial averaged) manner because e.g. by appli-

cation of the mode expansion methodology spatial effects are taken into account by calculation of the amplitude functions of the higher spatial modes and realistic assumptions to the higher mode spatial distributions (calculated by a 3D code). In order to analyse the in-phase and out-of-phase oscillation states, for instance, it is not necessary to solve the full space-dependent equations. In this case, it is sufficient to take into account only the fundamental mode and the first azimuthal mode. This is justified by reactor theory [48] as well as by results of stability tests [5].

The TUD-ROM was upgraded in two significant points:

- Development and implementation of a new calculation methodology for the mode feedback reactivity coefficients (void and fuel temperature reactivity)
- Development and implementation of a recirculation loop model, analysis and discussion of its impact on the in-phase and out-of-phase oscillation mode
- Development of a novel physically justified approach for the calculation of the ROM input data
- Discussion of the necessity of consideration of the effect of subcooled boiling in an approximate manner

With the upgraded ROM, nonlinear BWR stability analyses have been performed for three OPs (one for NPP Leibstadt (cycle7), one for NPP Ringhals (cycle14) and one for NPP Brunsbüttel (cycle16) for which measuring data of stability tests are available. In this thesis, the novel approach to nonlinear BWR stability analyses was extensively presented for NPP Leibstadt. In particular, the nonlinear analysis has been carried out for an operational point (OP), at which an out-of-phase power oscillation has been observed in the scope of a stability test at the beginning of cycle 7 (KKLc7_rec4). The ROM predicts a saddle-node bifurcation of cycles, occurring in the linear stable region, close to the KKLc7_rec4-OP. This result allows a new interpretation of the stability behaviour around the KKLc7_rec4-OP.

5.1 Modifications of the ROM

5.1.1 Recirculation loop

In the PSI-IIIinois-ROM, the outer loop was replaced by the constant external pressure drop boundary condition. This is a reasonable approximation to represent the real stability behaviour of an out-of phase oscillation mode. But the stability behaviour of the in-phase oscillation mode can not be simulated correctly. Hence, the ROM was extended by a recirculation loop model.

In the first step, the recirculation loop was implemented in a thermal-hydraulic one heated channel model based on data of the Saha facility [77]. In order to study the impact of the recirculation loop model on the thermal-hydraulic stability properties, the downcomer flow cross section A_{doc} was varied in the range of interest. In the scope of this analysis, it has been found that the larger the downcomer flow cross

section the more unstable the system is. From the linear point of view, the set of stable fixed points become less with increasing A_{doc} . On the other hand, the set of sub-critical fixed points (unstable limit cycles solution) increases for increasing A_{doc} values. It should be emphasized that an infinite large downcomer flow cross section ($A_{doc} \rightarrow \infty \hat{=} A_{ol} \rightarrow 0$) corresponds to the constant external pressure drop boundary condition ($\Delta P_{extern} = const$).

Further investigations have shown that the downcomer friction has a very small impact on the stability behaviour. Consequently, it can be neglected in further stability investigations. This result is in agreement with the RAMONA5 model where downcomer friction is also ignored.

In the second step, the recirculation loop model has been implemented in the simplified BWR model and its impact on the BWR stability behaviour has been analysed. In particular, the effect of the downcomer flow cross section on the in- and out-of-phase oscillation mode (corresponds to the in- and out-of-phase eigenstates) has been studied. The analysis of the downcomer flow cross section variation with the ROM has shown that A_{doc} have a strong impact on the stability property of the in-phase oscillation mode while the stability behaviour of the out-of-phase oscillation mode is not affected. The larger the downcomer flow cross section, the more unstable the in-phase oscillation mode is. The results of the ROM analysis are consistent with the results of the RAMONA5 analysis. It should be emphasized that the stability properties for the reference OP of KKLc7rec4 can only be reproduced correctly by the ROM if the correct downcomer flow cross section of the RAMONA5 model is used. Consequently, BWR stability analysis should be performed always including the recirculation loop.

5.1.2 Subcooled boiling

In the thermal-hydraulic model of the ROM, two axial regions, the single- and the two phase region, are considered. Thereby the two phase region is represented by a Drift-Flux model where thermodynamic equilibrium between the two phases is assumed. Two questions arise: 1) is it necessary to take into account the subcooled boiling phenomenon for BWR stability analyses? 2) which model for describing the subcooled boiling phenomenon is appropriated in the framework of this analysis approach? It has been found out that the ROM must be extended by a third region where a mechanistic model describes the thermodynamic non-equilibrium between the two phases and the void generation on the heated surface. But such a model extension requires extreme large effort. Therefore, in the scope of this work, the effect of the subcooled boiling on the BWR stability behaviour has been estimated by a modified profile fit model (Levy, 1966 [27]).

The first analysis with the included subcooled boiling model was performed with the simple thermal-hydraulic one heated channel model. The aim was to analyse the differences between the axial void profiles provided by the original two-phase flow model (bulk boiling model) and the subcooled boiling model. As a result, the relative

deviation between the channel averaged void fractions provided by the two-phase flow model and the subcooled boiling model is less than 5%.

Furthermore, an analysis was performed with the ROM for NPP Leibstadt. The aim was to compare the effect of using a uniform axial power profile in the ROM (instead of a real bottom peaked axial power profile) with the effect of ignoring subcooled boiling on the axial void profiles. As a result, it has been found out that the application of a uniform axial power profile instead of the real one causes relative deviations between channel averaged void fractions calculated by RAMONA5 and ROM of at least 16%. In contrast to that the disregard of subcooled boiling lead to relative deviations less than 5%, mentioned above. Furthermore, after applying the adjustment procedure for the axial void profile of the ROM, the deviation between the channel averaged void fraction calculated by RAMONA5 and ROM (original two phase flow model) are less than 1%. Consequently, from the thermal-hydraulic point of view and in the framework of the analysis approach of the thesis, the consideration of the subcooled boiling phenomenon is not necessary.

5.1.3 Calculation methodology for C_{mn} -coefficients

A new method to calculate the void and fuel temperature (Doppler) mode feedback reactivity coefficients ($C_{mn}^{Void,r}$ and $C_{mn}^{Doppler,r}$, section 3.2) has been developed at UPV Valencia (Spain) in cooperation with the TU Dresden (Germany). The new methodology was applied for NPP Leibstadt, NPP Ringhals and NPP Brunsbüttel.

The results of the new calculation methodology for $C_{mn}^{Void,r}$ and $C_{mn}^{Doppler,r}$ are compared with that of the original method used in the PSI-Illinois ROM. The comparison show that both methods provide similar results for NPP Leibstadt and NPP Ringhals. In addition to that the void and Doppler feedback reactivity coefficients of the technical documentation of NPP Leibstadt (beginning of cycle 7) have the same order of magnitude as calculated by the calculation methodology of the mode feedback reactivity coefficients. Consequently, the new calculation methodology for the void and Doppler mode feedback reactivity coefficients is qualified for ROM analysis.

5.2 Novel approach for calculation of the ROM input

The goal is to analyse the stability behaviour of the power plant with the ROM as close as possible to a real BWR (RAMONA5 model is the reference system) in a certain neighbourhood of the selected OP. At first, it is necessary to define the reference OP for which the nonlinear BWR stability analysis will be performed. For NPP Leibstadt, for instance, the KKLc7_rec4-OP was selected to be the reference OP but with a modified core inlet subcooling. Secondly, a novel approach for the ROM input calculation is applied. All ROM input parameters are calculated from the specific RAMONA5 model and its steady state solution corresponding to the reference OP. The basic demand on the procedure for calculating the ROM-input is that the steady state conditions of the reference OP, predicted by the RAMONA5 model, are simu-

lated correctly by the ROM using the calculated input parameters. Only in this case it is reasonable to perform specific system code analyses which are based on the ROM analysis results.

In the framework of the novel calculation methodology of the ROM input parameters, it is assumed that, when the steady state solution of the reference OP is described by the ROM as close as possible to the real one (system code prediction), the stability behaviour of the BWR system can be represented properly by the ROM in a close neighbourhood of the reference OP. In particular the specific thermal-hydraulic and neutron kinetic states has to be described correctly.

The novel calculation methodology of the ROM input parameters was applied for three NPPs. The results of the steady state properties of the ROM are consistent with that of RAMONA5.

5.3 Nonlinear stability analysis for NPP Leibstadt (KKLc7_rec4)

Stability and bifurcation analysis for KKLc7_rec4 has been performed. For this purpose, the KKLc7_rec4-OP is defined to be the reference OP. The stability boundaries and the nature of the PAH-B are determined and visualized in appropriated two-dimensional parameter spaces. In particular, the subcooling number N_{sub} and the steady state external pressure drop DP_{ext} are selected to be the iteration and bifurcation parameters. The variation of DP_{ext} corresponds to a variation of the pump head which changes the coolant mass flow. When the coolant mass flow is changed, the power will also be changed while the spatial neutron flux distribution will not be changed significantly because the control rod positions are kept constant. As a consequence, the stability properties of fixed points and periodical solutions along the rod-line of the power flow map which crosses the reference OP can be examined.

Note that, the two parameters N_{sub} and N_{pch} can also be selected to be the iteration and bifurcation parameters in bifurcation analyses with BIFDD. The $N_{sub} - N_{pch}$ -parameter space, used as stability map, is related to the thermal-hydraulic states within the hydraulic nuclear-heated channels of the BWR. It is important to note that, in the $N_{sub} - N_{pch}$ -parameter space, operational points only exist on the curve $N_{pch}(N_{sub})$ for a fixed parameter configuration of a BWR. Hence, the bifurcation analysis carried out in the $N_{sub} - N_{pch}$ -parameter space reveals the stability characteristics of all fixed points which are located on the curve $N_{pch}(N_{sub})$ (see section 4.6). Consequently, the functional dependence between N_{sub} and N_{pch} (the curve $N_{pch}(N_{sub})$) should always be taken into account for an interpretation of the stability characteristics calculated in the $N_{sub} - N_{pch}$ -parameter space.

In contrast, the bifurcation analysis carried out in the $N_{sub} - DP_{ext}$ -parameter space yield the most practical information about BWR operating conditions. This statement is verified in section 4.6 where the stability boundary calculated in the $N_{sub} - DP_{ext}$ -parameter space and its relation to the $N_{sub} - N_{pch}$ -parameter space has been discussed. If the bifurcation analysis is carried out in the $N_{sub} - DP_{ext}$ -parameter space, a

larger parameter region can be analysed in comparison to an bifurcation analysis carried out in the $N_{sub} - N_{pch}$ -parameter space.

5.3.1 Local consideration

The terminology “local analysis” means that the close neighbourhood of the steady state solution \bar{X}_0 (equilibrium point or singular fixed point) is taken into account in the phase space.

The following conclusions of the local nonlinear stability analyses for the KKLc7_rec4-OP of NPP Leibstadt were derived:

- Unstable periodical solutions (unstable limit cycle) in the stable region close to the KKLc7_rec4-OP are predicted by the semi-analytical bifurcation analysis. Note that, the asymptotic decay ratio for these fixed points is $DR < 1$. A linear analysis is not capable to examine the stability properties of limit cycles.
- For independent confirmation of the results which are predicted by the bifurcation analyses, numerical integration of the ROM equation system has been carried out for selected parameters. The results of the numerical integration method confirm the predictions of the local bifurcation analysis.
- The local nonlinear analysis has shown that the stability behaviour of the reference OP and its close neighbourhood can be simulated reliably by the new ROM. In this OP, the results of RAMONA5 and ROM are locally consistent. Under stability related parameter variations the stability behaviour calculated by both, ROM and RAM, are consistent.
- The relative location of the reference OP with respect to the stability boundary is simulated correctly with the new ROM. This is mainly affected by the application of the novel approach for calculation of the ROM input data.
- The new ROM simulates correctly the oscillation mode: the out-of-phase oscillation is excited and the in-phase mode is decaying. As mentioned in the introduction of the thesis, the original ROM was not able to predict the correct oscillation mode. The reason for the correct simulation of the oscillation mode is the implemented recirculation loop model, in which the downcomer flow cross section of the RAMONA5 (DC2) model is used as input parameter, and the increased artificial factor $fact_m$ with $m \neq n$.

The good agreement between the local RAMONA5 and ROM investigations could be verified for NPP Brunsbüttel and NPP Ringhals1 (see Appendix H and Appendix G). Hence, the new ROM and the new procedure for the calculation of the ROM input data are qualified for BWR stability analysis in the framework of the new approach.

5.3.2 Global consideration

The bifurcation analysis with BIFDD is valid only in a small **neighbourhood of the Hopf bifurcation point** of the parameter space and in the vicinity of the equilibrium point (origin or singular fixed point) of the phase space (see Figure 4.54). In order to study the global character of the nonlinear system, numerical integration beyond the local bifurcation findings is necessary. For this purpose, numerical integration of the ROM equation system has been carried out for a larger parameter region. In addition to that, a larger phase space region for the calculation of the solution of the system of ROM equations was taken into account. In this analysis, the subcooling number N_{sub} was selected to be the control parameter and was varied in a specific range.

The global nonlinear stability analysis has shown that there is a critical core inlet subcooling $N_{sub,t}$ at which the system undergoes a saddle-node bifurcation of a cycle. This bifurcation type, which is also called turning point or fold bifurcation, belongs to the class of global bifurcations. The major feature of this bifurcation type is that a **stable limit cycle** and an **unstable limit cycle** are “born” (“out the clear blue sky” [17]) at $N_{sub,t}$ and **coexist** either with stable or with unstable **fixed points**.

The numerical integration (global consideration) predicts stable limit cycles for $N_{sub,t} < N_{sub} < 0.9$, even though the bifurcation analysis predicts only unstable limit cycles for $N_{sub} < N_{sub,c}$. $N_{sub,c}$ is the critical bifurcation parameter, for which the Hopf conditions are fulfilled. Due to (numerical) convergence problems of the numerical integration around the bifurcation point, $N_{sub,t}$ cannot be calculated exactly. The estimated value of $N_{sub,t}$ is $N_{sub,t} \approx 0.63$.

At the reference OP the state variables will also be attracted by the limit cycle. In addition to that, for $N_{sub} \in [N_{sub,t}, \dots, N_{sub,c}]$ with $N_{sub,t} < N_{sub,c}$ stable fixed point, unstable limit cycle and stable limit cycle coexist. In this region, the amplitudes of the unstable limit cycle correspond to the boundary which separates the basin of attraction of the singular fixed point and basin of attraction of the stable limit cycle. Below $N_{sub,t}$, only stable fixed point solutions exist.

The nonlinear analyses results for NPP Ringhals, presented in Appendix H, have also shown that at the reference OP and in its neighbourhood stable limit cycle exist even though the bifurcation analysis predicts only subcritical Hopf bifurcations. This result can also be explained by the existence of a saddle-node bifurcation of cycles occurring in the linear stable region.

As mentioned in the introduction, Rizwan-udding [38] (using the simple March-Leuba five-equation system) and van Bragt et al. [54] (using the thermal-hydraulic one heated channel model) also showed the existence of turning points with their simple models. However, this is the first time that a saddle-node bifurcation of cycles is revealed by an advanced ROM for a real operational point of a BWR.

5.4 Conclusions

The following conclusions from nonlinear BWR stability analyses can be made:

- The recirculation loop model is an essential sub-model of the ROM for simulating correctly the in-phase oscillation mode. BWR stability analysis should always be performed including the recirculation loop.
- The subcooled boiling phenomenon can be ignored as long as a uniform axial power profile is used by the ROM.
- The new calculation methodology for the void and Doppler mode feedback reactivity coefficients is qualified for ROM analyses.
- The application of the novel approach for calculation of the ROM input data is one of the crucial tasks of a successful use of the RAM-ROM methodology. It enables that the TUD-ROM simulates correctly the steady state conditions of the reference OP. Thus the novel approach to calculate the ROM input is strongly recommended for the RAM-ROM methodology.
- At the reference OP and its close neighbourhood, the results of RAMONA5 and the TUD-ROM are qualitatively consistent. Hence, the TUD-ROM is qualified for nonlinear BWR stability analyses in the framework of the novel approach demonstrated in this thesis.
- The nonlinear stability analysis for NPP Leibstadt (KKLc7_rec4) has shown that the stability behaviour occurring in a certain region around the reference OP can be explained by the existence of a saddle-node bifurcation of cycles which occurs in the linear stable region. This result allows a new possible interpretation of the stability behaviour around the KKLc7_rec4-OP.
- The results of this thesis confirm that the RAM-ROM methodology is qualified for nonlinear BWR stability analyses.

5.5 Recommendations to future work

In order to increase the reliability of the RAM-ROM methodology the following future work is recommended:

- assessment of the sensitivities and uncertainties of parameters which are significant for the BWR stability behaviour.
- deepen the physical interpretation of the shape of the stability boundaries and their change under parameter variations
- in-depth analysis of global bifurcations and the conditions of their occurrence, in particular, of those generating large limit cycle amplitudes
- Post-analysis for the SIRIUS-N (T) facility to “validate” the TUD-ROM

- A critical discussion of the sub-models of the ROM is recommended. In particular, the necessity of consideration of real axial power profiles should be discussed. Another unsolved problem is the physical interpretation of the artificial factor $fact_{mn}$.
- In many analyses using BIFDD, there are convergence problems to find the critical bifurcation parameter at which the Hopf conditions are fulfilled. This problem causes interruptions during the bifurcation analysis. Here, a critical review of the algorithms employed by BIFDD is necessary. In addition to that, as explained in section 2.3, the user of BIFDD has to provide the Jacobian matrix of the system of differential equations. If the ROM will be modified, all corresponding Jacobian matrix elements (in the TUD-ROM there are 22x22 elements) must be analytically recalculated. Hence, ROM modifications are difficult and cumbersome, when it is coupled with BIFDD. Hence, it is recommended to develop a new bifurcation code which avoids the disadvantages, mentioned above, and allows a more flexible use, e.g. global bifurcation analyses.

The reliability of system code analyses should be studied more in detail because it was figured out that the simulated stability behaviour in the close neighbourhood of bifurcation points strongly depend on algorithms employed. In addition to that, a critical discussion of some approximations of RAMONA5 regarding their impact on the stability behaviour is necessary (like $\nabla P = 0$).

6 Literatur

- [1] J. March-Leuba; J.M. Rey; “*Coupled thermohydraulics-neutronic instabilities in boiling water nuclear reactors: a review of the state of the art*”, Nucl. Eng. Des. **145**, pp. 97–111; 1993.
- [2] F.D’Auria (Editor); “*State of the Art Report on BWR Stability*”; NEA/CSNI/ R(96)21; OECD/GD(97)13; 1997.
- [3] Lahey, Jr., T.R.; *Boiling Heat Transfer; Modern Developments and Advances*; Elsevier Science Publishers; Amsterdam, London, New York, 1992.
- [4] S.Kakac; B.Bon; “*A Review of two-phase flow dynamic instabilities in tube boiling systems*”; International Journal of Heat and Mass Transfer; **51**; pp.399-433; 2008.
- [5] Aguirre, C.; Hennig, D.; “*Stability measurement at NPP Leibstadt Cycle 7 Sep. 6-th 1990*”; NACUSP; 5-th EURATOM FRAMEWORK PROGRAMME 1998-2002; November 2001.
- [6] Blomstrand, J.; “*The KKL Core Stability Test, Conducted in September 1990*”; ABB-Report; BR91-245; 1992.
- [7] D. Hennig; “*Boiling Water Reactor Stability Analysis-A Challenge for the Study of Complex Nonlinear Dynamical Systems*”; PSI Annual Report; Annex IV; Nuclear Energy and Safety; 1996.
- [8] D.Hennig; “*A Study of BWR Stability Behavior*”; Nuclear Technology; Volume 126; pp.10-31; 1999.
- [9] A. Dokhane; D. Hennig; Rizwan-uddin; R. Chawla; “*Analytical Modelling of Nonlinear Stability Behaviour of BWR’s*”; PSI scientific report 2001/Volume IV; Nuclear Energy and safety ISSN 1423-7334; March; 2002.
- [10] A. Dokhane; D. Hennig; Rizwan-uddin; R. Chawla; “*Nonlinear Stability Analysis with a Novel BWR Reduced Order Model*”; Proceedings of PHYSOR’02; Seoul; Korea; Oct. 7-10; 2002. (CD-ROM)
- [11] A. Dokhane, D. Hennig, R. Chawla, and Rizwan-uddin, “*Nonlinear stability analysis of boiling water reactor on the basis of system codes and reduced order models*,” Proceedings of Annual Meeting on Nuclear Technology, Vol. 126, pp.15-19, 2003.
- [12] A. Dokhane, “*BWR Stability and Bifurcation Analysis using a Novel Reduced Order Model and the System Code RAMONA*,” Doctoral Thesis, EPFL, Switzerland, 2004.
- [13] A. Dokhane, D. Hennig, Rizwan-uddin, and R. Chawla, “*Semi-analytical Bifurcation Analysis of Two-phase Flow in a Heated Channel*,” International Journal of Bifurcation and Chaos, **15**(8), 2005.
- [14] A. Dokhane, D. Hennig, R. Chawla, and Rizwan-uddin, “*Nuclear-Coupled Thermal-Hydraulic Nonlinear Stability Analysis Using a Novel BWR Reduced Order Model: part 1- The Effects of Using Drift Flux Versus Homogeneous Equilibrium Models*,” Proc. Of 11th International Conference on Nuclear Engineering, Tokyo, Japan, 2003.
- [15] A. Dokhane, D. Hennig, R. Chawla, and Rizwan-uddin, “*Nuclear-Coupled Thermal-Hydraulic Nonlinear Stability Analysis Using a Novel BWR Reduced Order Model: part 2- stability limits of in-phase and out-of-phase modes*; Proc. Of 11th International Conference on Nuclear Engineering,” Tokyo, Japan, 2003.

-
- [16] D. Hassard, D. Kazarinoff, and Y-H Wan, "*Theory and Applications of Hopf Bifurcation*," Cambridge University Press, New York, 1981.
- [17] S. H. Strogatz; "*Nonlinear dynamics and chaos*"; Addison-Wesley Publishing Company; 1994.
- [18] J. Guckenheimer and P. Holmes, "*Nonlinear Oscillation, Dynamical Systems, and Bifurcation in Vector Fields*," Applied Mathematical Sciences 42, Springer Verlag, 1984.
- [19] A. Neyfeh and B. Balachandran, "*Applied nonlinear dynamics: analytical, computational, and experimental methods*"; John Wiley & Sons, Inc., New York, 1995.
- [20] M. W. Hirsch; S. Smale; *Differential Equations, Dynamical Systems, and Linear Algebra*; ACADEMIC PRESS, INC; 1974.
- [21] A. Neyfeh; *Introduction to Perturbation Techniques*; John Wiley & Sons; 1981.
- [22] G. Nicolis; "*Introduction to nonlinear science*"; Cambridge University Press; 1995.
- [23] C.Lange; D.Hennig; V.G.Llorens; G.Verdù; "*Advanced BWR stability analysis with a reduced order model and system code*"; Proceedings of the 15th International Conference on Nuclear Engineering; Nagoya; Japan; April 22-26; 2007.
- [24] C.Lange; D.Hennig; V.G.Llorens; G.Verdù; "*BWR Stability and Bifurcation analysis on the basis of system codes and reduced order models*"; Annual meeting on Nuclear Technology, Karlsruhe; Mai 22.24; 2007.
- [25] C.Lange; D.Hennig; V.G.Llorens; G.Verdù; *Methodology of nonlinear BWR stability analysis*; 1st Workshop on Advanced BWR Stability Analysis Valencia (Spain); October 22-23; 2007.
- [26] C.Lange; D.Hennig; A.Hurtado; V.G.Llorens; G.Verdù; "*In depth analysis of the nonlinear stability behavior of BWR-Systems*"; Proceedings of PHYSOR'08; Interlaken; 15-18 September; Interlaken; Switerland; 2008
- [27] Levy, S.; "Forced convection subcooled boiling-prediction of vapour volumetric fraction", Int.J.Heat Mass Transfer; Vol.10, pp, 951-965; 1967.
- [28] Tomas Lefvert; "*BWR STABILITY BENCHMARK*"; Nuclear Science Committee; OECD/NEA; 1994.
- [29] Van Teefflen; „*Stabilitätsmessung Mitte des 16. Zyklus*“, Technischer Bericht; KKB; Kernkraftwerk Brunsbütel GmbH; 2001.
- [30] W.Wulff; H.S.Cheng; D.J.Diamond; M.Khatib-Rhabar; "*A Description and Assessment of RAMONA-3B Mod.0,cycle4,: A Computer Code with 3D Neutron Kinetics for BWR System Transients*"; NUREG/CR-3664; BNL-NUREG-51746; Brookhaven National Laboratory; 1984.
- [31] Th. Smed; P. Lansakar; "*RAMONA in 10 Minutes-Frequency Domain Analysis*"; Studsvick-Scandpower; European User Group Meeting; Lake Windermere; England; Sep.1999.
- [32] Studsvik/Scandpower RAMONA5.5 Manual, 2003
- [33] M.P. Paulsen; J.G. Shadford; J.L. Westacott; "*A Nondiffusive Solution Method for ETRAN-03 BWR Stability Analysis*"; Nuclear Technology; Volume 100; pp.162-173; November; 1992.
- [34] R.M. Miller; T.J. Downar; "*Complation Report for the Coupled TRACM-PARCS Code*";

- Technical Report Perdue University; PU-NE-99-20; 1999.
- [35] J.March-Leuba; Dan G. Cacuci; R.B.Perez; "*Nonlinear Dynamics and Stability of Boiling Water Reactors: Qualitative Analysis*", Nucl. Science and Eng.; **93**; Part1: pp. 111-123; Part2: pp. 124-136; 1986.
- [36] J.March-Leuba; "*A Reduced-Order Model of BWR Linear Dynamics*"; Nucl. Technology; **75**; pp.15-22; 1986.
- [37] J.March-Leuba; "*Dynamic Behaviour of Boiling Water Reactors*"; Ph.D. Dissertation; University of Tennessee; USA; 1984.
- [38] Rizwan-uddin, "*Turning points and sub- and supercritical bifurcations in a simple BWR model*," to appear in Nuclear Engineering and Design; 2005.
- [39] J.L. Munoz-Cobo; G.Verdu; "Application of Hopf bifurcation Theory and Variational Methods to the study of Limit Cycles in Boiling Water Reactors"; Annals of Nuclear Energy; Volume 18; No.5; pp.269-302; 1991.
- [40] J. Munoz-Cobo; M. Podowski; S. Chiva; "*Parallel channel instabilities in boiling water reactor systems: boundary conditions for out of phase oscillations*"; Annals of Nucl. Energy;" **29**, pp. 1891–1917; 2002.
- [41] J.L. Munoz-Cobo; O.Rosello; R.Miro; A.Escriva; D.Ginestar; G.Verdu; "*Coupling of density wave oscillations in parallel channels with high order modal kinetics: Application to BWR Out-of-Phase Oscillations*"; Annals of Nucl. Energy; Volume 27; Number 15; pp. 1345-1371; 2000.
- [42] J.L.Munoz-Cobo; R.B. Perez; D.Ginestar; A.Escriva; G.Verdu; "*Nonlinear Analysis of Out-of-Phase Oscillations in BWR*"; Annals of Nucl. Energy; Volume 23; Number 16; pp. 1301-1335; 1996.
- [43] J.L.Munoz-Cobo; S. Chiva; A. Sekhri; "A reduced order model of BWR dynamics with sub-cooled boiling and modal kinetics: application to out of phase oscillations"; Annals of Nucl. Energy; Volume 31; pp. 1135-1162; 2004.
- [44] K. Hashimoto; "*Linear Modal Analysis of Out-of-Phase Instability in BWR Cores*"; Ann. Nucl. Engineering; **20**; Number 12; pp. 789-797; 1993.
- [45] K. Hashimoto; A. Hotta; T. Takeda; "*Neutronic Model for Modal Multichannel Analysis of Out-of-Phase Instability in Boiling Water Reactor Cores*"; Ann. Nucl. Energy; **24**; Number 2; pp. 99-111; 1997.
- [46] M. Miro; D. Ginestar; D. Hennig; G. Verdu; "*On the Regional Oscillation Phenomenon in BWR's*"; Progress in Nuclear Energy; Vol. 36; No. 2; pp. 189-229; 2000.
- [47] A.A.Karve; "Nuclear-Coupled Thermal-hydraulic Stability Analysis of Boiling Water Reactors"; Ph.D. Dissertation; Virginia University; USA; 1998.
- [48] A.F. Henry; "*Nuclear Reactor Analysis*"; MIT Press; Cambridge; Massachusetts; USA; pp. 300-329; 1975.
- [49] A. CLAUSSE;R. T. LAHEY, Jr., "*The Analysis of Periodic and Strange Attractors During Density-Wave Oscillations in Boiling Flows*"; Chaos; Solitons & Fractals, 1; 167; 1991.
- [50] Achard, J.; Drew, D.A.; Lahey, R.T.; "*The Analysis of Nonlinear Density-Wave Oscillations in Boiling Channels*"; J. Fluid Mech.**155**; 213; 1985.
- [51] Y.M. Farawila; D.W. Pruitt; „*A Study of Nonlinear Oscillation and Limit Cycles in Boiling Water Reactors*"; Part 1: The Global Mode; Part2: The Regional Mode; Nuclear Science

and Engineering; Volume 154; No. 3; pp.302-327; Technical Paper; November, 2006.

- [52] D.D.B. van Bragt; Analytical Modeling of Boiling Water Reactor Dynamics; Ph.D. Dissertation; Department of Reactor Physics of the Interfaculty Reactor Institute; Delft University of Technology; Netherlands; 1998.
- [53] D.D.B. van Bragt; Rizwan-uddin; T.H.J.J. van der Hagen; „*Nonlinear Analysis of a Natural Circulation Boiling Water Reactor*“; Nuclear Science and Engineering; **131**; pp.23-44; 1999.
- [54] D.D.B. van Bragt; Rizwan-uddin; T.H.J.J. van der Hagen; “Effect of Void Distribution Parameter and Axial Power Profile on Boiling Water Reactor Bifurcation Characteristics”; Nuclear Science and Engineering; **134**; pp.227-235; 2000.
- [55] Quan Zhou, Rizwan-uddin, 2002, “Bifurcation Analyses of in-phase and out-of-phase Oscillations in BWRs”, Physor2002, Proc. of International Conference on the new Frontiers of Nuclear Technology Reactor Physics, Safety and high performance Computing, Seoul, Korea, Oct. 7-10, 2002, CD-ROM.
- [56] Quan Zhou; Rizwan-uddin; “In-phase and Out-of-Phase Oscillations in BWRs: Impact of Azimuthal Asymmetry and Second Pair of Eigenvalues”; Nuclear Science and Engineering; **151**; pp.95-113; 2005.
- [57] Quan Zhou; “Stability and Bifurcation Analyses of Reduced-Order Models of Forced and Natural Circulation BWRs”; Ph.D. Dissertation; University of Illinois at Urbana-Champaign; 2006.
- [58] Rizwan-uddin; “*Linear and Nonlinear Stability Analyses of Density-Wave Oscillations in Heated Channels*”; Ph.D. Dissertation of University of Illinois, USA; 1981.
- [59] Rizwan-uddin; “*Nonlinear Dynamics of Two-Phase Flow*”; Trans. Am. Nucl. Soc.; **53**; 238; 1986.
- [60] Rizwan-uddin; “*On Density-Wave Oscillations in Two-Phase Flow*”; Int.J. Multiphase Flow; **20**; No4; pp. 721-737; 1994.
- [61] Rizwan-uddin; “PHYSICS OF DENSITY-WAVE OSCILLATIONS”; International Conference on **NEW TRENDS IN NUCLEAR SYSTEM THERMOHYDRAULICS**; Proceedings Volume 1; “Primary and Secondary Thermohydraulics”; May 30th – June 2nd; Pisa; Italy; 1994.
- [62] G.Verdù; D.Ginestar; V.Vidal; J.L.Munoz-Cobo; “*3D λ -Modes of the Neutron Diffusion Equation*”; Ann. of Nuclear Energy; Vol 21; No.7; pp.405-221; 1994.
- [63] R.Miro; D.Ginestar; G.Verdù; D.Hennig; “*A nodal modal method for the neutron diffusion equation. Application to BWR instabilities analysis*”; Ann. Of Nuclear Energy; Vol 29; pp.1171-1194; 2002.
- [64] S. Glasstone; M.C. Edlund; “The Elements of Nuclear Reactor Theory”; Fourth Printing; D.VAN NOSTRAND COMPANY, INC.; Princeton, New Jersey, Toronto, New York, London; 1952.
- [65] L.D. Hetrick; “*Dynamics of Nuclear Reactors*”; American Nuclear Society; INC. La Grange Park; Illinois USA; 1993.
- [66] M.W. Stacey; “*Nuclear Reactor Physics*”; A Wiley-Interscience Publication; John Wiley & Sons; INC.; New York, Chichester, Weinheim, Brisbane, Singapore, Toronto; 2001.
- [67] M. Ash; “*Nuclear Reactor Kinetics*”; Second Edition; McGraw-Hill, INC.; New York, St. Louis, San Francisco, Auckland, Bogotá, Guatemala, Hamburg, Johannesburg, Lisbon, London, Madrid, Mexico, Montreal, New Delhi, Panama, Paris, San Juan, Sao Paulo, Singapore, Sydney, Tokyo, Toronto; 1979.

- [68] V.G.Llorens; C.Lange; D.Hennig; R.Mirò; G.Verdù; "Feedback Reactivity Calculations Using Exact Expressions from LAMBDA-REAC Code"; Proceedings of PHYSOR'06 (ID 157537); September 10-14; Vancouver; BC; Canada 2006.
- [69] M. Ishii; X. Sun; S. Kuran; "*NUCLEAR-COUPLED FLOW INSTABILITIES AND THEIR EFFECTS ON DRYOUT*"; Final Progress Report; PU/NE-04-13; 2004.
- [70] Ishii, M.; *Thermo-fluid Dynamic Theory of Two-Phase Flow*; Eyrolles, Scientific and Medical Publication of France, Paris, 1975.
- [71] Ishii, M.; *One dimensional drift flux model and constitutive equations for relative motion between phases in various two-phase flow regimes*; Technical Report ANL-77-47; Argonne National Laboratory, 1977.
- [72] Collier, G.J.; Thome, R.J.; *Convective Boiling and Condensation*; Third Edition; Clarendon Press, Oxford, 1996.
- [73] Lahey, Jr., T.R.; Moody, J.F.; *The Thermal-Hydraulics of a Boiling Water Nuclear Reactor*; Second Edition; American Nuclear Society; La Grange Park, Illinois USA. 1993
- [74] Todreas, E.N.; Kazimi, S.M.; *Thermal Hydraulic Fundamentals*; Nuclear Systems 1; Hemisphere Publishing Corporation; A Member of the Taylor & Francis Group, New York, Washington, Philadelphia, London, 1990.
- [75] Zuber, N.; Staub, F.W.; "*An Analytical Investigation of the Transient Response of the Volumetric Concentration in a Boiling Forced-Flow System*"; Nuclear Science and Engineering; **30**; 268-278; 1967.
- [76] Zuber, N.; Staub, F.W.; "*The Propagation and the Wave Form of the Vapor Volumetric Concentration in Boiling, Forced Convection System under Oscillatory Conditions*"; J.Heat Mass Transfer; **9**; 871-895; 1966.
- [77] P. Saha; M. Ishii; N. Zuber; "An Experimental Investigation of Thermally Induced Flow Oscillations in Two-Phase Systems"; J. Heat Transfer; **98**; 616-622; 1976.
- [78] R. Wehle; A. Schmidt; S. Opel; R. Velten; *Non-linear BWR Stability Analysis*; Proceedings of the 16th International Conference on Nuclear Engineering; May 11-15; Orlando; Florida; USA; 2007.
- [79] Hennig, D.; Aguirre, C.; "Post-calculation of the stability measurement records #4 and #5 at NPP Leibstadt (Cycle 7), 1990"; PSI Technical Report, TM-41-03-15; 2003.
- [80] G.C. Park; M.Z.Podowski; M.Becker; R.T. Lahey Jr.; S.H.Peng; "*The Development of a Closed Form Analytical Model for the Stability Analysis of Nuclear-Coupled Density-Wave Oscillations in Boiling Water Nuclear Reactors*"; Nucl. Engineering and Design; **92**; pp.252-281; 1986.
- [81] M. Tsuji, K. Nishio, M. Narita, Y. Ogawa, and M. Mori, "*Stability Analysis of BWR's Using Bifurcation Theory*," J. Nucl. Sciences and Technology, 30, (11), pp. 1107-1119, 1993.
- [82] G. Grandi; K. S. Smith; "*BWR Stability Analysis with SIMULATE3K*"; Proceedings PHYSOR'02; Oct. 7-10; Seoul; Korea; 2002.
- [83] Ginestar, D.; Verdù, G.; March Leuba, J.; "*Thermal-hydraulics oscillations and numerical integration*"; Proceedings of the 9th International Topical Meeting on Nuclear Reactor thermalhydraulics (NURETH-9); USA; (ANS -2-700275); 1999.

Appendix A: Nonlinear stability analysis

Generally, stability analysis is the investigation of the temporal behaviour of the dynamical variables after an internal or external perturbation is imposed on the dynamical system, while one or more system parameters will be varied in their domain of definition. If the system is stable, all dynamical variables return to the fixed point (or in a close neighborhood of the fixed point, which is also called “Ljapunov stability” [1-3]). If the system is unstable, at least one dynamical variable is diverging in an oscillatory or exponential manner. Thereby the critical value of the system parameter(s) which separates stable fixed points from the unstable one is so-called as stability boundary.

For a mathematical description, the autonomous dynamical system

$$\frac{d}{dt} \vec{X}(t) = \vec{F}(\vec{X}(t), \gamma) \quad (\text{A1})$$

is considered [2]. Thereby, $\vec{X}(t)$ with

$$\vec{X}(t) = \begin{pmatrix} x_1(t) \\ \vdots \\ x_n(t) \end{pmatrix} \in \mathbb{R}^n \quad (\text{A2})$$

is the state vector describing the state of the dynamical system in the state space, \vec{F} with

$$\vec{F} = \begin{pmatrix} F_1 \\ \vdots \\ F_n \end{pmatrix} \quad \text{and} \quad \vec{F} : \mathbb{R}^n \times \mathbb{R} \rightarrow \mathbb{R}^n \quad \text{is } C^\infty \quad (\text{A3})$$

is a vector field describing the dynamical behaviour of the state variables and $\gamma \in \mathbb{R}^m$ is a parameter vector (also referred to as control parameter vector with m components).

Let \vec{X}_0 be the steady state solution of the dynamical system (A1) for all γ , where \vec{X}_0 is satisfying

$$\frac{d\vec{X}_0}{dt} = 0 = \vec{F}(\vec{X}_0, \gamma) \quad (\text{A4})$$

In order to get information about the stability properties of the steady state solution \vec{X}_0 and its vicinity, the dynamical system will be linearized around \vec{X}_0 . To this end, the ansatz

$$\vec{X}(t) = \vec{X}_0 + \delta\vec{X}(t) \quad (\text{A5})$$

is substituted in (A1) and a Taylor-expansion is applied

$$\begin{aligned} \underbrace{\frac{d}{dt} \vec{X}_0}_{=0} + \frac{d}{dt} \delta \vec{X} &= F(\vec{X}_0 + \delta \vec{X}, \gamma_0) \\ &= \underbrace{F(\vec{X}_0, \gamma_0)}_{=0} + \underbrace{D_x F(\vec{X}_0, \gamma_0)}_J \underbrace{[\vec{X} - \vec{X}_0]}_{=\delta \vec{X}} + \underbrace{0(\|\delta \vec{X}\|^2)}_{\approx 0} , \end{aligned} \quad (\text{A6})$$

where the linear term is taken into account only.

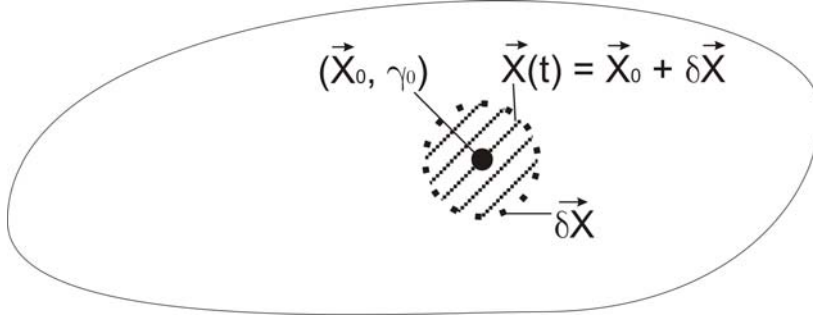


Figure 1: This figure depicts the linearization of the dynamical system (A1) around the steady state solution \vec{X}_0 . This means, the states $\vec{X}(t)$ can be approximated by the steady state solution plus a small perturbation $\delta \vec{X}(t)$ of the steady state. This method is common practice in perturbation theory [5].

The result of the linearization is given by

$$\frac{d}{dt} \delta \vec{X} = J \delta \vec{X} , \quad (\text{A7})$$

where J is the Jacobian matrix defined as

$$J = \begin{pmatrix} \frac{\partial F_1}{\partial x_1} & \dots & \frac{\partial F_1}{\partial x_n} \\ \vdots & \ddots & \vdots \\ \frac{\partial F_n}{\partial x_1} & \dots & \frac{\partial F_n}{\partial x_n} \end{pmatrix} . \quad (\text{A8})$$

Equation (A7) is the linearized system of (A1) at \vec{X}_0 . The solution of equation (A7) can be written as

$$\delta \vec{X}(t) = e^{Jt} \delta \vec{X}_0 . \quad (\text{A9})$$

Roughly speaking, the solution (A9) describes the time evolution of the small perturbation $\delta \vec{X}$ which is imposed on the steady state \vec{X}_0 at $t=t_0=0$ with $\delta \vec{X}(t=t_0) = \delta \vec{X}_0$. According to equation (A9), the time evolution of $\delta \vec{X}$ only depends on J . In turn, J depends on the parameter vector γ . This means, the local stability behaviour of the dynamical system (A1) around \vec{X}_0 depends only on the characteristic of the Jacobian matrix, from the linear point of view. It should be noted that transformation (A5) transform the singular fixed point \vec{X}_0 into the origin $\delta \vec{X} = 0$.

This is the reason that the terminologies: “the origin is stable locally” or “the origin is unstable locally” exist.

In order to evaluate (A9), the linear transformation

$$\delta\vec{X}(t) = P\vec{U}(t) \quad (\text{A10})$$

is performed in such a way that the Jacobian matrix can be transformed into the Jordan normal form [1-4]. To this end, the eigenvalue problem

$$J\vec{p}_i = \lambda_i\vec{p}_i \quad (\text{A11})$$

has to be solved, where \vec{p}_i are the eigenvectors with their corresponding eigenvalues λ_i of the Jacobian matrix. This procedure corresponds to a change of the basis vectors which span the state space of the dynamical system. The transformation matrix P can according to $P = [\vec{p}_1, \dots, \vec{p}_i, \dots, \vec{p}_n]$ be written in terms of the eigenvectors \vec{p}_i . With other words, the columns of P are the eigenvectors \vec{p}_i of the Jacobian matrix.

In the linear system (A7) the vector $\delta\vec{X}$ is substituted by ansatz (A10) and the final equation is multiplied by P^{-1} from the left hand side. The result can be written as

$$\frac{d}{dt}\vec{U} = P^{-1}JP\vec{U} = D\vec{U} \quad , \quad (\text{A12})$$

where D with

$$D = P^{-1}JP = \begin{pmatrix} \lambda_1 & \dots & \dots & \dots & 0 \\ \vdots & \ddots & & & \vdots \\ \vdots & & \begin{pmatrix} a_i & b_i \\ -b_i & a_i \end{pmatrix} & & \vdots \\ \vdots & & & \ddots & \vdots \\ 0 & \dots & \dots & \dots & \lambda_n \end{pmatrix} \quad (\text{A13})$$

is the Jacobian matrix transformed into the Jordan normal form. If all eigenvalues of J are real and distinct, matrix D will have a diagonal form [3].

The solution of (A12) can be written as

$$\vec{U}(t) = e^{D(t-t_0)}\vec{U}_0 \quad , \quad (\text{A14})$$

where $\delta\vec{X}_0 = P\vec{U}_0$. The back transformation gives

$$\delta\vec{X} = P\vec{U}(t) = Pe^{D(t-t_0)}\vec{U}_0 = Pe^{D(t-t_0)}P^{-1}\delta\vec{X}_0 \quad . \quad (\text{A15})$$

The general solution of the linearized system (A7) can be written as

$$\vec{X}(t) = \vec{X}_0 + \sum_{i=1}^n c_i \vec{P}_i e^{\lambda_i t}$$

$$\begin{pmatrix} x_1(t) \\ \vdots \\ x_n(t) \end{pmatrix} = \begin{pmatrix} x_{01}(t) \\ \vdots \\ x_{0n}(t) \end{pmatrix} + \sum_{i=1}^n c_i \begin{pmatrix} p_{i1} \\ \vdots \\ p_{in} \end{pmatrix} e^{\lambda_i t} \quad , \quad (\text{A16})$$

where the constants c_i can be calculated from the initial conditions.

From the general solution (A16) it can be seen that the stability behaviour in the vicinity of \bar{X}_0 of the linearized system depends on the real parts of the eigenvalues λ_i of J with $\lambda_i = \lambda_i(\gamma)$. According to (A16) all components $x_i(t)$ of the general solution contain all eigenvalues λ_i of J . This means, if there is at least one pair of complex conjugated eigenvalue with a positive real part, the system will be unstable. If all eigenvalues have strictly negative real parts, the system will be stable. When a selected control parameter is changed and the eigenvalue with the largest real part becomes zero, additional analyses such as Hopf bifurcation analyses are necessary. The statements

$$\begin{aligned} \operatorname{Re}(\lambda_i) < 0 &\rightarrow \text{local stable} \\ \operatorname{Re}(\lambda_i) > 0 &\rightarrow \text{local unstable} \\ \operatorname{Re}(\lambda_i) = 0 &\rightarrow \text{additional analyses are necessary} \end{aligned} \tag{A17}$$

are basic characteristics of linear systems which are expressed by the theorem of Hartmann and Großmann [1-3].

Theorem of Hartmann and Großmann: Let \bar{X}_0 be the steady state solution for a given parameter configuration γ and J be the Jacobian matrix of the dynamical system. Roughly speaking, if all eigenvalues have real parts strictly different from zero (the corresponding fixed points are so-called hyperbolic fixed points), in this case, the orbits of the nonlinear dynamical system can be mapped (locally, homeomorphic) on the orbits of the linear system. This means, if the fixed point is a hyperbolic one, the stability behaviour of the nonlinear dynamical system can be described locally by the linear system.

This theorem is of particular importance because it satisfies the application of linear analysis methods for stability analyses of nonlinear dynamical systems. But if the condition of the theorem is not fulfilled, this means $\operatorname{Re}(\lambda_i) = 0$, additional investigations such as bifurcation analyses are necessary.

In general, the stability boundary which separates linear stable fixed points from linear unstable one, is a multi dimensional structure in the m -dimensional parameter space. The task "calculation of the stability boundary" means: 1) selection of one or more parameters γ_k which will be varied within the domain of definitions and 2) calculate the critical parameters $\gamma_{k,c}$ for which $\operatorname{Re}(\lambda_i) = 0$ with $\lambda_i(\gamma_{k,c})$. This means, the parameter γ_k will be varied as long as the condition

$$\begin{aligned} \frac{d}{dt} \bar{X}(t) &= 0 \\ \operatorname{Re}(\det[J - i\omega I]) &= 0 \\ \operatorname{Im}(\det[J - i\omega I]) &= 0 \end{aligned} \tag{A18}$$

is fulfilled for $\gamma_{k,c}$. In condition (A18) there is i with ($i^2 = -1$) the complex number, ω is the frequency of the oscillation, Re and Im stand for real and imaginary parts, respectively and \det is the determinant.

Hopf bifurcation theorem

In the framework of the nonlinear BWR stability research (in particular, the semi-analytical bifurcation analysis), the so-called Hopf bifurcations play a dominant role. The occurrence of such type of dynamical bifurcations is ensured by the Hopf theorem [1-4]. This theorem, which is also called Poincarè-Andronov-Hopf bifurcation (PAH-B) theorem, guarantees the existence of stable and unstable periodic solutions of nonlinear differential equations if certain conditions are satisfied [4]. For a mathematical description, the autonomous dynamical system (A1) and its steady state solution \bar{X}_0 is considered. If the following Hopf conditions are fulfilled:

- 1) For a critical parameter $\gamma_{k,c}$ there exists a pair of complex conjugate eigenvalues $\lambda_1(\gamma_{k,c}) = \pm i\omega$, (this means $\text{Re}(\lambda_1(\gamma_{k,c})) = 0$)
- 2) all the other eigenvalues have strictly negative real parts ($\forall \lambda_i, i \neq 1 \rightarrow \text{Re}(\lambda_i(\gamma_{k,c})) < 0$), and
- 3) $\frac{\partial \lambda(\gamma_k = \gamma_{k,c})}{\partial \gamma_k} \neq 0$

a family of periodic solutions

$$\bar{X}(t, \gamma) = \bar{X}_0(\gamma_{k,c}) + \varepsilon \text{Re} \left[e^{\frac{i2\pi t}{T(\varepsilon)}} \bar{p}_1 \right] + 0(\varepsilon^2) \quad (\text{A19})$$

of (A1) with small amplitude ε exist in \bar{X}_0 for $\gamma_{k,c}$ [4], where \bar{p}_1 is the eigenvector of the linearized system associated with the pair of complex conjugated eigenvalues responsible for the bifurcation (λ_1) and T is the period of the oscillation.

To summarize, from the linear point of view, the condition $\text{Re}(\lambda_i(\gamma_{k,c})) = 0$ separates stable fixed points ($\text{Re}(\lambda_i(\gamma_k)) < 0$ with $\gamma_k < \gamma_{k,c}$ or $\gamma_k > \gamma_{k,c}$) from the unstable one ($\text{Re}(\lambda_i(\gamma_k)) > 0$ with $\gamma_k > \gamma_{k,c}$ or $\gamma_k < \gamma_{k,c}$). Note, the linear analysis is possible as long as the theorem of Hartmann and Goßmann is fulfilled. In nonhyperbolic fixed points ($\text{Re}(\lambda_i(\gamma_{k,c})) = 0$) additional analyses are necessary. The Hopf theorem implies that periodical solutions exist in fixed points where the Hopf conditions are satisfied. The stability properties of the periodical solutions can be analysed by applying the Foquet theory.

Floquet theory

In order to get information about the stability property of the periodic solution, the (linear) Floquet theory is applied where the so-called Floquet exponent (Floquet parameter) β appears [2,4] which determine the stability of the periodic solution. If $\beta < 0$, the periodic solution is stable (supercritical bifurcation) while if $\beta > 0$, the periodic solution is unstable (subcritical bifurcation) [2,4]. In simpler terms, the Floquet parameter can be interpreted to be a stability indicator for limit cycles and is a result of a special technique from the nonlinear dynamics.

If one or more system parameters γ_k are varied and a Hopf bifurcation exist for $\gamma_{k,c}$ the system bifurcates from an equilibrium solution \vec{X}_0 to a periodic solution (denoted by \vec{X}). It is assumed that the considered dynamical system is time continuous one. The solution of $\dot{\vec{X}} = \vec{F}(\vec{X})$ is period with least period T if $\vec{X}(t+T) = \vec{X}(t)$ and $\vec{X}(t+\tau) \neq \vec{X}(t)$ for $0 < \tau < T$. In order to analysis the stability properties of the periodic solution, a small disturbance $\vec{Y}(t)$ is superimposed on \vec{X} , resulting in

$$\vec{X}(t) = \vec{X}(t) + \vec{Y}(t) \quad . \quad (\text{A20})$$

Substituting (A20) into (A1), expanding the result in a Taylor series about \vec{X} and retaining only the linear term in the perturbation lead to

$$\begin{aligned} \frac{d}{dt} \vec{X}(t) + \frac{d}{dt} \vec{Y}(t) &= F(\vec{X} + \vec{Y}(t), \gamma_0) \\ \underbrace{\frac{d}{dt} \vec{X}(t) - F(\vec{X}, \gamma_0)}_0 + \frac{d}{dt} \vec{Y}(t) &= \underbrace{D_x F(\vec{X}, \gamma_0)}_{A(t, \gamma_0)} \underbrace{[\vec{X} - \vec{X}]}_{\approx \vec{Y}(t)} + \underbrace{0(\|\vec{Y}(t)\|^2)}_{\approx 0} \end{aligned} \quad (\text{A21})$$

$$\frac{d}{dt} \vec{Y}(t) = A(t, \gamma_0) \vec{Y}(t) \quad ,$$

where $A(t, \gamma_0)$ is a matrix of the first partial derivatives of the vector field F and is periodic in time with the period T . It should be emphasized that the stability analysis of the periodic solution is local because of the linearization in $\vec{Y}(t)$.

The system (A21) is a n -dimensional linear system with n linearly independent solutions \vec{Y}_i summarized in the form of an $n \times n$ matrix $\hat{Y}(t) = [\vec{Y}_1(t), \vec{Y}_2(t), \dots, \vec{Y}_n(t)]$ where $i = 1, 2, \dots, n$. The linear independent solutions are referred to as fundamental set of solutions. Matrix \hat{Y} satisfies the matrix equation

$$\frac{d}{dt} \hat{Y}(t) = A(t, \gamma_0) \hat{Y}(t) \quad . \quad (\text{A22})$$

Because of the periodicity of $A(t, \gamma_0)$ it can be written as $A(\tau, \gamma_0) = A(\tau - T, \gamma_0)$ and thus

$$\frac{d}{dt} \hat{Y} = A(\tau - T, \gamma_0) \hat{Y} = A(\tau, \gamma_0) \hat{Y} \quad , \quad (\text{A23})$$

where the dependent variable was changed according to $\tau = t + T$. If matrix $\hat{Y}(t)$ is a fundamental matrix solution, then $\hat{Y}(t+T)$ is also a fundamental matrix solution. This means, the matrix $\hat{Y}(t+T)$ can be expressed as linear combination

$$\hat{Y}(t+T) = \hat{Y}(t) \cdot \hat{\Phi} \quad , \quad (\text{A24})$$

where $\hat{\Phi}$ is so-called monodromy matrix. The monodromy matrix is an $n \times n$ -matrix with constant coefficients and is not unique. $\hat{\Phi}$ can be specified by the initial condition $\hat{Y}(0) = \hat{I}$ and thus

$$\begin{aligned} \hat{Y}(0+T) &= \hat{Y}(T) = \hat{I} \cdot \hat{\Phi} = \hat{\Phi} \\ \underline{\underline{\hat{Y}(T)}} &= \underline{\underline{\hat{\Phi}}} \quad , \end{aligned} \quad (\text{A25})$$

where \hat{I} is $n \times n$ -identity matrix.

Furthermore, the transformation $\hat{Y}(t) = V(t) \cdot \hat{P}^{-1}$ (matrix \hat{P} is different from matrix P introduced in transformation (A10)) can be introduced, where \hat{P} is an $n \times n$ -matrix with constant coefficients. This transformation can be substituted in (A24). It follows

$$\begin{aligned} \hat{Y}(t+T) &= \hat{Y}(t) \cdot \hat{\Phi} \\ &= V(t) \cdot \hat{P}^{-1} \hat{\Phi} = V(t+T) \cdot \hat{P}^{-1} \end{aligned} \quad (\text{A26})$$

and thus

$$V(t+T) = V(t) \cdot \underbrace{\hat{P}^{-1} \hat{\Phi} \hat{P}}_{\hat{\Psi}} = V(t) \cdot \hat{\Psi} \quad . \quad (\text{A27})$$

The back transformation gives

$$V(t) = \hat{Y}(t) \hat{P} \quad (\text{A28})$$

and

$$V(t+T) = \hat{Y}(t+T) \hat{P} \quad . \quad (\text{A29})$$

Matrix \hat{P} should be chosen in such a way that the matrix $\hat{\Psi}$ has the simplest possible form, depending on the eigenvalues and eigenvectors of $\hat{\Phi}$. Let φ_m be the eigenvalues of $\hat{\Phi}$. If all eigenvalues φ_m are distinct, matrix \hat{P} can be selected in such a way that the eigenvectors \vec{p}_m are the columns of \hat{P} with $\hat{P} = [\vec{p}_1, \dots, \vec{p}_n]$. Thus the eigenvalue problem

$$\hat{\Phi} \vec{p}_m = \varphi_m \vec{p}_m \quad (\text{A30})$$

is to be solved. Afterwards, $\hat{\Psi}$ with

$$\hat{\Psi} = \begin{pmatrix} \varphi_1 & \cdots & \cdots & \cdots & 0 \\ \vdots & \varphi_2 & & & \vdots \\ \vdots & & \ddots & & \vdots \\ \vdots & & & \ddots & \vdots \\ 0 & \cdots & \cdots & \cdots & \varphi_n \end{pmatrix} \quad (\text{A31})$$

has a diagonal form.

The eigenvalues φ_m of the monodromy matrix are called Floquet multiplier and provides a measure of the local orbital divergence or convergence along a particular direction. If all φ_m are distinct, then

$$v_m(t+T) = \varphi_m v_m(t) \tag{A32}$$

for $m = 1, 2, \dots, n$, where the v_m are the components of V . Generalization of (A32) gives

$$v_m(t+NT) = \varphi_m^N v_m(t) \tag{A33}$$

The evaluation of (A33) can be summarized as

$$\begin{aligned} |\varphi_m| < 1 &\rightarrow v_m \rightarrow 0 \\ |\varphi_m| > 1 &\rightarrow v_m \rightarrow \infty \\ |\varphi_m| = 1 &\rightarrow v_m = \text{const with } T \\ |\varphi_m| = -1 &\rightarrow v_m = \text{const with } 2T \end{aligned} \tag{A34}$$

Hence, if $|\varphi_m| = 1$, v_m is periodic with T and if $|\varphi_m| = -1$, v_m has the period of $2T$. If only one Floquet multiplier is located on the unit circle of the complex plane (e.g. $|\varphi_m| = 1$ and $|\varphi_m| = -1$), the periodic solution is referred to as a hyperbolic periodic solution. A hyperbolic periodic solution is asymptotically stable, when all the other Floquet multiplier φ_i with $i \neq m$ are inside the unit circle of the complex plane. A hyperbolic periodical solution is unstable, when one or more of the other Floquet multiplier are located outside the unit circle. If **all** φ_i for $i = 1, \dots, n$ and $i \neq m$ (φ_m is located on the unit circle) lie **outside the unit circle**, then all trajectories of the periodical solution are repelled from it, thus the periodical solution corresponds to an unstable limit cycle or a period repeller. On the other hand, an unstable hyperbolic periodical solution is called unstable limit cycle of the saddle type, when some of the Floquet multiplier are located inside the unit circle of the complex plane.

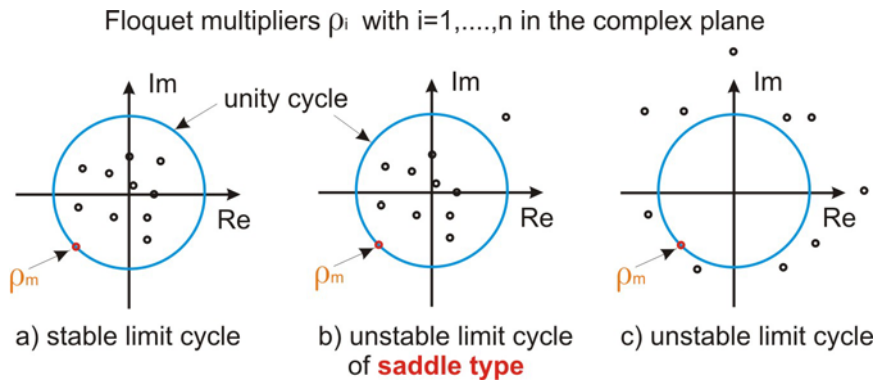


Figure 2: Three fundamental scenarios for hyperbolic periodical solutions

Figure 2 depicts three fundamental scenarios for hyperbolic periodical solutions (φ_m is located on the unit circle for all three scenarios) and the corresponding locations of the Floquet multipliers:

- a) All Floquet multipliers φ_i with $i \neq m$ lie inside the unit circle. Thus the limit cycle is asymptotic stable.
- b) only one of the Floquet multipliers lie outside the unit circle. All the others lie inside the unit circle. In this case, the limit cycle is unstable of the saddle type.

This means, the limit cycle is locally unstable but global considerations are necessary because, in this case, the system behaviour cannot be determined from local considerations alone [2,6,7]. Recalling, the name “saddle” used in bifurcation analysis, is always connected with creation and destroying of solutions (“annihilating”, “destroying”, “colliding”, “exploding” solutions such as saddle-node bifurcation of cycles also called turning points) [2,7]. E.g. in the one dimensional case, fixed points can be created or destroyed.

- c) In this case all Floquet multipliers φ_i with $i \neq m$ are located outside the unit circle. The hyperbolic periodical solution is unstable [2].

A periodical solution is called nonhyperbolic periodical solution if two of the Floquet multipliers are located on the unit circle of the complex plane [2]. A nonhyperbolic periodical solution is unstable, if one or more of the Floquet multiplier are located outside the unit circle. But a nonlinear analysis is necessary if all the Floquet multiplier of the nonhyperbolic periodical solution lie inside the unit circle [2].

Equation (A32) can be extended as

$$e^{-\beta_m(t+T)}v_m(t+T) = \varphi_m e^{-\beta_m(t+T)}v_m(t) \quad (\text{A35})$$

where β_m are called the characteristic (or Floquet) exponents and can be defined such that

$$\varphi_m = e^{\beta_m T} \quad . \quad (\text{A36})$$

Hence, equation (A35) can be rewritten as

$$e^{-\beta_m(t+T)}v_m(t+T) = e^{-\beta_m t}v_m(t) \quad . \quad (\text{A37})$$

Equation (A37) show that $e^{-\beta_m t}v_m(t)$ is a period vector and thus v_m can be written in the normal or Floquet form

$$v_m(t) = e^{-\beta_m t}\phi_m(t) \quad , \quad (\text{A38})$$

where $\phi_m(t+T) = \phi_m(t)$. From this equation can be seen that if the real part of β_m is negative then $v_m \rightarrow 0$ for $t \rightarrow \infty$. On the other hand, if the real part of β_m is positive, then $v_m \rightarrow \infty$ for $t \rightarrow \infty$.

The Floquet exponents β_m are defined only after the solution of (A21) is known. In the scope of the present stability research, the Floquet exponents of the periodical solution are calculated numerically by BIFDD. In order to determine the solution of (A21), the Floquet form (A38) can be used

$$\vec{Y}(t) = e^{-\beta t}\phi(t) \quad , \quad (\text{A39})$$

where $\phi(t+T) = \phi(t)$. After substituting (A39) into (A21), the result can be rewritten into the form

$$\dot{\phi} = [A(t, \gamma_0) - \beta I]\phi \quad (\text{A40})$$

where ϕ is expanded in a Fourier series and is usually carried out numerically. A more in detail description is given in [2].

To summarize, every fundamental matrix solution of (A21) can be written in the form (A39) for some $n \times n$ T-periodic (differentiable) matrix $\phi(t)$ and some constant matrix B . The eigenvalues of B are called characteristic exponents or Floquet exponents β_m determining the stability of periodical solutions arising in a Hopf-Bifurcation point. Hence, in the framework of the bifurcation analyses with BIFDD, one of the crucial tasks is the estimation of β_m .

Center manifold theorem

In the following the linearized dynamical system (A7) corresponding to the fixed point \bar{X}_0 is considered. Generally, a linear system can be broken into its dynamically invariant parts. The eigenspaces of a linear flow or map are invariant subspaces of the dynamical system (A1) [2]. The dynamical behaviour on all subspaces is determined by the eigenvalues which corresponds to these subspaces.

If the Jacobian matrix J of the system (A7) has s eigenvalues with negative real parts, c eigenvalues with zero real parts and u eigenvalues with positive real parts, then the space \mathbb{R}^n can be represented by the sum of the three subspaces E^s , E^c and E^u according to $\mathbb{R}^n = E^s \otimes E^u \otimes E^c$. Each subspace is defined by

$$\begin{aligned} E^s &= \text{span}\{\bar{p}_1, \bar{p}_2, \dots, \bar{p}_s\} \quad \text{with} \quad \text{Re}(\lambda_s) < 0 \\ E^u &= \text{span}\{\bar{p}_{s+1}, \dots, \bar{p}_{s+u}\} \quad \text{with} \quad \text{Re}(\lambda_u) > 0 \\ E^c &= \text{span}\{\bar{p}_{s+u+1}, \dots, \bar{p}_{s+u+c}\} \quad \text{with} \quad \text{Re}(\lambda_c) = 0 \end{aligned} \tag{A41}$$

where $\bar{p}_1, \bar{p}_2, \dots, \bar{p}_s$ are the s eigenvectors associated with the s eigenvalues whose real parts are negative, $\bar{p}_{s+1}, \dots, \bar{p}_{s+u}$ are the u eigenvectors associated with the u eigenvalues whose real parts are positive and $\bar{p}_{s+u+1}, \dots, \bar{p}_{s+u+c}$ are the c eigenvectors associated with the c eigenvalues whose real parts are positive. This means, each of the subspaces is spanned by the corresponding eigenvectors. The subspaces E^s , E^c and E^u are called stable, center and unstable subspaces or local manifolds. The main characteristic of the local invariant subspaces is that the solution of the linear system which is initiated in one of the three invariant subspaces remains in this subspace for all times. In a nonlinear system, the stable manifold is denoted as W^s , the center manifold is denoted as W^c and the unstable manifold is denoted as W^u .

Generally, simplification methods are often necessary to allow the investigation of dynamical systems [2]. One class of simplification methods deals with techniques of reducing the order of the system equation and/or eliminating as many nonlinearities as possible in the system of equations. The center manifold reduction technique is one of these methods.

Recalling, when a dynamical system loses its stability, the number of eigenvalues and eigenvectors which are responsible for this change is typically small. E.g. in the Hopf bifurcation case, only one pair of complex conjugated eigenvalues are associated with the bifurcating solution. Hence the crucial point of the center manifold re-

duction technique is that the dynamics of the system near the bifurcation point is governed by the evolution of these critical modes (c eigenvalues), while the stable modes (s eigenvalues) can be considered to be “enslaved” (or they are following a passive fashion). With other words, when $E^u = \emptyset \rightarrow \mathbb{R}^n = E^s \otimes E^c$, the dynamical behaviour of the n -dimensional dynamical system can be described by the c -dimensional system in a close neighbourhood of the fixed point undergoing the bifurcation. In the Hopf bifurcation case the dynamics of the n -dimensional dynamical system can be reduced to a two-dimensional system. Thus, the center subspace is spanned according to

$$E^c = \text{span}\{\bar{p}_1, \bar{\bar{p}}_1\} \quad \text{with} \quad \lambda_1(\gamma_{k,c}) = \pm i\omega \quad , \quad (\text{A42})$$

where $\bar{p}_1 = \text{Re}(\bar{p}_1) + i \text{Im}(\bar{p}_1)$ and $\bar{\bar{p}}_1 = \text{Re}(\bar{p}_1) - i \text{Im}(\bar{p}_1)$. Considering the linearized system, the solution of (A12) can be written as

$$\vec{U}(t) = \begin{pmatrix} u_1(t) \\ \vdots \\ u_n(t) \end{pmatrix} = \begin{pmatrix} \vec{u}_s(t) \\ \vec{u}_c(t) \end{pmatrix} \quad (\text{A43})$$

where $\vec{u}_c(t)$

$$\vec{u}_c(t) = \begin{pmatrix} e^{i\omega t} u_{c,0} \\ e^{-i\omega t} u_{c,0} \end{pmatrix} \quad (\text{A44})$$

and $\vec{u}_s(t)$

$$\vec{u}_s(t) = \begin{pmatrix} \vdots \\ e^{\lambda_i t} u_{i,0} \\ \vdots \end{pmatrix} \quad (\text{A45})$$

$\forall \lambda_i, i=1, \dots, s \rightarrow \text{Re}(\lambda_i(\gamma_{k,c})) < 0$. Thus, for $t \rightarrow \infty$ the elements of the vector $\vec{u}_s(t)$ becomes zero $\vec{u}_s(t) \rightarrow \vec{0}$ and the solution is collapsed to $\vec{u}_c(t)$. This means, all orbits are converging to the center manifold E^c for $t \rightarrow \infty$, where W^c is tangent to E^c . In the case of ideal smoothness of W^c , both, W^c and E^c are equal. A more in detail description is given in [1-4].

Lindstedt Poincarè asymptotic expansion

Generally, exact solutions are rare in many branches of dynamical problems [5]. Hence, approximate solutions of the problems are necessary. There are numerous analytical and numerical techniques to determine solution of the problem. E.g. the application of perturbation theory is common practice. In nonlinear system analysis by applying perturbation theory, it is important to account for the nonlinear dependence of the frequency on the nonlinearity. It is turned out, that each expansion that does not account for a nonlinear frequency is doomed to failure [5]. Hence, a number of techniques that yield uniformly valid expansions have been developed in the past.

In the scope of the bifurcation analysis with BIFDD, the so-called Lindstedt Poincaré asymptotic expansion is applied. The main advantage of this method is to account for the frequency dependence on the nonlinear terms [5]. To this end, the transformation $\bar{t} = \omega t$ is introduced, where ω is the actual frequency of the system. According to

$$\frac{d}{dt} = \frac{d\bar{t}}{dt} \frac{d}{d\bar{t}} = \frac{d(\omega t)}{dt} \frac{d}{d\bar{t}} = \omega \frac{d}{d\bar{t}} \quad (\text{A46})$$

the frequency ω of the system appears explicitly in the differential equation system, where both the state variable $\vec{X}(\bar{t})$ and ω are unknowns. Hence, the solutions for them are approximated by the expansion in the form of power series in terms of a small perturbation ε as

$$\begin{aligned} \vec{X}(\bar{t}) &= \vec{X}_0 + \varepsilon \vec{X}_1(\bar{t}) + \varepsilon^2 \vec{X}_2(\bar{t}) + \dots + \varepsilon^k \vec{X}_k(\bar{t}) + \dots \\ \frac{1}{\omega} &= \frac{1}{\omega_0} + \varepsilon \tau_1 + \varepsilon^2 \tau_2 + \dots + \varepsilon^k \tau_k + \dots \\ t &= \left(\frac{1}{\omega_0} + \varepsilon \tau_1 + \varepsilon^2 \tau_2 + \dots + \varepsilon^k \tau_k + \dots \right) \bar{t}, \end{aligned} \quad (\text{A47})$$

where τ_i can be considered to be a correction factors for the oscillation frequency. Furthermore, the quantity μ is introduced and is defined as $\mu = \gamma_k - \gamma_{k,c}$ the distance between the actual value γ_k and the critical value $\gamma_{k,c}$ of the bifurcation parameter. μ is expanded as

$$\mu = \varepsilon \mu_1 + \varepsilon^2 \mu_2 + \dots + \varepsilon^k \mu_k + \dots \quad (\text{A48})$$

and thus γ_k can be written as

$$\gamma_k = \gamma_{k,c} + \varepsilon \mu_1 + \varepsilon^2 \mu_2 + \dots + \varepsilon^k \mu_k + \dots \quad (\text{A49})$$

The Floquet exponent which determines the stability of the periodical solution is expanded as

$$\beta = \varepsilon \beta_1 + \varepsilon^2 \beta_2 + \dots + \varepsilon^k \beta_k + \dots \quad (\text{A50})$$

Notice, the solutions after applying perturbation theory are only valid for small ε . Thus, the predictions of the bifurcation analysis are only valid for small distance μ from the critical value $\gamma_{k,c}$ in the bifurcation diagram.

To summarize, the transformation $\bar{t} = \omega t$ and the expansions (A47) to (A50) are substituted in the equation system that results after applying the center manifold reduction. As will be discussed below, this two dimensional equation system will be transformed into the Poincaré normal form by applying the near identity transformation method.

Poincarè normal form

According to the definition given in [2], normal forms of bifurcations are simplified system of equations that approximates the dynamics of the system in the vicinity of the bifurcation point. After the application of simplification techniques, the resulting equation system can be transformed into the specific normal form of the bifurcation. As described above, if the Hopf theorem is satisfied, the nonlinear equation system can be reduced to a two-dimensional nonlinear equation system by applying the center manifold reduction approach [1-5]. The resulting equation system, will be transformed into the Poincarè normal form [2] by applying a near identity transformation. From this equation system parameters (in particular the Floquet exponents) which determine the stability properties of the fixed point, can be extracted numerically by employing BIFDD.

The Poincarè normal form is defined as

$$\begin{aligned}\frac{dx_1}{dt} &= \alpha x_1 - \omega x_2 + [\operatorname{Re}(c_1)x_1 - \operatorname{Im}(c_1)x_2][x_1^2 + x_2^2] \\ \frac{dx_2}{dt} &= \omega x_1 + \alpha x_2 + [\operatorname{Re}(c_1)x_2 - \operatorname{Im}(c_1)x_1][x_1^2 + x_2^2]\end{aligned}\tag{A51}$$

where α and ω are real and imaginary parts of the pair of complex conjugated eigenvalues of the Jacobian matrix of the two dimensional system of equations. The coefficient c_1 is a complicated term which is calculated numerically by BIFDD. c_1 is the result of the application of center manifold reduction technique and transformation of the resulting equation system into the Poincarè normal form. Thus the coefficient comprises all information which are necessary to evaluate the stability properties of the periodical solution occurring in the Hopf bifurcation point. Finally, the Floquet parameter β_2 , μ_2 and τ_2 can be calculated as

$$\begin{aligned}\beta_2 &= 2 \cdot \operatorname{Re}[c_1(\gamma_c)] \\ \mu_2 &= -\frac{\operatorname{Re}[c_1(\gamma_c)]}{\alpha'(\gamma_c)} \\ \tau_2 &= -\frac{\operatorname{Im}[c_1(\gamma_c) + \mu_2 \omega'(\gamma_c)]}{\omega_0}\end{aligned}\tag{A52}$$

where τ_2 is a correction of the oscillation frequency and μ_2 relates the oscillation amplitude to the value $\gamma_{k,c}$ of the bifurcation parameter as

$$\varepsilon = \sqrt{\frac{\gamma_k - \gamma_{k,c}}{\mu_2}}.\tag{A53}$$

A more in detail description is given in [1-3].

Summary

In order to analyse the stability behaviour of nonlinear dynamical systems, linear stability analysis can be applied locally in fixed points where the theorem of Hartmann and Großmann is fulfilled. It should be emphasized that in this case, the results of the linear analysis of the nonlinear system are only valid in the neighbourhood of the considered fixed point. When the theorem of Hartmann and Großmann is not fulfilled, additional investigations are necessary. In the scope of this work, Hopf bifurcation analysis with the bifurcation code BIFDD is applied.

The Hopf bifurcation analysis using BIFDD starts with the selection of the iteration and bifurcation parameter. The iteration parameter will be varied in the interval defined by user. For each iteration step, BIFDD computes the critical value $\gamma_{k,c}$ of the bifurcation parameter where the Hopf bifurcation occurs and thus a periodic solution exists. Up to the present computation of $\gamma_{k,c}$ linear analysis is performed. But for the critical value $\gamma_{k,c}$ the considered fixed point is a nonhyperbolic one. For the further nonlinear analysis, center manifold reduction and Lindsted Poincarè asymptotic expansion techniques are applied. The resulting two dimensional equation system is transformed into the Poincarè normal form by employing the near identity transformation method. Finally, the Floquet parameter and all the other parameters characterizing the nature of the bifurcation can be computed from the Poincarè normal form.

To summarize, in the scope of the bifurcation analysis using BIFDD, the nonlinear system behaviour is determined only by local considerations. This means, global phenomena cannot be recognized by this theory. E.g. BIFDD applies the Floquet theory only for the resulting two dimensional equation system after the center manifold reduction is performed. Consequently, there are only two Floquet exponents, β_1 and β_2 . The first one is equal to zero $\beta_1 = 0$ (because the corresponding Floquet multiplier is located on the unit circle $|\varphi_1| = 1$) and the second one is either inside or outside the unit circle. If the second Floquet multiplier lie outside the unit circle $|\varphi_2| > 1$ which corresponds to a positive second Floquet exponent $\beta_2 > 0$ then information about the locations of all the other Floquet multipliers of the n -dimensional system are not known. In this case, it is not possible to keep apart scenario b) (unstable limit cycle of saddle type) and scenario c) (unstable limit cycle) depicted in Figure 2. In order to study the system behaviour more far away from the bifurcation point, numerical integration is necessary.

Literature

- [1] J. Guckenheimer and P. Holmes, "*Nonlinear Oscillation, Dynamical Systems, and Bifurcation in Vector Fields*," Applied Mathematical Sciences 42, Springer Verlag, 1984.
- [2] A. Neyfeh and B. Balachandran, "*Applied nonlinear dynamics: analytical, computational, and experimental methods*," John Wiley & Sons, Inc., New York, 1995
- [3] M. W. Hirsch; S. Smale; *Differential Equations, Dynamical Systems, and Linear Algebra*; ACADEMIC PRESS, INC; 1974.
- [4] D. Hassard, D. Kazarinoff, and Y-H Wan, "*Theory and Applications of Hopf Bifurcation*," Cambridge University Press, New York, 1981.
- [5] A. Neyfeh; *Introduction to Perturbation Techniques*; John Wiley & Sons; 1981.
- [6] G. Nicolis; "*Introduction to nonlinear science*"; Cambridge University Press; 1995.
- [7] S. H. Strogatz; "*Nonlinear dynamics and chaos*"; Addison-Wesley Publishing Company; 1994.

Appendix B: ROM description

1.1 Neutronkinetic model

The neutron kinetics model is based on the following assumptions:

- 1) The neutron kinetics model is based on an effective two energy groups (thermal and fast neutrons).
- 2) Spatial mode expansion approach of the neutron flux in terms of lambda modes (λ -modes).
- 3) Only the first two modes (fundamental and the first mode) are considered.
- 4) Only an effective one group of delayed neutron precursors is considered.
- 5) The contribution of the delayed neutron precursors to the feedback reactivity is neglected.

Taking into account these assumptions, four mode kinetic equations could be developed, coupled with the equations of the heat conduction and the thermal-hydraulic via the feedback reactivity terms (void and Doppler feedback reactivities).

The time dependent two-group neutron diffusion equation can be written compactly as

$$[\mathbf{v}^{-1}] \cdot \frac{\partial \vec{\Phi}(\vec{r}, t)}{\partial t} = \left[(1 - \beta) \cdot \hat{\mathbf{F}}(\vec{r}, t) - \hat{\mathbf{L}}(\vec{r}, t) \right] \cdot \vec{\Phi}(\vec{r}, t) + \sum_{l=1}^6 \lambda_l \cdot C_l(\vec{r}, t) \cdot \vec{X}_l^v \quad (\text{B1})$$

$$\frac{\partial}{\partial t} C_l(\vec{r}, t) \vec{X}_l^v = \beta_l \hat{\mathbf{F}} \cdot \vec{\Phi}(\vec{r}, t) - \lambda_l \cdot C_l(\vec{r}, t) \vec{X}_l^v$$

where $\vec{X}_l^v = \begin{bmatrix} 1 \\ 0 \end{bmatrix}$ [1-5].

$\vec{\Phi}(\vec{r}, t)$ is the neutron flux vector consisting of

$$\vec{\Phi}(\vec{r}, t) = \begin{bmatrix} \Phi_1(\vec{r}, t) \\ \Phi_2(\vec{r}, t) \end{bmatrix} \quad (\text{B2})$$

the fast (first component) and thermal neutron fluxes (second component), $\hat{\mathbf{L}}$ is the net-loss operator including leakage by diffusion, scattering and absorption, and $\hat{\mathbf{F}}$ is the fission production operator. λ_l, C_l and β_l are the decay constants, concentrations and delayed neutron fractions, respectively, for the l -th delayed neutron precursor group [6].

Next, the operators are presented (for two energy groups). The net-loss operator $\hat{\mathbf{L}}$ can be written as

$$\hat{\mathbf{L}}(\vec{r}, t) = \begin{bmatrix} -\nabla(D_1(\vec{r}, t)\nabla) + \Sigma_{1 \rightarrow 2}^s + \Sigma_1^a & 0 \\ -\Sigma_{1 \rightarrow 2}^s & -\nabla(D_2(\vec{r}, t)\nabla) + \Sigma_2^a \end{bmatrix} \quad (\text{B3})$$

where ∇ is the Nabla operator, D_1 is the diffusion constant of the first group, D_2 is the diffusion constant of the second group, Σ_1^a is the macroscopic absorption cross section of the first group, Σ_2^a is the macroscopic absorption cross section of the second group and $\Sigma_{1 \rightarrow 2}^s$ is the macroscopic scattering (from the first into the second energy group) cross section. The fission production operator \hat{F} is defined as

$$\hat{F} = \begin{bmatrix} \nu \Sigma_1^f & \nu \Sigma_2^f \\ 0 & 0 \end{bmatrix} \quad (\text{B4})$$

with Σ_1^f the macroscopic fission cross section of the first group, Σ_2^f the macroscopic fission cross section of the second group and ν the number of neutrons per fissions. The matrix $[v^{-1}]$ in (B1) is called neutron inverse velocity matrix and is defined as

$$[v^{-1}] = \begin{bmatrix} v_1^{-1} & 0 \\ 0 & v_2^{-1} \end{bmatrix} \quad (\text{B5})$$

where v_1 and v_2 are the neutron velocities corresponding to the two neutron energy groups.

By using the introduced operators, the time dependent two-group neutron diffusion equation can be written as

$$\begin{aligned} & \begin{bmatrix} v_1^{-1} & 0 \\ 0 & v_2^{-1} \end{bmatrix} \frac{d}{dt} \begin{bmatrix} \Phi_1(\vec{r}, t) \\ \Phi_2(\vec{r}, t) \end{bmatrix} = \\ & \begin{bmatrix} (1-\beta)\nu\Sigma_1^f & (1-\beta)\nu\Sigma_2^f \\ 0 & 0 \end{bmatrix} \cdot \begin{bmatrix} -\nabla(D_1(\vec{r}, t)\nabla) + \Sigma_{1 \rightarrow 2}^s + \Sigma_1^a & 0 \\ -\Sigma_{1 \rightarrow 2}^s & -\nabla(D_2(\vec{r}, t)\nabla) + \Sigma_2^a \end{bmatrix} \cdot \begin{bmatrix} \Phi_1(\vec{r}, t) \\ \Phi_2(\vec{r}, t) \end{bmatrix} \\ & + \begin{bmatrix} \sum_{l=1}^6 \lambda_l \cdot C_l(\vec{r}, t) \\ 0 \end{bmatrix} \end{aligned} \quad (\text{B6})$$

and the precursor concentration equation can be expressed accordingly as

$$\frac{\partial}{\partial t} (C_l(\vec{r}, t)) \begin{bmatrix} 1 \\ 0 \end{bmatrix} = \beta_l \begin{bmatrix} \nu \Sigma_1^f & \nu \Sigma_2^f \\ 0 & 0 \end{bmatrix} \cdot \begin{bmatrix} \Phi_1(\vec{r}, t) \\ \Phi_2(\vec{r}, t) \end{bmatrix} - \lambda_l \cdot C_l(\vec{r}, t) \begin{bmatrix} 1 \\ 0 \end{bmatrix} . \quad (\text{B7})$$

The evaluation of (B6) and (B7) lead to the neutron diffusion equation corresponding to the first group

$$\begin{aligned} & v_1^{-1} \frac{d}{dt} \Phi_1(\vec{r}, t) = \\ & \left(\nabla(D_1\nabla) - \Sigma_{1 \rightarrow 2}^s - \Sigma_1^a \right) \Phi_1(\vec{r}, t) + (1-\beta)\nu \left[\Sigma_1^f \Phi_1(\vec{r}, t) + \Sigma_2^f \Phi_2(\vec{r}, t) \right] + \sum_{l=1}^6 \lambda_l \cdot C_l(\vec{r}, t), \end{aligned} \quad (\text{B8})$$

the neutron diffusion equation corresponding to the second group

$$v_2^{-1} \frac{d}{dt} \Phi_2(\vec{r}, t) = \Sigma_{1 \rightarrow 2}^s \Phi_1(\vec{r}, t) + \left(\nabla(D_2\nabla) - \Sigma_2^a \right) \Phi_2(\vec{r}, t) \quad (\text{B9})$$

and to the 6 precursor concentration equations

$$\frac{\partial}{\partial t}(C_l(\vec{r}, t)) = \beta_l v \left[\Sigma_1^f \Phi_1(\vec{r}, t) + \Sigma_2^f \Phi_2(\vec{r}, t) \right] - \lambda_l \cdot C_l(\vec{r}, t). \quad (\text{B10})$$

In the steady state case of (B1), the so-called λ -Eigenvalue problem is written as:

$$\frac{1}{k_n} \hat{F}_0(\vec{r}) \vec{\Psi}_n(\vec{r}) = \hat{L}_0(\vec{r}) \vec{\Psi}_n(\vec{r}) \quad (\text{B11})$$

with $n = 0, \dots, \infty$.

where $\vec{\Psi}_n(\vec{r})$ are the eigenvectors, $k_n = 1/\lambda_n$ are the corresponding eigenvalues and \hat{F}_0 , \hat{L}_0 are the steady state fission production and steady state net-loss operators. The eigenvectors $\vec{\Psi}_n(\vec{r})$ are so-called Lambda-Modes (λ -modes) and satisfy the biorthogonality relation

$$\int_V dV \vec{\Psi}_m^\dagger \hat{F}_0 \vec{\Psi}_n = \left\langle \vec{\Psi}_m \left| \hat{F}_0 \right| \vec{\Psi}_n \right\rangle = \delta_{mn} F_n \quad (\text{B12})$$

where $\vec{\Psi}_m^\dagger$ are the adjoint eigenvectors satisfying the adjoint equation

$$\frac{1}{k_n^\dagger} \hat{F}_0^\dagger(\vec{r}) \vec{\Psi}_n^\dagger(\vec{r}) = \hat{L}_0^\dagger(\vec{r}) \vec{\Psi}_n^\dagger(\vec{r}) \quad (\text{B13})$$

The Eigenvalue problem (B11) can be written in components as

$$\begin{aligned} \int_V dV \vec{\Psi}_m^\dagger \hat{F}_0 \vec{\Psi}_n &= \delta_{mn} F_n \\ &= \int_V dV \begin{bmatrix} \Psi_m^{1\dagger}(\vec{r}) \\ \Psi_m^{2\dagger}(\vec{r}) \end{bmatrix} \cdot \begin{bmatrix} v\Sigma_1^f & v\Sigma_2^f \\ 0 & 0 \end{bmatrix} \cdot \begin{bmatrix} \Psi_n^1(\vec{r}) \\ \Psi_n^2(\vec{r}) \end{bmatrix} = v \int_V dV \Psi_m^{1\dagger}(\vec{r}) \left[\Sigma_1^f \Psi_n^1(\vec{r}) + \Sigma_2^f \Psi_n^2(\vec{r}) \right]. \end{aligned} \quad (\text{B14})$$

The space and time dependent neutron flux $\vec{\Phi}(\vec{r}, t)$ and the space and time dependent delayed neutron precursor concentration $C_l(\vec{r}, t)$ of (B1) can be expanded in terms of the λ -modes as

$$\vec{\Phi}(\vec{r}, t) = \sum_n \hat{P}_n(t) \cdot \vec{\Psi}_n(\vec{r}) \quad (\text{B15})$$

$$C_l(\vec{r}, t) \vec{X}_l^v = \sum_n C_{nl}(t) \hat{F}_0 \vec{\Psi}_n(\vec{r}) \Lambda_n \quad (\text{B16})$$

where

$$\hat{P}_n(t) = \begin{bmatrix} P_n^{11}(t) & P_n^{12}(t) \\ P_n^{21}(t) & P_n^{22}(t) \end{bmatrix} \equiv \begin{bmatrix} P_n^1(t) & 0 \\ 0 & P_n^2(t) \end{bmatrix}. \quad (\text{B17})$$

$P_n^1(t)$ are the time dependent expansion functions of the first energy group, $P_n^2(t)$ are the time dependent expansion functions of the second energy group and $C_{nl}(t)$ are the time dependent expansion functions of the delayed neutron precursor concentration. Physically, the time and space dependent neutron flux $\vec{\Phi}(\vec{r}, t)$ is proportional to the reactor power $\dot{Q}(t)$. Thus, in the current neutron kinetic model it is assumed that both neutron energy groups have the same time evolution. In this case, according to $P_n^1(t) = P_n^2(t) = P_n(t)$, the matrix (B17) reduces (the matrix is ‘‘collapsing’’ to a scalar) to

$$\hat{P}_n(t) = \begin{bmatrix} P_n(t) & 0 \\ 0 & P_n(t) \end{bmatrix} \quad (\text{B18})$$

and expansion (B15) can be written as

$$\vec{\Phi}(\vec{r}, t) = \sum_n P_n(t) \cdot \vec{\Psi}_n(\vec{r}) \quad (\text{B19})$$

Substituting of (B19) in the biorthogonality relation (B12)

$$\int_V dV \vec{\Psi}_m^\dagger(\vec{r}) \hat{F}_0 \vec{\Phi}_n(\vec{r}, t) = \sum_n P_n(t) \underbrace{\int_V dV \vec{\Psi}_m^\dagger(\vec{r}) \hat{F}_0 \vec{\Psi}_n(\vec{r})}_{\delta_{mn} F_n} = P_n(t) F_m \quad (\text{B20})$$

justifies the definition of the time dependent amplitude functions $P_n(t)$ according to

$$P_m(t) = \frac{1}{F_m} \int_V dV \vec{\Psi}_m^\dagger(\vec{r}) \hat{F}_0 \vec{\Phi}_n(\vec{r}, t) = \frac{1}{F_m} \langle \vec{\Psi}_m | \hat{F}_0 | \vec{\Phi}_n(\vec{r}, t) \rangle \quad (\text{B21})$$

In order to solve the diffusion equation (B1) for the space and time dependent neutron flux $\vec{\Phi}(\vec{r}, t)$ expansion (B19) and (B16) are substituted in (B1)

$$\begin{aligned} \sum_n [v^{-1}] \vec{\Psi}_n(\vec{r}) \frac{\partial P_n(t)}{\partial t} &= \sum_n P_n(t) \left[(1-\beta) \cdot [\hat{F}_0 + \delta\hat{F}] \right] \cdot \vec{\Psi}_n(\vec{r}) \\ &- \sum_n P_n(t) [\hat{L}_0 + \delta\hat{L}] \vec{\Psi}_n(\vec{r}) + \sum_{l=1}^6 \lambda_l \cdot \sum_n C_{nl}(t) \hat{F}_0 \vec{\Psi}_n(\vec{r}) \Lambda_n \end{aligned} \quad (\text{B22})$$

and

$$\begin{aligned} \sum_n \hat{F}_0 \vec{\Psi}_n(\vec{r}) \Lambda_n \frac{\partial}{\partial t} (C_{nl}(t)) &= \sum_n \beta_l P_n(t) \hat{F}_0 \cdot \vec{\Psi}_n(\vec{r}) + \sum_n \beta_l P_n(t) \delta\hat{F} \cdot \vec{\Psi}_n(\vec{r}) \\ &- \sum_n \hat{F}_0 \vec{\Psi}_n(\vec{r}) \Lambda_n \lambda_l C_{nl}(t) \end{aligned} \quad (\text{B23})$$

where the operators \hat{L} and \hat{F} are expressed as

$$\hat{L} = \hat{L}_0 + \delta\hat{L} \quad (\text{B24})$$

$$\hat{F} = \hat{F}_0 + \delta\hat{F} \quad (\text{B25})$$

in terms of a steady state plus an oscillating term, respectively. In the next step, (B22) and (B23) will be multiplied by $\vec{\Psi}_m^\dagger$ from the left hand side, afterwards the equations are weighted (divided) by (B12) and integrated over the whole multiplying medium of the reactor core. It follows

$$\begin{aligned} \sum_n \frac{\langle \vec{\Psi}_m | [v^{-1}] | \vec{\Psi}_n \rangle}{\langle \vec{\Psi}_m | \hat{F}_0 | \vec{\Psi}_n \rangle} \frac{dP_n(t)}{dt} &= \sum_n \frac{\langle \vec{\Psi}_m | [\hat{F}_0 - \hat{L}_0] | \vec{\Psi}_n \rangle}{\langle \vec{\Psi}_m | \hat{F}_0 | \vec{\Psi}_n \rangle} P_n(t) + \sum_n \frac{\langle \vec{\Psi}_m | [\delta\hat{F} - \delta\hat{L}] | \vec{\Psi}_n \rangle}{\langle \vec{\Psi}_m | \hat{F}_0 | \vec{\Psi}_n \rangle} P_n(t) \\ &+ \sum_n \frac{\langle \vec{\Psi}_m | \beta \hat{F}_0 | \vec{\Psi}_n \rangle}{\langle \vec{\Psi}_m | \hat{F}_0 | \vec{\Psi}_n \rangle} P_n(t) + \sum_n \frac{\langle \vec{\Psi}_m | \beta \delta\hat{F} | \vec{\Psi}_n \rangle}{\langle \vec{\Psi}_m | \hat{F}_0 | \vec{\Psi}_n \rangle} P_n(t) + \sum_{l=1}^6 \lambda_l \cdot \sum_n C_{nl}(t) \frac{\langle \vec{\Psi}_m | \hat{F}_0 | \vec{\Psi}_n \rangle}{\langle \vec{\Psi}_m | \hat{F}_0 | \vec{\Psi}_n \rangle} \Lambda_n \end{aligned} \quad (\text{B26})$$

and

$$\sum_n \frac{\langle \bar{\Psi}_m | \hat{F}_0 | \bar{\Psi}_n \rangle}{\langle \bar{\Psi}_m | \hat{F}_0 | \bar{\Psi}_n \rangle} \Lambda_n \frac{\partial}{\partial t} (C_{nl}(t)) = \sum_n \beta_l \frac{\langle \bar{\Psi}_m | \hat{F}_0 | \bar{\Psi}_n \rangle}{\langle \bar{\Psi}_m | \hat{F}_0 | \bar{\Psi}_n \rangle} P_n(t) + \sum_n \beta_l P_n(t) \frac{\langle \bar{\Psi}_m | \delta \hat{F} | \bar{\Psi}_n \rangle}{\langle \bar{\Psi}_m | \hat{F}_0 | \bar{\Psi}_n \rangle} - \sum_n \frac{\langle \bar{\Psi}_m | \delta \hat{F} | \bar{\Psi}_n \rangle}{\langle \bar{\Psi}_m | \hat{F}_0 | \bar{\Psi}_n \rangle} \Lambda_n \lambda_l C_{nl}(t) . \quad (\text{B27})$$

In the next step, the following definitions will be introduced in (B26) and (B27):

$$\Lambda_{mn} = \frac{\langle \bar{\Psi}_m | [V^{-1}] | \bar{\Psi}_n \rangle}{\langle \bar{\Psi}_m | \hat{F}_0 | \bar{\Psi}_n \rangle}; \quad \rho_{mn}^F = \frac{\langle \bar{\Psi}_m | [\delta \hat{F} - \delta \hat{L}] | \bar{\Psi}_n \rangle}{\langle \bar{\Psi}_m | \hat{F}_0 | \bar{\Psi}_n \rangle}; \quad \rho_m^s = \frac{\langle \bar{\Psi}_m | [\hat{F}_0 - \hat{L}_0] | \bar{\Psi}_n \rangle}{\langle \bar{\Psi}_m | \hat{F}_0 | \bar{\Psi}_n \rangle} \quad (\text{B28})$$

$$\rho_{mn}^D = \beta \frac{\langle \bar{\Psi}_m | \delta \hat{F} | \bar{\Psi}_n \rangle}{\langle \bar{\Psi}_m | \hat{F}_0 | \bar{\Psi}_n \rangle}; \quad \rho_{mn}^{D_l} = \beta_l \frac{\langle \bar{\Psi}_m | \delta \hat{F} | \bar{\Psi}_n \rangle}{\langle \bar{\Psi}_m | \hat{F}_0 | \bar{\Psi}_n \rangle} \quad (\text{B29})$$

Taking into account that $\Lambda_{mm} \gg \Lambda_{mn}$ with $n \neq m$ [6] and the definitions in (B28) and (B29), the final neutron kinetics (spatial) mode equations can be written as

$$\frac{d}{dt} P_m(t) = \frac{1}{\Lambda_{mm}} [(\rho_m^s - \beta) P_m(t)] + \frac{1}{\Lambda_{mm}} \left[\sum_n \rho_{mn}^F P_n(t) - \sum_n \rho_{mn}^D P_n(t) \right] + \sum_l \lambda_l C_{ml}(t) \quad (\text{B30})$$

$$\frac{d}{dt} C_{ml}(t) = \frac{1}{\Lambda_m} \left[\beta_l P_m(t) + \sum_n \rho_{mn}^{D_l} P_n(t) \right] - \lambda_l C_{ml}(t)$$

where ρ_m^s is the static reactivity, ρ_{mn}^F are the dynamical feedback reactivities, and ρ_{mn}^D , $\rho_{mn}^{D_l}$ are the delayed feedback reactivities.

As mentioned above, in the current neutron kinetics model only a single group of delayed neutron precursors $l=1$ is considered and the contributions of ρ_{mn}^D and $\rho_{mn}^{D_l}$ are neglected. Furthermore, only the fundamental and the first modes are considered. Hence the modal kinetic equations can be written as

$$\frac{d}{dt} P_0(t) = \frac{1}{\Lambda_0} [(\rho_{00}^F - \beta) P_0(t) + \rho_{01}^F P_1(t)] + \lambda C_0 \quad (\text{B31})$$

$$\frac{d}{dt} C_0(t) = \frac{\beta}{\Lambda_0} P_0(t) - \lambda C_0(t)$$

$$\frac{d}{dt} P_1(t) = \frac{1}{\Lambda_0} [\rho_{10}^F P_0(t) + (\rho_1^s - \beta) P_1(t) + \rho_{11}^F P_1(t)] + \lambda C_1 \quad (\text{B32})$$

$$\frac{d}{dt} C_1(t) = \frac{\beta}{\Lambda_0} P_1(t) - \lambda C_1(t) .$$

The dynamical feedback reactivities, ρ_{mn}^F represent the coupling between the λ -modes and describe the main feedback mechanism between the neutron kinetics and thermal hydraulics via void fraction in the two-phase flow region and fuel temperature. In the framework of the ROM development the approximate calculation of

the mode feedback reactivities is one of the crucial tasks. In the approximations used in previous works [6], the required reactivities ρ_{mn} were given by $\rho_{mn} \sim \rho_{00} \cdot (\text{weighting factors})_{mn}$; this means that in both cases certain weighting factors for terms different from $n = m = 0$ have to be calculated.

In general, the total power generated by nuclear fissions within the multiplying medium of the reactor core is given by

$$\dot{Q}(t) = \varepsilon \cdot \int dV \sum_{i=1}^{NOG} \Sigma_i^f \cdot \Phi_i(\vec{r}, t) \quad (\text{B33})$$

where ε is the energy per fission and Σ_i^f is the macroscopic fission cross section of the i -th group. Considering only two neutron energy groups ($i = 2$) and substituting (B19) in (B33) lead to

$$\begin{aligned} \dot{Q}(t) &= \sum_n P_n(t) \int dV \underbrace{\varepsilon \cdot [\Sigma_1^f \Psi_n^1(\vec{r}) + \Sigma_2^f \Psi_n^2(\vec{r})]}_{\dot{Q}_n(\vec{r})} \\ \dot{Q}(t) &= \sum_n P_n(t) \int dV \dot{Q}_n(\vec{r}) = \sum_n P_n(t) \cdot \dot{Q}_n \end{aligned} \quad (\text{B34})$$

where $\dot{Q}_n(\vec{r})$ are the so called power modes.

The power density $q'''(t)$ in the fuel is defined as

$$q'''(t) = \frac{\dot{Q}(t)}{V_{fuel}} \quad (\text{B35})$$

the total power divided by the fuel element volume V_{fuel} . It should be noted that the power density in the fuel is assumed to be constant in all considered fuel elements in the reduced order model (but is a function of time). Taking into account only the fundamental and the first azimuthal mode, the power density (B35) can be expressed as

$$q_j'''(t) = \frac{1}{V_{fuel}^j} [P_0 \dot{Q}_0^j + P_1 \dot{Q}_1^j] \quad (\text{B36})$$

where \dot{Q}_n^j is defined as

$$\dot{Q}_n^j(\vec{r}) = \int_{V_j} dV \varepsilon \cdot [\Sigma_1^f \Psi_n^1(\vec{r}) + \Sigma_2^f \Psi_n^2(\vec{r})] \quad (\text{B37})$$

and j is the considered core region.

In the steady state core, all the higher modes are zero. Consequently, equation (B34) is reduced to

$$\dot{Q}(t) = \underbrace{P_0(t)}_{=1} \cdot \dot{Q}_0 = \dot{Q}_0 \quad (\text{B38})$$

and the steady state power density in the fuel is given as

$$q_0'''(t) = \frac{\dot{Q}_0}{V_{fuel}} = \frac{\dot{Q}_0^j}{V_{fuel}^j} \quad (\text{B39})$$

The final expression for the power density in the fuel can be written as

$$q_j'''(t) = \frac{\dot{Q}_0^j}{\underbrace{V_{fuel}^j}_{c_q}} [P_0(t) + P_1(t) q_1^j] \quad (\text{B40})$$

$$q_j'''(t) = c_q [P_0(t) + P_1(t) q_1^j] \quad ,$$

where q_1^j is the ratio $\dot{Q}_1^j / \dot{Q}_0^j$. In the fuel rod heat conduction model where two representative heated channels including the fuel elements are taken into account there is $\xi = q_1^j = \pm 1$ (to simplify the nomenclature).

1.2 Fuel heat conduction model

The fuel rod heat conduction model in the current reduced order model was completely adopted from Karve et al. [8]. This model is based on the one-dimensional (radial), time-dependent heat conduction equation for the fuel rod and is based on the following assumptions:

- 1) two axial regions, corresponding to the single and two-phase regions, are considered,
- 2) three distinct radial regions, the fuel pellet, the gap and the clad are modelled in each of the two axial regions,
- 3) azimuthale symmetry for heat conduction in the radial direction is assumed,
- 4) heat conduction in the z-direction is neglected,
- 5) time-dependent, spatially uniform volumetric heat generation is assumed.

These assumptions result in a one-dimensional (radial) time dependent partial differential equation (PDE). By assuming a two-piecewise quadratic spatial approximation for the fuel rod temperature, the PDE can be reduced to a system of ODEs by applying the variation principle approach. A detailed derivation is presented in [6,8].

In the scope of this section a brief description about the fuel heat conduction model is given. As mentioned above the fuel rod is modelled separately in the two axial regions corresponding to the single and two-phase regions of the boiling channel. In each of these regions, it is modelled with three distinct radial regions, the fuel pellet ($0 < r < r_p$), the gap ($r_p < r < r_g$), and the clad ($r_g < r < r_c$).

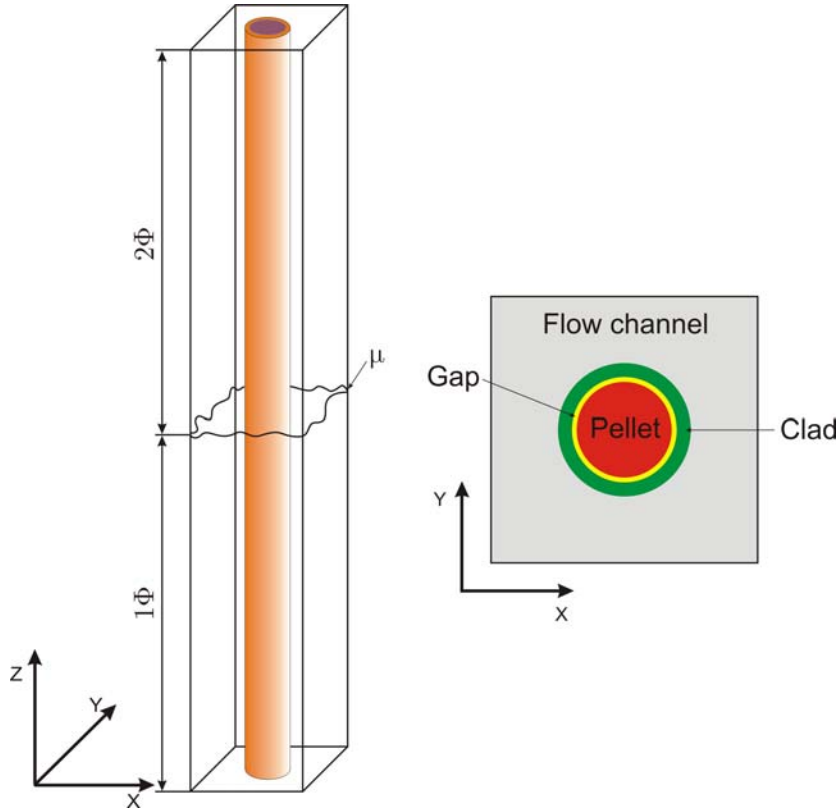


Figure 1: Flow channel including fuel rod.

The heat conduction equations for the fuel rod in dimensionless form can be written as

$$\frac{1}{\alpha_p} \frac{\partial \theta_p(r,t)}{\partial t} = \frac{\partial^2 \theta_p(r,t)}{\partial r^2} + \frac{1}{r} \frac{\partial \theta_p(r,t)}{\partial r} + q'''(t), \quad (B41)$$

$$0 \leq r \leq r_p$$

and

$$\frac{1}{\alpha_c} \frac{\partial \theta_c(r,t)}{\partial t} = \frac{\partial^2 \theta_c(r,t)}{\partial r^2} + \frac{1}{r} \frac{\partial \theta_c(r,t)}{\partial r}, \quad (B42)$$

$$r_g \leq r \leq r_c$$

where θ_p and θ_c are the deviations from the steady state for the pellet and clad temperatures respectively. $q'''(t)$ is the dimensionless power density. Note that all the variables and parameters are in dimensionless form in this chapter. This results in a transparent formulation of the equations and gives more insight into the key parameters determining the system dynamics. The various dimensionless variables and parameters are given in [6,8].

The clad heat conduction dynamics can be modeled without solving the transient heat conduction equation. The idea behind this is that there is no significant change in the clad temperature profile from its initial steady-state distribution, due to the large clad thermal diffusivity α_c , which is about ten times larger than that of the pellet α_p .

Based on the logarithmic spatial distribution of the steady-state clad temperature, the space and time dependence for $\theta_c(r, t)$ can be written as

$$\theta_c(r, t) = b_2(t) \log r + b_3(t) \quad . \quad (\text{B43})$$

The ODEs for the fuel pellet are deduced by reducing the PDEs for the time-dependent heat conduction equation for the fuel pellet by employing the variational principle approach. To this end, the fuel rod temperature is assumed to be captured by two piecewise quadratic spatial approximations

$$\begin{aligned} \theta_p(r, t) &= T_1(t) + \alpha_1(t)r + \alpha_2(t)r^2, \quad 0 < r < r_d \\ &= T_2(t) + \beta_1(t)r + \beta_2(t)r^2, \quad r_d < r < r_p \end{aligned} \quad (\text{B44})$$

where r_d is the point of discontinuity between $r=0$ and $r=r_p$. The value of r_d was determined empirically [7,8] to be $r_d = 0.83 \cdot r_p$. The $\alpha_i(t)$ and $\beta_i(t)$ with $i=1,2$ are determined using the continuity and boundary equations [8].

A variational principle approach is then used to get the final ODEs for $T_1(t)$ and $T_2(t)$, which represent the BWR fuel rod heat conduction dynamics. These equations are

$$\frac{dT_1(t)}{dt} = ll_{1,1}T_1(t) + ll_{2,1}T_2(t) + ll_{3,1} \left[c_q(P_0(t) - \tilde{P}_0) + c_q \xi P_1(t) \right] \quad (\text{B45})$$

$$\frac{dT_2(t)}{dt} = ll_{1,2}T_1(t) + ll_{2,2}T_2(t) + ll_{3,2} \left[c_q(P_0(t) - \tilde{P}_0) + c_q \xi P_1(t) \right] \quad (\text{B46})$$

where $ll_{1,s}$, $ll_{2,s}$, and $ll_{3,s}$ are complicated constants which depend on the design parameters.

In summary, for each channel, four ODEs are developed from the heat conduction PDE. These ODEs are for the two coefficients of each of the two spatially piecewise quadratic representations of the fuel pellet temperature in the single and two-phase regions of the channel. In an explicit index form, these ODEs can be written as

$$\frac{dT_{1,j\phi,l}(t)}{dt} = ll_{1,1,j\phi,l}T_{1,j\phi,l}(t) + ll_{2,1,j\phi,l}T_{2,j\phi,l}(t) + ll_{3,1,j\phi,l} \left[c_q(P_0(t) - \tilde{P}_0) + c_q \xi P_1(t) \right] \quad (\text{B47})$$

$$\frac{dT_{2,j\phi,l}(t)}{dt} = ll_{1,2,j\phi,l}T_{1,j\phi,l}(t) + ll_{2,2,j\phi,l}T_{2,j\phi,l}(t) + ll_{3,2,j\phi,l} \left[c_q(P_0(t) - \tilde{P}_0) + c_q \xi P_1(t) \right] \quad (\text{B48})$$

where $\xi = \pm 1$, $j\phi$ stands for single (1ϕ) or two-phase (2ϕ) region, l stands for channel number (1 or 2) and \tilde{P}_0 is the steady state value of the amplitude function. Notice, the final ODEs were developed by using the symbolic toolbox of MATLAB. A detail description is given in [8].

1.3 Thermal hydraulic model

The thermal hydraulic behavior of the BWR is represented by two heated channels coupled by the neutron kinetics and by the recirculation loop. This sub-model is based on the following assumptions [6]:

- 1) The heated channel, which has a constant flow cross section, is divided into two axial regions, the single and the two-phase region.
- 2) All thermal hydraulic values are averaged over the flow cross section
- 3) The dynamical behavior of the two-phase region is presented by a drift flux model (DFM) [7] where mechanical non equilibrium (difference between the two phase velocities, and a radial non-uniform void distribution is considered) is assumed (the DFM represents the stability behavior of the two-phase more accurately than a homogeneous equilibrium model, in particular for high void content).
- 4) The two phases are assumed to be in thermodynamic equilibrium.
- 5) The system pressure is considered to be constant.
- 6) The fluid in both axial regions and the downcomer is assumed to be incompressible.
- 7) Around the closed flow path, mechanical energy terms are very small compared with the thermal energy terms. Consequently, the kinetic energy, potential energy, pressure gradient and friction dissipation are neglected in the energy balance.
- 8) The PDEs (three-dimensional mass, momentum and energy balance equation) are converted into the final ODEs by applying the weighted residual method in which spatial approximations (spatially quadratic but time-dependent profiles) for the single phase enthalpy [6,8] and the two-phase quality are used (is equivalent to a coarse grained axial discretization).
- 9) The downcomer (constant flow cross section) region is considered to be a single phase region.
- 10) All physical processes which are connected with energy increase and energy decrease are neglected in the downcomer. Consequently the core inlet sub-cooling is a boundary condition which is nearly realized by the nuclear power plants.
- 11) The pump head due to the recirculation pumps is considered to be constant ($\Delta P_{head} = const$)

Figure 2 depicts a schematic sketch of the thermal hydraulic model including the recirculation loop. The sub-model consists of three parts. These are the two heated channels and the downcomer section. The common lower plenum and the common upper plenum are only shown to indicate that all channels are coupled hydraulically.

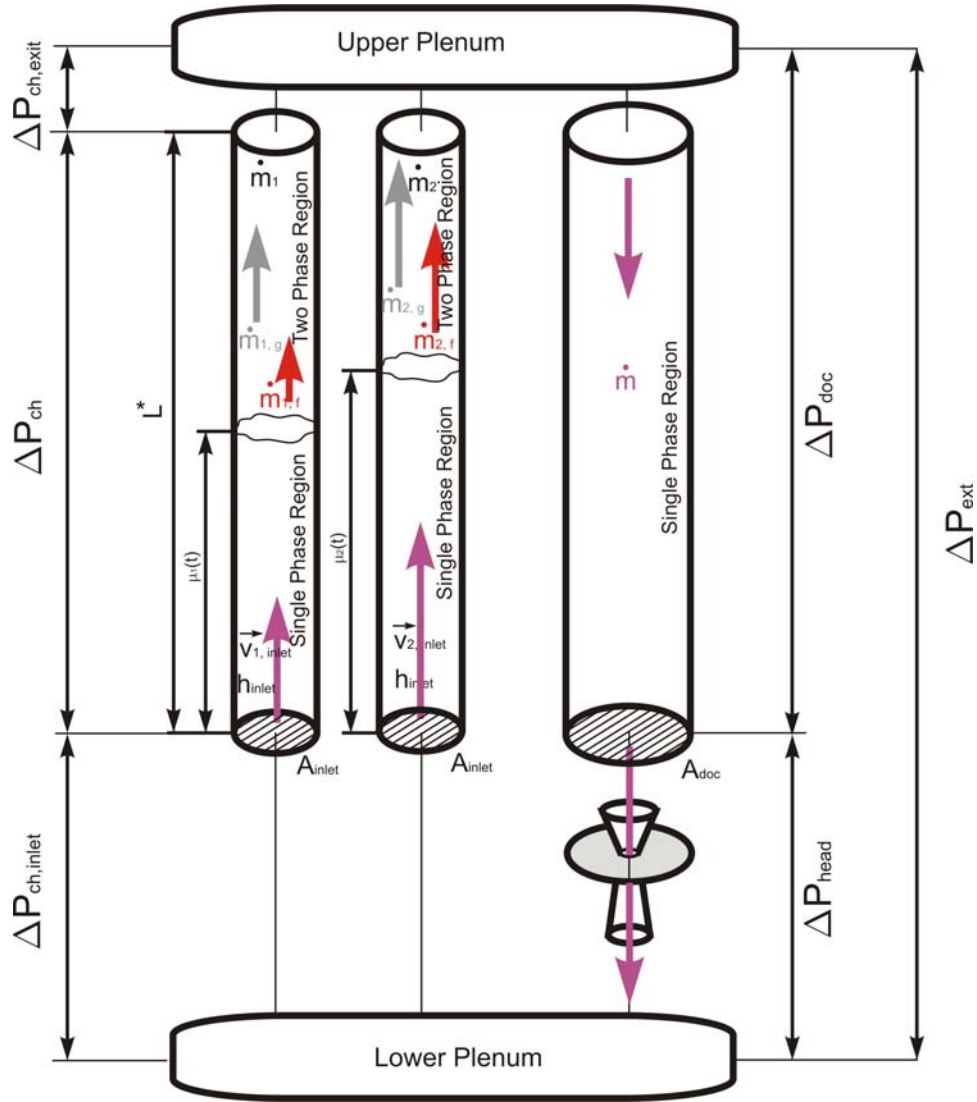


Figure 2: Schematic sketch of the thermal hydraulic two-channel model including outer loop section.

The coolant enters the core channel i inlet (single phase region) with the inlet velocities $v_{i,inlet}$ and the inlet enthalpy h_{inlet} and the heat is released by nuclear fissions in the fuel, conducted to the coolant. At a certain axial level (boiling boundary $\mu(t)$), where the coolant reaches the saturation state, the coolant starts to boil. Above the boiling boundary (two-phase region), the coolant is a mixture of water and steam. Because of the thermodynamic equilibrium between the two phases, the heat generated in the fuel is completely used for steam production.

Single phase region [6,8]

The mass balance is reduced to

$$\rho_l^* \frac{\partial}{\partial z^*} v^*(z^*, t^*) = 0 \quad \text{with} \quad \rho_l^*(z^*, t^*) = \rho_l^* = \text{const} \quad (\text{B49})$$

due to the incompressibility of the coolant. Consequently, the velocity $v^*(z^*, t^*)$ within the single phase region is according to $v^*(z^*, t^*) = v_{inlet}^*(t^*)$ not a function of z^* .

The energy balance can be written as

$$\rho_l^*(z^*, t^*) \frac{\partial h^*(z^*, t^*)}{\partial t^*} + \rho_l^*(z^*, t^*) v_{inlet}^*(t^*) \frac{\partial h^*(z^*, t^*)}{\partial z^*} = \frac{q_{1\Phi}''(t^*) \xi_h^*}{A^*} \quad (B50)$$

where the source term on the right hand side describes the heat density in the coolant created by the wall heat flux $q_{1\Phi}''$. The single phase wall heat flux $q_{1\Phi}''$ is related to the single phase convective heat transfer coefficient $h_{\infty,1\Phi}^*$ as $q_{1\Phi}'' = h_{\infty,1\Phi}^* (T_{s,1\Phi}^*(t^*) - T_{bulk,1\Phi}^*(t^*))$ where $h_{\infty,1\Phi}^*$ is estimated by the Dittus-Boelter correlation

$$h_{\infty,1\Phi}^* = 0.023 \frac{k_f^*}{D_h^*} (\text{Re})^{0.8} (\text{Pr})^{0.4} \quad \text{with } 0.7 < \text{Pr} < 100 \text{ and } \text{Re} > 1000 \quad . \quad (B51)$$

In expression (B51), k_f^* is the liquid thermal conductivity, D_h^* is the hydraulic diameter of the heated channel, Re is the Reynolds-Number and Pr is the Prandl-Number.

The momentum balance of the single phase region can be expressed as

$$-\frac{\partial}{\partial z} P_{1\Phi}^*(z^*, t^*) = \rho_l^*(z^*, t^*) \left[\frac{d}{dt} v_{inlet}^*(t^*) + \frac{f_{1\Phi}^*}{2D_h^*} v_{inlet}^{*2}(t^*) + g^* \right] \quad (B52)$$

where the first term on the right hand side describes the pressure drop due to inertial effects, the second term describes the friction in the coolant and the last term describes the pressure drop due to the gravitation.

Next, the conservative equations will be transformed into the dimensionless form (not presented here). The mass, energy and momentum balance can be written as

$$\frac{\partial}{\partial z} v(z, t) = 0 \quad (B53)$$

$$\text{with } v(z, t) = v_{inlet}(t) \quad ,$$

$$\frac{\partial h(z, t)}{\partial t} + v_{inlet}(t) \cdot \frac{\partial h(z, t)}{\partial z} = N_\rho \cdot N_r \cdot N_{pch,1\Phi}(t) \quad (B54)$$

$$-\frac{\partial}{\partial z} P_{1\Phi} = \frac{d}{dt} v_{inlet} + N_{f,1\Phi} v_{inlet}^2(t) + Fr^{-1} \quad , \quad (B55)$$

where $N_{pch,1\Phi}(t)$ is the time-dependent phase change number in the single-phase region, which is proportional to the wall heat flux in the single-phase region; and $N_{pch,1\Phi}(t) = N_{cov,1\Phi} (T_{s,1\Phi}(t) - T_{bulk,1\Phi})$. The dimensionless numbers Fr , N_ρ , N_r and $N_{cov,1\Phi}$ are defined in the appendix.

In order to convert the energy balance (B54) from a PDE into a ODE, a time-dependent, spatially quadratic distribution

$$h(z, t) \approx h_{inlet} + a_1(t)z + a_2(t)z^2 \quad (B56)$$

for the enthalpy is introduced [6,8]. Thereby the enthalpy has to satisfy the boundary conditions

$$h(z=0,t) = h_{inlet} \quad (B57)$$

and

$$h(z=\mu,t) = h_{sat} \quad , \quad (B58)$$

where h_{inlet} is the inlet enthalpy of the boiling channel and h_{sat} is the saturation enthalpy. The time dependent coefficients $a_1(t)$ and $a_2(t)$ are describing the dynamics of the single phase enthalpy and can be assumed to be phase space variables.

In the next step, equation (B54) will be rewritten in operator form

$$\begin{aligned} \frac{\partial h(z,t)}{\partial t} + v_{inlet}(t) \cdot \frac{\partial h(z,t)}{\partial z} - N_\rho \cdot N_r \cdot N_{pch,1\Phi}(t) = 0 = \hat{A} \cdot h - S \\ \text{with } \hat{A} = \frac{\partial}{\partial t} + v_{inlet} \frac{\partial}{\partial z} \quad \text{and} \quad S = N_\rho \cdot N_r \cdot N_{pch,1\Phi}(t) \end{aligned} \quad (B59)$$

and the weighted residual method

$$0 = \langle wg, \hat{A}h - S \rangle = \int_0^\mu wg \cdot (\hat{A}h - S) dz \quad (B60)$$

will be applied. To this end, the time-dependent, spatially quadratic distribution (B56) is substituted in (B60) where the weight function $wg=1$ and $wg=z$ are used. The integration from the inlet of the channel $z=0$ to the boiling boundary $z=\mu$ accordant to

$$\begin{aligned} 0 = \langle 1, \hat{A}h - S \rangle \\ = \int_0^\mu \left(\frac{\partial}{\partial t} + v_{inlet} \frac{\partial}{\partial z} \right) \cdot (h_{inlet} + a_1(t) \cdot z + a_2(t) \cdot z^2) dz - \int_0^\mu N_\rho \cdot N_r \cdot N_{pch,1\Phi}(t) dz \end{aligned} \quad (B61)$$

and

$$\begin{aligned} 0 = \langle z, \hat{A}h - S \rangle \\ = \int_0^\mu z \cdot \left(\frac{\partial}{\partial t} + v_{inlet} \frac{\partial}{\partial z} \right) \cdot (h_{inlet} + a_1(t) \cdot z + a_2(t) \cdot z^2) dz \\ - \int_0^\mu N_\rho \cdot N_r \cdot N_{pch,1\Phi}(t) \cdot z \cdot dz \end{aligned} \quad (B62)$$

lead to the final ODEs

$$\frac{d}{dt} a_1(t) = -2v_{inlet}(t)a_2(t) + \frac{6}{\mu} [N_\rho \cdot N_r \cdot N_{pch,1\Phi}(t) - v_{inlet}(t)a_1(t)] \quad (B63)$$

$$\frac{d}{dt} a_2(t) = -\frac{6}{\mu^2} [N_\rho \cdot N_r \cdot N_{pch,1\Phi}(t) - v_{inlet}(t)a_1(t)] \quad . \quad (B64)$$

The boiling boundary $\mu(t)$ is the level at which the enthalpy is equal to the saturation enthalpy h_{sat} and can be calculated by evaluating the boundary conditions (B57) and (B58)

$$h(z = \mu, t) = h_{sat} = h_{inlet} + a_1(t) \cdot \mu + a_2(t) \cdot \mu^2 \quad . \quad (B65)$$

The boiling boundary can be written as

$$\mu(t) = 2 \frac{N_\rho N_r N_{sub}}{a_1(t) + \sqrt{a_1(t)^2 + 4 a_2(t) N_\rho N_r N_{sub}}} \quad , \quad (B66)$$

where the relation $N_\rho N_r N_{sub} = h_{sat} - h_{inlet}$ is used.

Two phase region [6]

The two phase region extends from the boiling boundary $\mu(t)$ to the channel exit. As mentioned above the dynamical behaviour within this region is represented by a drift flux model which is based on four conservative equations. This is the continuity equation of the gas phase and the three conservative equations (mass, energy and momentum) for the two phase mixture. In the current work, the density wave phenomenon play a dominant role so that the mass transport problem was transformed into the void propagation formulation (In the scope of the report the derivation of the void propagation equation is not presented). The drift flux equations [6,7] can be written as

$$\frac{\partial}{\partial t^*} \alpha^*(z^*, t^*) + C_k^* \frac{\partial}{\partial z^*} \alpha^*(z^*, t^*) = \omega^* \quad (B67)$$

$$\Gamma_g^* \Delta h_{fg}^* = q_{2\Phi}^* \frac{\xi^*}{A^*} \quad (B68)$$

$$\begin{aligned} -\frac{\partial}{\partial z^*} P_{2\Phi}^* &= \rho_m^*(z^*, t^*) \cdot \left[\frac{\partial}{\partial t^*} v_m^*(z^*, t^*) + v_m^*(z^*, t^*) \frac{\partial}{\partial z^*} v_m^*(z^*, t^*) \right] \\ &+ \rho_m^*(z^*, t^*) g^* + \rho_m^*(z^*, t^*) \frac{f_{2\Phi}^*}{2D_h^*} v_m^{*2}(z^*, t^*) + \frac{\partial}{\partial z^*} \left(\frac{\alpha^*(z^*, t^*)}{1 - \alpha^*(z^*, t^*)} \frac{\rho_g^* \rho_f^* \bar{V}_{gi}^2}{\rho_m^*(z^*, t^*)} \right) \end{aligned} \quad (B69)$$

where (B67) is the void propagation equation, (B68) is the energy equation and (B69) is the momentum balance [6,7]. Because of the two phases are assumed to be in thermodynamic equilibrium and to be incompressible, the energy balance is reduced to (B68) and the characteristic reaction frequency ω^* can be expressed as

$$\omega^*(z^*, t^*) = \Gamma_g^* \frac{\rho_m^*(z^*, t^*)}{\rho_f^* \rho_g^*} \quad . \quad (B70)$$

It should be noted that the equation

$$\frac{\partial}{\partial z^*} J^* = \Gamma_g^* \frac{\rho_f^* - \rho_g^*}{\rho_f^* \rho_g^*} \quad (B71)$$

is implicitly comprised by the void propagation equation (B67).

The dimensionless conservative equations [6,7] of the two phase region can be written as

$$\frac{\partial}{\partial t} j(z,t) = N_{pch,2\Phi}(t) \quad (B72)$$

$$\frac{\partial}{\partial t} \alpha(z,t) + (C_0 j(z,t) + V_{gj}) \frac{\partial}{\partial z} \alpha(z,t) = N_{pch,2\Phi}(t) [N_r - C_0 \alpha(z,t)] \quad (B73)$$

$$\begin{aligned} -\frac{\partial}{\partial z} P_{2\Phi} = \rho_m(z,t) \left[Fr^{-1} + \frac{\partial}{\partial t} v_m(z,t) \right] + \rho_m(z,t) \left[v_m(z,t) \frac{\partial}{\partial z} v_m(z,t) + N_{f,2\Phi} v_m^2(z,t) \right] \\ + N_\rho \frac{\partial}{\partial z} \left(\frac{\alpha}{1-\alpha} \frac{\bar{V}_{gj}^2}{\rho_m(z,t)} \right) \end{aligned} \quad (B74)$$

where

$$\bar{V}_{gj} = V_{gj} + (C_0 - 1) \cdot j(z,t) \quad (B75)$$

$$j(z,t) = v_{inlet}(t) + N_{pch,2\Phi}(t)(z - \mu(t)) \quad (B76)$$

$$\rho_m(z,t) = 1 - \frac{\alpha(z,t)}{N_r} \quad (B77)$$

$$v_m(z,t) = j(z,t) + \bar{V}_{gj} \left[1 - \frac{1}{\rho_m(z,t)} \right] \quad (B78)$$

The drift flux relation between the void fraction and the equilibrium quality $x(z,t)$ can be written as a sum of the void fraction due to the homogenous equilibrium model α_{hom} and a correction term α_{corr}

$$\alpha(z,t) = \frac{1}{C_0} \left(\alpha_{hom}(z,t) - V_{gj} \cdot \alpha_{corr}(z,t) \right) \quad (B79)$$

[3] where the corresponding relations are

$$\alpha_{hom}(z,t) = \frac{x(z,t)N_r}{(x(z,t) + N_\rho N_r)} \quad (B80)$$

and

$$\alpha_{corr}(z,t) = \frac{x(z,t)N_r}{(x(z,t) + N_\rho N_r)(C_0 j(z,t) + V_{gj})} \quad (B81)$$

As already mentioned (for the conversion from PDE into ODEs), the quality $x(z,t)$ in the two phase region will be described by a time-dependent, spatially quadratic distribution

$$x(z,t) \approx N_\rho N_r \left[s_1(t)[z - \mu(t)] + s_2(t)[z - \mu(t)]^2 \right] \quad (B82)$$

analogously to the enthalpy distribution in the single phase region. The ODEs can be obtained after substituting (B82) and (B76) in (B79), the resulting equation will be substituted in the void propagation equation (B73) and finally, performing the weighted residuals method with the weight functions $w_g = 1$ and $w_g = z$. Thereby, it will be integrated from the boiling boundary to the channel exit. The final ODEs can be written as

$$\frac{ds_1}{dt} = \frac{1}{ff_5(t)} \left[ff_1(t) \frac{d\mu(t)}{dt} + ff_2(t) \frac{dv_{inlet}(t)}{dt} \right] + \frac{1}{ff_5(t)} \left[ff_3(t) \frac{dN_{pch,2\Phi}(t)}{dt} + ff_4(t) \right] \quad (B83)$$

$$\frac{ds_2}{dt} = \frac{1}{ff_{10}(t)} \left[ff_6(t) \frac{d\mu(t)}{dt} + ff_7(t) \frac{dv_{inlet}(t)}{dt} \right] + \frac{1}{ff_{10}(t)} \left[ff_8(t) \frac{dN_{pch,2\Phi}(t)}{dt} + ff_9(t) \right]. \quad (B84)$$

The derivative of the ODE for the channel inlet velocity is summarized in the main text in subsection 3.1.3.

1.4 Summary of the ROM

Mode-kinetic equations (4 equations):

$$\begin{aligned} \frac{d}{dt} P_0(t) &= \frac{1}{\Lambda_0} \left[(\rho_{00}^F - \beta) P_0(t) + \rho_{01}^F P_1(t) \right] + \lambda C_0 \\ \frac{d}{dt} C_0(t) &= \frac{\beta}{\Lambda_0} P_0(t) - \lambda C_0(t) \end{aligned} \quad (\text{B85})$$

$$\begin{aligned} \frac{d}{dt} P_1(t) &= \frac{1}{\Lambda_0} \left[\rho_{10}^F P_0(t) + (\rho_0^s - \beta) P_1(t) + \rho_{11}^F P_1(t) \right] \\ &+ \lambda C_1 \\ \frac{d}{dt} C_1(t) &= \frac{\beta}{\Lambda_0} P_1(t) - \lambda C_1(t) \end{aligned} \quad (\text{B86})$$

Fuel heat conduction equations (8 equations):

$$\frac{dT_{1,j\phi,l}(t)}{dt} = ll_{1,1,j\phi,l} T_{1,j\phi,l}(t) + ll_{2,1,j\phi,l} T_{2,j\phi,l}(t) + ll_{3,1,j\phi,l} \left[c_q (P_0(t) - \tilde{P}_0) + c_q \xi P_1(t) \right] \quad (\text{B87})$$

$$\frac{dT_{2,j\phi,l}(t)}{dt} = ll_{1,2,j\phi,l} T_{1,j\phi,l}(t) + ll_{2,2,j\phi,l} T_{2,j\phi,l}(t) + ll_{3,2,j\phi,l} \left[c_q (P_0(t) - \tilde{P}_0) + c_q \xi P_1(t) \right] \quad (\text{B88})$$

with $j = 1, 2$ (single phase and two-phase regions) and $l = 1, 2$ (two heated channels)

Thermal-hydraulic equations (10 equations):

$$\frac{d}{dt} a_1(t) = -2v_{inlet}(t)a_2(t) + \frac{6}{\mu} \left[N_\rho \cdot N_r \cdot N_{pchl,1\Phi}(t) - v_{inlet}(t)a_1(t) \right] \quad (\text{B89})$$

$$\frac{d}{dt} a_2(t) = -\frac{6}{\mu^2} \left[N_\rho \cdot N_r \cdot N_{pchl,1\Phi}(t) - v_{inlet}(t)a_1(t) \right] \quad (\text{B90})$$

$$\frac{ds_1}{dt} = \frac{1}{ff_5(t)} \left[ff_1(t) \frac{d\mu(t)}{dt} + ff_2(t) \frac{dv_{inlet}(t)}{dt} \right] + \frac{1}{ff_5(t)} \left[ff_3(t) \frac{dN_{pchl,2\Phi}(t)}{dt} + ff_4(t) \right] \quad (\text{B91})$$

$$\frac{ds_2}{dt} = \frac{1}{ff_{10}(t)} \left[ff_6(t) \frac{d\mu(t)}{dt} + ff_7(t) \frac{dv_{inlet}(t)}{dt} \right] + \frac{1}{ff_{10}(t)} \left[ff_8(t) \frac{dN_{pchl,2\Phi}(t)}{dt} + ff_9(t) \right] \quad (\text{B92})$$

$$\frac{d}{dt} v_{n,inlet}(t) = A_n(t) - B_n(t) \cdot \left(\sum_n \frac{d}{dt} v_{n,inlet}(t) \right) - B_n(t) N_{f1\Phi} A_{ol} D_{ol} \left(\sum_n v_{n,inlet}(t) \right)^2 \quad (\text{B93})$$

where (B93) is described in the full text and n corresponds to the n -th channel.

Literature

- [1] A.F. Henry; "*Nuclear Reactor Analysis*"; MIT Press; Cambridge; Massachusetts; USA; pp. 300-329; 1975.
- [2] K. Hashimoto; "*Linear Modal Analysis of Out-of-Phase Instability in BWR Cores*"; Ann. Nucl. Engineering; **20**; Number 12; pp. 789-797; 1993.
- [3] K. Hashimoto; A. Hotta; T. Takeda; "*Neutronic Model for Modal Multichannel Analysis of Out-of-Phase Instability in Boiling Water Reactor Cores*"; Ann. Nucl. Energy; **24**; Number 2; pp. 99-111; 1997.
- [4] J.L.Munoz-Cobo; S. Chiva; A. Sekhri; "A reduced order model of BWR dynamics with sub-cooled boiling and modal kinetics: application to out of phase oscillations"; Annals of Nucl. Energy; Volume 31; pp. 1135-1162; 2004.
- [5] M. Miro; D. Ginestar; D. Hennig; G. Verdu; "*On the Regional Oscillation Phenomenon in BWR's*"; Progress in Nuclear Energy; Vol. 36; No. 2; pp. 189-229; 2000.
- [6] A. Dokhane, "*BWR Stability and Bifurcation Analysis using a Novel Reduced Order Model and the System Code RAMONA*," Doctoral Thesis, EPFL, Switzerland, 2004.
- [7] Rizzwan-uddin; "*Linear and Nonlinear Stability Analyses of Density-Wave Oscillations in Heated Channels*"; Ph.D. Dissertation of University of Illinois, USA; 1981.
- [8] A.A.Karve; "Nuclear-Coupled Thermal-hydraulic Stability Analysis of Boiling Water Reactors"; Ph.D. Dissertation; Virginia University; USA; 1998.

Appendix C: RAMONA description

Stability analyses with system codes can be performed, depending from the analysis goal, in the time domain or in the frequency domain. Time domain codes contain a nonlinear BWR model and can be used for detailed nonlinear BWR stability analysis, while frequency domain codes, containing a linearized BWR model, are used for linear stability analysis, in particular, for searching for the (linear) stability boundary. RAMONA5 works in the time domain and simulates the coupled 3 dimensional neutron kinetics, fuel dynamics and thermal hydraulics. A detailed description of RAMONA is given in [1,2]. Figure 1 shows a schematic sketch of a BWR plant model (GE-Type) and Figure 2 shows the RAMONA5 BWR plant model. In the following, the main features of the sub models are briefly presented [1-6].

RAMONA5 is an extended and improved code version of RAMONA3. But similar to RAMONA3 it is a 'hardwired' nine component model, the neutron diffusion process in the core is treated 3-dimensional and the thermal-hydraulics is a one-dimensional parallel channel model.

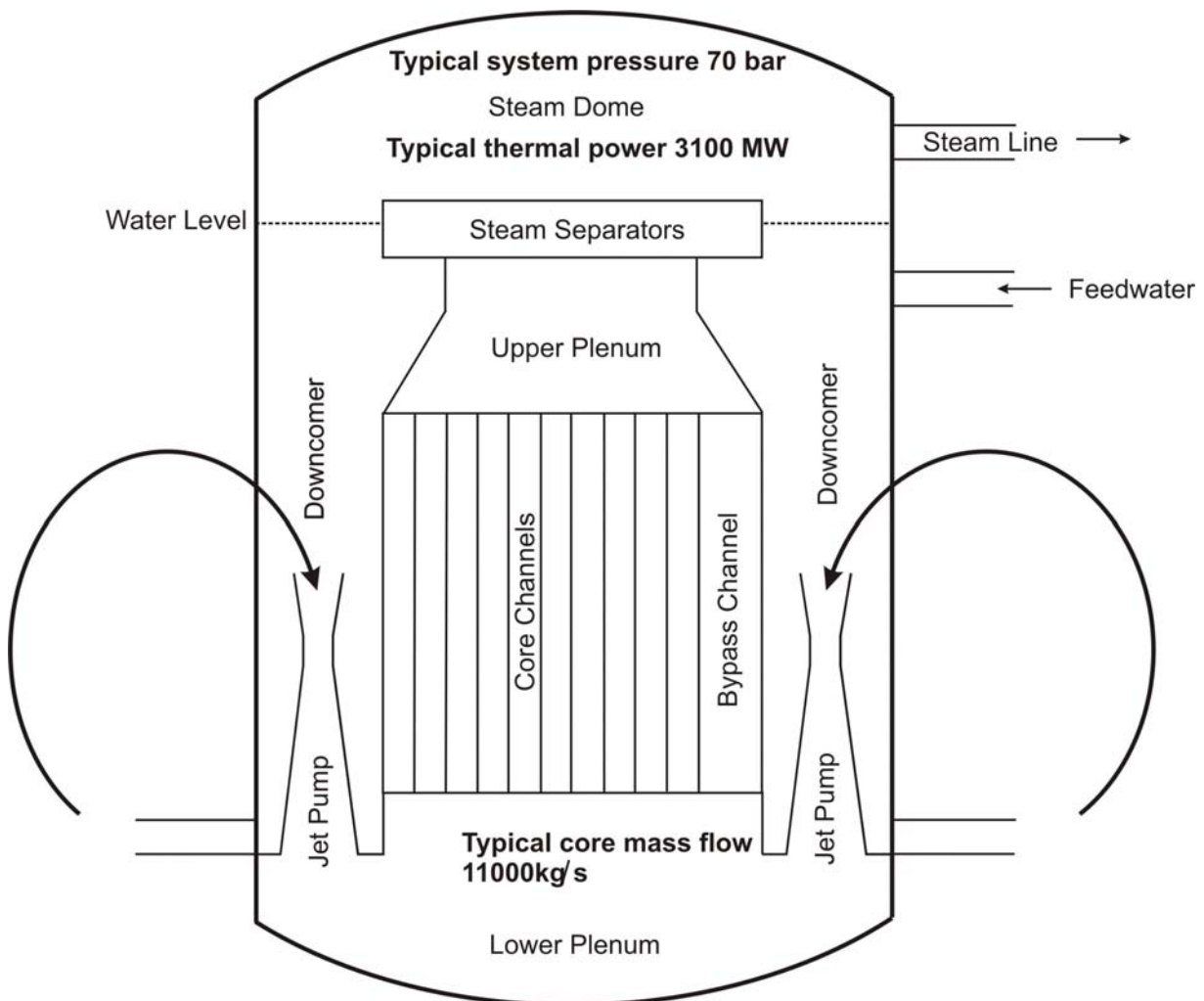


Figure 1: Schematic BWR plant model (GE) [1]

As depicted in Figure 2, the 'hardwired' nine components are:

- Downcomer 1 and Downcomer 2
- Lower Plenum 1 and Lower Plenum2
- Core
- Riser → Upper Plenum, Stand Pipes and Steam Separator
- Steam Dome

All recirculation loops (and all steam lines) are represented by a single recirculation loop with a single jet pump (and a single steam line).

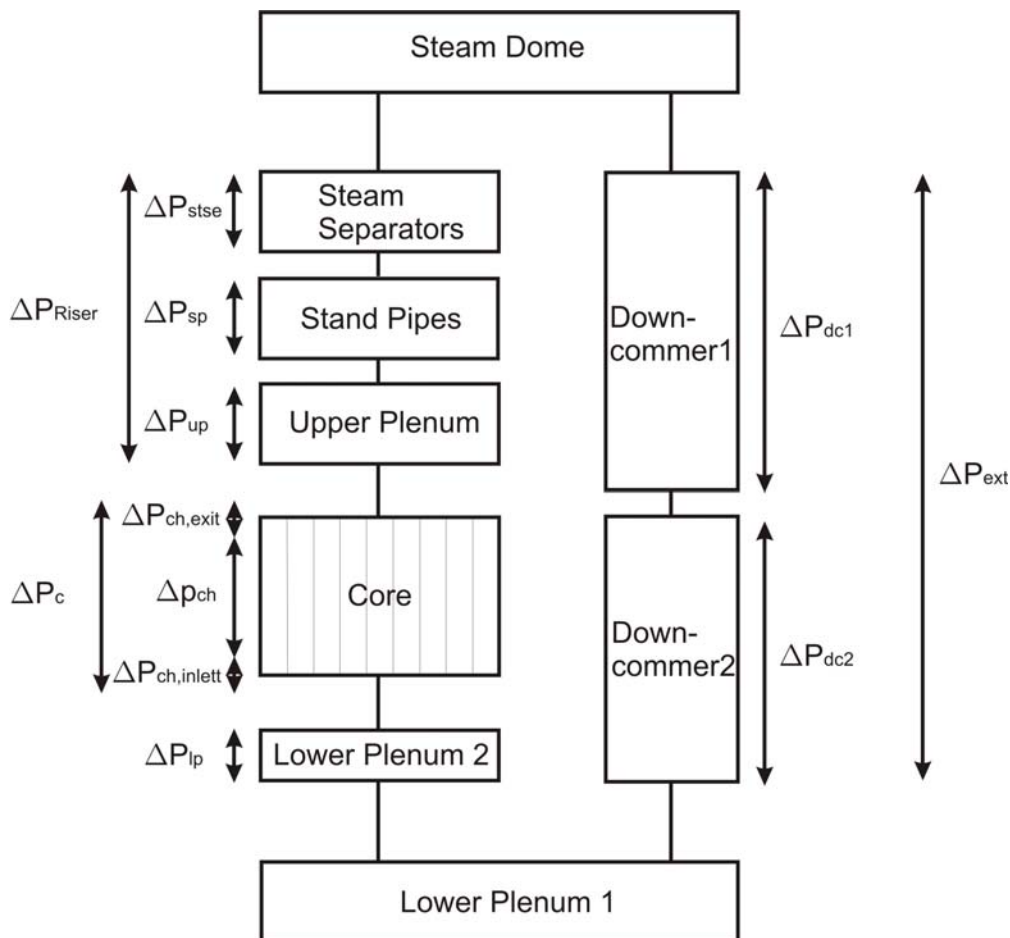


Figure 2: RAMONA BWR model [1]

Neutron transport model:

RAMONA5 provides the PRESTO 1 option (RAMONA 3) and PRESTO 5 option. In PRESTO 1 option, the neutron transport is approximated by the $1 \frac{1}{2}$ group time-dependent neutron diffusion equation where 6 groups of delayed neutrons are taken into account. Thereby finite difference spatial discretization in a coarse mesh lattice is used and the time integration bases on a implicite predictor/corrector scheme. A real reflector is not considered. Instead of this, reflector information are taken into account in boundary conditions (Albedo like extrapolation length).

PRESTO2 option is an extended 2 group nodal kinetic model as it is used in the core simulator PRESTO2. The spatial diffusion problem (the governed equations are presented in Appendix B) is solved by applying analytical nodal methods where two methods for temporal integrations are available. These are the Θ -method (Estimation of the time derivative of the flux by using finite difference technique where the Θ -parameter determines whether explicit or implicit integration is carried out) and the frequency transformation method (exponential time behaviour in the nodes, like quasi-static method). A detail description is given in [1]. Boundary conditions are given by specifying the extrapolation distance and albedo values for thermal flux.

The cross section model is based on a TABGEN cross section model. Thereby the cross section data are given by polynomial coefficients to RAMONA5 where the phenomena exposure (E), density history (ρ_X), instantaneous density (ρ), fuel temperature ($\sqrt{T_F}$), control insertion (CF), soluble boron (N_B) and xenon (N_X) are taken into account. Hence, the nuclear parameters that represent the two-group data are thus functions

$$NP = NP(E, \rho_X, \rho, \sqrt{T_F}, CF, N_B, N_X) \quad (C1)$$

of seven independent variables. These data are given separately for each fuel type implemented in the core.

For nuclear data transfer the core simulator PRESTO2 should run in a standard calculation option RAMONA5 (computes xs, discontinuity factors (DCF), reflector data like albedos for RAMONA5-2). In the RAMONA5 input file, there is stored the cross section data, DCF, albedos, power, density, fuel temperature, Xe concentration, burnup, active flow and the core loading.

Thermal-hydraulic model [1,2]:

RAMONA5 provides two thermal-hydraulic models, namely, standard thermal-hydraulic model and advanced thermal-hydraulic model. In the scope of the present stability analysis with RAMONA5, the advanced thermal-hydraulic model (seven equation model) is not used because of the analysis approach (RAM and ROM). The standard thermal-hydraulic model applies a four equation model based on vapor mass balance, mixture mass balance, mixture energy balance, mixture momentum equation including the corresponding constitutive equations. This model is similar to the drift flux model used in the ROM but with the difference that thermodynamic non-equilibrium is assumed and the different velocities of the phases are modelled by a phase-slip model. For the time integration different explicit integration techniques are available and can be selected by the user.

The mass conservation equation for the gas phase is

$$\frac{\partial}{\partial t} \alpha \rho_g + \frac{\partial}{\partial z} \alpha \rho_g v_g = \Gamma_g \quad , \quad (C2)$$

where Γ_g is local evaporation rate, α is the volumetric void fraction, ρ_g is the gas density and v_g is the gas velocity. The mass conservation equation of the mixture can be written as

$$\frac{\partial}{\partial t} \rho_m + \frac{\partial}{\partial z} \rho_m v_m = 0 \quad , \quad (C3)$$

where ρ_m with

$$\rho_m = \alpha \rho_g + [1 - \alpha] \rho_l \quad (C4)$$

is the mixture density and v_m with

$$v_m = \frac{\alpha \rho_g v_g + [1 - \alpha] \rho_l v_l}{\alpha \rho_g + [1 - \alpha] \rho_l} \quad (C5)$$

is the mixture velocity. The mixture momentum balance is given by

$$\frac{\partial}{\partial t} G + \frac{\partial}{\partial z} (\alpha \rho_g v_g^2 + [1 - \alpha] \rho_l v_l^2) = \rho_m g - \frac{\partial}{\partial z} P + \frac{\partial F}{\partial z} \quad , \quad (C6)$$

where the second term describes the local pressure drop and the third term describes the local friction with

$$\frac{\partial F}{\partial z} = f \Phi^2 \frac{G |G|}{2 \rho_l d_h} \quad . \quad (C7)$$

In the friction term, there is f the single phase friction factor, Φ is the two phase multiplier d_h the hydraulic diameter ρ_l is the density of the liquid phase and G is the mass flux defined as

$$G = \alpha \rho_g v_g + [1 - \alpha] \rho_l v_l \quad . \quad (C8)$$

The mixture energy balance can be written as

$$\frac{\partial}{\partial t} (\alpha \rho_g u_g + (1 - \alpha) \rho_l u_l) + \frac{\partial}{\partial z} (\alpha \rho_g h_g v_g + (1 - \alpha) \rho_l h_l v_l) = \frac{q_w'}{A} + q_l''' (1 - \alpha) \quad , \quad (C9)$$

where u_g and u_l are the specific internal energies, h_g and h_l are the specific enthalpy of the gas and liquid phase, respectively. A is the flow cross section, q_w' is the heat input per unit length of the heated wall and q_l''' is the heat per unit volume released directly in the coolant.

The most essential assumptions are: (a) spatial variation of system pressure is ignored $grad(P(z,t)) = 0$ and (b) vapor is assumed to be at saturation. Assumption (a) decouples the momentum and energy equation. Thus, the momentum equations are uncoupled from the rest of the equations, and may to a certain extent, be treated separately. In particular, assumption (a) enables that the momentum equation can be integrated around the full reactor loop independent on the energy equation. Hence, this assumption eliminates the numerical diffusion effected by the momentum equation spatial discretization. All assumptions of the thermal-hydraulic model are summarized and discussed in [2].

As shown in Figure 2, the hydraulic loop is divided into nine main parts where only vertical flow is taken into account. The core is divided into (isolated) parallel channels with a common lower and upper plenum. Thereby, heat exchange between the parallel channel and heat loss to the surroundings are neglected. A more in detail description of the thermal-hydraulic model is presented in [1].

Finally, the thermal hydraulic parallel channel model of RAMONA5 provides the 3D (steam) void distribution (void content in all channel, radially and axially, in the max. 25 axial sections per channel) and the axial coolant velocities. The detailed core predictions are combined with the capability to describe phase separation and liquid subcooling or superheating in the two-phase coolant mixture [1,2].

Empirical correlations: Slip (Bankoff-Malnes, Bankoff-Jones, Solberg), 2-phase multipliers (Becker correlation, Martinelli-Nelson, Rolstad), heat transfer correlation (forced convection in single phase liquid: Dittus-Boelter, nucleate boiling: Jens and Lottes), evaporation rate correlation.

The fuel model [1,2]:

The fuel model calculates the transport of heat (generated in the fuel pin) to the coolant. Since the fuel temperature field within the fuel pin is known, it is used as feedback to calculate the fuel enthalpy rise. The released heat transferred into the coolant constitutes the volumetric heat source (power density) of the coolant and thus the hydraulic feedback via void generation.

The fuel model of RAMONA5 is very similar to that one of the ROM. The main characteristics are: One average pin per neutronic node, radial heat conduction only, radial pellet discretization (less, equal 3 ring zones), temperature dependent data on heat capacity and conductance, empirical correlations on gap conductance. Furthermore, it is assumed that all fuel rods within one hydraulic node have the same behaviour. This means, the nodal calculation is only done for one average rod unless the user selects the hot pin model (not considered for the stability analysis).

The one dimensional radial fuel heat conduction equation can be written as

$$(\rho_f C_{p,f}) \frac{\partial T_f}{\partial t} = \frac{1}{r} \frac{\partial}{\partial r} (r \cdot k_f) \frac{\partial T_f}{\partial r} + q_f \quad , \quad (\text{C10})$$

where ρ_f is the density of the fuel, $C_{p,f}$ is the specific heat of the fuel, k_f is the conductivity of the fuel, r is the special coordinate, T_f is the fuel temperature and q_f is the power deposited in the fuel. q_f is predicted by the neutron kinetics.

The heat is transported from the surface of the fuel through the gap and cladding to the coolant. The heat transport in the gap is described by

$$0 = \frac{\partial}{\partial r} k_{gp} \frac{\partial T_{gp}}{\partial r} \quad , \quad (\text{C11})$$

where k_{gp} is the heat transfer coefficient of the gap and T_{gp} is the gap temperature. Furthermore, the heat transport in the cladding is given by

$$(\rho_c C_{p,c}) \frac{\partial T_c}{\partial t} = \left(k_c \frac{\partial T_c}{\partial r} \right) , \quad (\text{C12})$$

where ρ_c is the density, $C_{p,c}$ is the specific heat, k_c is the conductivity and T_c is the temperature of the cladding, respectively.

Finally, the heat flux from the cladding surface to the coolant is described by

$$\left(-k_c \frac{\partial T_c}{\partial r} \right) = h(T_c - T_{fl}) , \quad (\text{C13})$$

where h is the heat transfer coefficient and T_{fl} is the bulk temperature of the coolant.

All material properties are functions of the temperature and burnup. More information of the fuel model is presented in [1,2].

To summarize, the main advantage of the system code RAMONA5 is the decoupling of the momentum and energy equation due to ignoring the spatial variation of the system pressure. The assumption of a constant system pressure along the closed flow path corresponds to neglecting pressure waves. In addition to that all thermodynamic properties of the reactor vessel are determined by the same system pressure. This assumption allows that the momentum balance can be integrated along the closed flow path independent on the energy balance. Furthermore, numerical diffusion (can cause numerical damping of power oscillation) effected by the momentum equation spatial discretization is eliminated.

Literatur

- [1] Studsvik/Scandpower RAMONA5.5 Manual, 2003.
- [2] W.Wulff; H.S.Cheng; D.J.Diamond; M.Khatib-Rhabar; "*A Description and Assessment of RAMONA-3B Mod.0,cycle4,: A Computer Code with 3D Neutron Kinetics for BWR System Transients*"; NUREG/CR-3664; BNL-NUREG-51746; Brookhaven National Laboratory; 1984.
- [3] D. Hennig, "*Boiling Water Reactor Stability Analysis-A Challenge for the Study of Complex Nonlinear Dynamical Systems*," PSI Annual Report 1996, Annex IV, Nuclear Energy and Safety.
- [4] A. Dokhane, "*BWR Stability and Bifurcation Analysis using a Novel Reduced Order Model and the System Code RAMONA*," Doctoral Thesis, EPFL, Switzerland, 2004.
- [5] Hennig, D.; Aguirre, C.; "Post-calculation of the stability measurement records #4 and #5 at NPP Leibstadt (Cycle 7), 1990"; PSI Technical Report, TM-41-03-15; 2003.
- [6] D.Hennig, "A Study of BWR Stability Behavior", Nuclear Technology, Vol.126, p.10-31, 1999.

Appendix D: Nomenclature

Stability analysis:

\vec{X}	state vector
\vec{F}	vector field
γ	parameter vector (γ_k with $k \in [1, \dots, m]$ is the k -th component of the parameter vector, m is the dimension of the parameter vector, $\gamma_{k,c}$ critical value of the k -th component of the parameter vector)
J	Jacobian matrix
P	transformation matrix
\vec{U}	state vector, spanned by the new basis
\vec{p}_i	eigenvectors of J
λ_i	eigenvalues of J
$D = P^{-1}JP$	Jacobian matrix transformed into the Jordan normal form
c_i	constant in general solution of the linearized dynamical system, determined by the initial conditions
Re	real part
Im	imaginary part
det	determinant
ε	small amplitude of the periodical solution
T	period of the periodical solution
β	Floquet parameter
τ	Correction factor of the oscillation frequency
SB	Stability boundary
BCH	Bifurcation characteristics, nature of PAH bifurcation
PAH	Poincarè-Andronov-Hopf

Neutronkinetic model:

$\vec{\Phi}$	neutron flux vector
$[v^{-1}]$	neutron inverse velocity matrix
v_1 and v_2	neutron velocities corresponding to the two neutron energy groups
\hat{L}	net-loss operator
\hat{F}	fission production operator
λ_l	decay constants
C_l	precursor concentrations
β_l	delayed neutron fractions
Subscript l	l -th delayed neutron precursor group
∇	Nabla operator
D_1 and D_2	diffusion constant of the first and second group
Σ_1^a and Σ_2^a	macroscopic absorption cross section of the first and second group
$\Sigma_{1 \rightarrow 2}^s$	macroscopic scattering (from the first into the second energy group) cross section
Σ_1^f and Σ_2^f	macroscopic fission cross section of the first and second group
ν	number of neutrons per fissions
$\vec{\Psi}_n$	Eigenvectors (Lambda-Modes, (λ -modes)) of the steady state problem (steady state two group diffusion equation)
$k_n = 1/\lambda_n$	eigenvalues of the steady state problem (steady state two group diffusion equation)
δ_{mn}	Delta function ($\delta_{mn} = 1$ with $m = n$ and $\delta_{mn} = 0$ with $m \neq n$)
$P_n(t)$	Amplitude function or time dependent expansion functions of the corresponding λ -modes ($\vec{\Psi}_n$)
\dot{Q}	total power generated by nuclear fissions within the multiplying medium of the reactor core

ε	energy per fission
ρ_{mn}^F	dynamical feedback reactivities
ρ_{mn}^D	delayed feedback reactivities
$q'''(t)$	power density
$c_q = q_0'''$	steady state power density
V_{fuel}	fuel volume of the core
\dot{Q}_n	power modes
WD_{mn}^r	weighting factor
$C_{mn}^{Void,r}$	Void mode feedback reactivity coefficients
$C_{mn}^{Doppler,r}$	Doppler mode feedback reactivity coefficients
$fact_{mn}$	artificial factor, introduced to increase the feedback gain coupling the first and fundamental mode

Fuel heat conduction model:

r_p	fuel pellet radius
r_g	clad inner radius
r_c	clad outer radius
r_d	point of discontinuity $0 < r_d < r_p$
c_c	clad specific heat
c_p	fuel pellet specific heat
k_c	clad thermal conductivity
k_p	pellet thermal conductivity
p_c	BWR lattice cell pitch
θ_p	temperature, deviations from the steady state for the pellet temperatures
θ_c	temperature, deviations from the steady state for the clad temperatures
α_c	clad thermal diffusivity
α_p	pellet thermal diffusivity
$T_1(t)$ and $T_2(t)$	temperatures
$ll_{1,s}$, $ll_{2,s}$, and $ll_{3,s}$	complicated constants, calculated by employing the symbolic toolbox of MATLAB

Thermal hydraulic model:

ΔP_{head}	pump head
$a_1(t)$	state variable: coefficient of the linear term in the enthalpy profile
$a_2(t)$	state variable: coefficient of the quadratic term in the enthalpy profile
$s_1(t)$	state variable: coefficient of the linear term in the quality profile
$s_2(t)$	state variable: coefficient of the quadratic term in the quality profile
$v_{i,inlet}$	channel inlet velocity of the i -th channel
h_{inlet}	core inlet enthalpy
h	enthalpy
μ	boiling boundary
$\rho_l = \rho_f$	coolant density (liquid)
ρ_g	coolant density (gas)
ρ_m	mixture density
$q_{1\Phi}''$	wall heat flux (single phase region)
$q_{2\Phi}''$	wall heat flux (two phase region)
$h_{\infty,1\Phi}$	single phase convective heat transfer coefficient
$h_{\infty,2\Phi}$	single phase convective heat transfer coefficient
A	cross section of the heated channel
$T_{bulk,1\Phi}$	single phase bulk temperature
$T_{bulk,2\Phi}$	two phase bulk temperature
$T_{s,1\Phi}$	single phase clad surface temperature

$T_{s,2\Phi}$	two phase clad surface temperature
k_f^*	liquid thermal conductivity
D_h^*	hydraulic diameter of the heated channel
Re	Reynolds-Number
Pr	Prandl-Number
P	pressure
$f_{1\Phi}$	single phase friction factor
$f_{2\Phi}$	two phase friction factor
Fr	Froude number
$N_{f,1\Phi}$	single phase friction number
$N_{f,2\Phi}$	two phase friction number
$N_{cov,1\Phi}$	conversion number of the single phase region
$N_{cov,2\Phi}$	conversion number of the two phase region
$N_{pch,1\Phi}$	Phase change number or Zuber number (single phase region)
$N_{pch,2\Phi}$	Phase change number or Zuber number (two phase region)
N_{sub}	subcooling number
h_{sat}	liquid saturation enthalpy
g	gravity constant
α	volumetric void fraction
ω^*	characteristic reaction frequency
Γ_g^*	rate of mass formation of the vapor
j	volumetric flux density
Δh_{fg}	$\Delta h_{fg} = h_g - h_f$ difference of the saturation enthalpy of the vapour (gas) and the saturation enthalpy of the liquid

	phase
C_0	Drift flux parameter characterising the radial void distribution
$V_{gj} = v_g - j$	Drift flux parameter describing the local drift velocity
v_g	velocity of the vapor
v_l	velocity of the liquid
v_0	steady state inlet velocity
v_m	mixture velocity
x	flow quality
$\Delta P_{extern} = \Delta P_{ext}$	steady state external pressure drop
\dot{m}_{tot}	total mass flow
\dot{m}_n	mass flow of the n -th heated channel
$A_{n,inlet}$	flow cross section of the n -th heated channel
A_{doc}	flow cross section of the downcomer
D_{doc}	hydraulic diameter of the downcomer
A_{ol}	$A_{ol} = A_{inlet}^* / A_{doc}^*$
D_{ol}	$D_{ol} = D_h^* / D_{doc}^*$
α_{scool}	true void fraction, where subcooled boiling is included
x_{scool}	true flow quality, where subcooled boiling is included
x_{eq}	equilibrium quality
x_d	equilibrium quality at void departure point
μ_d^*	void departure point
c_{pl}^*	specific heat
T_0	saturation temperature

ξ_h heated perimeter

$\Delta\rho = \rho_l - \rho_g = \rho_f - \rho_g$

L^* heated channel length

Appendix E: Dimensionless variables

$$N_{pch,l\Phi} = \frac{q_{l\Phi}^* \xi_h^* L^* \Delta \rho^*}{A_{inlet}^* \Delta h_{fg}^* v_0^* \rho_g^* \rho_f^*} \quad \text{with } l=1,2$$

$$N_{sub} = \frac{h_{sat}^* - h_{inlet}^*}{\Delta h_{fg}^*} \frac{\Delta \rho^*}{\rho_g^*}$$

$$N_{cov,1\Phi} = \frac{h_{\infty,1\Phi}^* T_0^* \xi_h^* L^* \Delta \rho^*}{A_{inlet}^* \Delta h_{fg}^* v_0^* \rho_g^* \rho_f^*}$$

$$N_{cov,2\Phi} = \frac{2.56 e^{4P^*/(6.2 \cdot 10^6)} T_0^{*4} \xi_h^* L^* \Delta \rho^*}{A_{inlet}^* \Delta h_{fg}^* v_0^* \rho_g^* \rho_f^*}$$

$$N_{\rho} = \frac{\rho_g^*}{\rho_f^*}$$

$$N_{f,l\Phi} = \frac{f_{l\Phi}^* L^*}{2D_h^*}, \quad \text{with } l=1,2$$

$$N_r = \frac{\rho_f^*}{\Delta \rho^*}$$

$$Fr = \frac{v_0^{*2}}{g^* L^*}$$

$$D_{ol} = \frac{D^*}{D_{doc}^*}$$

$$A_{ol} = \frac{A_{inlet}^*}{A_{doc}^*}$$

$$DP_{ext} = \frac{DP_{ext}^*}{\rho_f^* v_0^{*2}}$$

$$t = \frac{t^* v_0^*}{L^*}$$

$$v_{inlet} = \frac{v_{inlet}^*}{v_0^*}$$

$$z = \frac{z^*}{L^*}$$

$$h_i = \frac{h_i^*}{\Delta h_{fg}^*}$$

$$\rho = \frac{\rho^*}{\rho_f^*}$$

A detailed summary of all dimensionless numbers of the ROM is given in [6,8].

Literature

- [1] M. Ishii; X. Sun; S. Kuran; "NUCLEAR-COUPLED FLOW INSTABILITIES AND THEIR EFFECTS ON DRYOUT"; Final Progress Report; PU/NE-04-13; 2004.
- [2] Ishii, M.; *Thermo-fluid Dynamic Theory of Two-Phase Flow*, Eyrolles, Scientific and Medical Publication of France, Paris, 1975.
- [3] Ishii, M.; *One dimensional drift flux model and constitutive equations for relative motion between phases in various two-phase flow regimes*; Technical Report ANL-77-47; Argonne National Laboratory, 1977.

- [4] Collier, G.J.; Thome, R.J.; *Convective Boiling and Condensation*; Third Edition; Clarendon Press, Oxford, 1996.
- [5] Lahey, Jr., T.R.; Moody, J.F.; *The Thermal-Hydraulics of a Boiling Water Nuclear Reactor*; Second Edition; American Nuclear Society; La Grange Park, Illinois USA. 1993
- [6] A. Dokhane, "*BWR Stability and Bifurcation Analysis using a Novel Reduced Order Model and the System Code RAMONA*," Doctoral Thesis, EPFL, Switzerland, 2004.
- [7] Rizzwan-uddin; "*Linear and Nonlinear Stability Analyses of Density-Wave Oscillations in Heated Channels*"; Ph.D. Dissertation of University of Illinois, USA; 1981.
- [8] A.A.Karve; "Nuclear-Coupled Thermal-hydraulic Stability Analysis of Boiling Water Reactors"; Ph.D. Dissertation; Virginia University; USA; 1998.

Appendix F: ROM input parameters

ROM input parameters for NPP Brunsbüttel (KKB), NPP Leibstadt (KKL) and NPP Ringhals (KKR) are summarized in the following.

Table 1: Operational points

Operational Points	KKB	KKL	KKR
Power	1079.50 MW (47.1%)	1867.11 MW (59.5%)	1648.02 MW (72.6%)
Flow (total mass flow including bypass)	2367.00 kg / s (26.14%) 14.35% (bypass mass flow)	4070.12 kg / s (36.5%) 11.29% (by- pass mass flow)	3694.00 kg / s (31.98%) 13.30% (by- pass mass flow)
Total mass flow without bypass mass flow	2027.33 kg / s	3610.656 kg / s	3202.7 kg / s
Core inlet subcooling	118.5 kJ / kg	125 kJ / kg	131 kJ / kg
System Pressure	69.85 bar	69.7 bar	70.1 bar

Table 2: Design and operational parameters

	KKB	KKL	KKR
$P_0^* = P_0$ fundamental mode amplitude	1	1	1
v_0^* steady state mean coolant inlet velocity	0.532 m / s	0.77 m / s	0.68 m / s
T_{inlet}^* steady state coolant inlet temperature	535.93 °K	534.46 °K	533.61 °K
$T_{sat}^* = T_0^*$ saturation temperature	558.83 °K	558.69 °K	559.08 °K
h_{inlet}^* steady state coolant inlet en-	1148.4 kJ / kg	1141.1 kJ / kg	1136.9 kJ / kg

thalpy			
$h_{sat}^* = h_f^*$ saturation liquid enthalpy	1266.9 kJ / kg	1266.1 kJ / kg	1268.2 kJ / kg
P^* system pressure	6.985 MPa	6.97 MPa	7.01 MPa
$\alpha_0^* = \alpha_0$ steady state mean void fraction	0.463	0.550667	0.472784
$T_{avg,0}^*$ steady state mean fuel temperature	674.7492°K	778.5833°K	754.3652°K
DP_{ext}^* external pressure drop	$7.82217 \cdot 10^4$ Pa	$7.3875 \cdot 10^4$ Pa	$9.57 \cdot 10^4$ Pa
$q_0^* = c_q^*$ steady state volumetric heat generation rate	$100.451 \cdot 10^6$ W / m ³	$143.3134311 \cdot 10^6$ W / m ³	$121.2189 \cdot 10^6$ W / m ³
A^* heated channel flow cross section	$1.064 \cdot 10^{-4}$ m ²	$1.530 \cdot 10^{-4}$ m ²	$1.543 \cdot 10^{-4}$ m ²
D^* heated channel hydraulic diameter	0.01072 m	0.0139 m	0.0118 m
h_g^* saturation gas enthalpy	2772.8 kJ / kg	2773.0 kJ / kg	2772.5 kJ / kg
ρ_f^* liquid density	739.99 kgm ⁻³	740.26 kgm ⁻³	739.55 kgm ⁻³
ρ_g^* gas density	36.438 kgm ⁻³	36.350 kgm ⁻³	36.583 kgm ⁻³
μ_f^* liquid viscosity	$91.304 \cdot 10^{-6}$ Nm ⁻² s	$91.360 \cdot 10^{-6}$ Nm ⁻² s	$91.212 \cdot 10^{-6}$ Nm ⁻² s
c_f^* liquid specific heat	5399.5 J / (kgK)	5396.5 J / (kgK)	5404.5 J / (kgK)
k_f^* liquid thermal conductivity	0.57212 W / (mK)	0.57235 W / (mK)	0.57172 W / (mK)
Λ^* mean neutron life time	$3.0 \cdot 10^{-5}$ s	$3.0 \cdot 10^{-5}$ s	$3.32 \cdot 10^{-5}$ s
R^* core radius	2.32 m	2.32 m	2.32 m
L^* core length (=downcomer length)	3.76 m	3.81 m	3.68 m
c_c^* clad specific heat	330.0 J / (kgK)	312.32 J / (kgK)	290.15 J / (kgK) is used in the ROM 287.0 J / (kgK) technical documentation (Lefvert)

c_p^* fuel pellet specific heat	476.6 J/(kgK)	301.03 J/(kgK)	108.12 J/(kgK)
g^* gravity constant	9.81 m/s ²	9.81 m/s ²	9.81 m/s ²
k_c^* clad thermal conductivity	16.0 W/mK	16.0 W/(mK)	16.0 W/(mK) technical documentation (Lefvert)
k_p^* pellet thermal conductivity	4.9 W/(mK)	4.8525 W/(mK)	4.9762 W/(mK)
p_c^* BWR lattice cell pitch	16.2·10 ⁻³ m	16.2·10 ⁻³ m	16.2·10 ⁻³ m
r_c^* clad outer radius	5.025·10 ⁻³ m	6.135·10 ⁻³ m	6.125·10 ⁻³ m technical documentation (Lefvert)
r_s^* clad inner radius	4.42·10 ⁻³ m	5.325·10 ⁻³ m	5.325·10 ⁻³ m technical documentation (Lefvert)
r_p^* fuel pellet radius	4.335·10 ⁻³ m	5.321·10 ⁻³ m (RAMONA-Output) BUT→ 5.205·10 ⁻³ m from technical documentation (Adreani report) and is used in the ROM	5.325·10 ⁻³ m (RAMONA-Output) BUT→ 5.220·10 ⁻³ m from technical documentation (Lefvert) and is used in the ROM
r_d^* point of discontinuity	0.83· r_p^*	0.83· r_p^*	0.83· r_p^*
λ^* delayed neutron precursors mean life time	0.08 s ⁻¹	0.08 s ⁻¹	0.08 s ⁻¹
β fraction of delayed neutrons	0.0056 s	0.0056 s	0.0057 s
ρ_c^* clad density	6.5·10 ³ kgm ⁻³	6.5·10 ³ kgm ⁻³	6.5·10 ³ kgm ⁻³
ρ_p^* pellet density	10.422·10 ³ kgm ⁻³	10.422·10 ³ kgm ⁻³	10.5·10 ³ kgm ⁻³ technical documentation (Lefvert)
h_g^* gap heat transfer		3754.28 W/(m ² K)	3487.26 W/(m ² K)
ξ_h^* heated perimeter	31.573·10 ⁻³ m	19.27·10 ⁻³ m	19.24·10 ⁻³ m
Pr _l liquid Prandl number	0.8617	0.86140	0.86222
Pr _g liquid Prandl number	1.613	1.6117	1.6151

v_l liquid kin. Viscosity	$0.0012339 \text{ cm}^2 / \text{s}$	$0.0012342 \text{ cm}^2 / \text{s}$	$0.0012333 \text{ cm}^2 / \text{s}$
v_g vapor kin. Viscosity	$0.0052016 \text{ cm}^2 / \text{s}$	$0.0052123 \text{ cm}^2 / \text{s}$	$0.0051839 \text{ cm}^2 / \text{s}$
$\text{Re} = v_0 \cdot L / v_l$ liquid Reynolds number	$16.21 \cdot 10^6$	$26.54837 \cdot 10^6$	$23.27414 \cdot 10^6$
$h_{\infty,1\Phi}^*$ single phase heat transfer coefficient	$677.67 \cdot 10^3 \text{ W} / (\text{m}^2 \text{K})$	$775.6878 \cdot 10^3 \text{ W} / (\text{m}^2 \text{K})$	$821.8175 \cdot 10^3 \text{ W} / (\text{m}^2 \text{K})$
$V_{fuel}^* = \pi \cdot (r_p^*)^2 \cdot L \cdot 64 \cdot 6$ Volume of the fuel elements of the whole core	10.7465 m^3 $V_{fuel}^* = \pi \cdot (r_p^*)^2 \cdot L \cdot 91 \cdot 532$	13.02815 m^3 $V_{fuel}^* = \pi \cdot (r_p^*)^2 \cdot L \cdot 62 \cdot 648$	13.59539 m^3

Table 3: Void and Doppler mode feedback reactivity coefficients

	KKB	KKL	KKR
Channel 1			
$C_{00}^{Void,1}$	$-1.0992673 \cdot 10^{-1} \text{ pcm} / \text{Void}$	$-6.9592224 \cdot 10^{-2} \text{ pcm} / \text{Void}$	$-5.37730960 \cdot 10^{-2} \text{ pcm} / \text{Void}$
$C_{01}^{Void,1}$	$3.3292959 \cdot 10^{-2} \text{ pcm} / \text{Void}$	$-5.6921974 \cdot 10^{-2} \text{ pcm} / \text{Void}$	$-5.0783521 \cdot 10^{-2} \text{ pcm} / \text{Void}$
$C_{10}^{Void,1}$	$7.3885333 \cdot 10^{-2} \text{ pcm} / \text{Void}$	$-5.5877601 \cdot 10^{-2} \text{ pcm} / \text{Void}$	$-5.2646601 \cdot 10^{-2} \text{ pcm} / \text{Void}$
$C_{11}^{Void,1}$	$-1.0870970 \cdot 10^{-1} \text{ pcm} / \text{Void}$	$-6.5884191 \cdot 10^{-2} \text{ pcm} / \text{Void}$	$-5.7744819 \cdot 10^{-2} \text{ pcm} / \text{Void}$
$C_{00}^{Doppler,1}$	$-1.0561384 \cdot 10^{-5} \text{ pcm} / \text{K}$	$-1.0561384 \cdot 10^{-5} \text{ pcm} / \text{K}$	$-1.08166290 \cdot 10^{-5} \text{ pcm} / \text{K}$
$C_{01}^{Doppler,1}$	$-8.6464111 \cdot 10^{-6} \text{ pcm} / \text{K}$	$-8.6464111 \cdot 10^{-6} \text{ pcm} / \text{K}$	$-9.9173564 \cdot 10^{-6} \text{ pcm} / \text{K}$
$C_{10}^{Doppler,1}$	$-8.2821048 \cdot 10^{-6} \text{ pcm} / \text{K}$	$-8.2821048 \cdot 10^{-6} \text{ pcm} / \text{K}$	$-1.006068 \cdot 10^{-5} \text{ pcm} / \text{K}$
$C_{11}^{Doppler,1}$	$-9.8178657 \cdot 10^{-6} \text{ pcm} / \text{K}$	$-9.8178657 \cdot 10^{-6} \text{ pcm} / \text{K}$	$-1.0856649 \cdot 10^{-5} \text{ pcm} / \text{K}$
Channel 2			
$C_{00}^{Void,2}$	$-1.0992673 \cdot 10^{-1} \text{ pcm} / \text{Void}$	$-6.9592224 \cdot 10^{-2} \text{ pcm} / \text{Void}$	$-5.37730960 \cdot 10^{-2} \text{ pcm} / \text{Void}$
$C_{01}^{Void,2}$	$-3.3292959 \cdot 10^{-2} \text{ pcm} / \text{Void}$	$5.6921974 \cdot 10^{-2} \text{ pcm} / \text{Void}$	$5.0783521 \cdot 10^{-2} \text{ pcm} / \text{Void}$
$C_{10}^{Void,2}$	$-7.3885333 \cdot 10^{-2} \text{ pcm} / \text{Void}$	$5.5877601 \cdot 10^{-2} \text{ pcm} / \text{Void}$	$5.2646601 \cdot 10^{-2} \text{ pcm} / \text{Void}$
$C_{11}^{Void,2}$	$-1.0870970 \cdot 10^{-1} \text{ pcm} / \text{Void}$	$-6.5884191 \cdot 10^{-2} \text{ pcm} / \text{Void}$	$-5.7744819 \cdot 10^{-2} \text{ pcm} / \text{Void}$
$C_{00}^{Doppler,2}$	$-1.0561384 \cdot 10^{-5} \text{ pcm} / \text{K}$	$-1.0561384 \cdot 10^{-5} \text{ pcm} / \text{K}$	$-1.08166290 \cdot 10^{-5} \text{ pcm} / \text{K}$
$C_{01}^{Doppler,2}$	$-8.6464111 \cdot 10^{-6} \text{ pcm} / \text{K}$	$8.6464111 \cdot 10^{-6} \text{ pcm} / \text{K}$	$9.9173564 \cdot 10^{-6} \text{ pcm} / \text{K}$
$C_{10}^{Doppler,2}$	$-8.2821048 \cdot 10^{-6} \text{ pcm} / \text{K}$	$8.2821048 \cdot 10^{-6} \text{ pcm} / \text{K}$	$1.006068 \cdot 10^{-5} \text{ pcm} / \text{K}$

$C_{11}^{Doppler,2}$	$-9.8178657 \cdot 10^{-6} \text{ pcm} / \text{K}$	$-9.8178657 \cdot 10^{-6} \text{ pcm} / \text{K}$	$-1.0856649 \cdot 10^{-5} \text{ pcm} / \text{K}$
----------------------	---	---	---

Table 4: Pressure drops extracted from the steady state RAMONA5 output

	KKB	KKL	KKR
ΔP_{riser}^{RAM}	$-1.4570 \cdot 10^4 \text{ Pa}$	$-1.573 \cdot 10^4 \text{ Pa}$	$-2.1457 \cdot 10^4 \text{ Pa}$
$\Delta P_{ch,exit}^{RAM}$	$-0.0773 \cdot 10^4 \text{ Pa}$	$-0.0811 \cdot 10^4 \text{ Pa}$	$-0.0975 \cdot 10^4 \text{ Pa}$
ΔP_{ch}^{RAM}	$-2.3080 \cdot 10^4 \text{ Pa}$	$-2.778 \cdot 10^4 \text{ Pa}$	$-2.474 \cdot 10^4 \text{ Pa}$
$\Delta P_{ch,inlet}^{RAM}$	$-1.1157 \cdot 10^4 \text{ Pa}$	$-1.5805 \cdot 10^4 \text{ Pa}$	$-1.2707 \cdot 10^4 \text{ Pa}$
ΔP_{lp2}^{RAM}	$-2.8632 \cdot 10^4 \text{ Pa}$	$-1.3759 \cdot 10^4 \text{ Pa}$	$-3.5812 \cdot 10^4 \text{ Pa}$
ΔP_{lp1}^{RAM}	$-0.0007 \cdot 10^4 \text{ Pa}$	$-3.42 \cdot 10^{-2} \text{ Pa}$	$-0.0006 \cdot 10^4 \text{ Pa}$
ΔP_{dc1}^{RAM}	$2.0195 \cdot 10^4 \text{ Pa}$	$3.8005 \cdot 10^4 \text{ Pa}$	$4.8015 \cdot 10^4 \text{ Pa}$
ΔP_{dc2}^{RAM}	$5.8027 \cdot 10^4 \text{ Pa}$	$3.5871 \cdot 10^4 \text{ Pa}$	$4.7685 \cdot 10^4 \text{ Pa}$
ΔP_c^{RAM}	$-3.5012 \cdot 10^4 \text{ Pa}$	$-4.439 \cdot 10^4 \text{ Pa}$	$-3.8425 \cdot 10^4 \text{ Pa}$
ΔP_{ext}^{RAM}	$-7.8222 \cdot 10^4 \text{ Pa}$	$-7.3875 \cdot 10^4 \text{ Pa}$	$-9.57 \cdot 10^4 \text{ Pa}$

Table 5: ROM pressure drops

	KKB	KKL	KKR
$\Delta P_{ch,exit}^s$	$-1.534 \cdot 10^4 \text{ Pa}$	$-1.654 \cdot 10^4 \text{ Pa}$	$-2.243 \cdot 10^4 \text{ Pa}$
ΔP_{ch}^s	$-2.308 \cdot 10^4 \text{ Pa}$	$-2.777 \cdot 10^4 \text{ Pa}$	$-2.474 \cdot 10^4 \text{ Pa}$
$\Delta P_{ch,inlet}^s$	$-3.979 \cdot 10^4 \text{ Pa}$	$-2.956 \cdot 10^4 \text{ Pa}$	$-4.853 \cdot 10^4 \text{ Pa}$

Tabelle 6: Drift flux paramters

	KKB	KKL	KKR
V_{gi}	0.3	0.35	0.25
C_0	1.02	1.02	1.01

Literature

- [1] Tomas Lefvert; "BWR STABILITY BENCHMARK"; Nuclear Science Committee; OECD/NEA; 1994.
- [2] F.D. Giust; B. Melkerson; L. Moberg; E. Rudbäck; "Out-of-phase azimuthal oscillations in the Ringhals-1 BWR reactor – measurements, data analysis and qualification of a predictive RAMONA model";
- [3] Van Teefflen; „Stabilitätsmessung Mitte des 16. Zyklus“; Technischer Bericht; KKB; Kernkraftwerk Brunsbüttel GmbH; 2001.
- [4] S. Lundberg; R.Schuster; J.Wenisch; „RAMONA5 qualification for the Brunsbüttel NPP (KKB)“; CMS Users Meeting; April 21-22; Turku; Finland; 2004.
- [5] J.Wenisch; "Qualification and Experience with Incore Fuel Management with Modern Methods at Vattenfall Europe Nuclear Energy"; Annual meeting on Nuclear Technology; Nürnberg; May 10-12; 2005.
- [6] Aguirre, C.; Hennig, D.; "Stability measurement at NPP Leibstadt Cycle 7 Sep. 6-th 1990"; NACUSP; 5-th EURATOM FRAMEWORK PROGRAMME 1998-2002; November 2001.
- [7] Blomstrand, J.; "The KKL Core Stability Test, Conducted in September 1990"; ABB-Report; BR91-245; 1992.
- [8] W.Wulff; H.S.Cheng; D.J.Diamond; M.Khatib-Rhabar; "A Description and Assessment of RAMONA-3B Mod.0,cycle4,: A Computer Code with 3D Neutron Kinetics for BWR System Transients"; NUREG/CR-3664; BNL-NUREG-51746; Brookhaven National Laboratory; 1984.
- [9] Studsvik/Scandpower RAMONA5.5 Manual, 2003
- [10] M. Miro; D. Ginestar; D. Hennig; G. Verdu; "On the Regional Oscillation Phenomenon in BWR's"; Progress in Nuclear Energy; Vol. 36; No. 2; pp. 189-229; 2000.
- [11] Hennig, D.; Aguirre, C.; "Post-calculation of the stability measurement records #4 and #5 at NPP Leibstadt (Cycle 7), 1990"; PSI Technical Report, TM-41-03-15; 2003.

Appendix G: Summary of the KKB-Analysis

NPP Brunsbüttel cycle 16

Preliminary stability investigations with the system code RAMONA-3 were performed for cycle 16 of KKB. The input data are valid for a burn-up state of 3000 VLS (Voll-Last-Stunden) [1,2]. As a result, a decay ratio of 0.8 was found for the case where 3 pumps were in operation on the 104% rod line.

In order to improve the validation-data of RAMONA-3 for the NPP Brunsbüttel a stability measurement in the middle of cycle 16 was performed on November 29, 2001. To this end, at first, the reactor state was appointed on the 104% rod line at 100% power (xenon-equilibrium). Next, the pump speed of all pumps was reduced to the minimum (corresponding to the minimum speed level "Linker Eckpunkt"). Thereby the power was reduced to 62.2%. After tripping 4 ZUP pumps, the power is reduced to 47% and the mass flow is reduced to 26%. In this new operational point, which is defined to be the reference OP for the present BWR stability analyses, a global power oscillation was growing. Because of the fast increasing oscillation amplitudes, control rods were inserted into the reactor core to suppress the oscillation after the amplitudes exceeded 5% [1,2].

The Brunsbüttel (KKB) stability data are acquired from the stability test conducted at the middle of cycle sixteen.

Operational point:

$$\begin{aligned}
 \text{Power} &= 1079.50 \text{ MW} \quad (47.10\%) \quad (100\% \text{ Power} = 2291.93 \text{ MW}) \\
 \text{Flow} &= 2367.00 \text{ kg/s} \quad (26.14\%) \quad (100\% \text{ Flow} = 9055.09 \text{ kg/s}) \\
 \text{Subcooling} &= 118.5 \text{ kJ/kg} \\
 \text{Pressure} &= 69.85 \text{ bar}
 \end{aligned}
 \tag{G1}$$

This operational point was selected for the nonlinear stability analyses because the onset of un-damped global power oscillations was observed. Thereby 4 pumps are tripped and the pump derivate is taken from the pressure drop over the pumps.

In the scope of the first RAMONA5 investigation for the NPP Brunsbüttel in the selected operational point, at first the steady state 3D-parameter distributions, most significant for the BWR stability behavior, will be evaluated (steady state analysis), secondly the stability behavior will be analysed (transient analysis) and thirdly the ROM input parameters will be calculated.

The first figure shows the core shape, the control rod positions and the corresponding numbers of fuel elements in a quarter core. This configuration is composed symmetrically around $x = 7$, $y = 7$.

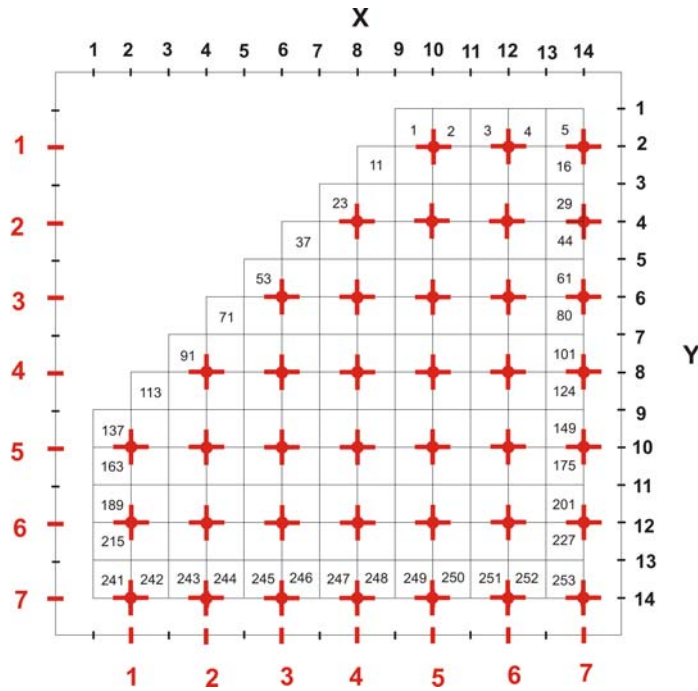


Figure 1: Control rod positions of a quarter core.

The control rod configuration of the entire core is shown next.

Insertion fraction: 2.46 %
 Total withdrawal : 45675.0 c.r. units

	1	2	3	4	5	6	7	8	9	10	11	12	13
1					363	363	363	363	363				
2				363	363	363	363	363	363	363			
3			363	363	363	363	363	363	363	363	363		
4		363	363	363	363	363	363	363	363	363	363	363	
5	363	363	363	363	363	75	363	363	363	363	363	363	363
6	363	363	363	363	363	363	363	363	75	363	363	363	363
7	363	363	363	363	363	363	363	363	363	363	363	363	363
8	363	363	363	363	75	363	363	363	363	363	363	363	363
9	363	363	363	363	363	363	363	75	363	363	363	363	363
10		363	363	363	363	363	363	363	363	363	363	363	363
11			363	363	363	363	363	363	363	363	363		
12				363	363	363	363	363	363	363			
13					363	363	363	363	363				

Figure 2: Control rod configuration for KKB cycle sixteen in cm. 363 cm means the control rod is complete out (withdrawn) of the core.

1.1 Steady state analysis

To summarize, the axial power and axial void profile, radially averaged, are plotted in Figure 3. Furthermore, radial power distribution, axially averaged is shown in Figure 4 and Figure 5.

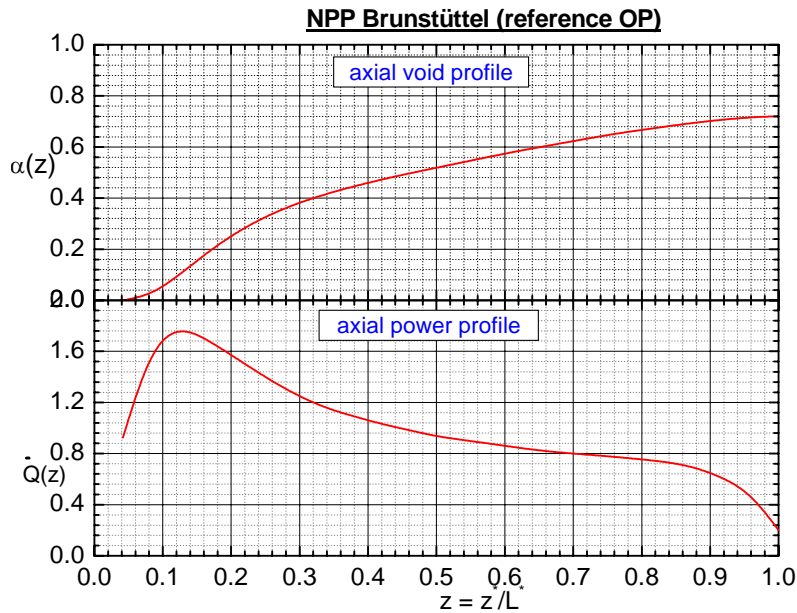


Figure 3: This figure shows the steady state axial power and void profile (radially averaged) calculated by RAMONA5.

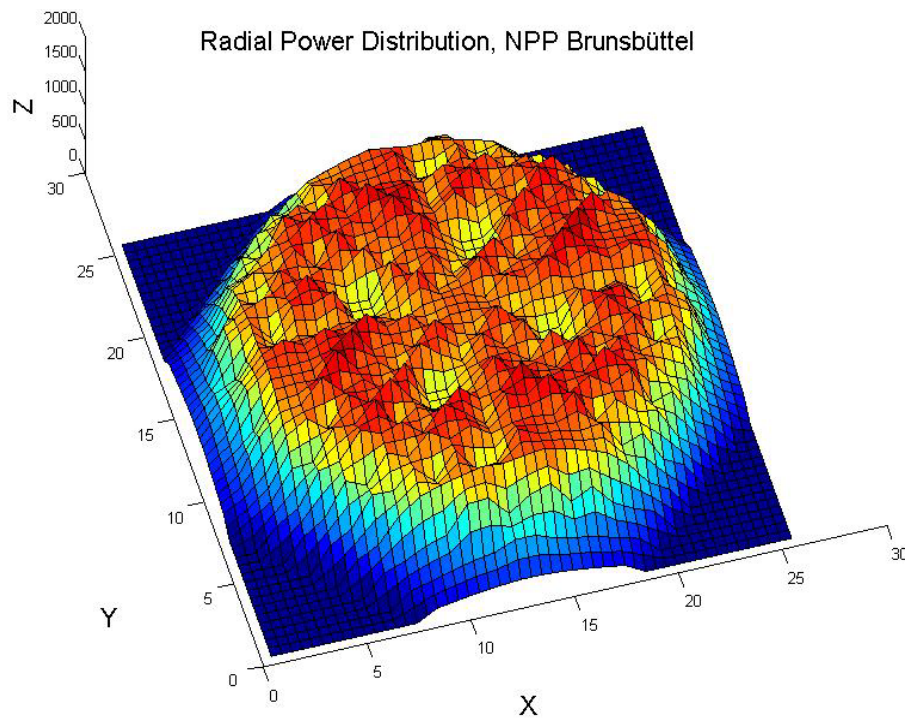


Figure 4: Three dimensional radial power distribution axially averaged for NPP Brunstüttel (reference OP). The Z-Axis corresponds to the relative power ($\cdot 10^{-1}$).

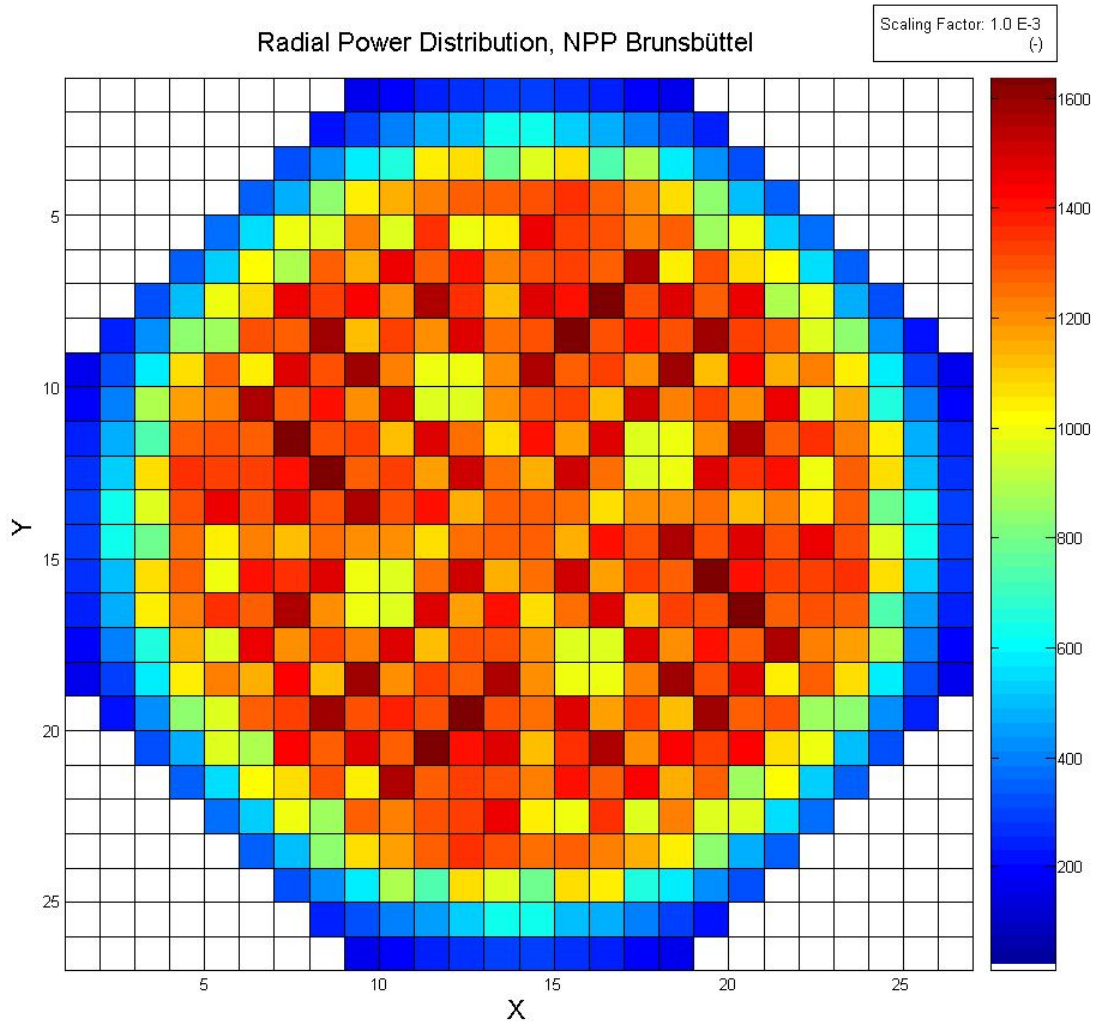


Figure 5: Radial power distribution axially averaged for NPP Brunsbüttel (reference OP).

Table 1: Results for the pressure drops extracted and calculated from the RAMONA5 output

$\Delta P_{riser}^{RAM} = -1.4570 \cdot 10^4 Pa$	$\Delta P_{lp1}^{RAM} = -0.0007 \cdot 10^4 Pa$
$\Delta P_{ch,exit}^{RAM} = -0.0773 \cdot 10^4 Pa$	$\Delta P_{dc1}^{RAM} = 2.0195 \cdot 10^4 Pa$
$\Delta P_{ch}^{RAM} = -2.3080 \cdot 10^4 Pa$	$\Delta P_{dc2}^{RAM} = 5.8027 \cdot 10^4 Pa$
$\Delta P_{ch,inlet}^{RAM} = -1.1157 \cdot 10^4 Pa$	$\Delta P_c^{RAM} = -3.5012 \cdot 10^4 Pa$
$\Delta P_{lp2}^{RAM} = -2.8632 \cdot 10^4 Pa$	$\Delta P_{ext}^{RAM} = -7.8222 \cdot 10^4 Pa$

1.2 Transient analysis

The transient behavior is induced by imposing a system pressure perturbation and recorded by the LPRM detector system ('STABILITY' Option). The different LPRM detector locations are depicted in Figure 6.

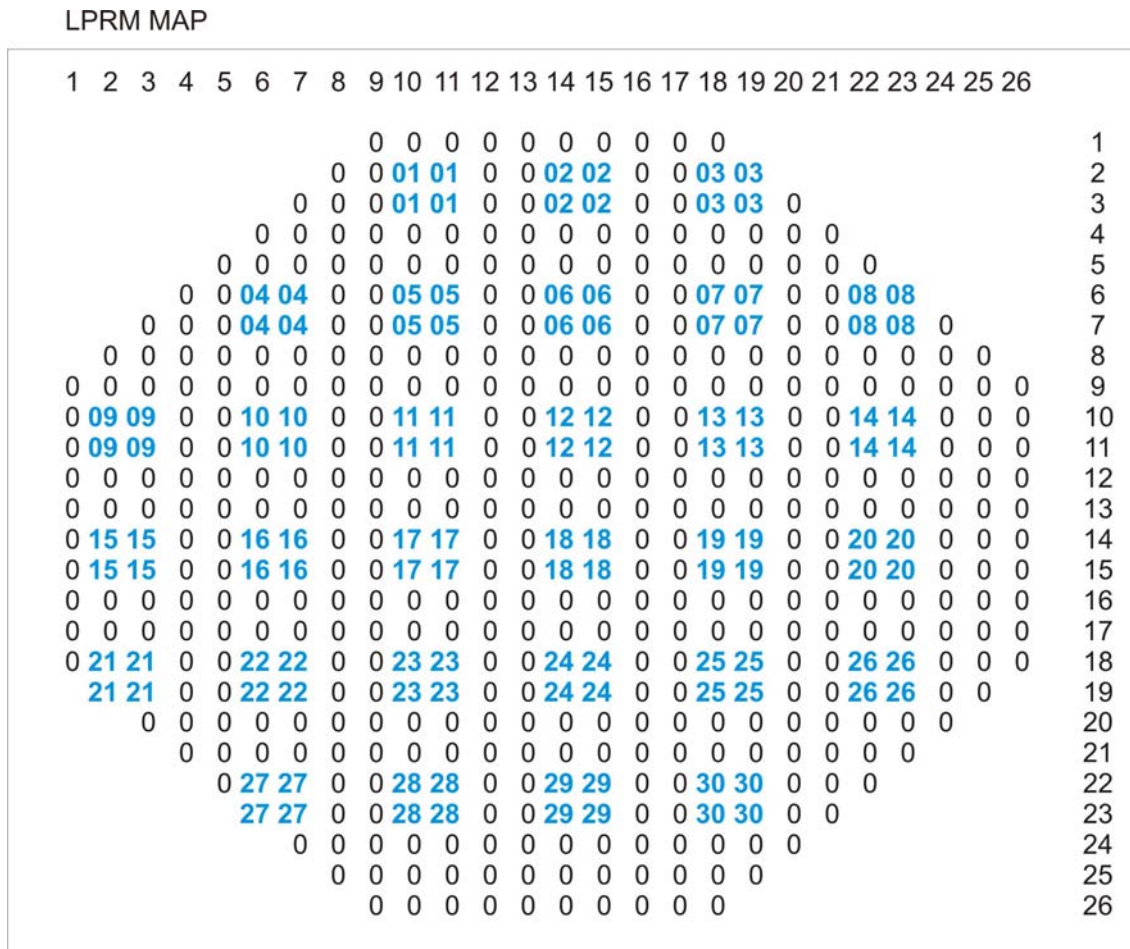


Figure 6: RAMONA 5.2-5 nomenclature for LPRM locations

Next, the LPRM signals of the fourth axial level in units of % are displayed in Figure 7. It can be seen that all signals are in phase. Accordingly, a global power oscillation is arising in the operational point considered. Furthermore, the oscillation is converging to a limit cycle (stable global power oscillation).

In Figure 8 the time evolution of the relative power is shown. Because of the global power oscillation, the oscillation amplitudes have qualitatively the same time evolution as the LPRM signals. In a regional power oscillation case, the amplitudes of the relative power would be zero.

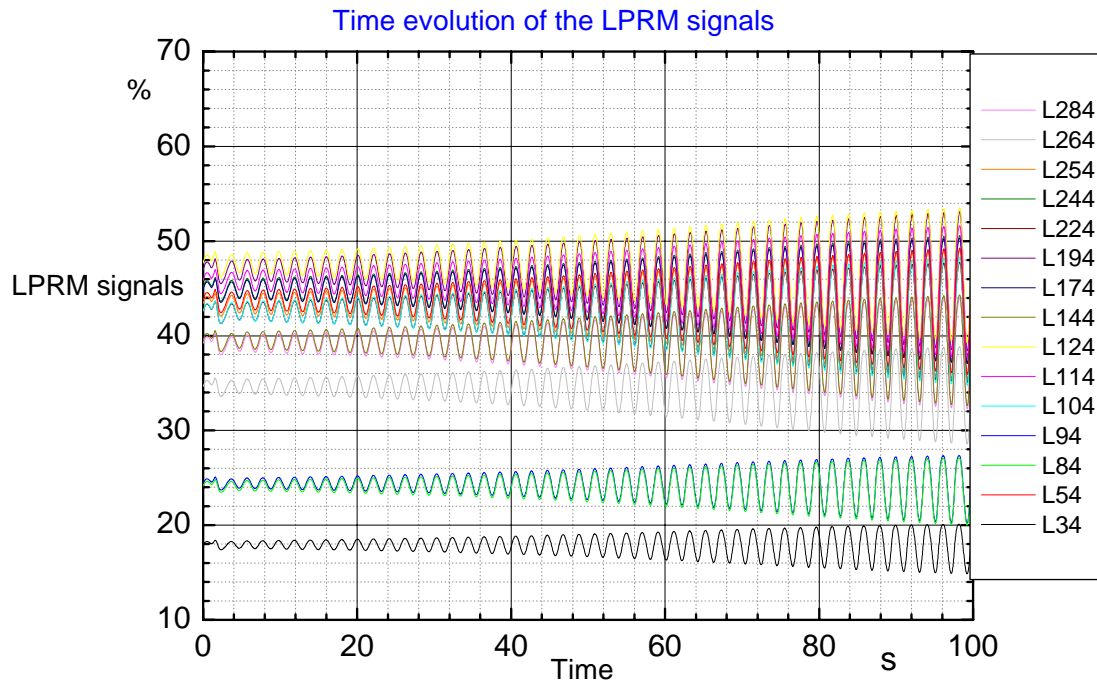


Figure 7: Signals (%) of selected LPRMs located in the fourth level are shown. All signals are in phase and converging to a stable limit cycle.

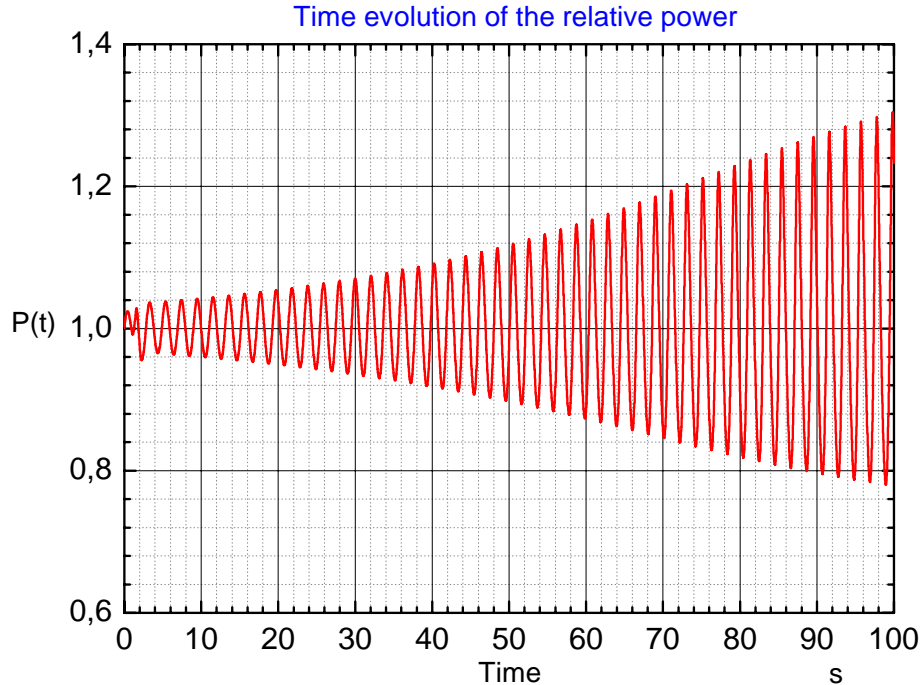


Figure 8: This figure presents the time evolution of the relative power.

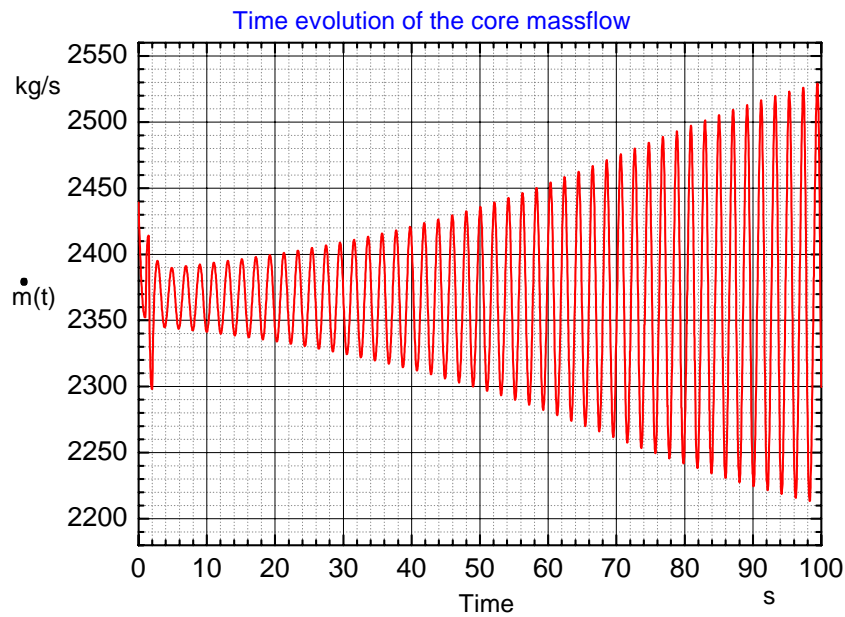


Figure 9: This figure presents the time evolution of the total mass flow.

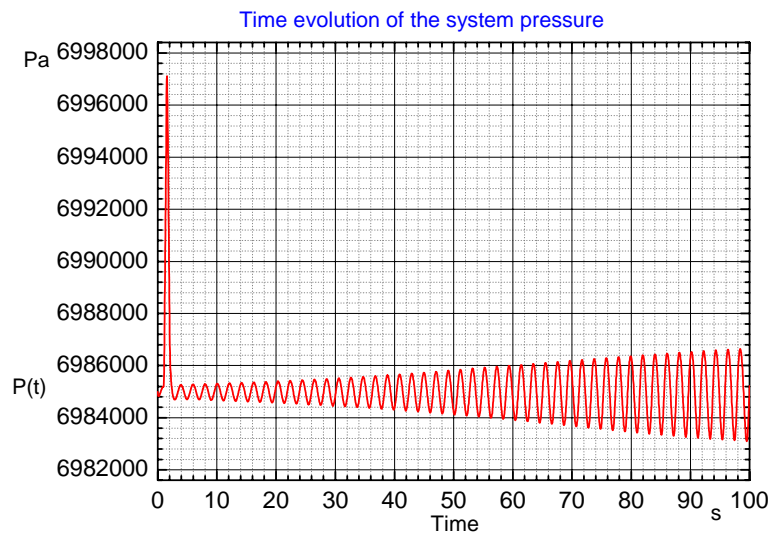


Figure 10: This figure shows the time evolution of the system pressure. The initial perturbation induced can be seen clearly.

The time evolution of the system pressure is presented in Figure 10. As stated previously, the transient is initiated by imposing a system pressure perturbation. The corresponding perturbation amplitude is displayed in this figure.

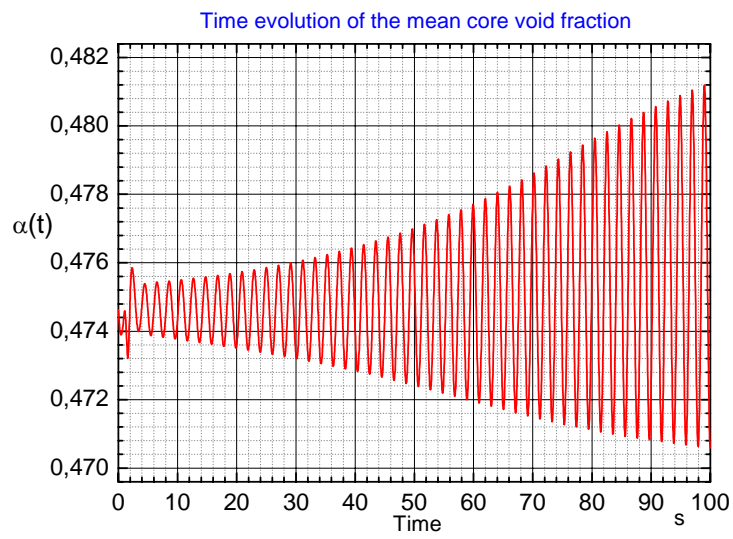


Figure 11: This figure displays the time evolution of the mean core void (volumetric) fraction.

1.3 Summary of the ROM analysis

The new calculation procedure for the ROM input parameters was applied for the reference OP.

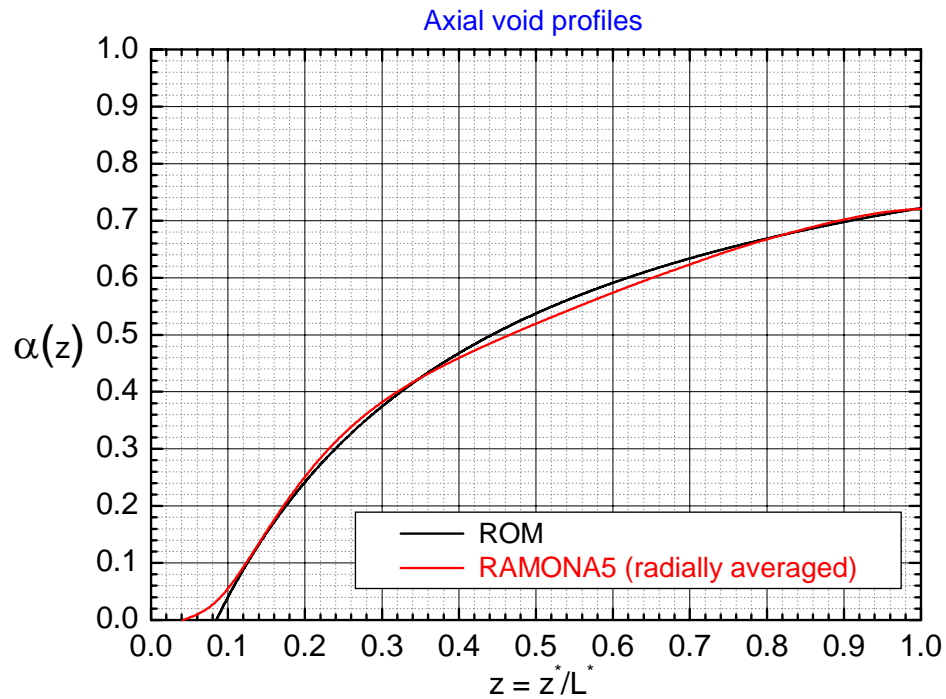


Figure 12: Comparison of the axial void profile calculated by RAMONA5 (radially averaged) with the axial void profile provided by the ROM.

In Table 2 are shown the pressure drops of RAMONA5 and ROM. The results of the RAMONA5- and ROM-pressure drops are consistent.

Table 2: Heated channel pressure drops provided by the RAMONA5 output and calculated by the ROM (reference-OP).

Pressure drop	RAMONA5	ROM
$\Delta P_{ch,inlet}^*$	$-3.979 \cdot 10^4 Pa$	$-3.979 \cdot 10^4 Pa$
ΔP_{ch}^*	$-2.308 \cdot 10^4 Pa$	$-2.305 \cdot 10^4 Pa$
$\Delta P_{ch,exit}^*$	$-1.534 \cdot 10^4 Pa$	$-1.538 \cdot 10^4 Pa$
DP_{ext}^*	$-7.8222 \cdot 10^4 Pa$	$-7.8222 \cdot 10^4 Pa$

Figure 13 summarizes the result of the numerical integration in the reference OP. As predicted by RAMONA5, a growing in-phase power oscillation is occurring in the reference OP.

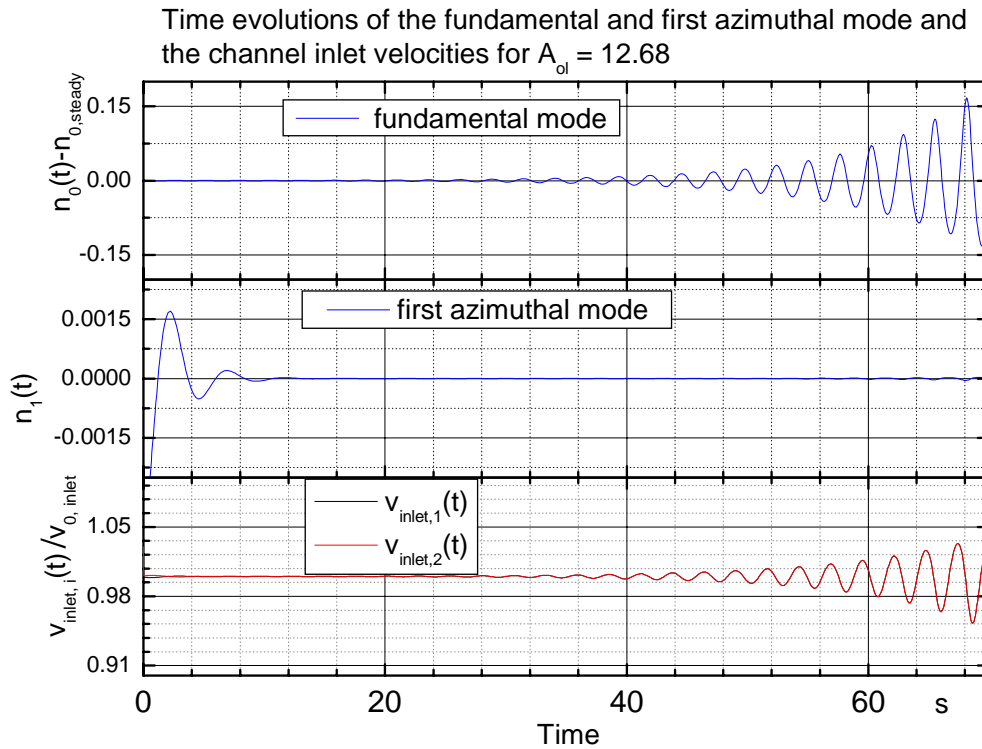


Figure 13: Time evolutions of the fundamental $n_0(t)$ and first azimuthal mode $n_1(t)$ and the channel inlet velocities $v_{1,inlet}(t)$ and $v_{2,inlet}(t)$.

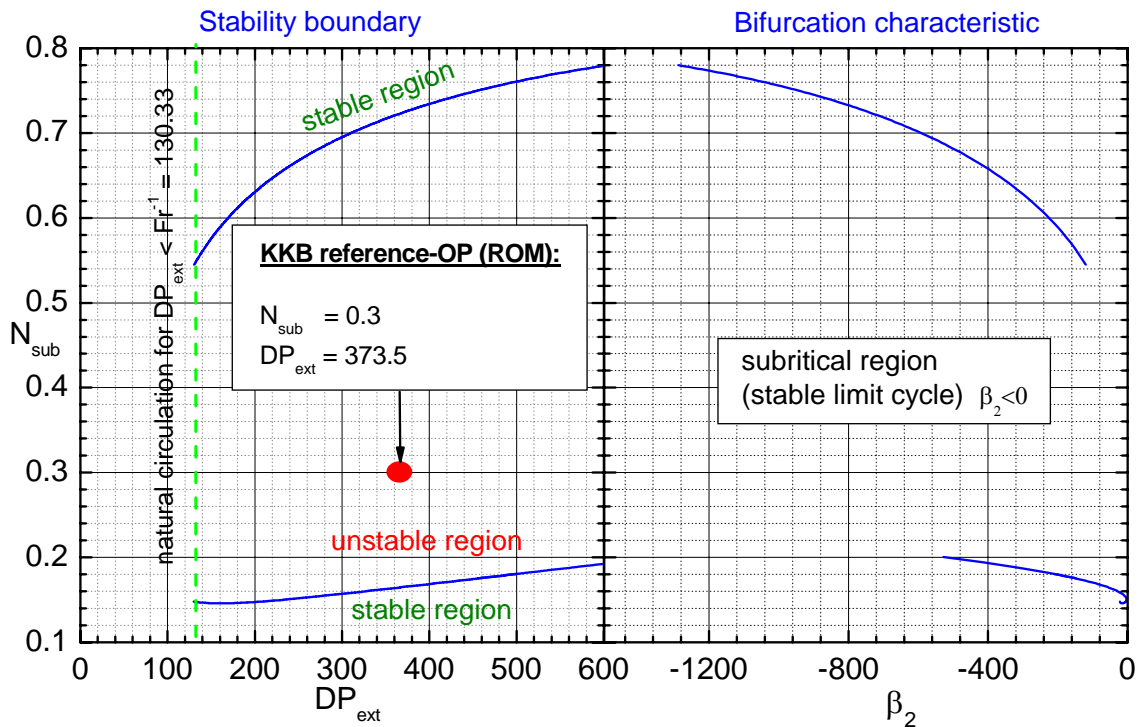


Figure 14: Stability boundary and bifurcation characteristic for the reference OP.

Figure 14 shows the result of the semi-analytical bifurcation analysis. The reference OP is located in the linear unstable region. The results are only plotted in the region, which is reasonable from the physical point of view. In this region, only supercritical PAH bifurcations are occurring. Hence, stable periodical solutions are predicted in the linear unstable region.

The stability boundary shown in Figure 14 was transformed into the power flow map. This result is presented in Figure 15 in which the 100% and 104% rodlines are included.

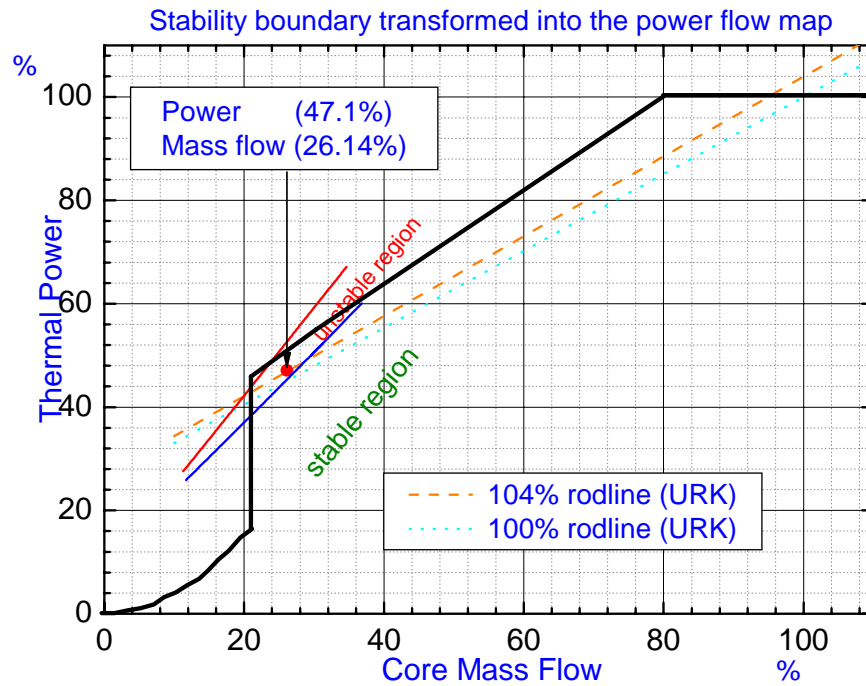


Figure 15: Stability boundary transformed into the power flow map.

1.3.1 Effect of the uncertainty of the measured total power, total mass-flow and core inlet subcooling on the axial void profiles calculated by RAMONA5

From the available technical documentation of the NPP Leibstadt, Ringhals and Brunsbüttel can be seen that the measuring instruments are calibrated for nominal conditions. The uncertainty of the measured total power, total core mass flow and core inlet temperature, corresponding to operational points located in the exclusion region, is relative large between 5% and 10% .

An uncertainty investigation with the system code RAMONA has shown that a power or core mass flow or core inlet temperature deviation of 5% corresponds to a deviation in the total volumetric void fraction of around 5% . A RAMONA assessment where the uncertainty of the power, mass flow as well as the core inlet temperature are considered, has shown that the deviation in the total volumetric void fraction is 9.2% . In order to calculate the total uncertainty of the total volumetric void fraction the uncertainty of all measured data has to be taken into account. Consequently, the total uncertainty of the real total volumetric void fraction is larger as assessed in the above RAMONA analysis.

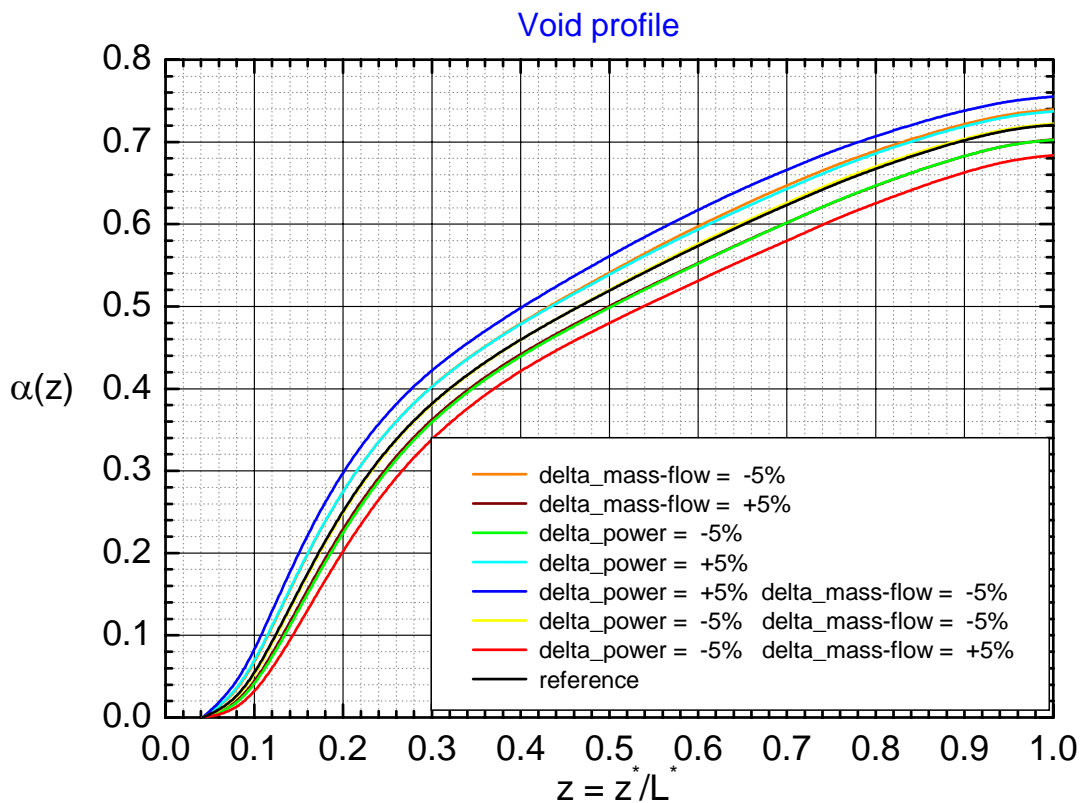


Figure 16: This figure shows axial profiles of the volumetric void fraction for different reactor power and coolant mass flow calculated by RAMONA 5. Thereby the power and core mass flow was changed by 5% respectively.

Literature

- [1] Van Teefflen; „*Stabilitätsmessung Mitte des 16. Zyklus*“; Technischer Bericht; KKB; Kernkraftwerk Brunsbüttel GmbH; 2001.
- [2] S. Lundberg; R.Schuster; J.Wenisch; „*RAMONA5 qualification for the Brunsbüttel NPP (KKB)*“; CMS Users Meeting; April 21-22; Turku; Finland; 2004.
- [3] J.Wenisch; „*Qualification and Experience with Incore Fuel Management with Modern Methods at Vattenfall Europe Nuclear Energy*“; Annual meeting on Nuclear Technology; Nürnberg; May 10-12; 2005.

Appendix H: Summary of the KKR-Analysis

NPP Ringhals1 cycle 14

At the beginning of cycle 14, a stability test was performed on the Ringhals-1 BWR. The intention was to determine the stability characteristics on the new minimum pump speed line, as well as to study the mode of power oscillation at different operating states. Thereby, the recordings were made in points arranged in a grid layout. These points are located in the high power low flow region of the power flow map where unstable behaviour is expected [1]. The measurement data of such instability events have been widely used in the past in order to tune and to validate various system codes. From these data, the decay ratio, statistical parameters and frequency were calculated.

During the stability test, a limit cycle regional out-of-phase power oscillation was occurring at 72% power and 32% coolant mass flow (cycle 14, record 9).

Operational point (KKRc14_rec9-OP):

$$\begin{aligned} \text{Power} &= 1648.02 \text{ MW} \quad (72.6\%) \\ \text{Flow} &= 3694.00 \text{ kg/s} \quad (31.98\%) \\ \text{Subcooling} &= 131 \text{ kJ/kg} \\ \text{Pressure} &= 70.1 \text{ bar} \end{aligned} \tag{H1}$$

Measuring data of this operational point and the corresponding RAMONA5 model of Ringhals-1 BWR are the basis for the nonlinear BWR stability analysis carried out with the ROM. The signal of LPRM 8 and its power spectral density is shown next.

INITIAL CONTROL ROD INSERTION (SCALE = -2)

Y/X	1	2	3	4	5	6	7	8	9	10	11	12	13	14	15	16	17	18	19	20	21	22	23	24	25	26	27	28	29	30	
1													--	--	--	--	--	--													
2													--	--	--	--	--	--	--	--											
3																															
4																															
5																1250	1250														
6																1250	1250														
7														350	350			150	150				150	150							
8														350	350			150	150				150	150							
9																						2225	2225								
10																						2225	2225								
11																							300	300							
12																							300	300							
13																															
14																															
15																															
16																															
17																															
18																															
19																															
20																															
21																															
22																															
23																															
24																															
25																															
26																															
27																															
28																															
29																															
30																															

Figure 3: Control rod configuration for the selected OP in mm .

1.1 Steady state summary (RAMONA5)

To summarize, the axial power and axial void profile, radially averaged, are plotted next. Furthermore, radial power distribution, axially averaged is shown in Figure 5 and Figure 6.

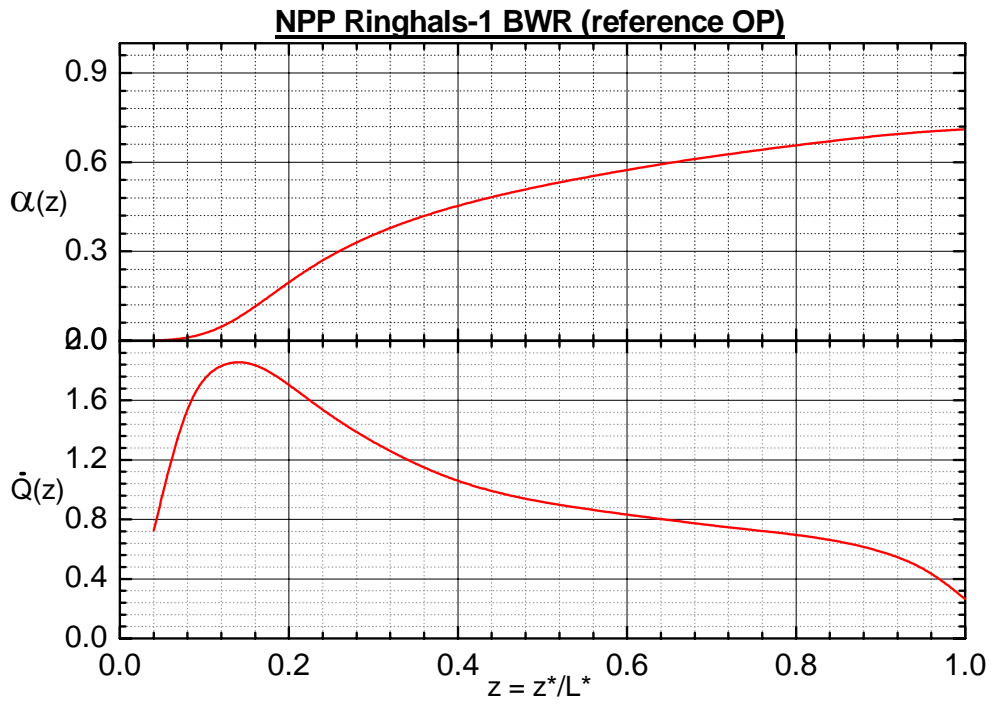


Figure 4: This figure shows the steady state axial power and void profile (radially averaged) calculated by RAMONA5.

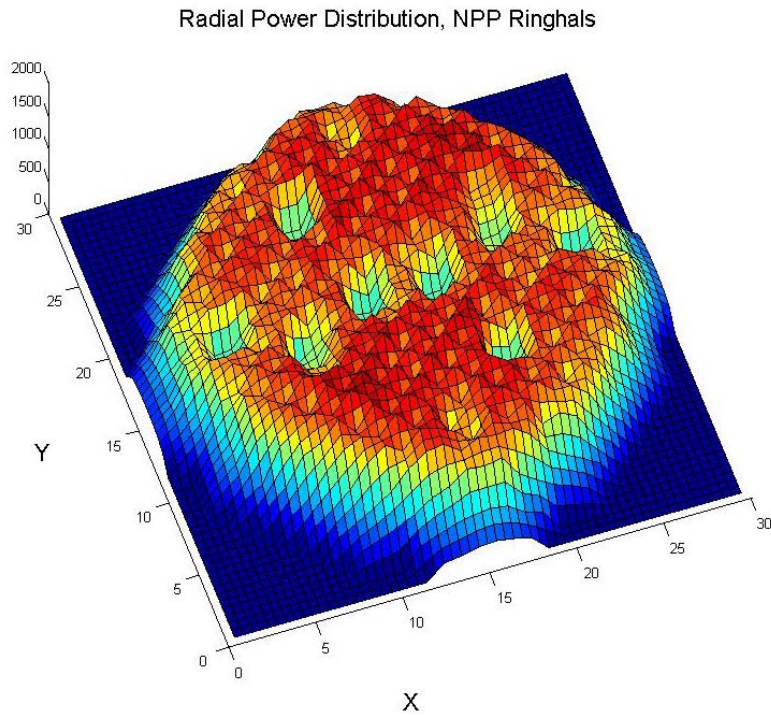


Figure 5: Three dimensional radial power distribution axially averaged for NPP Ringhals-1 (reference OP). The Z-Axis corresponds to the relative power ($\cdot 10^{-1}$).

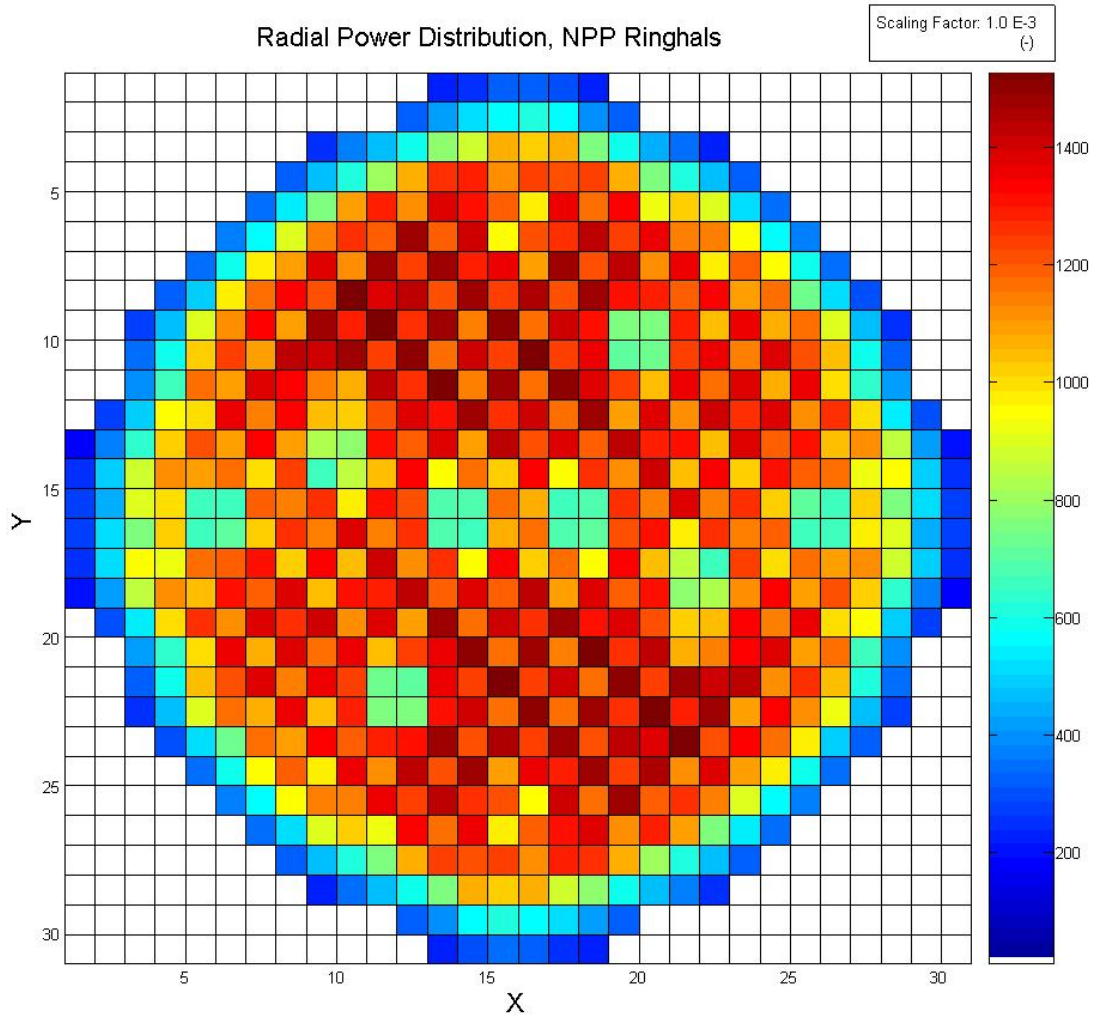


Figure 6: Radial power distribution axially averaged for NPP Ringhals-1 (reference OP).

Table 1: Results for the pressure drops extracted and calculated from the steady state RAMONA5 output (reference OP)

$\Delta P_{riser}^{RAM} = -2.1457 \cdot 10^4 Pa$	$\Delta P_{lp1}^{RAM} = -0.0006 \cdot 10^4 Pa$
$\Delta P_{ch,exit}^{RAM} = -0.0975 \cdot 10^4 Pa$	$\Delta P_{dc1}^{RAM} = 4.8015 \cdot 10^4 Pa$
$\Delta P_{ch}^{RAM} = -2.3080 \cdot 10^4 Pa$	$\Delta P_{dc2}^{RAM} = 4.7685 \cdot 10^4 Pa$
$\Delta P_{ch,inlet}^{RAM} = -1.2707 \cdot 10^4 Pa$	$\Delta P_c^{RAM} = -3.8425 \cdot 10^4 Pa$
$\Delta P_{lp2}^{RAM} = -3.5812 \cdot 10^4 Pa$	$\Delta P_{ext}^{RAM} = -9.57 \cdot 10^4 Pa$

1.2 Transient behaviour (RAMONA5)

The transient behaviour is initiated by introducing a 2 node control rod movement. Thereby an in-phase mode was triggered. The signals of the LPRM 8 and 32 of the fourth level and located in different core half's (RAMONA predicts a fixed symmetry line for the present case) are selected for the evaluation of the transient behaviour. The core shape, symmetry line and the locations of the LPRM detectors of the fourth level are summarized in Figure 7.

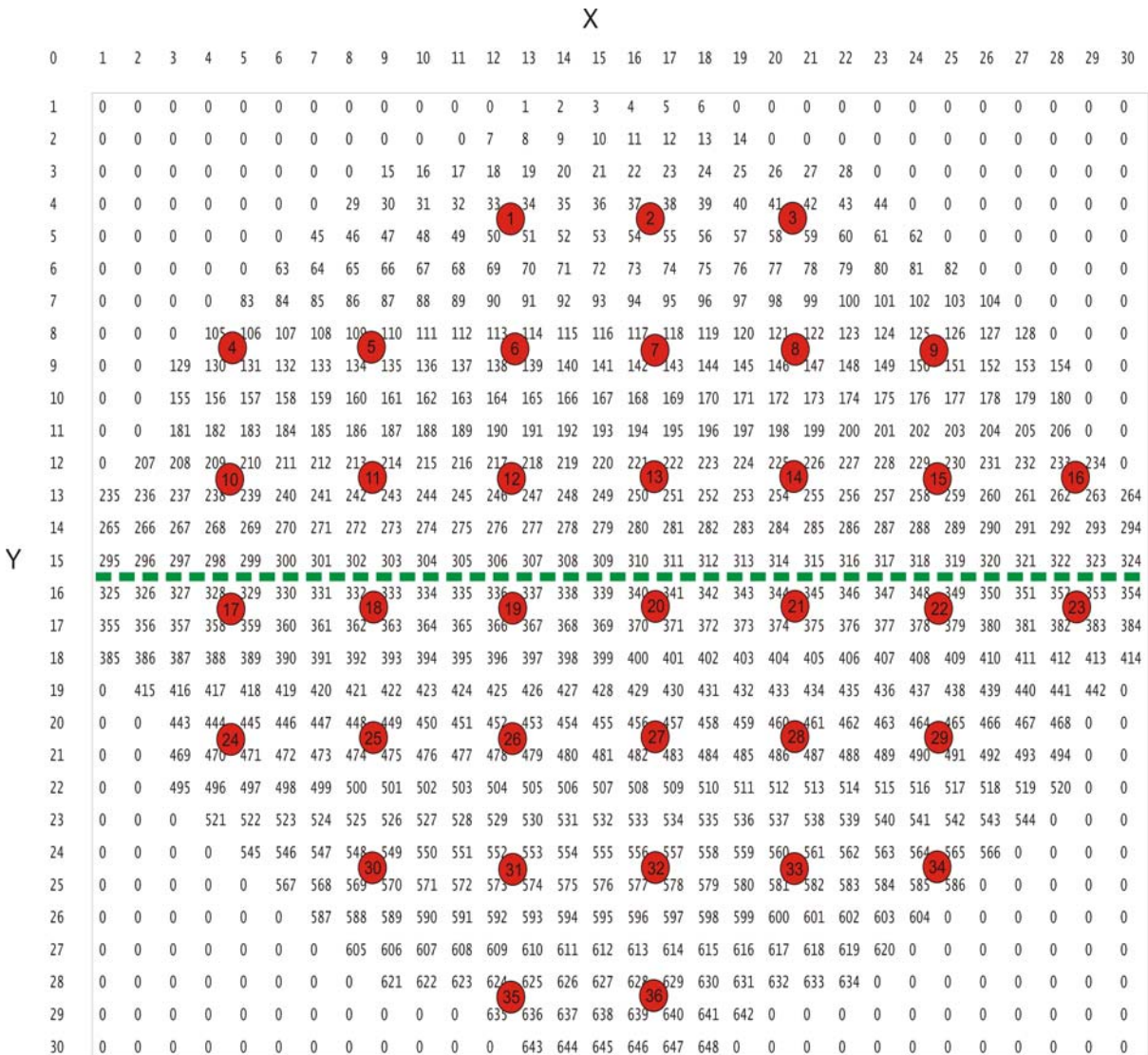


Figure 7: LPRM locations and symmetry line of the out-of-phase power oscillation

Figure 8 shows the time evolution of the LPRM signals 8 and 32. As can be seen, an out of phase power oscillation is occurring in the reference OP. The frequency of the oscillation is $NF^* = 0.48s^{-1}$. All RAMONA5 investigations for the reference OP and its close neighbourhood have shown that the out of phase power oscillation is discharged into a stable limit cycle.

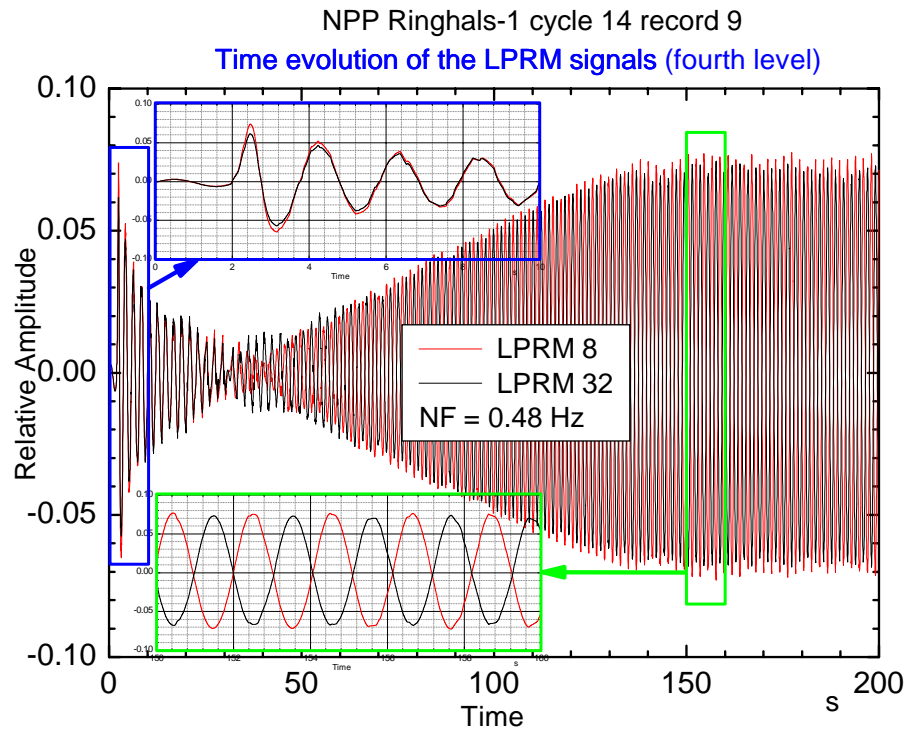


Figure 8: RAMONA5 result for the reference OP. The relative amplitudes of signals are shown for LPRM 8 and LPRM 32. Both LPRM signals have a phase shift of π .

The power spectral density of the LPRM 8 is shown in Figure 9.

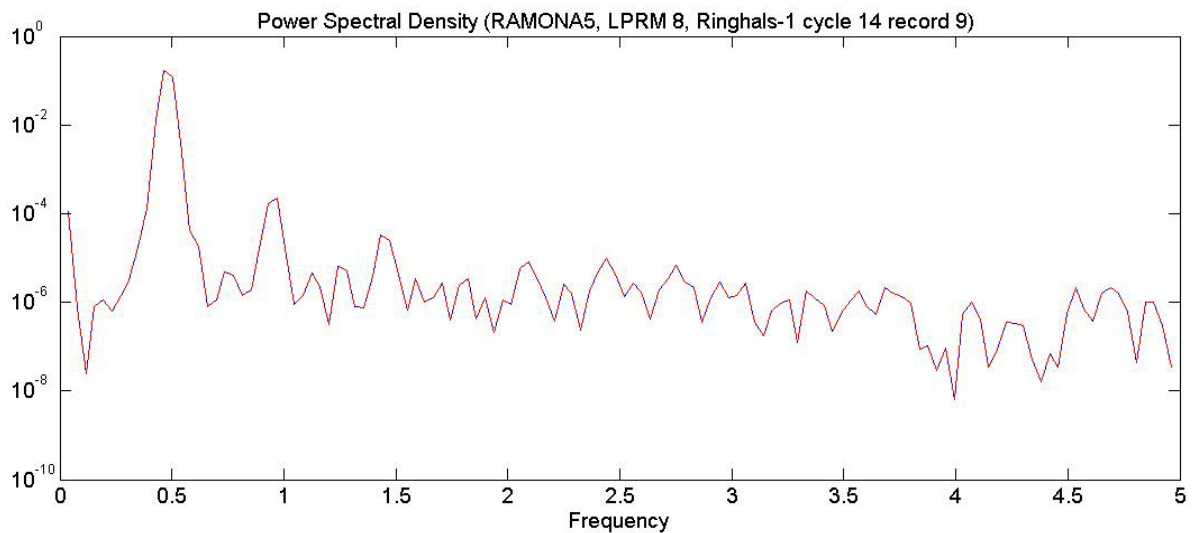


Figure 9: Power spectral density corresponding to LPRM 8 of the fourth level.

1.3 Summary of the ROM analysis

All design parameters of the ROM have been calculated from the Ringhals-1 RAMONA5 model for the reference OP (cycle 14 record 9). Thereby the new calculation procedure for the ROM input parameters was applied. As a result of the new calculation procedure, the steady state axial void profiles of RAMONA5 and ROM are consistent (see Figure 10).

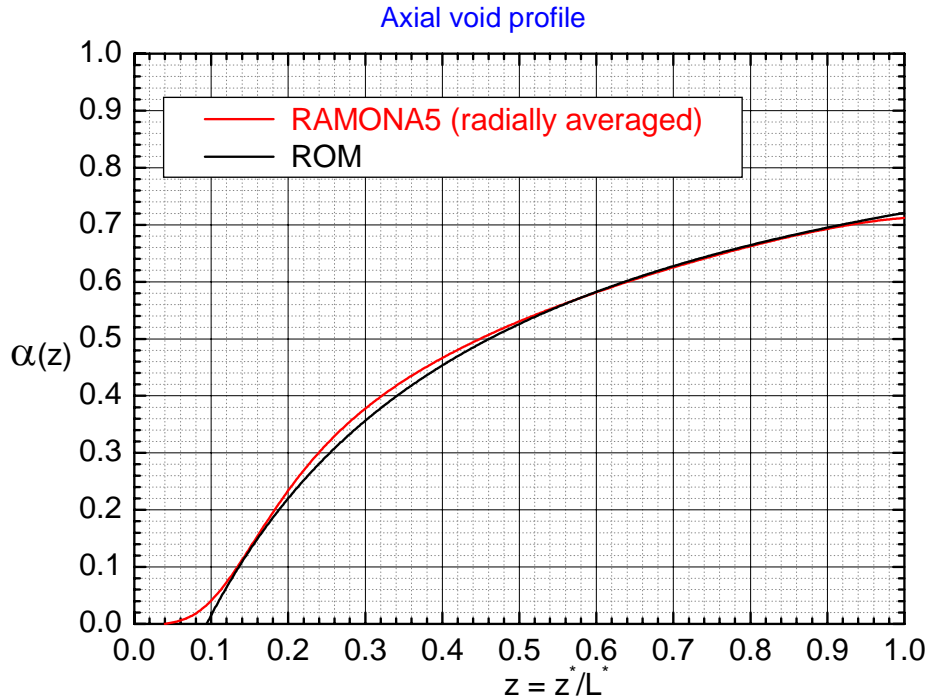


Figure 10: Comparison of the axial void profile calculated by RAMONA5 (radially averaged) with the axial void profile provided by the ROM.

In Table 2 are shown the pressure drops of RAMONA5 and ROM. The results of the RAMONA5- and ROM-pressure drops are consistent.

Table 2: Heated channel pressure drops provided by the RAMONA5 output and calculated by the ROM (KKRc14_rec9-OP).

Pressure drop	RAMONA5	ROM
$\Delta P_{ch,inlet}^*$	$-4.853 \cdot 10^4 Pa$	$-4.8556 \cdot 10^4 Pa$
ΔP_{ch}^*	$-2.474 \cdot 10^4 Pa$	$-2.4735 \cdot 10^4 Pa$
$\Delta P_{ch,exit}^*$	$-2.243 \cdot 10^4 Pa$	$-2.2409 \cdot 10^4 Pa$
DP_{ext}^*	$-9.57 \cdot 10^4 Pa$	$-9.57 \cdot 10^4 Pa$

Figure 11 summarizes the result of the numerical integration in the reference OP. As predicted by the RAMONA5 analysis, the oscillation is converging to a stable limit cycle.

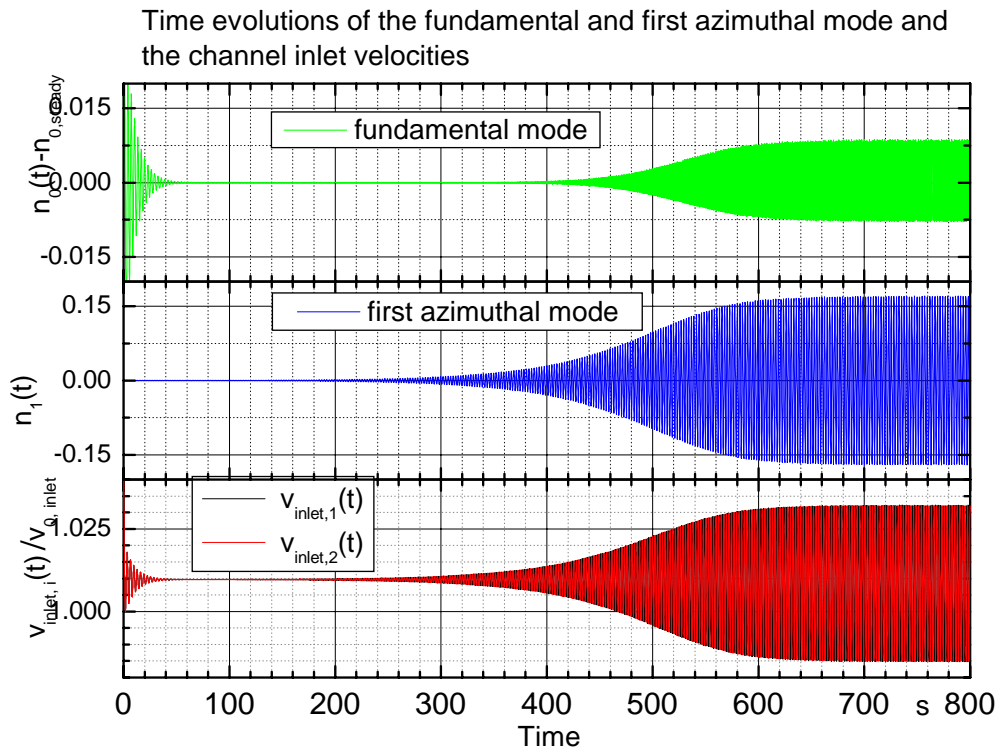


Figure 11: Time evolutions of the fundamental $n_0(t)$ and first azimuthal mode $n_1(t)$ and the channel inlet velocities $v_{1,inlet}(t)$ and $v_{2,inlet}(t)$.

In Figure 12 are shown the results of the bifurcation analysis. The stability boundary and the corresponding bifurcation characteristic are only plotted in the region which is reasonable from the physical point of view.

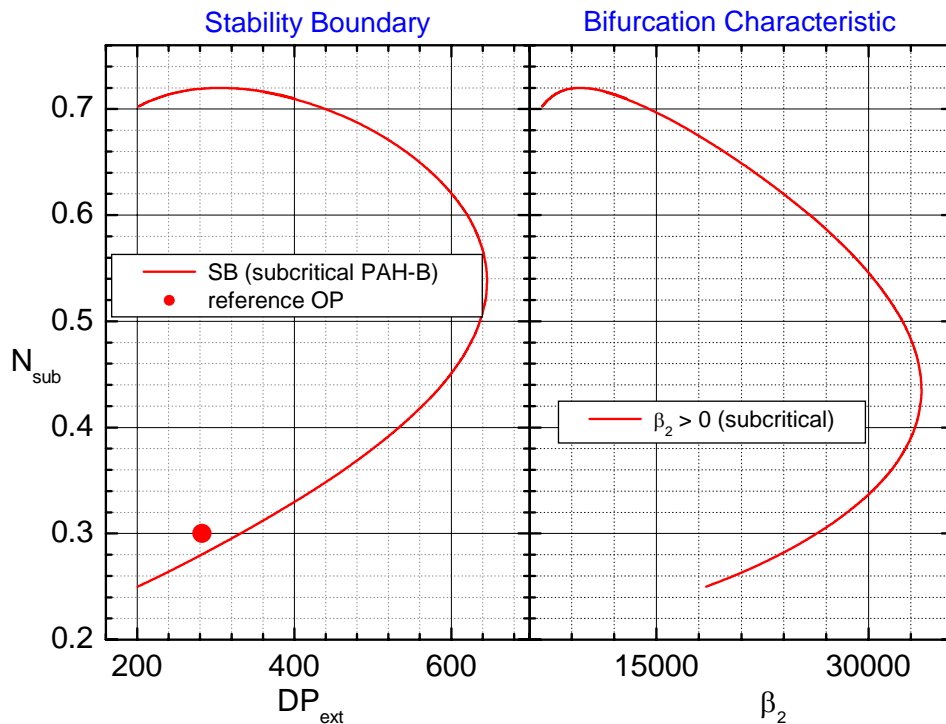


Figure 12: Stability boundary and bifurcation characteristic for the reference OP.

The reference OP is located in the linear unstable region close to the stability boundary. This result is consistent with the one of RAMONA5. Notice, in the scope of the nonlinear BWR stability analysis for KKRc14_rec9 a comprehensive RAMONA5 parameter variation study was performed (these results are not presented here) where selected parameters which have a significant impact on the BWR stability behaviour, were varied.

As shown in Figure 12 the bifurcation characteristic predicts unstable periodical solutions in the linear stable region. Supercritical PAH bifurcations do not exist in the N_{sub} - DP_{ext} parameter space. It should be stressed that stable limit cycle solution in the linear unstable region and unstable limit cycle solution in the linear stable region (but close to the SB) was found. Hence the occurrence of a saddle-node bifurcation of a cycle (similar to the KKLc7_rec4 case) can explain the stability behaviour of this analysis case.

In Figure 13 is presented the SB projected into the power flow map. In this map, the operating domain of the low flow-high power region of cycle 14 is included [1].

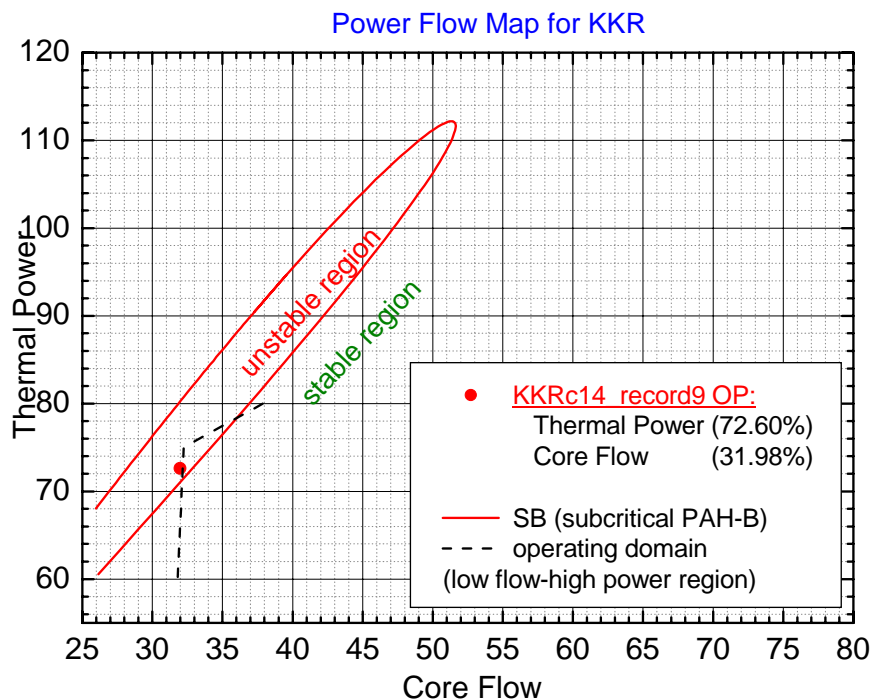


Figure 13: SB “transformed” into the power flow map.

Figure 14 presents the power flow map where the SB, the measurement points recorded during the stability test at the beginning of cycle 14, and their decay ratios [1] are included. It can be seen that the reduced order model predicts qualitatively well the location of the reference OP respect to the SB and to the other measurement points. The comparison study between RAMONA5 and ROM (results are not presented here) have shown that the qualitative stability behaviour in the reference OP and its neighbourhood is simulated correctly by the ROM. Existing quantitative discrepancies

between measurement data, RAMONA5 and ROM are due mainly to the uncertainties in evaluating the design and operating parameters as core averaged values.

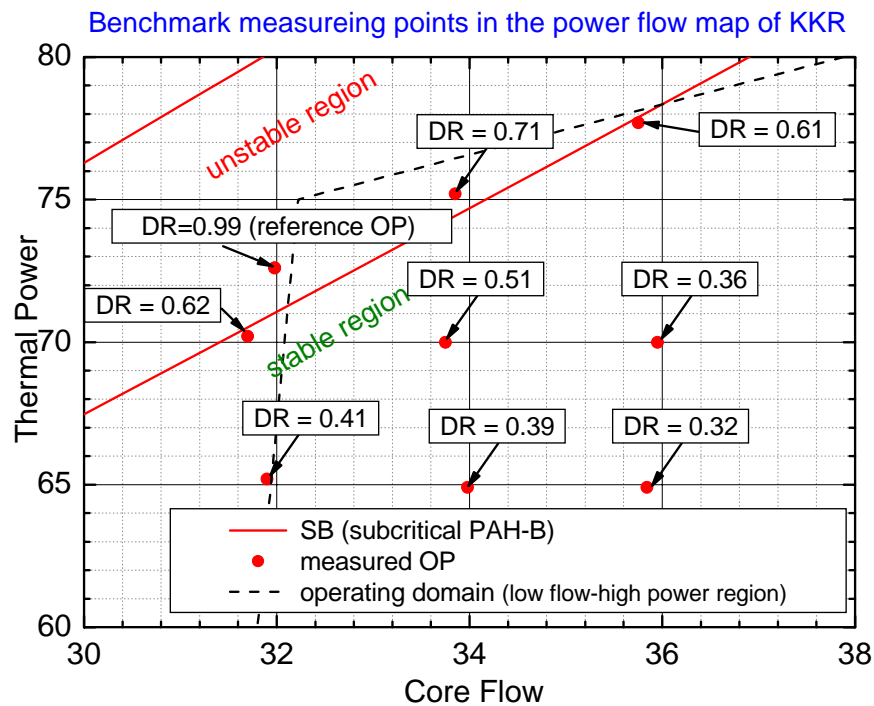


Figure 14: SB “transformed” into the power flow map. The measuring points of the stability test and the operating domain in the low flow-high power region are included this power flow map.

Literature

- [1] Tomas Lefvert; “*BWR STABILITY BENCHMARK*”; Nuclear Science Committee; OECD/NEA; 1994.
- [2] F.D. Giusti; B. Melkerson; L. Moberg; E. Rudbäck; “*Out-of-phase azimuthal oscillations in the Ringhals-1 BWR reactor – measurements, data analysis and qualification of a predictive RAMONA model*”;

Appendix I: Comparative study TOBI-ROM

Dokhane et al. carried out a detailed check of the thermal-hydraulic sub-model (TH-model) of the ROM [12,13] (see Literature of Chapter 6). One aspect was, the validation of the TH-model against experimental data and the comparison to several other analytical models able to simulate the stability characteristics of density waves [12,58,77,80]. Furthermore they compared the use of drift flux and homogeneous equilibrium models and carried out bifurcation analyses and numerical integrations of the TH-model equations. A sensitivity analysis was carried out, where the effects of different parameters (such as inlet and exit pressure loss coefficients, friction numbers...) on the stability characteristics have been investigated.

The objective of the current study is to replenish an additional check of the TH-model. To this end, appropriate results of the TOBI model which was developed by Wehle et al. [78] will be reproduced by the TH-model. TOBI is a simplified one heated channel BWR model, where the neutron kinetics, fuel heat transfer and thermal-hydraulics (boiling length, unheated length and riser) are taken into account. A detail description is given in [78]. In the scope of the comparative study TOBI-ROM, the results of the thermal-hydraulic sub-model of TOBI, without riser and unheated section, are compared with results of the TH-model of the ROM for specific OP's.

In Table 1 are presented the operational and design parameters used to generate the input parameters of the TH-model. Table 2 summarizes the main TOBI results for different powers. The pressure loss coefficients (K_{inlet} and K_{exit}) and the friction numbers ($N_{1\Phi}$ and $N_{2\Phi}$) of the TH-model have been calculated separately for each power.

Table 1: Operational and design parameters

system Pressure:	$P^* = 70 \text{ bar}$
channel inlet mass flow:	$\dot{m}^* = 5 \text{ kg} / \text{s}$
core inlet subcooling:	$h_{sub}^* = 100 \text{ kJ} / \text{kg}$ corresponds to $T_{sub}^* = 19.2 \text{ K}$
channel flow cross section:	$A^* = 0.01 \text{ m}^2$
hydraulic diameter:	$d_h^* = 0.011 \text{ m}$
length of the heated channel:	$L^* = 4.0 \text{ m}$
channel inlet pressure drop:	$\Delta p_{inlet}^* = 0.049 \text{ bar}$
axial power profile:	uniform axial power profile

Table 2: TOBI-results for different powers \dot{Q}^*

\dot{Q}^*	DR/Gr	x_{exit}	Δp_{exit}^*	Δp_{extern}^*
[kW]			[bar]	[bar]
2500	0.15	0.27	0.099	0.344
2750	0.20	0.30	0.110	0.354
3000	0.27	0.33	0.120	0.365
3250	0.33	0.37	0.130	0.378
3500	0.42	0.40	0.141	0.392
3750	0.51	0.43	0.151	0.406
4000	0.61	0.47	0.162	0.421
4250	0.74	0.50	0.172	0.436
4500	0.87	0.53	0.182	0.452
4750	1.01	0.56	0.193	0.469
5000	1.16	0.60	0.203	0.485
5250	1.33	0.63	0.214	0.502

Input data of the TH-model:

In the following the input data for the TH-model are presented for the reference power $\dot{Q}_{ref}^* = 4750 \text{ kW}$.

- $N_r = \frac{\rho_f^*}{\rho_f^* - \rho_g^*} = \frac{\rho_f^*}{\Delta \rho^*} = 1.051941496$
- $N_\rho = \frac{\rho_g^*}{\rho_f^*} = 0.04937679122$
- $Fr = \frac{v_0^{*2}}{g^* L^*} = 0.01164330537$, where v_0^* with $v_0^* = 0.676 \text{ m/s}$ is the reference channel inlet velocity.
- $K_{inlet} = 14.5$
- $K_{exit} = 8.1$
- $N_{1\Phi} = 2.5$
- $N_{2\Phi} = 4.4$
- $C_0 = 1.00$ (In this case, a uniform radial void distribution is assumed.)

- $V_{gj} = 0.8$ (V_{gj} was selected in such a way that the TH-model provides a DR/GR close to TOBI for the reference OP).

1.1 Results of the comparative study TOBI – ROM

After calculation of all input parameters, numerical integration of the TH-model equations is carried out for all powers given in Table 2. The time evolutions of the state variables are evaluated and the corresponding DR/GR is calculated. As a result, the function $DR/GR(\dot{Q}^*)$ is determined. The so-called grow ratios (GR) are calculated as

$$\langle GR \rangle = \frac{1}{k} \sum_{i=1}^k \frac{A_{i+1}}{A_i}, \quad (I1)$$

where A_i is the i -th amplitude. The approximation (I1) is only valid for sufficient small oscillation amplitudes or with other words: in a close neighbourhood of the singular fixed point in the phase space.

The results of the TOBI model and the TH-model are shown in Figure 1 and Figure 2.

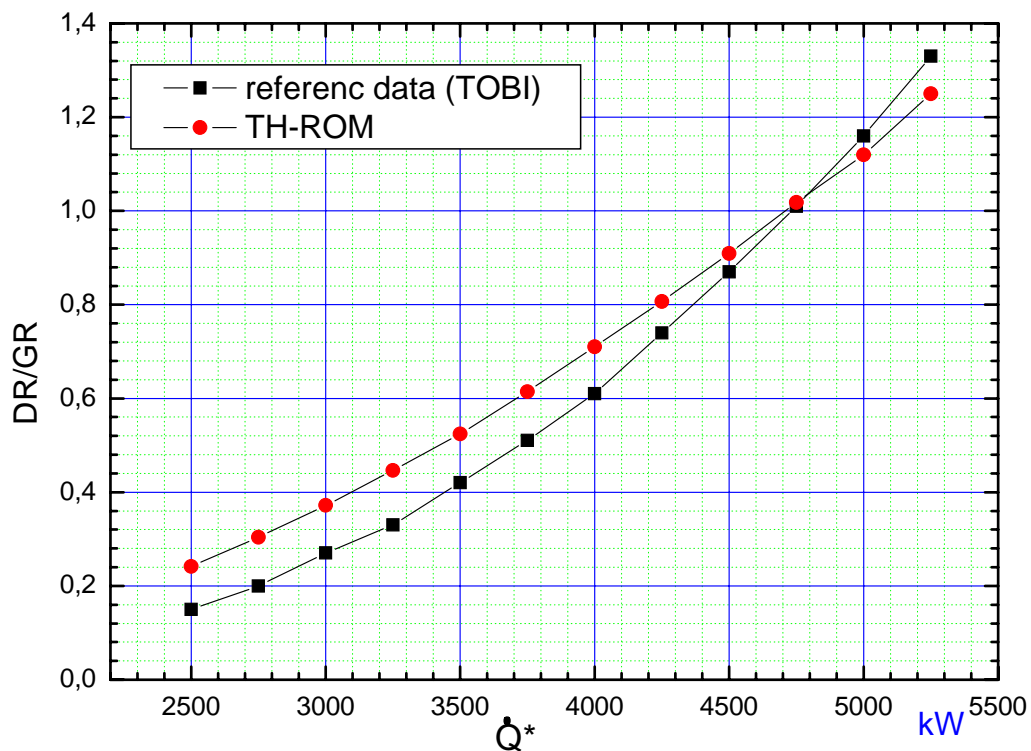


Figure 1: In this figure are shown the decay ratios (DR) and the grow ratios (GR) depending on the power imposed on the thermal-hydraulic channel ($DR/GR(\dot{Q}^*)$).

The comparison shows that the results of the TH-model (THM) are close to that one of TOBI. The best agreement between both functions $DR/GR^{TOBI}(\dot{Q}^*)$ and $DR/GR^{THM}(\dot{Q}^*)$ is achieved for the reference power $\dot{Q}^* = 4750 \text{ kW}$ because the input data are based on \dot{Q}_{ref}^* . The small deviation with increasing distance between \dot{Q}_{ref}^*

and the actual power \dot{Q}^* can be justified by, firstly, differences of model assumptions used in TOBI and TH-model and secondly, lack of knowledge about the single phase and two phase friction. Hence the dimensionless numbers $N_{1\phi}$ and $N_{2\phi}$ are unknown. For this analysis, both friction numbers are only estimated in an approximated manner.

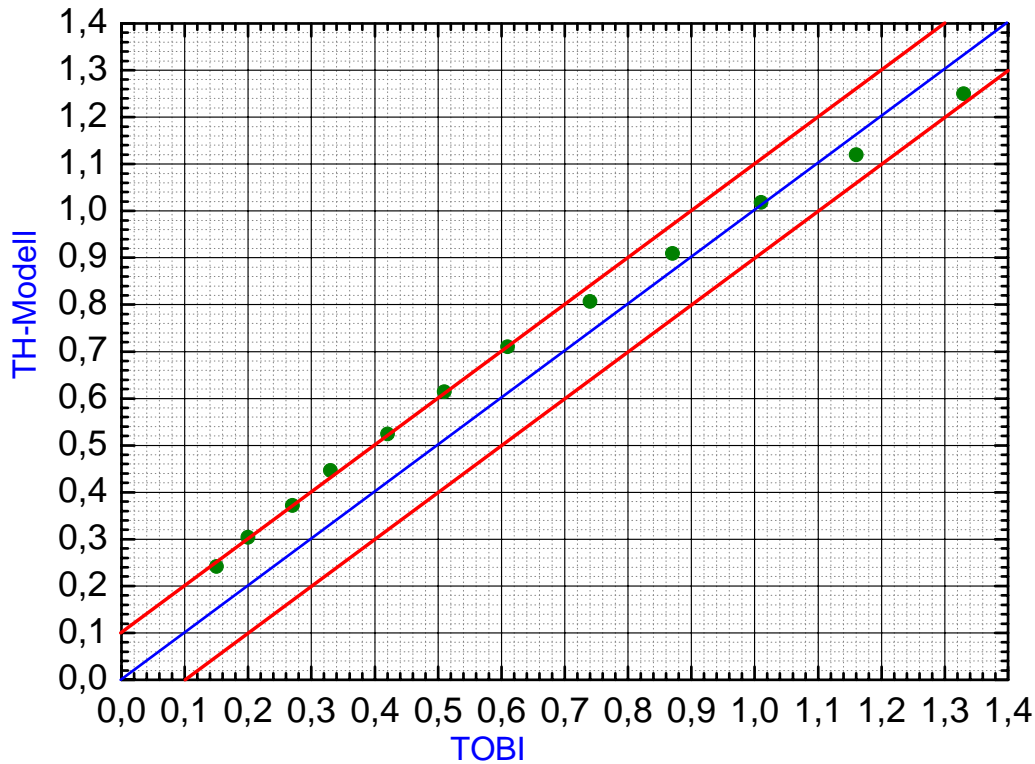


Figure 2: Comparison of the TOBI and TH-model results

1.2 Semi-analytical bifurcation analysis

In the scope of the bifurcation analysis using BIFDD, the core inlet subcooling h_{sub}^* and the thermal power \dot{Q}^* are selected to be the iteration and bifurcation parameter. This means, the bifurcation analysis is carried out in the $h_{sub}^* - \dot{Q}^*$ operating plane. While the core inlet mass flow is assumed to be constant, one point in this plane corresponds to a particular thermal-hydraulic state of the heated channel. The result of the bifurcation analysis is presented in Figure 3. Notice, the stability boundary and the bifurcation characteristic corresponds to the reference OP because all input data are based on it.

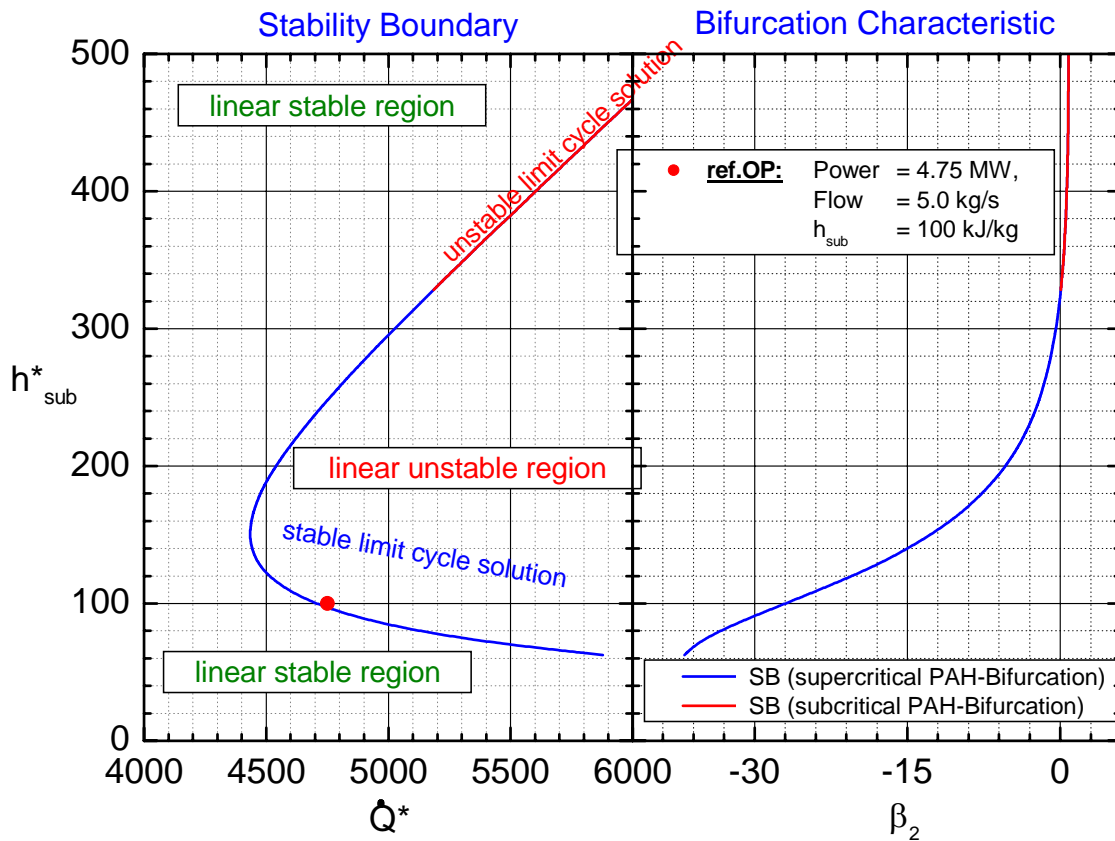


Figure 3: Stability boundary in the $h_{sub}^* - \dot{Q}^*$ parameter space and the corresponding bifurcation characteristic in the $h_{sub}^* - \beta_2$ plane.

The result of the bifurcation analysis shows that the reference OP is located in the linear unstable region close to the stability boundary. The Floquet parameter β_2 for $h_{sub}^* < 328$ kJ/kg is negative and for $h_{sub}^* \geq 328$ kJ/kg positive. This means, stable periodical solutions are predicted in the linear unstable region for $h_{sub}^* < 328$ kJ/kg and unstable periodical solutions are predicted in the linear stable region for $h_{sub}^* \geq 328$ kJ/kg. Hence, near the reference OP stable limit cycles are occurring. This result is consistent with the one of TOBI.

It should be pointed out that the maximum of the core inlet subcooling occurring in a real BWR is about $h_{sub}^* \approx 250$ kJ/kg which corresponds to $T_{sub}^* \approx 50$ K. Thus, only core

inlet subcoolings less than $h_{sub}^* \approx 250 \text{ kJ/kg}$ are taken into account. Consequently, for the present parameter configuration only stable limit cycles exist.

1.3 Numerical integration

In this section are shown some results of the numerical integration which was carried out in section 1.1. In order to demonstrate the thermal-hydraulic stability behaviour in the close neighbourhood of the stability boundary, the results for $\dot{Q}^* = 4680 \text{ kW}$, $\dot{Q}^* = 4708 \text{ kW}$, $\dot{Q}^* = 4750 \text{ kW}$ are shown firstly.

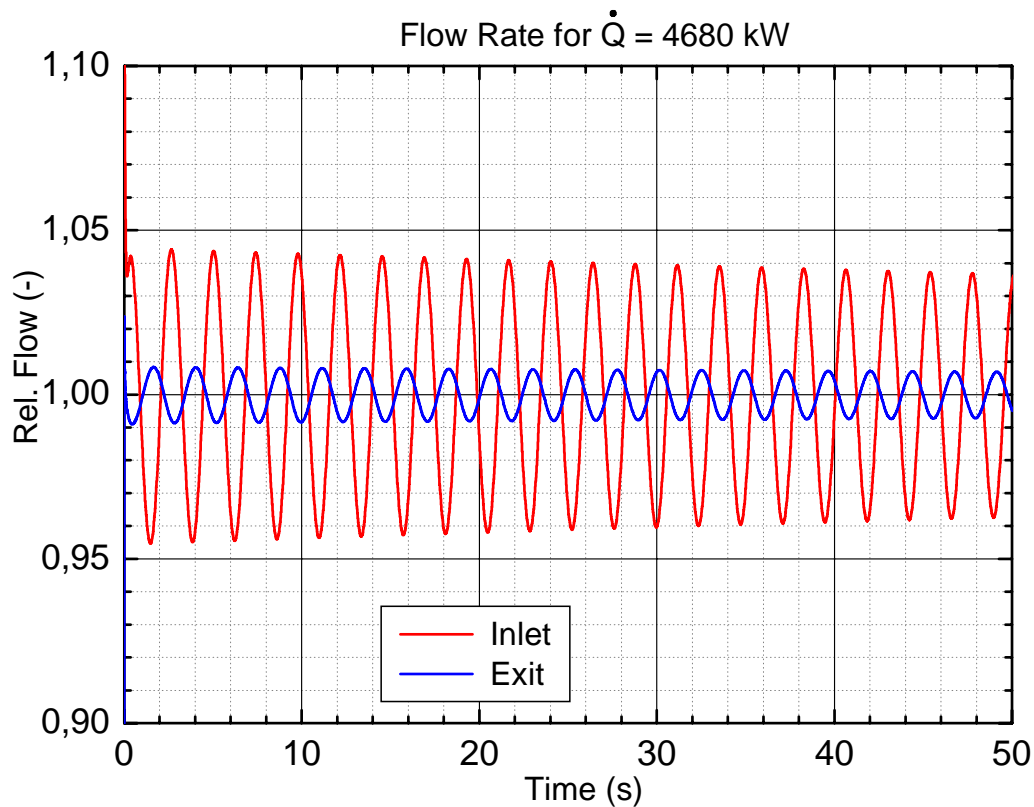


Figure 4: This figure show the time evolutions of the relative mass flow at the channel inlet and exit for $\dot{Q}^* = 4680 \text{ kW}$. This operational point is located in the stable region.

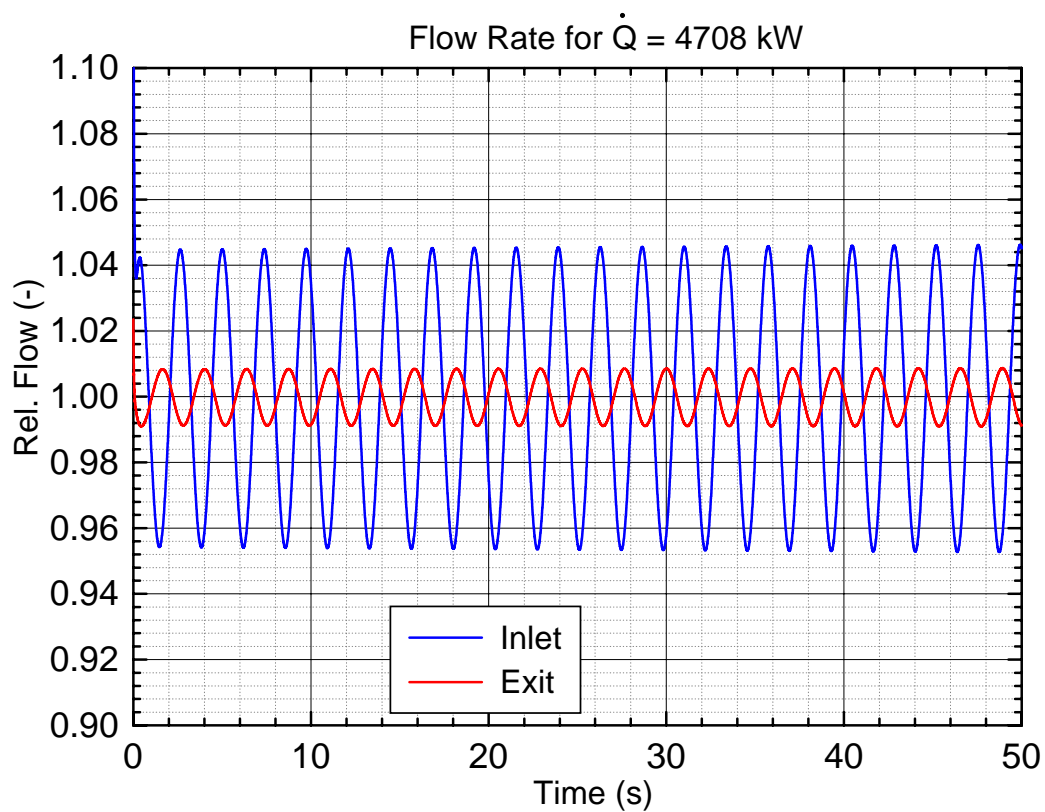


Figure 5: This figure show the time evolutions of the relative mass flow at the channel inlet and exit for $\dot{Q}^* = 4708 \text{ kW}$. This operational point is located in the unstable region close to the stability boundary.

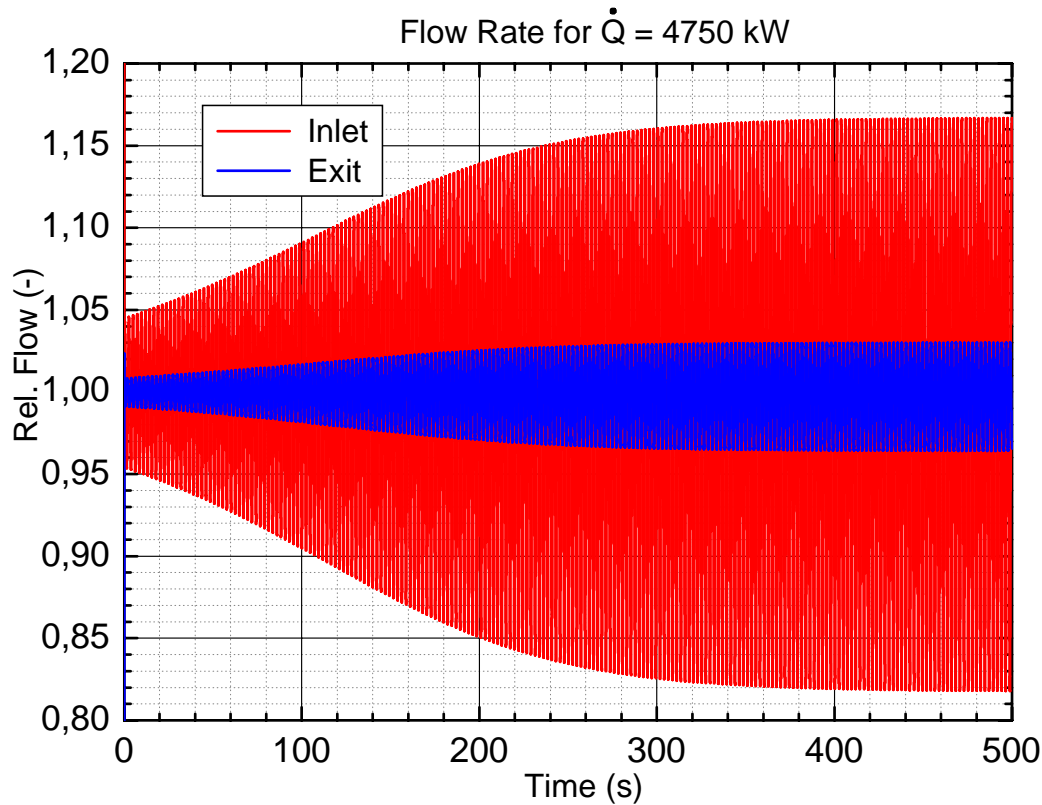


Figure 6: This figure show the time evolutions of the relative mass flow at the channel inlet and exit for $\dot{Q}^* = 4750 \text{ kW}$. In this operational point, a stable limit cycle is predicted by BIFDD and is confirmed by numerical integration.

1.4 Summary

In section 1.1, numerical integration of the TH-model equations is carried out for selected thermal powers. The time evolutions of the state variables are evaluated and the corresponding DR/GR is calculated. As a result, the function $\text{DR/GR}(\dot{Q}^*)$ is determined. The results of the TH-model are compared with the results of TOBI. The comparison shows that the results of the TH-model (THM) are close to that one of TOBI.

In section 1.2, semi-analytical bifurcation analysis with BIFDD was carried out. Thereby the core inlet subcooling h_{sub}^* and the thermal power \dot{Q}^* are selected to be the iteration and bifurcation parameter. The result of the bifurcation analysis shows that the reference OP is located in the linear unstable region close to the stability boundary. The bifurcation characteristic predicts stable limit cycles near the reference OP. This result is consistent with the one of TOBI.

The results of the numerical integration confirm the prediction of the bifurcation analysis.

Acknowledgment

I would like to thank Prof. Dr.-Ing. habil. A. Hurtado for giving me the opportunity to carry out this thesis work and for his support.

I would like to gratitude Dr. Hennig, my advisor, for introducing me into the worlds of nonlinear dynamics as well as reactor dynamics, for his continuous and contagious enthusiasm, for his permanent suggestions and encouragement, and for many valuable discussions.

Dr. A. Dokhane is greatly acknowledged for his warm hospitality during my stay at PSI, for introducing me into the BIFDD code and the numerical integration code, and for his valuable comments on the ROM modifications.

Many thanks to Prof. Rizwan-uddin for his valuable comments during PHYSOR 2008.

I wish to express my gratitude to Prof. R. Suarez for very useful discussions and comments to the research.

I wish to thank Prof. G. Verdù, R. Miro and V. G. Lorens for their warm hospitality and the nice time during my stays at UPV and for the interesting collaboration.

Thanks to Dr. Schuster and S. Böhlke for helping with all the small and big problems of everyday “department-life” and to S. Paufler for her administrative support.

I would like to thank Prof. Dr. rer. nat. W. Hansen, E. Liebscher, P. Tusheva and D. Thorn for the time they spend to correct the manuscript and for the useful discussions.

I'm indebted to Dr. S. Höche for the time he spent for discussions and recommendations to the manuscript.

Many thanks to A. Andris for his encourage service of my computers and their software.

I would like to thank my wife Claudia and her parents for their encouragement and patient. Without their support, the thesis work would not have been possible.

I'm indebted to my parents and to my grandparents for their support, encouragement and understanding through my whole life.